Ultra-Low Temperature Structural Investigations of Single-Molecule Magnets

Andrew Robert Farrell

M.Sci.

Submitted in fulfilment of the requirements

for the degree of Doctor of Philosophy

School of Chemistry

College of Science and Engineering

University of Glasgow

April 2013

Abstract

Previous studies of single-molecule magnets (SMMs) have interpreted their low-temperature (below 8 K) magnetic measurements on the basis of X-ray crystal structures measured at 100 K or even room temperature. The work presented herein describes the first structural measurements performed on SMMs in the temperature regime in which magnetisation studies are performed.

The ultra-low temperature (2 K) crystal structure of the prototypical SMM $[Mn_{12}O_{12}(O_2CMe)_{16}(H_2O)_4]\cdot 2MeCO_2H\cdot 4H_2O$ (Mn_{12}-acetate, **1**) was determined by using single-crystal X-ray and neutron diffraction. We have observed an additional hydrogen-bonding interaction in the disordered region of **1** that backs up the link between solvent disorder and disorder in the position of an acetate ligand. Two new desolvated species $[Mn_{12}O_{12}(O_2CMe)_{16}(H_2O)_4]\cdot 4H_2O$ (**2**) and $[Mn_{12}O_{12}(O_2CMe)_{16}(H_2O)_4]$ (**3**) were formed from **1** by single-crystal to single-crystal (SCSC) transformations and lead to the conclusion that the acetic acid of crystallisation in **1** is responsible for positional disorder in an acetate ligand. Another new $\{Mn_{12}\}$ derivative $[Mn_{12}O_{12}(O_2CMe)_{16}(CH_3CH_2OH)_4]\cdot CH_3CH_2OH$ (**4**) is formed by exposing the desolvated species to ethanol vapour.

The structure of the SMM $[Mn_3O(Et\text{-}sao)_3(ClO_4)(MeOH)_x(H_2O)_{3-x}]$ (**5**, Et-saoH$_2$ = C_6H_4-1-$CH(C_2H_5)$N(OH)-2-OH) at 2 K is also reported from a combination of single-crystal neutron and X-ray diffraction experiments. There is linked disorder in the identity of the coordinated solvent (methanol or water) and in the position of the ethyl substituent in the Et-sao^{2-} ligand. This leads to a number of possible isomers present in a single-crystal and is consistent with the observation of transverse anisotropy in **5** previously recorded by high-frequency- and high-field-electron paramagnetic resonance (HF-EPR) spectroscopy.

The crystal structure of the triangle intermediate $[Mn_3O(O_2CEt)_6(py)_3](ClO_4)$ (**6**, py = pyridine) formed during the synthesis of the SMM $[Mn_4O_3Cl_4(O_2CEt)_3(py)_3]\cdot 4MeCN$ (**7**) is reported for the first time. Additionally a related new compound $[Mn_4O_3Cl_7(O_2CEt)_3](C_5H_5NH)_3$ (**8**) that crystallises in the same space group as **7** is also reported.

The structure of the SMM $[Ni_4(dea)_4Cl_4]\cdot 4MeCN\cdot 0.6H_2O$ (**9**, deaH = $(HOCH_2CH_2)_2NH$) is reported at 1.7 K by using single-crystal neutron diffraction. The isostructural bromide complex $[Ni_4(dea)_4Br_4]\cdot 6MeCN$ (**12**) was synthesised for the first time and its structure is reported at 30 K. Methanol solvates of each species are also reported (**10** and **13**) and crystallise in the lower symmetry *P*-1 space group. **13** displays similar low-temperature (sub-3 K) magnetic behaviour to that reported for **9**, as well as an additional slow relaxation process at 4-6 K. Mass spectrometry is consistent with the formation of $\{Ni_4\}$ cubanes with *N*-substituted diethanolamine ligands, *N*-phenyl-deaH and triethanolamine (teaH); the former with chloride ligands and the latter with bromide ligands. Another new solvothermally-derived $\{Ni_4\}$ cubane species is described with a slightly different cubane core, $[Ni_4(dea)_4Br_2(H_2O)_2]Br_2$ (**14**).

We attempted to investigate two species based on a $\{Ni^{II}_{10}\}$ supertetrahedron (**16** and **17**); unfortunately the single-crystal neutron diffraction experiment carried out on these compounds was unsuccessful.

The structure of the SMM $(C(NH_2)_3)_8[Co_4(cit)_4]\cdot 4H_2O$ (**18**, H_4cit = $(HO_2CCH_2)_2C(OH)CO_2H$) was determined at 2 K using high-resolution neutron powder diffraction, single-crystal X-ray diffraction and single-crystal neutron diffraction. The former two measurements offer some evidence for disorder in the hydrogen bonding between the $\{Co_4\}$ clusters, guanidinium cations and solvent of crystallisation; however, the latter measurement does not support this. A series of inelastic and polarised neutron scattering measurements are presented for a deuterated sample of **18** (denoted **19**) and allow observation of scattering related to magnetic excitations.

Contents

Acknowledgments

The last three and a half years have been quite a journey: enjoyable, rewarding and frustrating in equal measure. And like any journey worth taking, it has not been taken alone. I would like to take this opportunity to acknowledge a few of the people who have helped and supported me along the way.

First I would like to express my gratitude to my supervisor, Mark Murrie, for giving me the opportunity to undertake this Ph.D. He has not only given me excellent advice and support, but it has also been a pleasure to have an ongoing rivalry between our football teams. I would also like to thank Simon Parsons for providing excellent training in crystallography and for his assistance with the many problems and questions I have had.

A good portion of my time has been spent either at the ILL, ISIS or Durham, or preparing proposals and looking at data in Glasgow. I am grateful to all those who have assisted me in this area: Garry McIntyre, Marie-Hélène Lemée-Cailleau, Silvia Capelli, Sax Mason and Aziz Daoud-Aladine for neutron diffraction; Grégory Chaboussant and Stefan Ochsenbein for neutron scattering; and Michael Probert and Jonathan Coome for X-ray diffraction. Thank you to Ross Inglis and Jonathan Hawkett for synthesising samples and making procedures available to me, and to Victoria Milway for assistance with my SQUID data.

The last few years would not have been the same without the other members of the Murrie group. Fraser, Laura, Vicki and Fraser: thank you for cake, lunches and visits to the pub, as well as being great companions on our trips to conferences and experiments. Also to Robbie, Steph, Smita, Chris, Niall, Claire, Kate, Jim, Anne, Neil, Susanne, Mark, Rebecca, Hannah and Jack, for a whole variety of reasons, thank you.

To mum and dad, thank you so much for all your love and support over the years, and especially in the last few months. I appreciate the practical support and encouragement you give me more than you know. Tim and David, thank you for your recommendations for new television shows to watch and for help and advice on all my technological questions.

And finally to Jennifer, words cannot express how much you mean to me. Thank you for everything. I cannot wait to begin our next adventure together.

Author’s declaration

The work contained in this thesis, submitted for the degree of doctor of philosophy, is my own original work, except where due reference is made to others. No material within has been previously submitted for a degree at this or any other university.

Chapter 1 Introduction

Theory of magnetism, X-ray crystallography and neutron scattering relevant to the research project

1.1 Magnetism and Single-Molecule Magnets

1.1.1 Magnetic Susceptibility

A material placed in an applied homogeneous magnetic field, *H*, gains a magnetisation, *M*. Equation 1.1 indicates the relationship between *H* and *M*; χ is the magnetic susceptibility.[1]

$$\chi = {}^{dM}/_{dH} \qquad (1.1)$$

If *H* is weak then *M* becomes independent of applied field and the equation for magnetic susceptibility can be simplified to that shown in equation 1.2.

$$\chi = {}^{M}/_{H} \qquad (1.2)$$

The magnetic susceptibility is the sum of diamagnetic (χ^D) and paramagnetic (χ^P) susceptibilies for the material, as shown in equation 1.3. These will be discussed further.

$$\chi = \chi^D + \chi^P \qquad (1.3)$$

Diamagnetic susceptibility is essentially independent of temperature and magnetic field strength, and can be estimated empirically as a function of molecular weight.[2] Diamagnetic ions have no unpaired electrons.[3] When placed in a magnetic field, a diamagnetic material is repelled by the field and possesses a negative induced magnetic moment. Paramagnetic materials contain unpaired electrons and when placed in a magnetic field will have a positive induced magnetic moment.[4]

The magnetic moments belonging to each ion in a paramagnetic material are oriented randomly in the absence of a magnetic field and so the bulk material does not exhibit a long-range ordering of moments. When a magnetic field is applied the individual moments will be aligned either parallel or antiparallel.[4]

1.1.2 The Curie Law

One of the most important equations in molecular magnetism is stated in equation 1.4.[1]

$$M = N_A \frac{\sum_n \frac{-dE_n}{dH} \exp(-\frac{E_n}{kT})}{\sum_n \exp(-\frac{E_n}{kT})} \qquad (1.4)$$

N_A is Avogadro's number, E_n is the energy of each thermally occupied state, n, and k is Boltzmann's constant. Van Vleck simplified this expression by making several approximations:[1] the field (H) must be weak and the temperature (T) must not be too small and it is assumed that we can expand the energies E_n by using an increasing power series in H. Application of these modifications gives the Van Vleck equation (1.5).

$$\frac{M}{H} = \chi = \frac{N_A \sum_n (\frac{E_n^{1(2)}}{kT} - 2E_n^{(2)}) \exp(\frac{-E_n^{(0)}}{kT})}{\sum_n \exp(\frac{-E_n^{(0)}}{kT})} \qquad (1.5)$$

The Van Vleck equation can be further simplified to give the Curie law (equation 1.6).[1] N is Avogadro's number, μ_B is the Bohr magneton, g is the electron spin g-factor, T is absolute temperature, k is the Boltzmann constant and S is the ground state. C is therefore a constant that depends on the ground state S of a complex.

$$\chi = \frac{Ng^2\mu_B^2}{3kT} S(S+1) \text{ or } \chi = \frac{C}{T} \qquad (1.6)$$

True paramagnets obey the Curie law; however, some paramagnets display spontaneous magnetic ordering below a specific temperature. Thus, we can introduce a further modification to take account of this.[4] The Curie-Weiss law (equation 1.7) has an additional constant, θ, known as the Weiss constant. Some paramagnets become ferromagnetic below a certain temperature, known as the Curie temperature (T_C). Spins become aligned parallel and the material exhibits a sharp increase in susceptibility. θ is positive for these materials. Other paramagnets become antiferromagnetic below a certain temperature, known as the Néel temperature (T_N). Neighbouring spins become aligned antiparallel and the material exhibits a decrease in susceptibility. θ is negative for these materials. Figure 1-1 illustrates qualitatively the behaviour of magnetic susceptibility for each of these materials.

$$\chi = \frac{C}{T-\theta} \qquad (1.7)$$

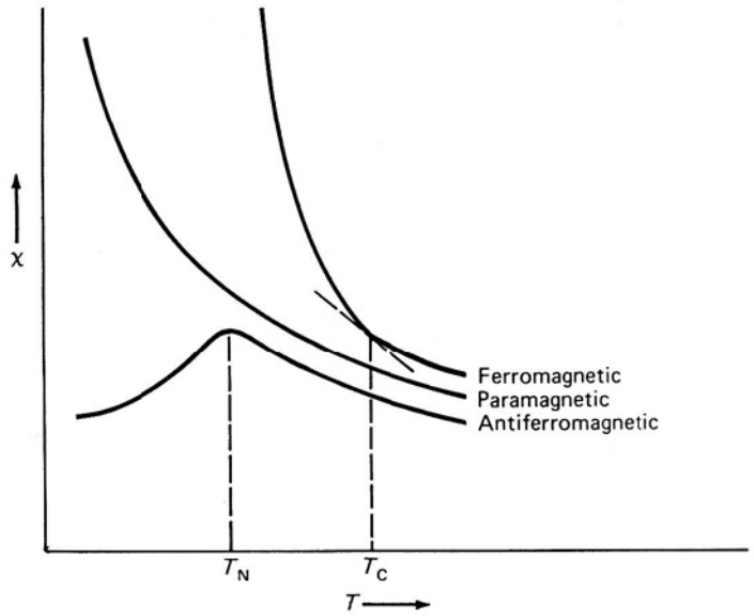

Figure 1-1: Temperature dependence of ferromagnetic, paramagnetic and antiferromagnetic behaviour. Reproduced from "Physical Methods for Chemists" by R. S. Drago.[5]

1.1.3 Exchange Interactions

Two paramagnetic ions can interact through an exchange interaction. Exchange interactions can occur through the direct overlap of metal orbitals containing unpaired electrons,[2] but this is uncommon since there is often insufficient overlap between neighbouring magnetic orbitals. More common is for the exchange interaction to occur between non-neighbouring magnetic ions through the *p*-orbitals of a mediating diamagnetic ion. This is known as superexchange and is strongly dependent on the characteristics of the orbital overlap.[2, 4, 6] The strength of the interaction depends on the distances between the ions involved, and the sign of the interaction (whether it is ferromagnetic or antiferromagnetic) depends on the M-L-M bridging angle.[7-9] For a bridging angle of 180° (figure 1-2), the unpaired electrons in the metal and ligand orbitals align antiparallel and consequently the interaction between identical paramagnetic ions is antiferromagnetic.

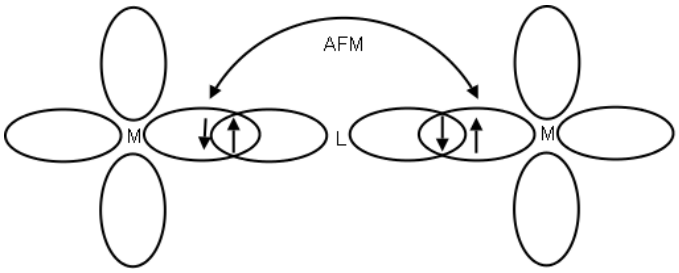

Figure 1-2: Superexchange between two paramagnetic ions, M, *via* a mediating ion, L, with a bridging angle of 180° giving rise to an antiferromagnetic (AFM) interaction.

For a bridging angle of 90° (figure 1-3), unpaired electrons in orthogonal *p*-orbitals of the non-magnetic ion undergo exchange stabilisation and tend to align with parallel spins. This results in a ferromagnetic coupling between the paramagnetic ions.[2] Thus, whether the interaction is ferromagnetic or antiferromagnetic depends strongly on the M-L-M bridging angle. For a series of analogous compounds there is normally a crossover point, below which an interaction is ferromagnetic and above which it is antiferromagnetic.[10] The exchange interaction between two paramagnetic ions is described using the Heisenberg spin Hamiltonian (one form is given in equation 1.8). For the Hamiltonian shown, a ferromagnetic interaction will have a positive value for *J* and an antiferromagnetic interaction will have a negative value for *J*. These definitions are arbitrary and depend on how the spin Hamiltonian is defined.

$$\hat{H} = -2\sum J_{ij}\hat{S}_i \cdot \hat{S}_j \qquad (1.8)$$

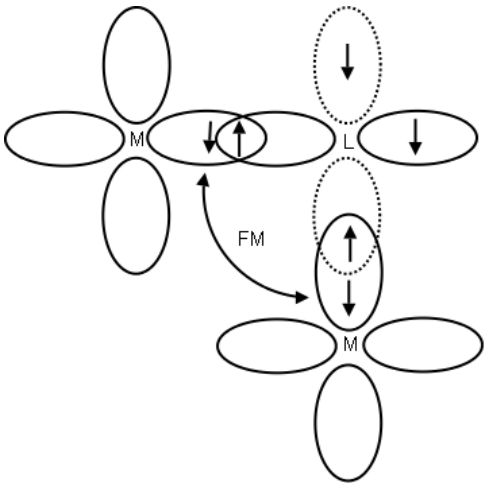

Figure 1-3: Superexchange between two paramagnetic ions, M, *via* a mediating ion, L, with a bridging angle of 90° giving rise to a ferromagnetic (FM) interaction.

1.1.4 Single-Molecule Magnetism

Magnetic materials are used in many applications, including devices for information storage. A hard disk contains a thin film of ferromagnetic material composed of a cobalt-based alloy. This is sub-divided into small magnetic regions, each of which has an associated magnetic moment that can be manipulated independently. In this manner the polarisation of each region can be altered such that it is possible to represent either state of a two-state system, depending on the direction of the magnetic moment. The minimum size of these particles is governed by thermal fluctuations which randomly reorient magnetic moments if they are sufficiently small. The maximum area density (related to the minimum magnetic particle size) was 635 Gbit/in² in 2010; this was conservatively projected to grow to 1300 Gbit/in² by 2014 assuming 20% growth year-on-year.[11] Increasing the areal density for data storage can only be achieved by decreasing the minimum particle size required to store one bit of information (a '1' or a '0').

Single-molecule magnets (SMMs) are comprised of paramagnetic metal ions bridged by organic ligands forming discrete clusters.[12] The paramagnetic ions interact with each other *via* superexchange interactions. SMMs retain their magnetisation after removal from a magnetic field below a blocking temperature, T_B.[13, 14] Normally T_B is only a few Kelvin; the highest reported blocking temperature for an SMM is 13.9 K (an N_2^{3-} radical-bridged terbium complex)[15] beating the previous record of 8.3 K set only a few months prior (an N_2^{3-} radical-bridged dysprosium complex).[16] This retention of magnetisation in the absence of an applied field occurs because SMMs have an energy barrier to reorientation of the magnetisation. The size of this energy barrier is given by equations 1.9 (integer ground state *S*) and 1.10 (non-integer ground state *S*).

$$U = S^2|D| \qquad (1.9)$$

$$U = (S^2 - ¼)|D| \qquad (1.10)$$

The properties of SMMs can be described well using quantum theory. Each unpaired electron in a paramagnetic ion contributes to an overall ground state, *S*, for the cluster, through superexchange with neighbouring ions. It can easily be seen from equations 1.9 and 1.10 that a non-zero ground state *S* is required for a non-zero energy barrier, *U*. *D* is the zero-field splitting (ZFS) of the ground state and must be large and negative (or axial) for SMM behaviour to occur. *D* results from the combination of the single-ion anisotropies

from each paramagnetic ion in the cluster. If D is negative, the ground state is split into $(2S+1)$ m_s levels, ranging from $-S$ to $+S$ in integer steps. The lowest energy m_s levels are the $-S$ and $+S$ levels and the highest energy level is $m_s = 0$. This gives rise to a characteristic double potential well of m_s states where positive and negative levels are separated by an energy barrier (figure 1-4 illustrates this arrangement for an SMM with S=10). Transition between positive and negative levels occurs thermally *via* the $m_s = 0$ level. U is the thermal energy barrier to spontaneous reorientation of the magnetisation. At sufficiently low temperatures the magnetic moment can be frozen on one side by application of a magnetic field. Hysteresis loops that are both temperature- and sweep-rate-dependent are observed in plots of magnetisation *vs*. field for SMMs.[6] An example is given in figure 1-5.

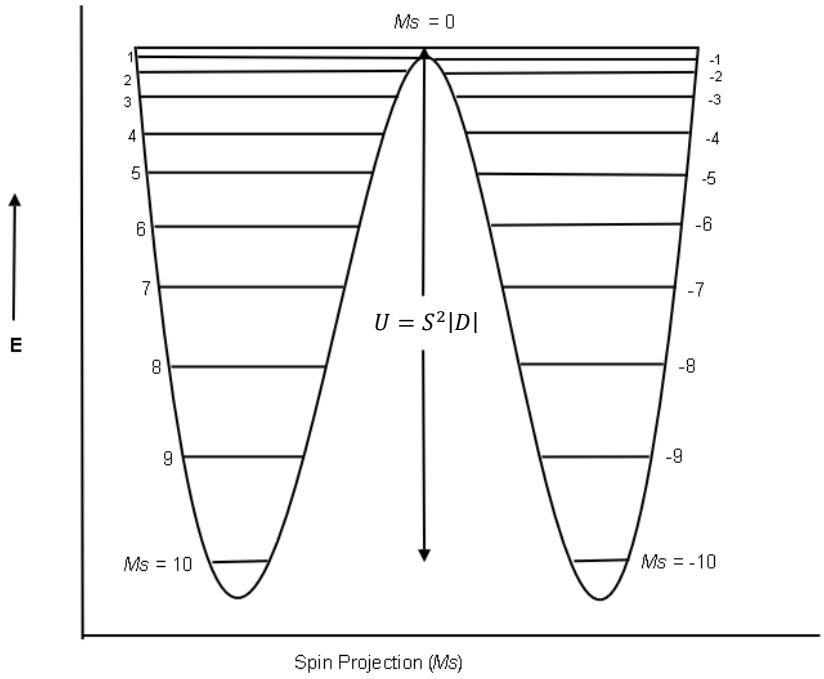

Figure 1-4: Double potential well of m_s states for a single-molecule magnet (SMM) with S = 10, *e.g.* Mn_{12}-acetate. $U=S^2|D|$. Adapted from a figure by Bagai and Christou.[17]

Magnetic susceptibility can be split into two components: in-phase (χ') and out-of-phase (χ''). SMMs exhibit a frequency-dependent out-of-phase magnetic susceptibility when placed in an ac field. This occurs because when the sample experiences an oscillating magnetic field, the reorientation of magnetisation cannot keep up with the changing field.[18] An ac out-of-phase susceptibility *vs*. temperature plot is shown in figure 1-6 for the SMM Mn_{12}-acetate. The relaxation time for an SMM follows the Arrhenius law for thermal activation over an energy barrier U, shown in equation 1.11.

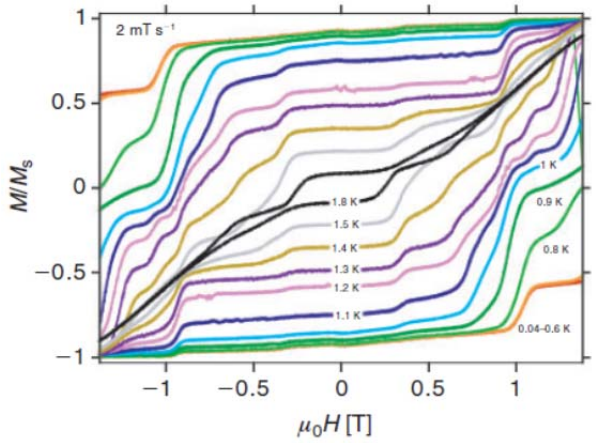

Figure 1-5: Sample magnetisation *vs*. field hysteresis loops, measured along the easy axis of magnetisation for a single crystal of $[Mn^{III}_3O(Et\text{-}sao)_3(ClO_4)(MeOH)_3]$.[19] (Et-saoH$_2$ = ethyl-salicylaldoxime).

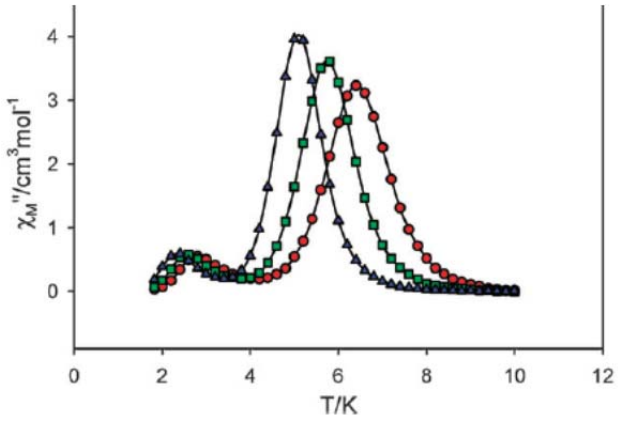

Figure 1-6: Plot of ac out-of-phase susceptibility *vs*. temperature for the SMM Mn_{12}-acetate. 3 frequencies are shown in this plot, coloured red, green and blue respectively. There are two frequency-dependent peaks (at 4-6 K and 2-3 K), thought to correlate with two distinct relaxation processes with different relaxation rates.[20, 21] Reproduced from a figure by Chakov *et al*.[22]

$$1/2\pi\nu = \tau_0 e^{\frac{U}{kT}} \qquad (1.11)$$

ν is the ac frequency in Hertz, T is the temperature (K) at which the maximum occurs in the out-of-phase ac susceptibility plot, k is the Boltzmann constant and τ_0 is a constant. Therefore if the measurement is repeated for a range of frequencies, *U* can be extracted. Figure 1-7 illustrates the linear relationship between $\ln(1/2\pi\nu)$ and 1/T.

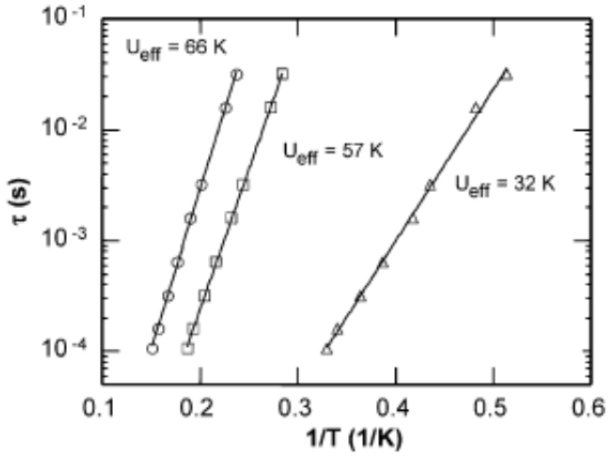

Figure 1-7: Logarithmic plot of relaxation time $(\tau = 1/2\pi\nu)$ *vs*. 1/T for three {Mn_{12}} SMMs using out-of-phase ac susceptibility data (using equation 1.11).[23] The solid lines are fits to the Arrhenius equation. In practice, this calculation gives the effective energy barrier (U_{eff}). U_{eff} is lower than U since the height of the energy barrier is lowered by quantum tunnelling.

SMMs are an ideal candidate for research towards higher density data storage, with one molecule potentially able to store one bit of information due to the magnetic bistability exhibited at low temperatures. It has been suggested that SMMs could store data at an areal density of up to 200 Tbit/in².[24] The application of SMMs as qubits in quantum computers has also been proposed.[25, 26] Recent work has focused strongly on integrating SMMs into surfaces and devices,[27] including carbon nanotubes,[28] with the aim of achieving a workable coupling between the nanoscale units and the macroscopic world.

1.1.5 Quantum Tunnelling

Thermal energy is not the only method of relaxation of the magnetisation in SMMs. Fast relaxation is observed at certain values of applied field that cannot be explained by over-barrier activation. The reason for this is quantum tunnelling of the magnetisation (QTM).[29, 30] Tunnelling occurs between two levels of the same energy. Application of a magnetic field raises the energy of one set of m_s states and lowers the energy of the other set.[31] There are certain values of field where a positive m_s state will be aligned with a negative m_s state. Mixing of the states can occur leading to under-barrier relaxation. This phenomenon is observed as steps in the magnetisation *vs*. field hysteresis loops caused by fast relaxation. It is a problem for potential data storage applications of SMMs; data storage relies on the magnetic moment of a molecule remaining frozen in one direction. QTM allows fast relaxation well below the calculated energy barrier (*e.g.* $U = S^2|D|$) and thus, the data

could more easily be lost. QTM is responsible for a lower effective energy barrier than what is expected ($U_{eff} < U$).[32] Figure 1-8 illustrates possible relaxation routes for SMMs.

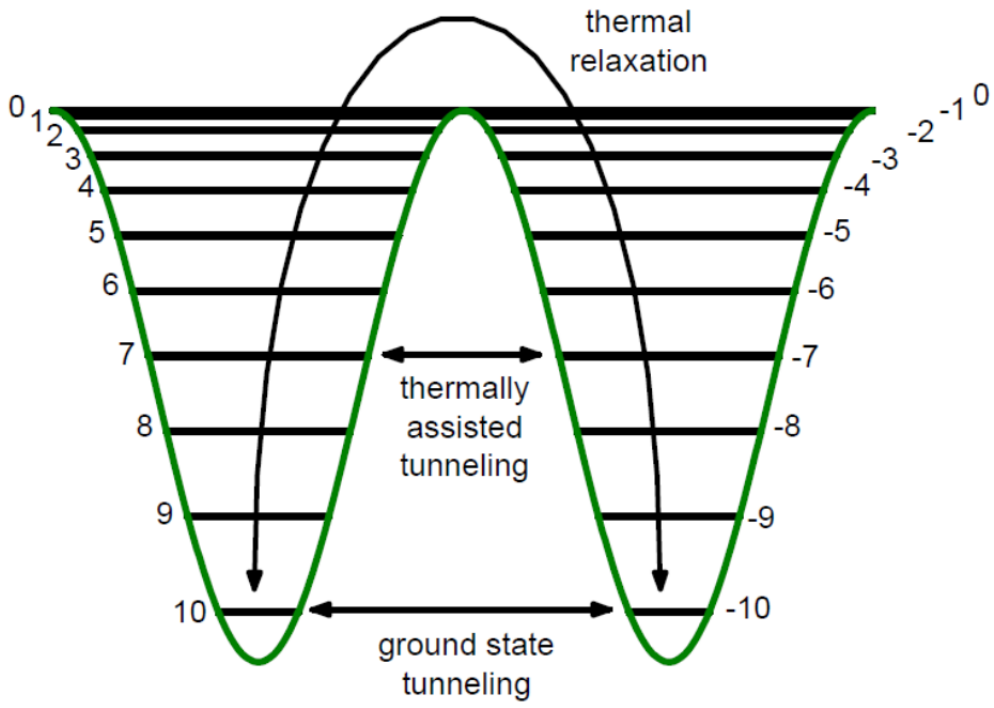

Figure 1-8: Routes for relaxation of the magnetisation in SMMs. Reproduced from "Frequency Domain Magnetic Resonance Spectroscopy on Molecular Magnets" by J. van Slageren.[33]

The general zero-field Hamiltonian for SMMs can be considered in the context of QTM (equation 1.12).[13, 34] D is the axial anisotropy, E is the transverse anisotropy, $\hat{S}_z$ is the spin operator projected onto the molecular easy axis and $\hat{O}^k{}_4$ are Stevens operators related to higher order anisotropy.[6, 35] Terms higher than second order are not physically reasonable but are often required to adequately model the data, indicating that the model is only an approximation for the physics taking place.

$$H = D\hat{S}_z^2 + E\left(\hat{S}_x^2 - \hat{S}_y^2\right) + B^0{}_4\hat{O}^0{}_4 + B^2{}_4\hat{O}^2{}_4 + B^4{}_4\hat{O}^4{}_4 \qquad (1.12)$$

The first identified SMM, Mn_{12}-acetate, possesses axial S_4 molecular symmetry; thus, the second order E term and the quartic term $B^2{}_4\hat{O}^2{}_4$ are forbidden. The D term describes the energy barrier to thermal relaxation and, consequently, QTM should only occur due to the $B^0{}_4\hat{O}^0{}_4$ and $B^4{}_4\hat{O}^4{}_4$ terms with the selection rule $\Delta m_s = 4$. However QTM is not only observed for these transitions.[36, 37] This will be discussed further in chapter 2.

1.2 X-ray Crystallography

X-ray crystallography is a particularly useful tool for characterising single-molecule magnets. It allows unambiguous determination of the structure of a material, with the caveat that it is necessary to grow high-quality single-crystals.

In order to observe objects on the atomic scale it is necessary to use a technique that uses wavelengths of the same order or smaller. Atoms and molecules are much smaller than the wavelength of visible light and so they cannot be observed optically. X-rays are commonly used since they have a smaller wavelength (typically 0.71-1.54 Å) than molecular distances (1-5 Å).[38]

In an optical microscope, magnifying lenses are used to recombine light waves scattered from an object and produce a much larger image of that object. It is greatly more difficult to focus X-rays and so only the pattern of scattered waves can be recorded with no recombination taking place. Mathematical operations are used instead to simulate the physical processes that would recombine the scattered X-rays.[39]

X-rays are scattered by electrons and consequently all atoms will scatter X-rays. Each element has different scattering characteristics that are dependent on the number of electrons it possesses and how they are distributed in its orbitals. Every atom in a molecule will scatter X-rays independently of the others. Constructive and destructive interference subsequently takes place between the scattered X-rays from all atoms. This interference depends on the relative positions of the atoms. The result is a complex pattern of scattered X-rays that is unique for a given material.

The scattering of X-rays from a single molecule or small group of molecules is too weak to be detected and so it is necessary to use a highly ordered sample, known as a single crystal. A single crystal has a small repeating unit (the unit cell, typically a few hundred to a few thousand cubic Angstrom though can be larger) that defines the structure of the whole crystal through application of translational symmetry. Therefore, each molecule in the unit cell has many equivalents aligned in precisely the same way, that will scatter X-rays in precisely the same manner. The scattering from all molecules in the crystal is combined and this is sufficiently strong to be detected by modern X-ray diffractometers.

1.2.1 The Bragg Equation and the Ewald Construction

X-rays that are diffracted from a single crystal produce waves that can be measured by a detector when they constructively interfere.[39] It is easier to consider the diffraction of X-rays from planes imagined to pass through the crystal rather than from individual atoms. Figure 1-9 illustrates the scattering of X-rays from ordered planes and allows us to derive the Bragg equation. For constructive interference between scattered X-rays from parallel planes we require the path difference to be an integer multiple of the wavelength. From figure 1-9 it can be seen that the path difference for X-rays from two adjacent planes is $2\Delta = 2d\sin\theta$ (equation 1.13).[39]

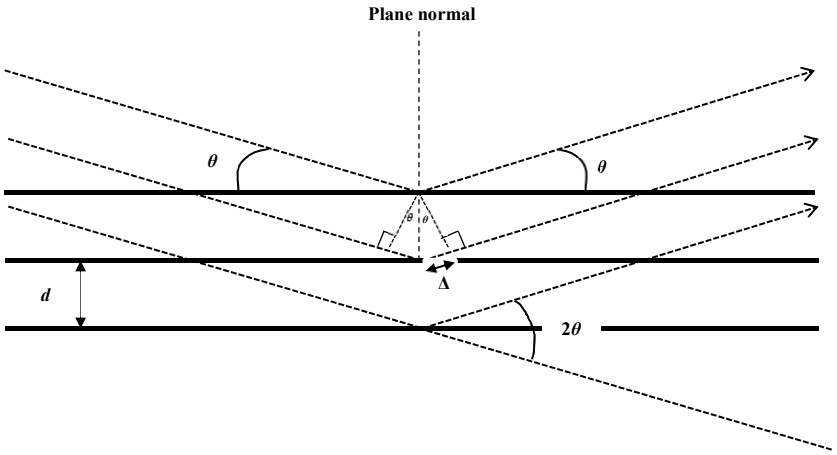

Figure 1-9: Bragg construction showing scattering of X-rays from ordered planes. Adapted from a figure by Clegg.[38]

$$\Delta = d\sin\theta \qquad (1.13)$$

$$n\lambda = 2d\sin\theta \qquad (1.14)$$

This path difference must be an integer multiple of the wavelength, *i.e.* nλ. Thus, we can derive Bragg's law (equation 1.14). Each plane (called a Bragg plane) is defined by its Miller indices (*hkl*). The values *h*, *k* and *l* are derived from the points along the *a*, *b* and *c* axes respectively that the plane cuts the axis. The (*hkl*) plane intercepts the points *a*/*h*, *b*/*k* and *c*/*l*. A reciprocal lattice can be constructed by taking the set of (*hkl*) planes as individual points. The *d*-spacing (separation between adjacent parallel lattice planes with the same (*hkl*) indices) can be calculated from the (*hkl*) indices and the unit cell parameters. The relationship for a simple cubic system is given in equation 1.15. This can be extended to lower symmetry systems by modification.

$$d = \frac{a}{\sqrt{h^2+k^2+l^2}} \qquad (1.15)$$

An X-ray diffraction (XRD) pattern typically consists of sharp, discrete points in a regular arrangement, the geometry of which is directly correlated with the geometry of the unit cell and the crystal lattice. The observed pattern is a two-dimensional slice of a three-dimensional lattice of points (the reciprocal lattice), each corresponding to diffraction from a different Bragg plane.[39] Reciprocal space has units of $Å^{-1}$ and °, compared to Å and ° for direct space. Points in the reciprocal lattice (observed as spots in the diffraction pattern) are equivalent to planes in direct space.[38] Reciprocal and direct space are related mathematically.

A good way of visualising the requirements for constructive interference, and consequently diffraction, to take place is by using the Ewald construction (figure 1-10). A sphere is drawn around the origin (the crystal) with radius $1/\lambda$. The reciprocal lattice of Bragg reflections is given an origin at the point where uninterrupted X-rays would exit the sphere.

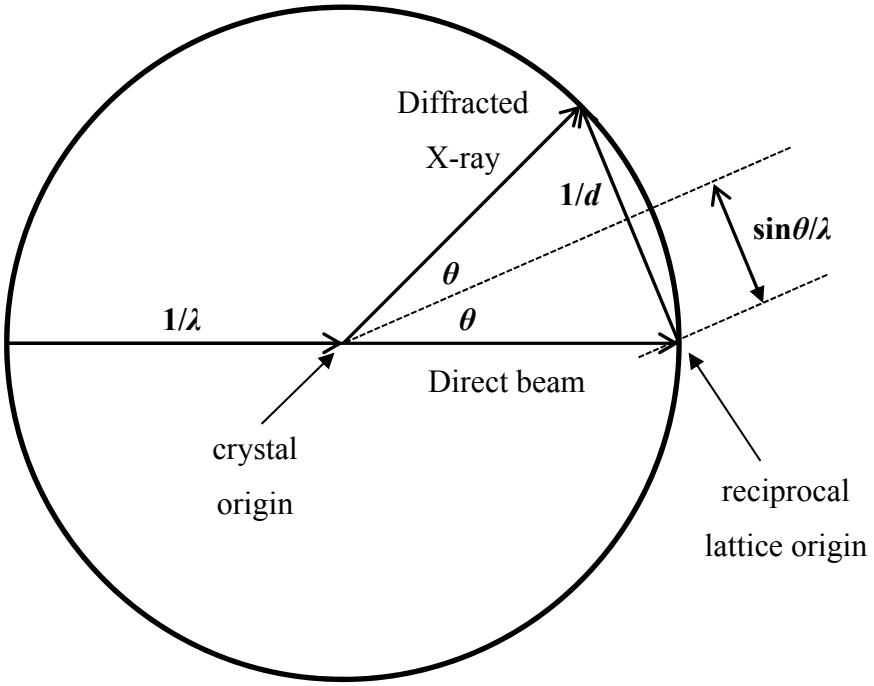

Figure 1-10: Ewald Construction. Although this is shown in 2D as a circle, in reality a sphere is a better representation since diffraction occurs in 3D. The geometry shown is fully applicable in three dimensions. Adapted from a figure by Glusker *et al*.[40]

By choosing a radius of $1/\lambda$, the length of the vector from the reciprocal lattice origin to the position of the observed reflection can be calculated as $2\sin\theta/\lambda$ (figure 1-10). From Bragg's law this can be rewritten as $1/d$. Therefore, it can be seen that for diffraction to occur, a

reciprocal lattice point corresponding to a Bragg plane will sit directly on the surface of the Ewald sphere.

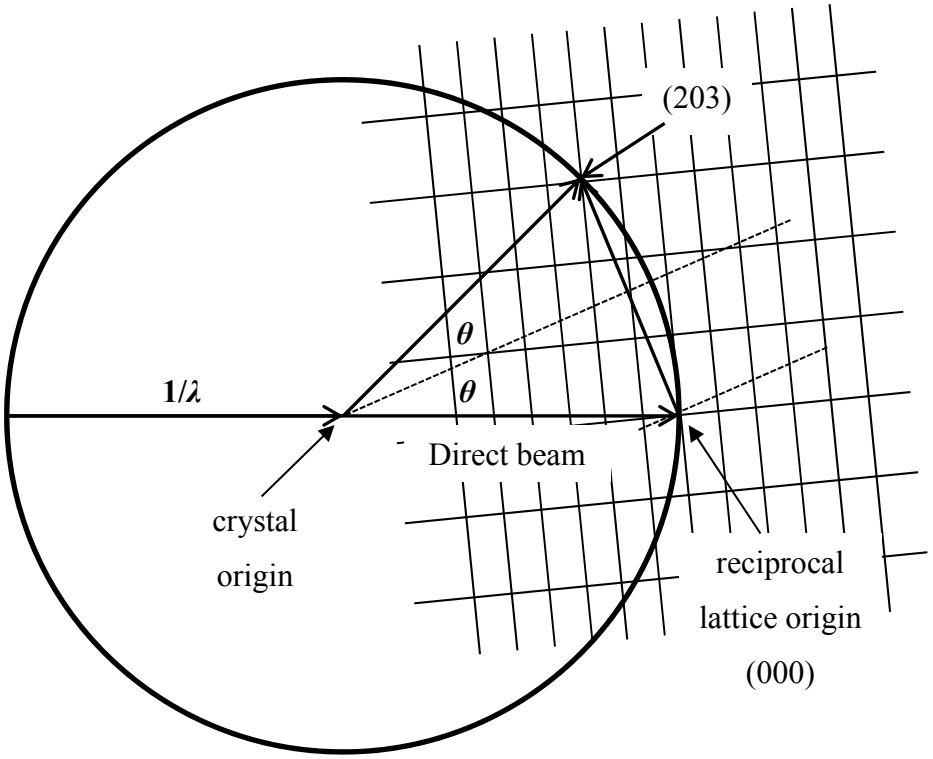

Figure 1-11: Ewald construction with overlaid reciprocal lattice showing that the (203) reflection sits on the edge of the sphere in this case and will be observed in the diffraction pattern. Adapted from a figure by Glusker *et al*.[40]

In part due to this condition and also due to the finite size of the detector, only a limited number of reflections will be observed for a single orientation of the crystal (figure 1-11). Rotating the crystal means that the reciprocal lattice is rotated relative to the Ewald sphere with the origin (000) reflection fixed at a single point. Moving the detector means that a larger number of reflections that do meet the diffraction condition for a given orientation are actually observed. Many reflections will be observed in this manner; however there is a physical limit related to X-ray wavelength that defines a point beyond which no reflections can be observed. The easiest way to consider this is to switch the stationary frame of reference to the reciprocal lattice and then rotate the Ewald sphere in all directions about the point fixed at the origin of the reciprocal lattice. This traces out a limiting sphere with radius $2/\lambda$, the diameter of the original sphere. Any lattice points that cannot pass within this sphere will not be observed. The size of the limiting sphere is governed only by the wavelength of X-ray radiation; the shorter the wavelength, the larger the sphere.[39]

1.2.2 Symmetry

There is often symmetry within the unit cell in addition to the translational symmetry between unit cells. This can include rotation (2-, 3-, 4- and 6-fold), improper rotation (or rotoinversion: $\bar{2}, \bar{3}, \bar{4}$ and $\bar{6}$), mirror planes, inversion centres, glide planes and screw axes.[38] A glide plane is defined as a reflection in a mirror plane followed by a translation; a screw axis is a rotation followed by a translation in the direction of the rotation axis. If a molecule has an inversion centre then it is centrosymmetric. The particular set of symmetry elements that a structure possesses defines its space group. There are 230 unique space groups each possessing a different combination of symmetry elements. These can be divided into seven types of crystal system, each of which has geometrical constraints placed upon it by its inherent symmetry. A summary of these is given in table 1.1.

Table 1.1: Restrictions on unit cell parameters set by symmetry elements.[41] For required symmetry, the type of rotation axis can be either proper or improper rotation, or a screw axis; mirrors can also be glide planes. The bracketed cell types are possible in theory, but are conventionally transformed into the non-bracketed type by a different choice of axes.

Crystal system	Required symmetry	Unit cell restrictions	Standard Cell Types
triclinic	none	none	*P*
monoclinic	2 and/or *m* for one axis	$\alpha=\gamma=90°$	*P, C*
orthorhombic	2 and/or *m* for three axes	$\alpha=\beta=\gamma=90°$	*P, C, I, F*
tetragonal	4 for one axis	$a=b$; $\alpha=\beta=\gamma=90°$	*P, I*
trigonal	3 for one axis	$a=b$; $\alpha=\beta=90°$, $\gamma=120°$	*P (R)*
hexagonal	6 for one axis	$a=b$; $\alpha=\beta=90°$, $\gamma=120°$	*P*
cubic	3 for four directions	$a=b=c$; $\alpha=\beta=\gamma=90°$	*P, I, F*

The unit cell is the smallest unique part of the structure by translation alone. However by considering the space group symmetry, an even smaller portion of the structure can uniquely define the whole crystal. This smaller portion is known as the asymmetric unit, and it can be the same as the unit cell or smaller depending on which symmetry elements are present. Application of all the space group symmetry elements to the asymmetric unit generates the complete unit cell.

1.2.3 Indexing and Data Collection

A small number of diffraction images are collected initially in order to determine the orientation matrix and consequently the unit cell. The orientation matrix describes how the

crystal is oriented relative to the diffractometer.[39] Once the diffractometer software has determined the orientation matrix it is able to compute an efficient strategy for measuring all reflections subject to the user's requirements concerning completeness, redundancy and collection time.

1.2.4 Data Reduction

Data are typically recorded on an X-ray diffractometer by an Image Plate (IP) or a Charge-Coupled Device (CCD). Both are area detectors but each works on a different principle. A detector based on a CCD contains a phosphorescent screen that absorbs X-rays and immediately emits visible photons that are observed by the CCD chip through a tapered fibre-optic bundle.[42] The readout time for an image on a CCD is negligible. X-rays hitting an IP detector excite electrons that are trapped in a higher energy state.[43] After exposure is complete, a laser is used to release the trapped electrons, which emit photons that can be detected by a reader.

After the data have been collected, the intensity of each reflection measured is determined by integration software. Some reflections are split between several recorded images; in such cases, the intensities must be integrated across all the images in which that reflection appears. Many reflections are measured more than once and can have different intensity despite their equivalence. One of the prime reasons for this is attenuation of X-rays by the crystal, particularly for crystals with one dimension significantly different from the other two. The distance that X-rays must travel through the crystal varies with orientation. According to the Beer-Lambert law, ($I=I_0e^{-\mu t}$) (I_0, I = incident, transmitted intensity; μ = attenuation coefficient; t = thickness),[41] absorption increases with thickness. In order to correct for this, a multi-scan correction is applied to the data. The intensities taken from each frame are scaled to ensure that multiple measurements of a single reflection are consistent.[39] This produces a list of reflections (defined by their Miller indices), the associated intensities and their uncertainties (used when applying a weighting scheme).

1.2.5 Fourier Transformations

The observed diffraction pattern is related to the crystal structure or more precisely, the electron density distribution of the crystal, by Fourier transforms. Each unique atom can be described by a set of parameters: the atomic scattering factor (f, known for each element),

thermal displacement parameters (U) and position coordinates (x, y, z). In a simple model where we assume the thermal displacement to be equal in all directions (isotropic), the Fourier equation can be written as shown below in equation 1.16.[38]

$$F(hkl) = \sum_{j=1}^{N} f_j(\theta) \cdot \exp(\frac{-8\pi^2 U_j \sin^2\theta}{\lambda^2}) \exp[2\pi i(hx_j + ky_j + kz_j] \qquad (1.16)$$

f_j is the atomic scattering factor of the jth atom and the first exponential term containing U_j accounts for isotropic thermal vibration. Integers h, k and l represent the miller indices of each particular reflection, and x, y and z represent the fractional coordinates of each atom contributing to that reflection. N is the number of atoms in the unit cell. The equation relates the structure factor for each reflection [$F(hkl)$] to the sum of contributions from every atom in the structure. The structure factor relating to the experimental (observed) data is called F_{obs} or F_o and consists of two parts: amplitude and phase. However, only the amplitude of F_o is obtained from an XRD experiment ($I \propto |F_o|^2$); the detector cannot measure any phase information for the reflections.[38]

If the crystal structure is known, equation 1.16 can be used to generate a set of calculated structure factors (denoted F_{calc} or F_c). The inverse Fourier transform that gives the electron density distribution in terms of the diffraction pattern is shown in equation 1.17.[38]

$$\rho(xyz) = \frac{1}{V}\sum_{hkl}|F(hkl)|\exp(i\phi_{hkl})\exp[-2\pi i(hx + ky + lz)] \qquad (1.17)$$

Equation 1.17 represents the theoretical process of recombining scattered X-rays that is impossible to achieve in practice and relates the electron density distribution to the observed structure factors for each reflection. The structure factor for each reflection is separated into amplitude and phase components in the above equation. Thus, it can easily be seen that it is necessary to know both amplitude and phase information for each reflection in order to apply equation 1.17.

1.2.6 Structure Solution Methods

There are various methods available that can attempt to derive phase information from a data set. One of the simplest is the Patterson function:[38] each structure factor is multiplied by its complex conjugate in order to remove the phase information and leave only $|F_{obs}|^2$,

which is known from the XRD experiment. Instead of calculating the electron density distribution, the Patterson function generates a map containing peaks corresponding to distances between two atoms. The intensity of peaks is directly proportional to the product of the atomic numbers of both atoms; thus, peaks representing vectors between the heaviest atoms in the structure will be much larger than those between the lighter atoms. Once a few atomic coordinates are known, approximate phases can be calculated using equation 1.16.

Another way of determining structure factor phases is by using direct methods. Various constraints are applied to ensure a physically reasonable electron density distribution will be generated.[39] A set of phases is assigned either randomly or from an approximate density map and subsequently refined subject to the defined constraints until a stable result is obtained. Functional tests are applied to every set of phases generated during this iterative process in order to calculate figures of merit (FOMs). The sets with the best FOMs are used to produce electron density maps. These are then considered chemically in order to determine the best possible match and, therefore, the most likely structure.

A more recent innovation in structure solution is the charge flipping algorithm.[44-47] This is termed a dual-space iterative method, as it is based on repeated modification of values in both direct and reciprocal space. A number of constraints are applied to the electron density based on experimental values and known facts. The structure factor amplitudes are known from the diffraction experiment; this constraint is based in reciprocal space. Some chemical knowledge can be used to apply constraints in direct space, similar to those used for direct methods. The charge-flipping algorithm applies an iterative procedure to find a solution that belongs to both the constraint sets in direct space and reciprocal space. It is a powerful tool and often is able to determine a solution when Patterson and direct methods cannot. A major advantage of charge-flipping over other methods is that the procedure does not use symmetry in the algorithm to determine a structure; structures are solved in a *P*1 space group. Furthermore because the electron density of the entire *P*1 unit cell is known, determination of symmetry can be carried out after structure solution. In practice the symmetry of the structure has usually been determined already so this process can confirm the original choice of space group.

1.2.7 Structure Refinement

The structure solution methods described above present a rudimentary model of atomic positions based on a calculated electron density map. Extra information can be added to this model to develop it further and improve its accuracy. Knowledge of the synthetic process used to grow the crystal can be used to fix incorrectly assigned C, N and O atoms (often wrongly assigned due to their similar *Z* values). A Fourier difference map can be generated by calculating the difference between F_{obs} and F_{calc} (using approximate phases from the model) in order to show discrepancies between the observed and calculated electron density distributions. This removes most of the strong electron density and allows missing atoms to be located.

Various parameters are used to model the structure including an overall scale factor, atomic coordinates, atomic displacement parameters (to describe thermal motion of each atom), site occupancy parameters and a Flack parameter (relating to absolute configuration). Least squares refinement is a process by which the difference between F_o and F_c can be minimised. There are two common ways of doing this in modern refinement programs. These are known as *F* refinement and F^2 refinement, and the relevant equations for each are given in equations 1.18 and 1.19 respectively.[38] F_c is the expected value of F_o; *w* is a weight that takes into account the reliability of that reflection.[39]

$$\chi^2 = \sum w(|F_o| - |F_C|)^2 \qquad (1.18)$$

$$\chi^2 = \sum w\left(F_o^{\,2} - F_C^{\,2}\right)^2 \qquad (1.19)$$

The refinement procedure attempts to minimise the function χ^2 by applying small shifts to the parameters described above. Considered simplistically, if the shifted parameter gives χ^2 a lower value the new parameter is deemed better. Restraints and constraints can also be added to the refinement. These restrict the range of possible values that each parameter can hold. An example of a restraint is to say that a C-H bond length must be 0.95 Å within a small standard uncertainty. Another restraint often used is to link the site occupancy parameters for a disordered molecule if it can be located in one of two positions. The sum of the occupancy parameters for both molecules must equal 1, with least squares refinement used to derive the best ratio of occupancies. A constraint is a more rigid restriction on parameters. A common constraint used on disordered solvent regions is to model a molecule as a rigid body. In this case a single set of parameters is used to define

the molecule rather than individual parameters per atom; these parameters are allowed to refine as normal. It is typical to perform several cycles of refinement consecutively, before reviewing the model and deciding if any improvements can be made. H atoms are often added in calculated positions with idealised parameters as they can be difficult to find in a difference map generated from X-ray diffraction data.

Two common expressions used to measure how well the model fits the experimental data are given in equations 1.20 and 1.21. These are based on the residuals from the least squares calculation.[39] Equation 1.21 is given for F^2 refinement.

$$R_1 = \frac{\sum||F_o|-|F_c||}{\sum|F_o|} \qquad (1.20)$$

$$wR_2 = \left\{\sum \frac{\left[w(F_o^2-F_c^2)^2\right]}{\sum\left[w(F_o^2)^2\right]}\right\}^{\frac{1}{2}} \qquad (1.21)$$

R_1 is the traditional '*R* factor' and is calculated from the sum of residuals divided by the sum of the observed structure factors. wR_2 is the 'weighted *R* factor' and also considers the weights given to each reflection. A lower value indicates better agreement between the model and the data.

X-ray crystallography using a laboratory diffractometer is an ideal way to quickly determine the structure of a new complex unambiguously. Diffractometers are routinely equipped with low-temperature instrumentation capable of cooling to 100 K. An Oxford Cryosystems HELIX low temperature device is able to cool to approximately 30 K and can be coupled to a laboratory diffractometer. The XIPHOS instrument at the University of Durham[48] is equipped with a Displex with an additional Joule-Thomson stage and can cool samples to 2 K. X-ray structure determinations were carried out at 100 K, 30 K and 2 K during the research project.

1.3 Neutron Scattering

Thermalised neutrons are ideally suited to probing the structure of condensed matter due to their unique properties. Although neutrons are classically described as particles (uncharged and having finite mass), they also exhibit wave-like behaviour. They have a wavelength

governed by de Broglie's theorem. They will be scattered or diffracted by a nucleus, in much the same way that electrons and photons are scattered by electrons. Additionally they are non-destructive and interact weakly with matter, leading to applications such as non-destructive analysis of historical artefacts and stress/strain studies of engineering components.[49]

The de Broglie wavelength of a thermal neutron is typically 0.5 - 10 Å. This is of the same order of magnitude as atomic spacings. The energy of such neutrons, which is related to wavelength by the expression $E = h^2/2m\lambda^2$ (h is Planck's constant, m is the mass of a neutron), is in the meV to eV range and so is appropriate for studying atomic movements. These two key properties are responsible for the ability of neutron scattering to yield information about structural features and also physical properties (*e.g.* molecular vibrations, magnetic transitions, quantum tunnelling and electronic transitions) simultaneously.[49]

Neutrons are produced either by a nuclear reactor or by using a pulsed spallation source. Each type has unique characteristics and is best suited for carrying out different types of experiment. A reactor source produces a steady output of neutrons from an enriched uranium core. The core is surrounded by a hydrogenous moderating material that slows the neutrons as well as cooling the core. A further moderator is used to provide neutrons of a specific wavelength; for example water at 300 K produces a Maxwellian distribution of neutrons with a peak at 1.2 Å. The neutrons are then sent through guide tubes to the experimental areas. An experiment can either use a 'white' beam, taking in the whole Maxwellian flux distribution, or use a monochromator to select a particular wavelength. The reactor at Institut Laue-Langevin (ILL), France, is currently the source of the most intense neutron flux in the world with a total output of 58 MW.[49]

A pulsed spallation source is very different to a reactor in the way that neutrons are produced. Charged particles are accelerated to high energies, usually using a linear accelerator and a small synchrotron, and then fired at a heavy metal target.[49] The target is usually composed of a combination of tantalum and tungsten. The impact of the charged particles on the target causes a series of nuclear reactions that each produces a large number of neutrons. Similar to those neutrons generated in a reactor source, these are high energy neutrons and must be moderated to achieve suitable energies for experiments on condensed matter. A hydrogenous material such as water or methane is ideal for

moderation due to the high scattering cross-section for neutrons exhibited by hydrogen.[49] Monochromators or 'choppers' (a series of rotating blades) can be used to select a specific wavelength for use in the experimental setup. Production of neutrons by spallation is significantly more efficient than from a reactor source; the total output of the most powerful pulsed spallation source in the world, SNS at Oak Ridge National Laboratory, USA, is currently only able to produce 1 MW. The pulsed spallation source at ISIS, UK has a power output of 160 kW.[49] By its very nature, a pulsed source is ideal for carrying out time-of-flight techniques. The linear accelerator- and synchrotron-based generation of a pulsed proton beam with tightly defined parameters means that the precise time each neutron is generated can be defined as the time the proton pulse hits the target. Neutrons of different wavelengths will travel at different speeds, defined by $\upsilon = h/m\lambda$, and so the wavelength of each neutron is known from its time of arrival at the instrument.[49]

There are two broad types of neutron scattering that can occur when neutrons are directed at a sample. Elastic scattering occurs when a neutron is scattered with no loss of energy and is commonly used for neutron diffraction. Inelastic scattering involves an energy change, with energy transferred from the neutrons to the sample or vice versa.

1.3.1 Neutron Diffraction

Elastic scattering can yield information about the positions of atoms and their thermal displacements. X-ray diffraction gives similar information but there are several key differences. X-rays scatter from electrons and so the intensity of diffracted X-rays increases with Z^2. Neutrons interact with the nucleus so the scattered intensity is dependent on nuclear properties. Although there is a general trend for scattering power to increase with atomic number, this is much less pronounced than for X-rays and there are wide variations between elements that are close together in the periodic table. In particular, the scattering power of hydrogen is much more similar in magnitude to heavier elements for neutrons than for X-rays. Additionally, scattering of X-rays by electrons falls off quickly as θ increases due to the diffuse nature of electrons around an atom, whereas scattering of neutrons by nuclei does not fall off with increasing scattering angle.[50] These properties have several consequences for neutron diffraction compared with X-ray experiments: it is much easier to accurately measure hydrogen atoms in the presence of heavier elements and data can be collected at very high resolutions not possible for laboratory X-ray experiments. Furthermore, it is possible to distinguish between elements of similar atomic

number – for example, Mn/Fe have scattering lengths with opposing signs - or even between isotopes of the same element – H/D also have scattering lengths with opposing signs, leading to the use of isotope contrast variation to highlight specific parts of a molecule. Another major advantage of neutrons is the ability to use bulky and complex sample environment equipment since they penetrate deeply into matter; pressure cells, low temperature devices or even reactor vessels can be constructed for use with neutron scattering. The use of such equipment with X-ray diffraction experiments, often using containers constructed from beryllium, results in broad powder lines on the diffraction images which must be masked out to avoid interference with the Bragg reflections. In the context of the work described herein, this allows the use of cryostats capable of reaching 2 K.

Two types of single-crystal neutron diffraction (elastic scattering) experiments were carried out during the research project, both using neutrons from the 58 MW research reactor at ILL, France. The first was performed using the single-crystal and fibre diffractometer D19, located on thermal beam H11 in the reactor hall.[51] The instrument is located directly adjacent to the reactor itself in order to maximise flux at the sample position. A monochromator is used to select a single wavelength of neutrons appropriate to the sample under study. Selecting a single wavelength greatly reduces flux compared with using a 'white' beam of neutrons and so the average minimum crystal size required is of the order of a few cubic millimetres, dependent on unit cell size and symmetry. The sample cradle and detector can be placed in one of three positions depending on the highest resolution required. D19 employs a large, curved, position-sensitive detector (PSD) covering 120° by 30°. The geometry of the sample cradle allows the use of large sample environment equipment. For the experiment described herein, a two stage Displex was used to cool below 20 K. An additional Joule-Thomson stage was specially modified for use on D19 and used to cool the sample to 2 K. The minimum achievable temperature using this modified setup is approximately 1.8 K, but it was decided to collect data at 2 K both for increased stability and also for consistency with the 2 K X-ray measurement carried out on XIPHOS at Durham University. Using monochromatic radiation and an area detector, the basic principles employed on D19 are similar to those used in conventional laboratory X-ray diffractometers with the sample being rotated through a range of ϕ, χ and ω positions in order to fulfil the Bragg conditions for observing each reflection. Data obtained using D19 will often be of similar or better quality than can be obtained on laboratory X-ray diffractometers providing sufficiently large single crystals can be grown.

Figures 1-12, 1-13 and 1-14 show a schematic and two photographs of the experimental setup on D19.

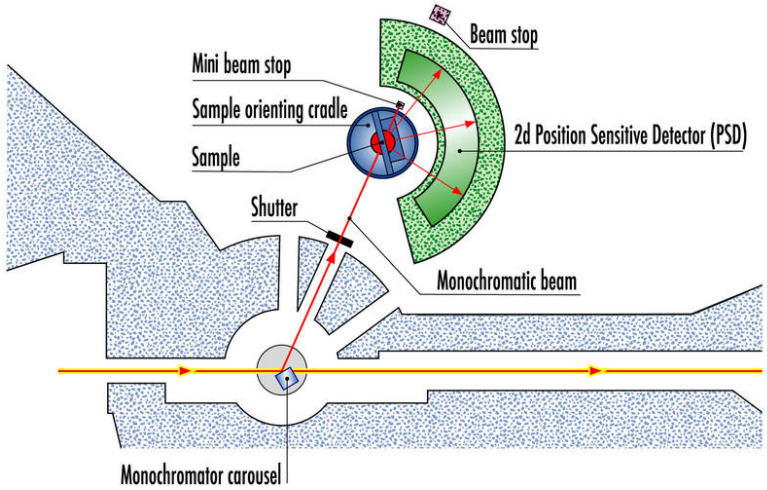

Figure 1-12: Schematic of the operation of the D19 single-crystal neutron diffractometer. Reproduced from the D19 user information guide.[52]

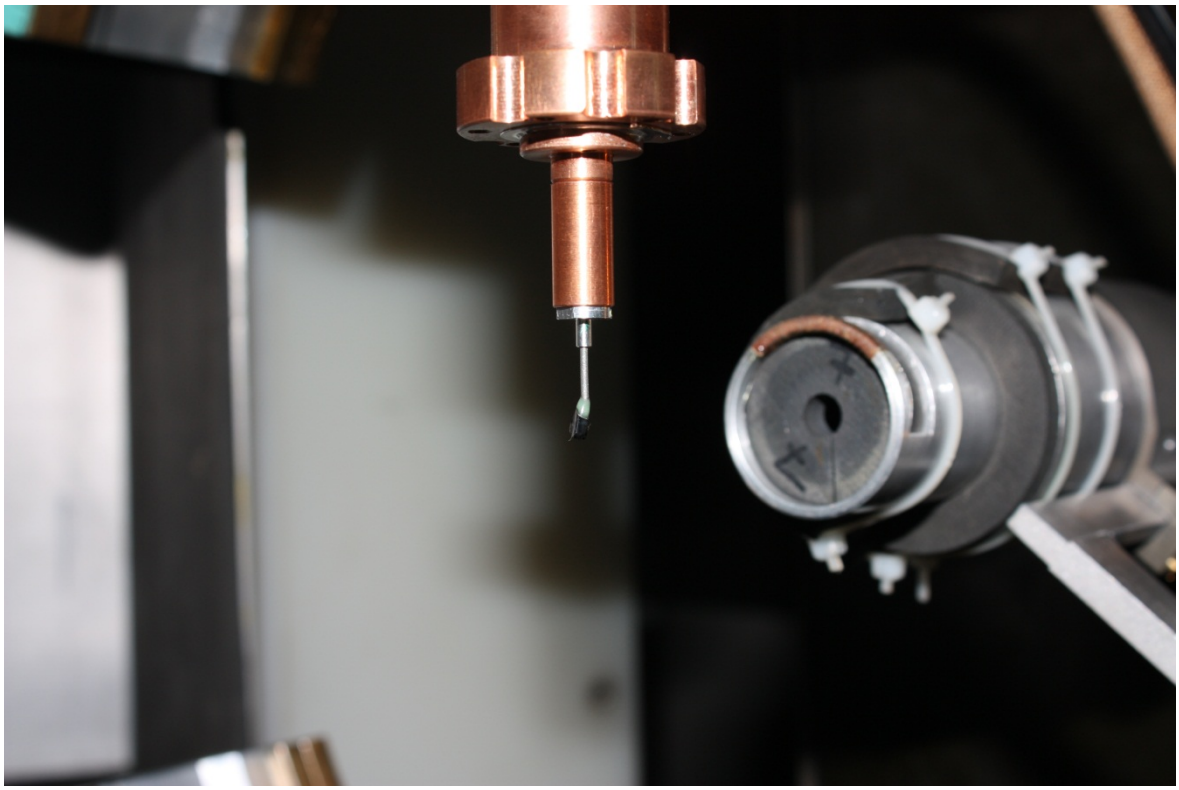

Figure 1-13: A black crystal of $[Mn_3O(Et\text{-}sao)_3(ClO_4)(MeOH)_3]$ is mounted on a vanadium rod prior to cooling inside the sample chamber. A large crystal is used in order to ensure that the diffraction data obtained are sufficiently strong since neutrons interact only weakly with matter. Photograph taken by the author.

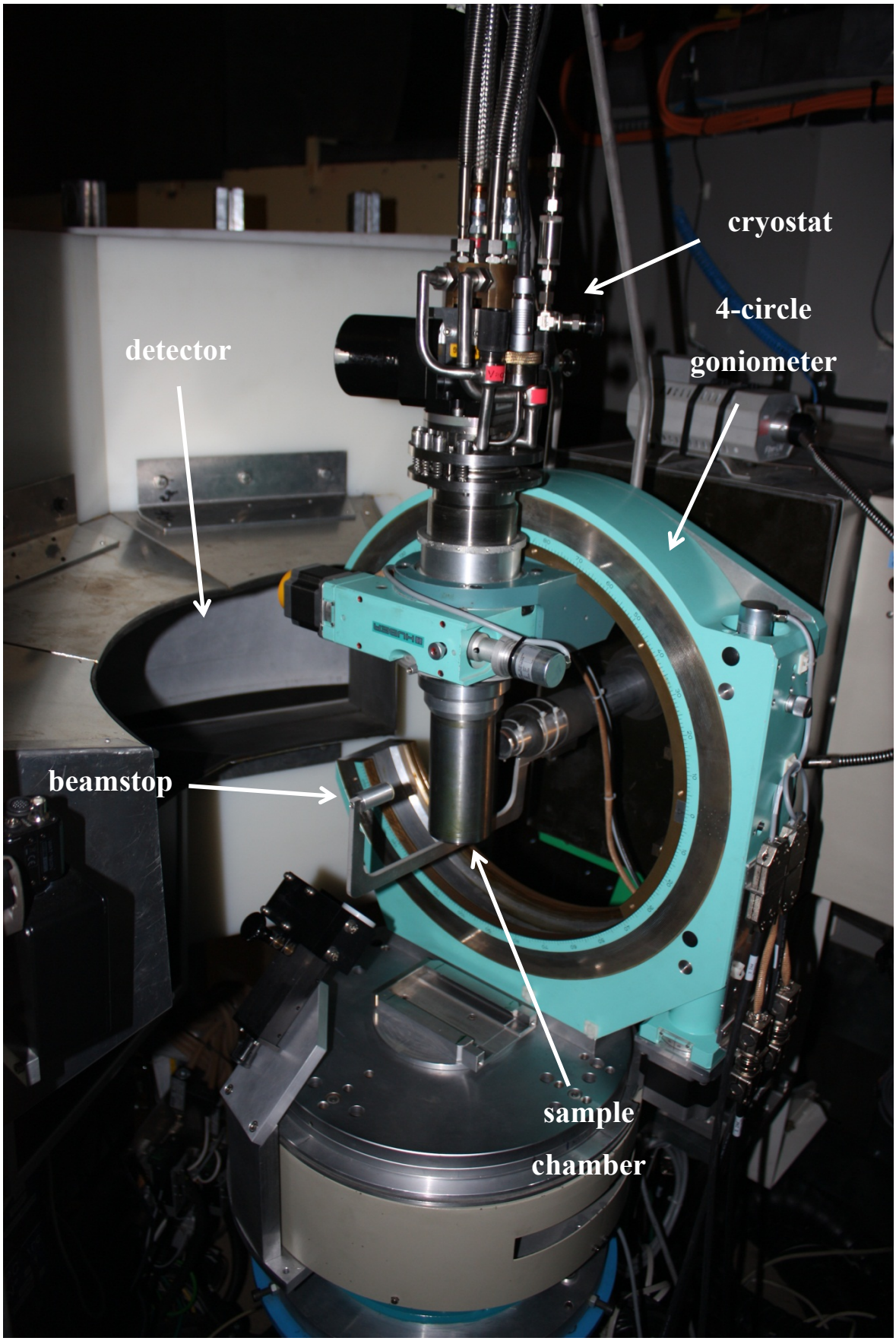

Figure 1-14: The D19 instrument at ILL, Grenoble. The crystal is mounted inside the sample chamber under vacuum in order that it can be cooled to 2 K. Photograph taken by the author.

The second single-crystal neutron diffraction technique employed was Laue single-crystal neutron diffraction using VIVALDI (Very Intense Vertical Axis Laue Diffractometer)[53, 54] at ILL, France, and KOALA[50] at the Australian Nuclear Science and Technology Organisation (ANSTO), Australia. These instruments are built to approximately the same design; KOALA has a slightly larger detector, and perhaps more importantly 2.5 times the flux at sample position compared with its equivalent at ILL making it suitable for studying smaller crystals. A schematic of VIVALDI is shown in figure 1-15; the set-up at KOALA is similar. A sample Laue image recorded on KOALA is shown in figure 1-16.

Laue diffraction utilises a 'white' beam of neutrons: a Maxwellian distribution of neutrons over a range of wavelengths. This allows much higher flux than monochromatic methods, meaning that smaller crystals and/or shorter collection times can be used. Typical sample size is 0.5 – 1.0 mm^3, although smaller samples can be studied given sufficiently long exposure times. For the samples under study here, the thermal neutron beam was filtered to provide a wavelength distribution between 0.8 Å and 3.0 Å. An image plate area detector wraps around the sample position in a cylindrical shape. The neutron-sensitive image plates are based on BaFBr doped with Eu^{2+} ions and Gd_2O_3. A disadvantage of this technique in practice is that any monochromatic instruments upstream of the diffractometer on the same neutron guide will remove certain parts of the neutron spectrum, meaning that some expected reflections are observed with less intensity or not at all. The sample is held in a series of fixed positions related by rotation about the axis of the cylindrical detector while diffraction images are recorded. Referring to the Ewald sphere construction (figure 1-17) for the conditions that must be met for Bragg reflections to be observed, using a distribution of wavelengths from 0.8 Å to 3.0 Å is akin to having an infinite series of spheres with all possible radii between 0.8 Å and 3.0 Å; reflections that fall anywhere within this volume will be observed on a single diffraction image. An advantage of this technique is that only a few images need to be measured in order to provide a complete set of reflections. An experiment carried out on either of these Laue diffractometers does not yield data that is as precise as that from D19, or from a laboratory X-ray diffractometer. However it is particularly useful for obtaining accurate hydrogen atom positions for samples where only small crystals can be grown.

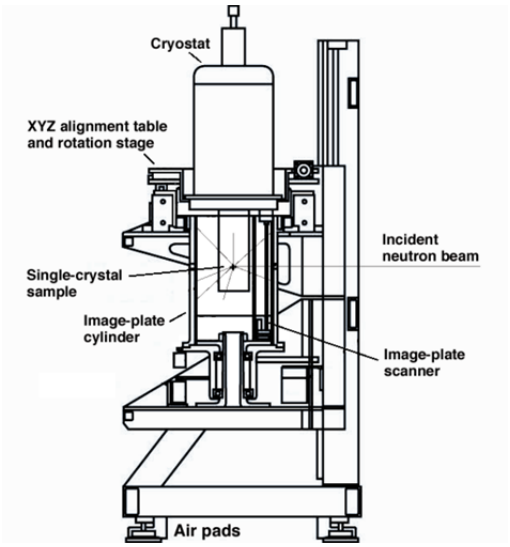

Figure 1-15: The VIVALDI neutron diffractometer at ILL, Grenoble. A schematic depicting the key elements of the instrument is shown. Reproduced from "High Speed Neutron Diffraction Comes Of Age" by G. J. McIntyre *et al*.[54]

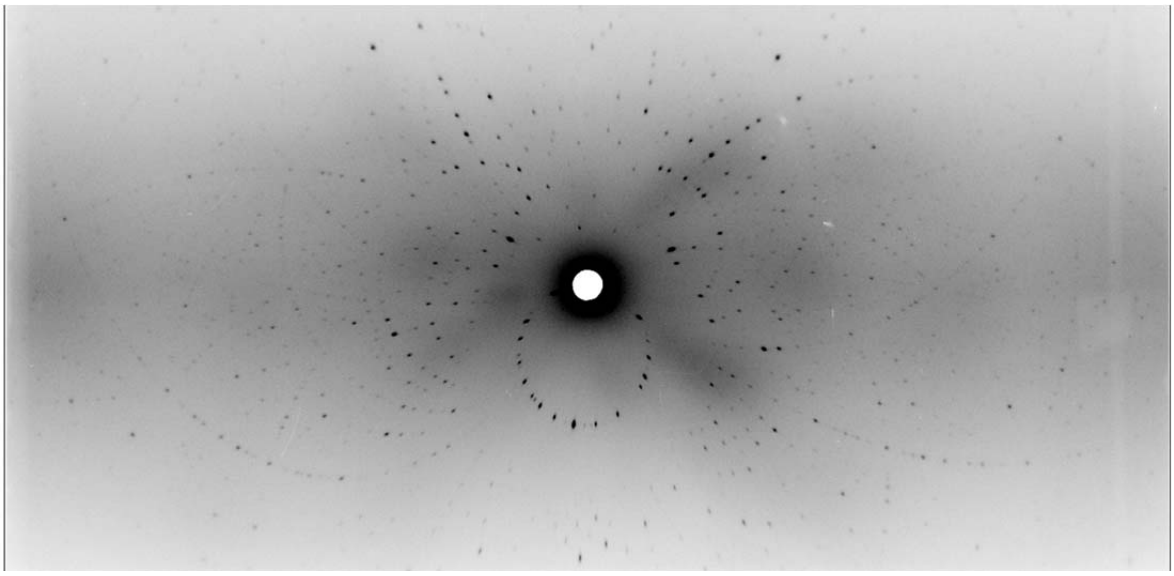

Figure 1-16: A sample neutron Laue diffraction image recorded on KOALA at ANSTO, Australia.

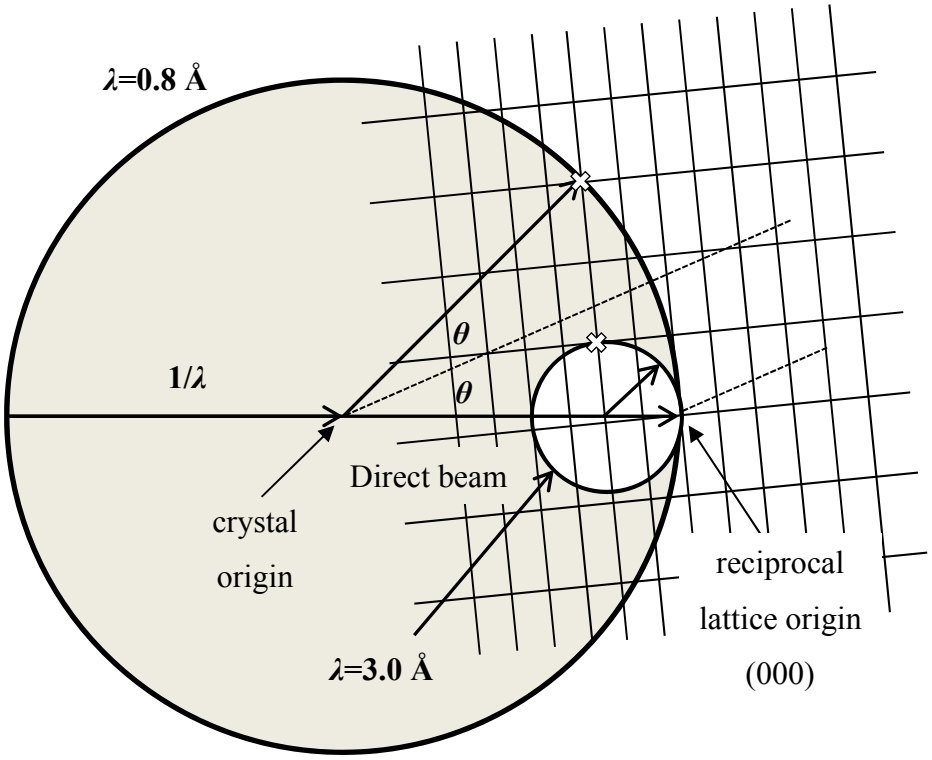

Figure 1-17: The Ewald construction for Laue diffraction with a wavelength range of 0.8 Å to 3.0 Å as observed on VIVALDI or KOALA. Reciprocal lattice points within the shaded region are excited. The limiting sphere for diffraction to be observed is calculated by taking the difference of the two $2/\lambda$ spheres traced out by λ = 0.8 Å and λ = 3.0 Å. Adapted from a figure by Wilson.[49]

It is also possible to carry out neutron powder diffraction. Due to the large incoherent scattering cross-section of hydrogen to neutrons, it is advantageous to use a sample in which all hydrogen atoms are replaced by deuterium. This is particularly important when using a powder sample since the incoherent scattering is manifested as an increased background signal. Powder diffraction does not give such complete information as is obtained from single-crystal measurements, but can be performed on samples where it is not possible to grow large single crystals. The High Resolution Powder Diffractometer (HRPD)[55] at ISIS, UK, is situated approximately 100 m from the target where neutrons are produced (figures 1-18, 1-19). A moderator of methane at 90 K is used to produce a white beam of neutrons with a peak at approximately 2 Å. This allows observation of Bragg reflections below 1 Å, a key requirement for studying molecular systems. The long path length reduces the error in the measured time-of-flight for each neutron and thus, increases the resolution of the instrument. Detectors are situated in fixed positions around the sample position, with all Bragg reflections observed simultaneously due to the polychromatic beam used. The highest resolution is obtained on the backscattering detectors; however detectors are also situated at 90° to the incident beam and at low angles in order that large d-spacings can be measured. Cooling the sample to 2 K is achieved using a standard

'orange' cryostat. Typical measurement time is anywhere from a few hours to a few days. Compared to an X-ray powder diffraction experiment, the data obtained from HRPD show no drop-off in intensity at high angle and so it is ideal for complete pattern refinement.

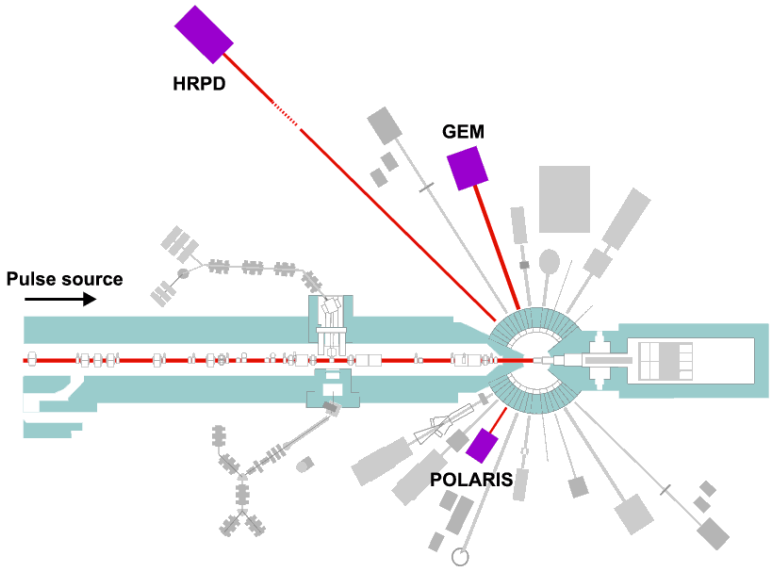

Figure 1-18: Target Station 1 at ISIS, Oxfordshire. HRPD is highlighted at the top left of the image. The instrument is located at the end of a 100m beam line in order to give the characteristic high resolution associated with the instrument. Reproduced from a figure by Cockcroft and Jacques.[56]

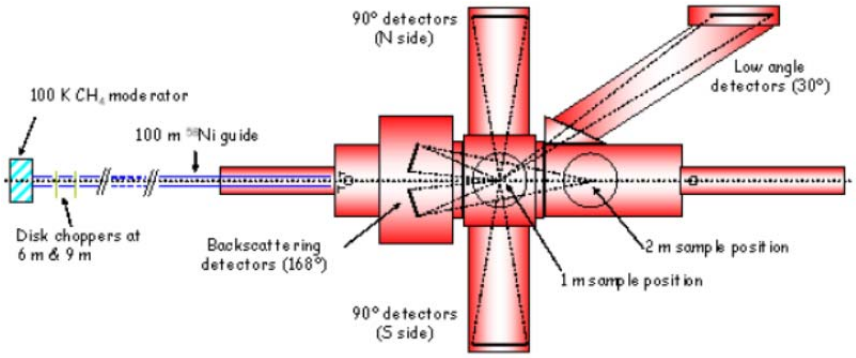

Figure 1-19: Schematic plan view of the HRPD detector configuration. Reproduced from the HRPD user manual.[57]

Neutron powder data can be treated using Rietveld refinement.[58, 59] In this method, various parameters are refined by least squares in order to minimise the difference between the observed profile and a calculated profile for the whole diffraction pattern. A measure of how well the model fits the observed pattern is given by the weighted profile factor R_{wp} and the goodness of fit, S (defined as the ratio between R_{wp} and $R_{exp,}$ the statistically expected R value).[60] The expressions for R_{wp} and R_{exp} are given in equations 1.22 and 1.23. $y_{i,obs}$ and $y_{i,calc}$ are the observed and calculated intensities and w_i is the weight at point i

in the diffraction profile. *N* is the number of observations and *P* is the number of parameters in the model.

$$R_{\mathrm{wp}} = \left(\frac{\sum_i w_i\left(y_{i,obs} - y_{i,calc}\right)^2}{\sum_i w_i\left(y_{i,obs}\right)^2}\right)^{1/2} \qquad (1.22)$$

$$R_{\mathrm{exp}} = \left(\frac{(N-P)}{\sum_i w_i\left(y_{i,obs}\right)^2}\right)^{1/2} \qquad (1.23)$$

1.3.2 Inelastic Neutron Scattering

Inelastic scattering occurs when a neutron is scattered with a loss or gain in energy, ω, and momentum, Q, to the nucleus. Inelastically-scattered neutrons exhibit minimal interference with each other. The scattering function, *S(q,ω)*, is often plotted as a function of ω and in this way the data can be treated as analogous to conventional spectroscopic data.[49] Depending on the energy of incident neutrons and the Q and ω range of the instrument, various physical effects can be observed; magnetic transitions, molecular vibrations and librations, and molecular rotations can be carried out using various instruments on both reactor and pulsed spallation sources.

Inelastic neutron scattering (INS) is a powerful technique for studying SMMs as it allows direct observation of peaks related to magnetic transitions.[61-63] INS can provide directly information about axial, rhombic and higher order magnetic anisotropy parameters. INS experiments were carried out using the recently upgraded spectrometer IN5 at ILL, Grenoble (figure 1-20),[64] FOCUS at PSI, Switzerland,[65] and polarised neutron spectrometer D7 at ILL, Grenoble. Both IN5 and FOCUS are direct geometry Time of Flight (ToF) spectrometers. IN5 has a detector of approximate area 30 m^2. INS measurements can be performed on single crystals but powders are typically used in order to increase the amount of sample present, and therefore produce a larger signal. The former two spectrometers use a cold neutron beam to study low energy transitions that are close to the elastic line. Peaks are mirrored on either side of this line and correspond to energy loss or energy gain in a neutron for the same transition. As with neutron powder diffraction, a deuterated sample is required in order to reduce the background from incoherent scattering. A cryomagnet can be used in conjunction with INS in order to probe magnetic transitions when the sample is under a magnetic field at low temperature.

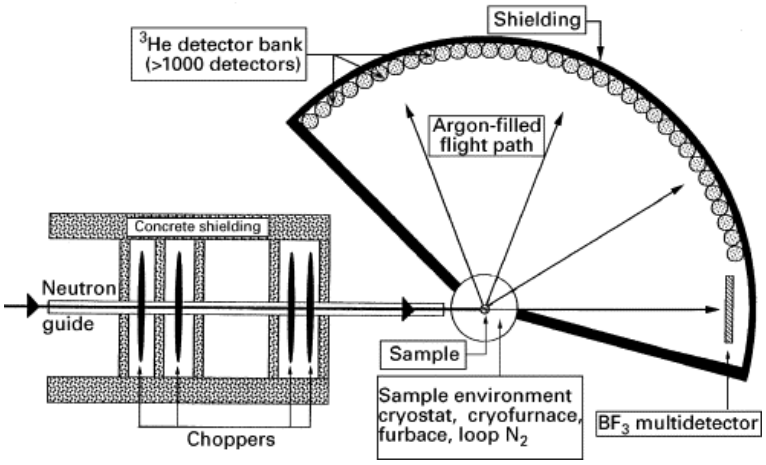

Figure 1-20: Schematic of the IN5 cold neutron spectrometer at ILL, Grenoble. Reproduced from "Inelastic Neutron Scattering, Instrumentation" by Stewart F. Parker.[66]

D7 is a polarised neutron spectrometer and can therefore provide polarisation analysis on inelastically-scattered neutrons.[67] The general information derived from this type of INS experiment is similar to that obtained from IN5 and FOCUS, but additionally the polarisation analysis allows separation of the coherent, spin incoherent and magnetic contributions from the total scattering intensity.[68]

1.4 General Techniques

1.4.1 Infrared Spectroscopy

Infrared (IR) spectroscopy is used to probe the molecular vibrational frequency range. For a vibration to be observed by IR spectroscopy, there must be a change in the dipole moment.[69] IR photons excite a particular molecular vibration according to their energy. The IR energy absorbed by the molecules in a sample can be quantified and used to generate an absorbance or transmittance spectrum as a function of wavenumber.

IR spectra were measured using a Shimadzu FTIR-8400S equipped with an ATR attachment. Attenuated total reflectance (ATR) is useful because solid samples can be analysed without the need for any special preparation. The sample is placed on a crystal with a high refractive index (typically ZnSe or Ge). Different crystal materials can be used for different energy ranges. Pressure is applied to the sample to ensure that there is no air between the sample and the crystal. IR light is directed into the crystal and allowed to undergo internal reflection many times. The presence of the sample on top of the crystal

alters the characteristics of the reflected light. These changes can be measured by the spectrometer and a Fourier transform is applied to generate a conventional infrared spectrum.[70]

IR spectroscopy is particularly selective for N-H, O-H and C=O stretches and so is a useful technique for confirming the presence of organic ligands in new materials that have been synthesised. Additionally the IR spectrum of a hydrogenous material is quite different from that of a material containing deuterium.[71] Thus, IR spectroscopy can be used to determine the extent of deuteration of a material (see chapter 4).

1.4.2 Magnetic Characterisation

Magnetic characterisation was carried out using a Quantum Design MPMS-XL utilising a Superconducting Quantum Interference Device (SQUID) magnetometer.[72] This allows measurement of dc magnetisation *vs*. field, dc magnetic susceptibility *vs*. temperature and ac magnetic susceptibility (both in-phase and out-of-phase) *vs*. temperature.

1.4.3 Synthesis of materials

Synthesis of the precursors and complexes studied during the research project was performed under aerobic conditions at ambient temperature and pressure unless otherwise stated. Starting materials and solvents were obtained from commercial suppliers and were used without further purification unless otherwise stated. Crystals were grown using several techniques including solvent-solvent diffusion ('layering'), vapour diffusion, slow evaporation, standing in a sealed vial and directly from solvothermal reactions as described in the relevant synthetic details.

1.4.3.1 Solvothermal reactions

Some of the reactions that produce the species described in this thesis are solvothermal in nature. Solvothermal synthesis is characterised by heating reagents and solvent in a sealed vessel to temperatures above the boiling point of the solvent.[73] The high temperature and the resultant high pressure inside the vessel serve to alter the viscosity and solubilising properties of the solvent which can lead to formation of different products to those formed

under ambient conditions. Examples of molecular clusters containing vanadium,[74-78] chromium,[79, 80] manganese,[81] iron,[82] cobalt[83] and nickel[84] that are formed by using solvothermal techniques can be found in the literature.

1.5 Structure and Magnetism

Magnetic measurements are generally performed on SMMs at temperatures below 10 K. The highest blocking temperature, T_B, for an SMM to date is 13.9 K.[15] Frequency-dependent peaks in out-of-phase ac susceptibility (χ'' *vs.* T) are normally observed below 10 K and hysteresis in magnetisation *vs*. field is seen to an appreciable degree below 2 K. The structures published to support these magnetic data are usually recorded at 100 K or even room temperature. Hitherto, the lowest temperature at which structural data have been collected for an SMM is 20 K.[85] Such measurement, however, is not routine within the field of molecular magnetism; most structures are measured at temperatures much higher than this.

Many high-symmetry molecular crystals undergo phase transitions upon cooling or upon application of pressure. These transitions can involve changes to molecular symmetry (*via* a change in space group), which in turn can alter the observed magnetic properties; QTM is subject to quantum selection rules related to local symmetry. Therefore it is not necessarily sensible to compare the higher-temperature structure with low temperature magnetic measurements. The primary goal of this research project was to collect ultra-low temperature structural data for several SMMs in order to observe if there are any structural details or changes that have not previously been noted, which could contribute to their magnetic properties.

Chapter 2 Structures containing Mn^{III}

Ultra-low temperature structural investigations of Mn^{III}-based SMMs and the interplay between lattice solvent and structural disorder in a $\{Mn_{12}\}$ SMM

2.1 Introduction to Mn^{III} SMMs

Although SMMs have been reported that contain a number of different 3*d* and/or 4*f* metal ions, by far the most studied are those based on Mn^{III}. Indeed the first reported and arguably most studied SMM, Mn_{12}-acetate[13] (discussed in more detail below), owes its interesting magnetic properties in large part to eight ferromagnetically-coupled Mn^{III} ions. Due to four unpaired electrons in the high spin configuration, the Mn^{III} ion exhibits a significant Jahn-Teller distortion. Mn^{III} also possesses Ising type magnetoanisotropy, which favours a significant negative ZFS parameter, *D*, when the Jahn-Teller elongated axes are in good alignment within a cluster.[86] Furthermore Mn^{III} often couples to neighbouring ions ferromagnetically, increasing the likelihood of a non-zero ground state.[86]

Several Mn^{III} SMMs from different families are discussed in this chapter. Other notable examples include a $\{Mn_{84}\}$ torus with an external diameter of 4.2 nm,[87] a family of $\{Mn^{III}_2Mn^{II}_2\}$ butterfly-shaped clusters with large ground states[88, 89] and recently a pair of $\{Mn^{III}_6Ln_2\}$clusters: one with an energy barrier to relaxation of 103 K.[90] A $\{Mn_6\}$ cluster consisting of two coupled $\{Mn^{III}_3O\}^{7+}$ triangles is significant since at the time of its publication it surpassed the highest blocking temperature for an SMM (previously held by Mn_{12}-acetate).[91]

2.2 Mn_{12}-acetate and related compounds

The first known SMM, $[Mn_{12}O_{12}(O_2CMe)_{16}(H_2O)_4]\cdot 4H_2O\cdot 2MeCO_2H$ (Mn_{12}-acetate, **1**), was reported in 1980, although it was not identified as an SMM until much later.[13, 34] **1** possesses an S=10 ground state and a significant axial anisotropy, $D \approx -0.5$ cm^{-1}.[14, 92] It has a blocking temperature of approximately 3 K.[93] The cluster consists of eight Mn^{III} centres surrounding a central $\{Mn^{IV}_4O_4\}$ cubane, bridged by oxide and acetate ligands. The interstitial voids are filled with water and acetic acid of crystallisation, both of which take part in hydrogen bonding to the complex. The acetic acid molecules are disordered about a 2-fold rotation axis and lie directly between two adjacent $\{Mn_{12}\}$ clusters. The $\{Mn_{12}\}$ cluster lies on a crystallographic S_4 axis and the eight Mn^{III} Jahn-Teller axes are approximately aligned, forming a magnetic easy axis.[94]

Scans of dc magnetisation *vs.* field show sharp steps in hysteresis loops at well-defined field strengths.[93, 95] The fast relaxation at these steps is caused by resonant magnetic quantum tunnelling (QTM). According to the fourfold symmetry of the clusters, tunnelling is only permitted for even-to-even M_s crossings, *i.e.* every fourth step is observable; however, QTM is observed for all steps.

A previous structural study by Cornia *et al*. has suggested that the two-fold disorder of the acetic acid of crystallisation leads to six different isomers that make up **1**.[36, 94] **1** contains 16 acetate ligands, 4 of which are disordered about two positions (1 unique ligand). This disorder is induced by disorder in the acetic acid of crystallisation. There are four symmetry-related acetate ligands whose positions can be affected by this disorder and thus, six isomeric forms exist for **1** that vary in the number of shifted ligands (n=0, 1, 2 [cis], 2 [trans], 3, 4).[94] Figure 2-1 illustrates the four sites around the cluster that each contain a disordered acetic acid of crystallisation. Figure 2-2 shows a single site enlarged for detail. Figure 2-3 illustrates the six isomeric forms of **1** that could exist. The disorder is discussed in more detail later.

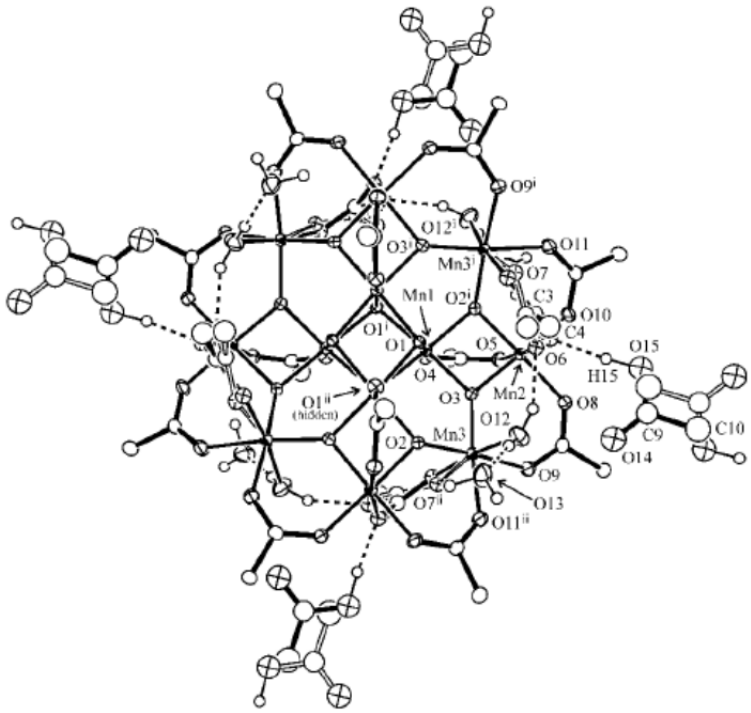

Figure 2-1: The structure of **1** at 83 K. The two positions for disordered acetic acid and acetate ligands are differentiated with solid and open bonds. Only the H atoms in the acetic acid and water molecules are shown for clarity. Hydrogen bonding is indicated by dashed lines. Figure reproduced from reference [92].

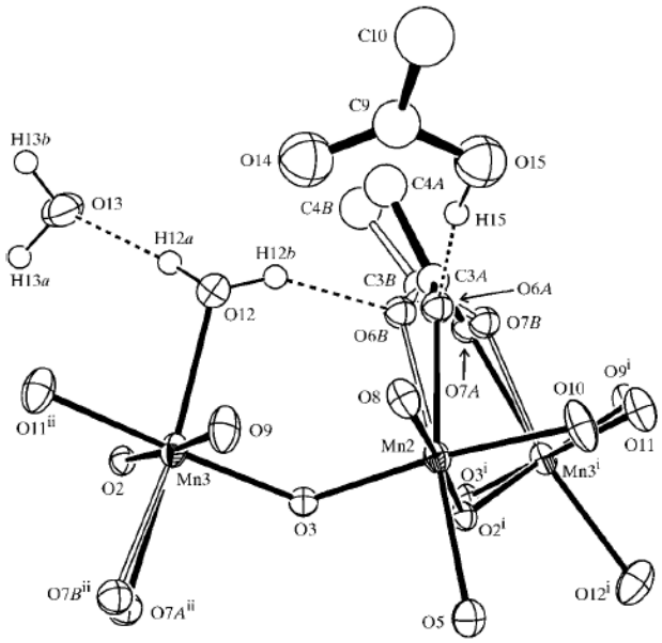

Figure 2-2: The disorder of an acetate ligand in **1** is clearly illustrated. The two components are differentiated with solid and open bonds. H atoms attached to carbon are omitted for clarity. Hydrogen bonding is indicated by dashed lines. Figure reproduced from reference [92].

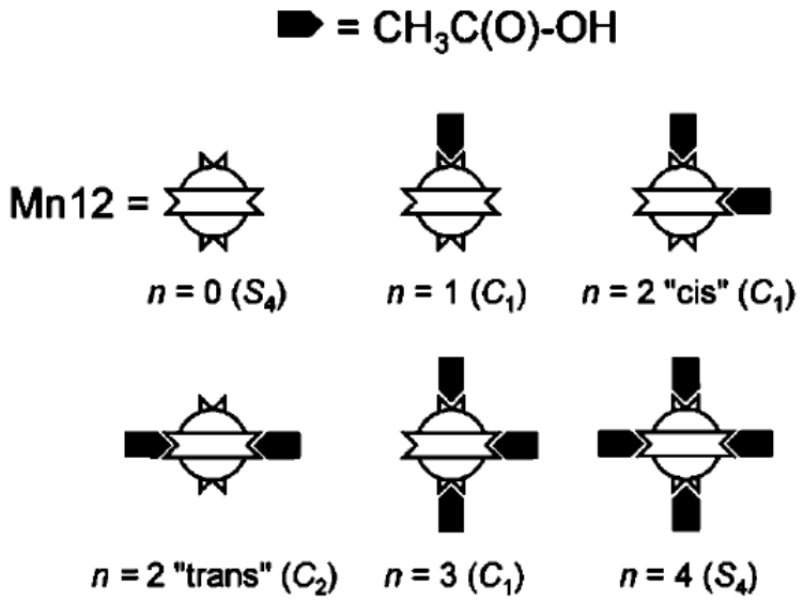

Figure 2-3: The six possible isomers of **1** discussed in the text and the associated molecular symmetry of each. The black shapes representing acetic acid of crystallisation are shown as present if the acid group is facing the $\{Mn_{12}\}$ cluster. Figure reproduced from reference [92].

Axial symmetry is retained for the n=0 and n=4 isomers but for the other four the symmetry is lowered. It has been suggested that this permits a transverse anisotropy and thus, provides an explanation for the odd-to-odd QTM steps in the hysteresis loops.[36] However, more recently published measurements on a $\{Mn_{12}\}$ analogue, $[Mn_{12}O_{12}(O_2CCH_2Bu^t)_{16}(CH_3OH)_4]\cdot CH_3OH$ (Mn_{12}-tBuAc), with full crystallographic axial symmetry show that quantum tunnelling occurs at odd-to-odd steps, even though this

should be forbidden.[96] Similarly there is no easy explanation for the odd-to-even and even-to-odd transitions observed for **1**. It was suggested that a further consequence of the solvent disorder is that the molecular easy axes are tilted discretely, inducing varying transverse fields.[97] However, this explanation seems to be ruled out by the previous observation of odd-to-odd transitions in both **1** and Mn_{12}-*t*BuAc. Furthermore it is unlikely that dipolar coupling or distributions of molecular environments are responsible either.[96] Antisymmetric exchange has been proposed as a possible explanation, both for this system[98] and for a similar observation in $\{Ni_4\}$ clusters.[99]

In addition to stepped hysteresis loops below its blocking temperature, **1** also exhibits frequency-dependent out-of-phase ac susceptibility, a feature common to all single-molecule magnets due to their slow relaxation of magnetisation at ultra-low temperature. A curious feature of **1** compared to other SMMs is that there are two frequency-dependent peaks rather than the usual single peak: a large peak at 5-7 K and a much smaller peak at 2-3 K[20] due to slow-relaxing (SR) and fast-relaxing (FR) species respectively (see figure 1-6). The existence of two magnetic species has also been confirmed by inelastic neutron scattering (INS) measurements and it has been estimated that a typical distribution is 5% FR, 95% SR isomers.[21, 100] It is unclear how these observations are related to the interesting quantum properties described above, or indeed the disorder observed crystallographically.

The lowest temperature at which structural data have previously been measured for **1** is 20 K by Langan *et al*.[85], however disorder in the acetate ligands was not modelled. Thus, the best data that are currently available for **1** were measured at 83 K.[94] It has previously been shown that application of pressure can change the structure of an analogue of the $\{Mn_{12}\}$ family, $[Mn_{12}O_{12}(O_2CCH_2{}^tBu)_{16}(H_2O)_4]\cdot CH_2Cl_2\cdot MeNO_2$, such that its magnetisation relaxes much more slowly. High pressure crystallography reveals a structural change commensurate with the change in relaxation rates, specifically related to the switching of a misaligned Jahn-Teller axis into alignment with the magnetic easy axis.[101] Many molecular crystals undergo structural transformations upon cooling as well as under pressure,[102-104] and it is possible that this could happen to **1** in a way that would influence the low temperature magnetic properties and quantum behaviour. Previous attempts to understand the properties of **1** by structural correlation have utilised structural data measured at much higher temperatures than those at which slow magnetic relaxation is observed.[85, 94]

2.2.1 Synthesis of {Mn_{12}} compounds

2.2.1.1 Synthesis of $[Mn_{12}O_{12}(O_2CCH_3)_{16}(H_2O)_4]\cdot 2CH_3CO_2H\cdot 4H_2O$ (1)

Crystals of **1** were synthesised using the standard procedure[105] and were prepared fresh for each experiment. A 60% (v/v) acetic acid solution in water was prepared. $KMnO_4$ (1.00 g, 6.33 mmol) was dissolved in a 25 mL portion of this solution; while $Mn(O_2CCH_3)_2\cdot 4H_2O$ (4.04 g, 16.49 mmol) was dissolved in a separate 15 mL portion of this solution. After stirring for one hour, the $KMnO_4$ solution was added to the solution of $Mn(O_2CCH_3)_2\cdot 4H_2O$ steadily over the course of approximately 2 minutes while stirring and the mixture quickly passed through a sintered glass funnel to remove any solids. The filtrate was then sealed and left to stand at room temperature. After several days crystals of **1** formed (3.04 g, 1.48 mmol, 78% yield based on available Mn). Their identity was confirmed by single-crystal X-ray diffraction.

2.2.1.2 Synthesis of $[Mn_{12}O_{12}(O_2CCH_3)_{16}(H_2O)_4]\cdot 4H_2O$ (2) and $[Mn_{12}O_{12}(O_2CCH_3)_{16}(H_2O)_4]$ (3)

Desolvation products $[Mn_{12}O_{12}(O_2CCH_3)_{16}(H_2O)_4]\cdot 4H_2O$ (**2**) and $[Mn_{12}O_{12}(O_2CCH_3)_{16}(H_2O)_4]$ (**3**) were prepared by heating a selection of crystals of **1** to 403 K for 2 hours under an N_2 flow. After cooling to room temperature the crystals had retained sufficient crystallinity in order to perform single-crystal X-ray diffraction measurements. Elemental analysis (%), calc (found) for $C_{32}H_{64}Mn_{12}O_{52}$ ($[Mn_{12}O_{12}(O_2CCH_3)_{16}(H_2O)_4]\cdot 4H_2O$): C 19.81 (19.96), H 3.33 (3.08). Elemental analysis was performed on the bulk sample obtained directly from the desolvation process.

2.2.1.3 Synthesis of $[Mn_{12}O_{12}(O_2CCH_3)_{16}(CH_3CH_2OH)_4]\cdot CH_3CH_2OH$ (4)

A portion of the bulk sample comprised of **2** and **3** was exposed to ethanol vapour for one week inside a sealed vial. A crystal was analysed by single-crystal X-ray diffraction upon removal from the vial and found to be species **4**. It was only possible to measure one crystal successfully. It was not possible to obtain a satisfactory elemental analysis result for **4**; however the single-crystal X-ray result proves that it is at least possible to perform the

solvent substitution operation successfully. Further work may be needed in order to optimise the process.

2.2.2 Structural disorder in Mn_{12}-acetate (1) at ultra-low temperature

2.2.2.1 Single-crystal X-ray diffraction at 2 K

A black crystal of **1** (size 0.1 x 0.1 x 1.0 mm) was mounted on a graphite rod and placed inside the cryostat of the XIPHOS diffractometer[48] (Mo K_α radiation, λ = 0.71073 Å) at Durham University and cooled to 2 K. The system has a minimum operating temperature of 1.9 K, achieved using a modified two-stage closed-cycle refrigerator enhanced with an additional Joule-Thomson stage. Data were integrated using SAINT[106] and empirical absorption corrections using equivalent reflections were performed with the program SADABS.[107]

2.2.2.2 Single-crystal neutron diffraction at 2 K

Neutron Laue data were collected using the Very-Intense Vertical-Axis Laue Diffractometer (VIVALDI) at Institut Laue-Langevin, Grenoble.[53, 108] The instrument has a minimum operating temperature of 1.5 K, achieved using a standard ILL 'orange' cryostat. A black crystal of **1** (size 0.2 x 0.2 x 1.0 mm) was mounted on a vanadium rod perpendicular to the incident beam. The sample used for the neutron study was not deuterated; indeed the negative scattering density from the hydrogen atoms was particularly advantageous in identifying their positions within the structure. 7 Laue patterns were collected for equally-spaced sample orientations, from 0° to 90° around the vertical rotation axis, covering a little more than a quadrant of reciprocal space. Cell parameters were taken from X-ray data at 2 K, and the Laue patterns were indexed using LAUEGEN. Background-corrected integrated intensities were extracted using ARGONNE_BOXES. Normalisation to a common wavelength was performed over the wavelength range 0.9-2.8 Å using LAUENORM. LAUEGEN[109] and LAUENORM[110] are part of the Daresbury Laue Suite, while ARGONNE_BOXES is an in-house two-dimensional adaptation of the three-dimensional minimum σ(I)/I routine.[111]

2.2.2.3 Single-crystal X-ray diffraction of {Mn_{12}} analogues at 100 K

Black crystals of $[Mn_{12}O_{12}(O_2CCH_3)_{16}(H_2O)_4]\cdot 4H_2O$ (**2**), $[Mn_{12}O_{12}(O_2CCH_3)_{16}(H_2O)_4]$ (**3**) and $[Mn_{12}O_{12}(O_2CCH_3)_{16}(CH_3CH_2OH)_4]\cdot CH_3CH_2OH$ (**4**) were cooled to 100 K on a Nonius Kappa CCD diffractometer.[112] Data were integrated using DENZO[113] and empirical absorption corrections using equivalent reflections were performed with SADABS.[107] The structures were solved using Superflip[45] and refined using the least-squares refinement routine implemented within CRYSTALS.[114]

2.2.2.4 Analysis of ultra-low temperature X-ray and neutron data

X-ray data were used to determine cell parameters at 2 K as these are not derived from the Laue experiment. The heavy atom structure of **1** was solved and refined from X-ray data using the programs SHELXS-97[115] AND SHELXL-97[115] respectively. All non-hydrogen atoms except those in the disordered acetate ligand and the disordered acetic acid of crystallisation were refined with anisotropic displacement parameters (ADPs); the other atoms were refined with isotropic displacement parameters. Hydrogen atoms in methyl groups were placed in calculated positions. This structural model was allowed to refine against the neutron data. Hydrogen atoms attached to coordinated and lattice water molecules, as well as the acidic hydrogen belonging to the solvent acetic acid, were found in a Fourier difference map calculated from the neutron data. The neutron data are especially useful in this regard due to the sensitivity of neutrons to hydrogen atoms. Finally the model was again refined against X-ray data with the located H atoms restrained. Full crystallographic data are given in table 2.1. The poor quality of the neutron Laue data recorded meant that only H atom positions were obtained from this technique by using a Fourier difference map. A full refinement was not performed against the neutron data.

Hitherto, no structural studies below 20 K[85] have been performed on **1**. At this temperature, the acetate ligand disorder was not observed and has only been modelled in a subsequent 83 K study.[94] Our ultra-low temperature structural study is designed to rectify this situation and provide good quality structural information for **1** below its blocking temperature, at 2 K. The previous 20 K neutron study[85] performed on a partially deuterated crystal of **1** in conjunction with an 83 K X-ray study[94] describes hydrogen bonding between the coordinated water molecule O12 and (i) the disordered acetate ligand [O12-

H12B---O62] and (ii) the water of crystallisation [O12-H12C---O13] (figures 2-4, 2-5). The water of crystallisation itself acts as a hydrogen bond donor to O5 and three other possible acceptors O7, O9 and O11. The hydrogen-bonded network of clusters is linked together through the solvent water in this way (figure 2-5). A hydrogen bond was also reported between the hydroxyl oxygen atom O15 in the solvent acetic acid and O61 of the disordered acetate ligand [O15-H15---O61] (figure 2-4).

Table 2.1: Crystallographic data for $\{Mn_{12}\}$ analogues **1**, **2**, **3** and **4**.

	1	**2**	**3**	**4**
Formula	$C_{36}H_{72}Mn_{12}O_{56}$	$C_{32}H_{64}Mn_{12}O_{52}$	$C_{32}H_{56}Mn_{12}O_{48}$	$C_{42}H_{78}Mn_{12}O_{49}$
Moiety formula	$[Mn_{12}O_{12}(OAc)_{16}(H_2O)_4]\cdot 4H_2O.2AcOH$	$[Mn_{12}O_{12}(OAc)_{16}(H_2O)_4]\cdot 4H_2O$	$[Mn_{12}O_{12}(OAc)_{16}(H_2O)_4]$	$[Mn_{12}O_{12}(OAc)_{16}(EtOH)_4]\cdot EtOH$
M_w	2060.22	1939.96	1867.90	2020.14
Crystal system	Tetragonal	Tetragonal	Tetragonal	Tetragonal
Space group	*I*-4	*I*-4	*I*-4	*I*-4
a [Å]	17.1875(2)	17.235(4)	16.0506(12)	17.540(10)
c [Å]	12.1717(2)	12.038(3)	11.9067(12)	12.224(16)
V [Å^3]	3595.64(8)	3576.0(14)	3067.4(4)	3761(6)
Z	2	2	2	2
T [K]	2.0(5)	100(2)	100(2)	100(2)
Radiation	X-ray Mo (K_α) / neutron	X-ray Mo (K_α)	X-ray Mo (K_α)	X-ray Mo (K_α)
λ [Å]	0.71073 / 'white'	0.71073	0.71073	0.71073
D_c [g cm^{-3}]	1.903	1.802	2.022	1.784
μ [mm^{-1}]	2.143	2.144	2.491	2.040
Meas./indep. refl.	24505/4861	10400/2469	18716/2694	12503/3161
R_{int}	0.0287	0.019	0.010	0.047
Obs. refl. [$I > 2\sigma(I)$]	4586	2351	2605	2960
wR_2 [a]	0.0888	0.0329	0.0457	0.0657
R_1 [b]	0.0366	0.0434	0.0234	0.0599
Goodness of fit on F²/F [c]	1.077	1.1297	0.9668	1.1159
$\Delta\rho_{max,min}$ [e Å^{-3}]	0.826/-0.674	0.40/-0.29	0.06/-0.07	0.35/-0.48

[a] $wR_2 = \{\sum[w(F_O^2 - F_C^2)^2]/\sum[w(F_O^2)^2]\}^{1/2}$ on F²; $wR_2 = \{\sum[w(F_O - F_C)^2]/\sum[w(F_O)^2]\}^{1/2}$ on F

[b] $R_1 = \sum\big||F_O| - |F_C|\big|/\sum|F_O|$

[c] Data for **1** were refined on F² in SHELXL; data for **2**, **3** and **4** were refined on F in CRYSTALS.

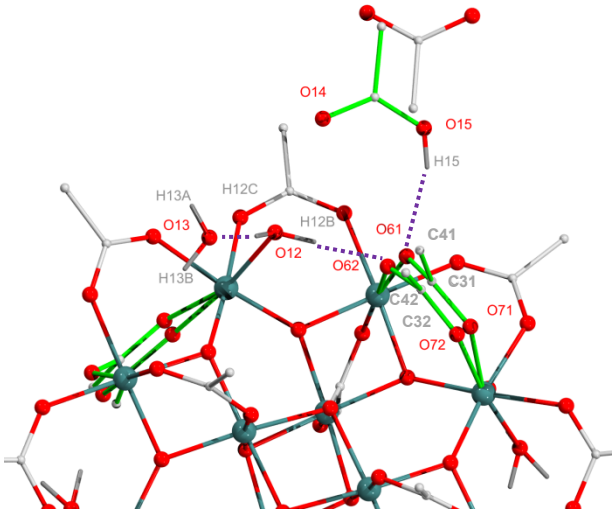

Figure 2-4: Model showing disorder and hydrogen bonding proposed by Cornia *et al.*[94] for $[Mn_{12}O_{12}(O_2CMe)_{16}(H_2O)_4]\cdot 4H_2O\cdot 2MeCO_2H$ (**1**). Hydrogen bonds from O12 to O62 and O13, and from O15 to O61 are indicated in purple. Most H atoms are omitted for clarity. Shown in green are acetic acid of crystallisation in the orientation in which it hydrogen bonds to the $\{Mn_{12}\}$ complex and both disorder components of the acetate ligand O6/O7/C3/C4 (denoted by the number '1' or '2' after the appropriate atom label, e.g. O61/O62, O71/O72). Atom colours: Mn, blue; O, red; C, light grey; H, dark grey (marked). H atoms except those involved in hydrogen bonding are omitted for clarity.

We found evidence for an additional hydrogen bonding interaction between the acetic acid of crystallisation and the water molecule O12 coordinated to Mn3 [O12-H12A---O14] by calculating a Fourier difference map from the neutron data (figure 2-6). This discovery neatly ties up a more complete understanding of hydrogen bonding in the region. We can expand on the previous model described by Cornia *et al.*[94] as follows. The whole disordered region can be thought of as two separate components each with 50% occupancy (figure 2-6); the occupancy is fixed by the location of the acetic acid of crystallisation on a 2-fold rotation axis.

Each disorder component is linked with one orientation of the acetic acid. When the acid moiety is facing away from the cluster (shown in orange), there is an intramolecular hydrogen bond from coordinated water O12 to the adjacent acetate ligand O62. When the acid moiety is facing towards the cluster (shown in blue), there are intermolecular hydrogen bonds from O15 to O61 and from O12 to O14. O61 and O62 are equivalent in that they are essentially the 'same' atom in the ligand but located in one of two different positions as dictated by either inter- or intra-molecular hydrogen bonding. The position of this atom influences the positions of the other atoms in the ligand: O71/O72, C31/C32 and C41/C42 and similar positional disorder is observed. It is clear that the disordered acetic acid is driving this disorder in the ligand atom positions and also in the nature of the

hydrogen bonds. The half-occupied hydrogen atoms H12A and H12B uncovered by our neutron experiment confirm the nature of the hydrogen bonding in the region.

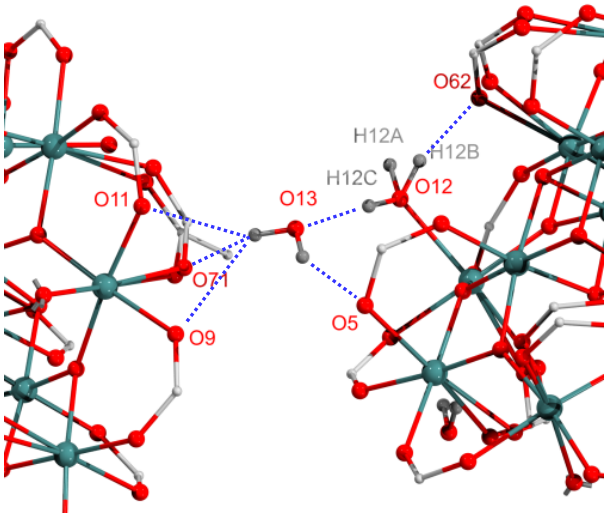

Figure 2-5: Hydrogen bonding between {Mn_{12}} clusters in compound **1** through water of crystallisation O13. Lattice acetic acid, some C atoms and most H atoms are omitted for clarity. Structure is taken from our new 2 K determination. Atom colours as previously defined.

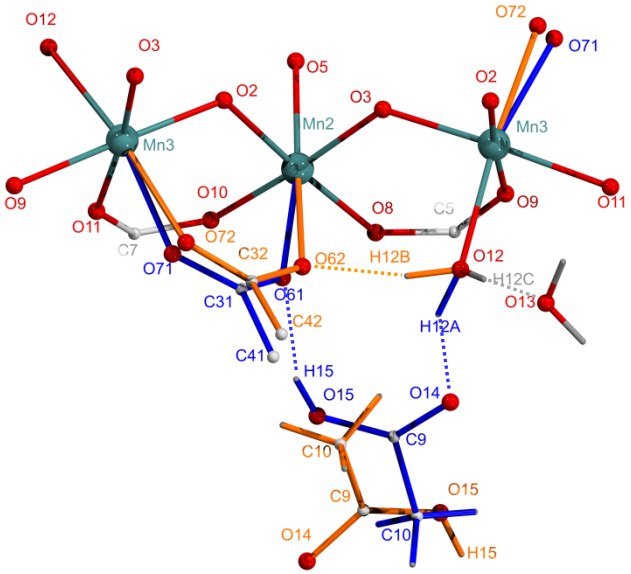

Figure 2-6: New disorder model for compound **1** derived from our 2 K X-ray and neutron structure determination. Shown in blue are the positions of all affected atoms when the lattice acetic acid is facing towards the complex. Shown in orange are the positions of all affected atoms when the acetic acid is facing away from the complex. Most H atoms and some C atoms are omitted for clarity. Hydrogen bonds in the two disorder components are also indicated in their respective colours. Atom colours are as previously defined. Tilt angles (angle between S_4 axis and approximate Jahn-Teller axis) are as follows. Blue: O12-Mn3-O71 35.52(8)°, O5-Mn2-O61 15.35(8)°. Orange: O12-Mn3-O72 35.57(8)°, O5-Mn2-O62 9.73(7)°.

The coordination environment of each Mn^{III} ion is broadly similar to that observed at higher temperatures. Around Mn2 there are four shorter bonds, ranging from 1.887(2) Å to 1.938(2) Å, and two longer axial bonds to O5 [2.224(2) Å] and O61/O62

[2.126(6)/2.247(5) Å]. This indicates a shortening of the axial elongation of approximately 0.12 Å when the acid moiety of the acetic acid of crystallisation is facing towards the cluster. This compares well with previously reported data by Cornia *et al.* for an 83 K X-ray structure (shortening of 0.09 Å).[94]

Mn3 also makes four shorter bonds, ranging from 1.889(2) Å to 1.979(3) Å, and two longer axial bonds to O12 [2.159(3) Å] and O71/O72 [2.126(6)/2.156(6) Å]. The solvent influence is evidently also felt in the coordination environment of Mn3, although the axial shortening of 0.03 Å is smaller. Interestingly, a lengthening of 0.05 Å for Mn3-O71 *vs*. Mn3-O72 was reported previously.[94] Angular distortions are not considerably different to those observed previously, being 13.9(2)° for O61-Mn2-O62 and 9.2(2)° for O71-Mn3-O72 [14.10(14)° and 6.8(3)° respectively at 83 K]. The Jahn-Teller axes associated with both Mn2 and Mn3 are pseudo-aligned with the crystallographic *c* axis in either disorder component, despite small differences between the two. A full list of relevant bond distances is given in table 2.2. Although the Jahn-Teller axes are approximately aligned, they are not precisely aligned with the crystallographic *c* axis that is approximately equivalent to the molecular easy axis given the tetragonal symmetry of the structure. The tilt angle (the angle between the Jahn-Teller axis and the easy axis) can be estimated by measuring the angle between the crystallographic *c* axis and the axis formed by the axially-elongated bonds. The tilt angles associated with Mn3 (O12-O71/O72) are similar at 2 K to those measured at 83 K, while those associated with Mn2 (O5-O61/O62) show small but measureable differences. Angle at 2 K [Angle at 83 K[36]] for O12-O72: 35.57(8)° [35.46(7)°], O12-O71: 35.52(8)° [35.69(1)°], O5-O62: 9.73(7)° [10.41(5)°] and O5-O61: 15.35(8)° [16.17(8)°]. More interesting perhaps is to note the difference in tilt angle of over 5° between O5-O62 and O5-O61 at either temperature (See table 2.3 for a full comparison of tilt angles). Another interesting comparison to make is on the angle between the planes formed by each ligand disorder component (*i.e.* the planes defined by O61/O71/C31/C41 and O62/O72/C32/C42 respectively, see figure 2-6). At 2 K this angle is just 6.1°, significantly lower than the 21.9° measured at 83 K.[94] This indicates that the atomic positions are significantly different at 2 K compared with 83 K.

Table 2.2: Bond distances from Mn2 and Mn3 to all atoms in their coordination spheres for species $[Mn_{12}O_{12}(O_2CMe)_{16}(H_2O)_4]\cdot 4H_2O\cdot 2MeCO_2H$ (**1**), $[Mn_{12}O_{12}(O_2CMe)_{16}(H_2O)_4]\cdot 4H_2O$ (**2**), $[Mn_{12}O_{12}(O_2CMe)_{16}(H_2O)_4]\cdot 4H_2O\cdot 2MeCO_2H$ (**3**) and $[Mn_{12}O_{12}(O_2CMe)_{16}(EtOH)_4]\cdot EtOH$ (**4**).

Distance (Å)	**1**	**2**	**3**	**4**
Mn2-O2	1.899(2)	1.910(4)	1.895(2)	1.902(4)
Mn2-O8	1.937(2)	1.939(4)	1.948(2)	1.928(4)
Mn2-O3	1.887(2)	1.890(4)	1.892(2)	1.873(4)
Mn2-O10	1.938(2)	1.940(4)	1.937(2)	1.936(4)
Mn2-O5	2.224(2)	2.239(4)	2.224(2)	2.215(5)
Mn2-O6	-	2.192(4)	2.172(2)	2.207(5)
Mn2-O61	2.126(6)	-	-	-
Mn2-O62	2.247(5)	-	-	-
Mn3-O2	1.889(2)	1.882(4)	1.907(2)	1.888(4)
Mn3-O9	1.967(3)	1.957(4)	1.967(2)	1.958(4)
Mn3-O3	1.894(2)	1.906(4)	1.865(2)	1.909(4)
Mn3-O11	1.979(3)	1.972(4)	1.944(2)	1.982(4)
Mn3-O12	2.159(3)	2.167(4)	2.290(3)	2.179(5)
Mn3-O7	-	2.153(4)	2.125(2)	2.123(4)
Mn3-O71	2.126(6)	-	-	-
Mn3-O72	2.156(6)	-	-	-

Table 2.3: Angular deviation from the crystallographic *c* axis for each of the unique Jahn-Teller axes in species **1**, **2**, **3** and **4** measured at selected temperatures and extracted from previously published data for **1**.

Species	Jahn-Teller axis	Measured tilt angle‡ at 2 K (°)	Measured tilt angle‡ at 83 K[94] (°)	Reported tilt angle# at 83 K[36] (°)	Measured tilt angle‡ at 100 K (°)
1	O12-Mn3-O72	35.57(8)	35.46(7)	37.1	-
	O12-Mn3-O71	35.52(8)	35.69(1)	37.2	-
	O5-Mn2-O62	9.73(7)	10.41(5)	10.7	-
	O5-Mn2-O61	15.35(8)	16.17(8)	11.6	-
2	O12-Mn3-O7	-	-	-	34.13(6)
	O5-Mn2-O6	-	-	-	11.84(6)
3	O12-Mn3-O7	-	-	-	36.38(4)
	O5-Mn2-O6	-	-	-	13.26(4)
4	O12-Mn3-O7	-	-	-	35.55(6)
	O5-Mn2-O6	-	-	-	9.20(6)

‡ Measured tilt angles are calculated from the angle between the crystallographic *c* axis and the axis formed by the relevant oxygen atoms.

Reported tilt angles are those reported by Cornia *et al.* in ref. [36]. These were calculated by using the angular overlap model (AOM).

2.2.3 Structural modification by removal of lattice solvent

It has long been postulated that the solvent acetic acid strongly influences the structure of the $\{Mn_{12}\}$ cluster in **1**. In order to determine the true extent of this influence we carried out an experiment to desolvate crystals of **1**.[116] Thermogravimetric analysis of **1** shows a large weight loss step at 383 K that is thought to correspond to loss of solvent acetic acid and water. Solvent was removed using a procedure similar to that devised by Larionova *et*

al.,[116] described in section 2.2.1.2. The previous authors characterised the desolvated sample using powder X-ray diffraction and determined that the product retained the same space group and unit cell parameters as **1**. They claim that this product has both acetic acid and water removed, citing the previous TGA data and the experimentally observed Mn:C ratio as evidence[116] but crucially they did not succeed in recording a single-crystal structure of the product.

Initial single-crystal X-ray analysis of our products indicated that there were two new types of crystal that, although visually identical, have different unit cells. Full structure determinations revealed the existence of the two new species $[Mn_{12}O_{12}(O_2CMe)_{16}(H_2O)_4]\cdot 4H_2O$ (**2**) and $[Mn_{12}O_{12}(O_2CMe)_{16}(H_2O)_4]$ (**3**). It is worth noting that the Mn:C ratio for both these species is the same (1.72).

Both crystallise in the same space group as **1**, *I*-4 (table 2.1). **2** has approximately the same unit cell lengths as **1** and is comprised of $\{Mn_{12}\}$ clusters and lattice water in the same packing arrangement observed in **1** with voids corresponding to the removal of acetic acid of crystallisation. The unit cell of **3** is approximately 14% smaller than that of the other two compounds and contains only $\{Mn_{12}\}$ clusters. All Mn^{III} centres in both new structures **2** and **3** show the same pseudo-aligned axially-elongated bonds observed in **1**. A comparison of bond distances between **1**, **2** and **3** is given in table 2.2. Intermolecular interactions are quite different in species **2** and **3**. Similar to **1**, **2** exhibits hydrogen bonding through lattice water O13 and the packing arrangement of $\{Mn_{12}\}$ clusters is preserved (figure 2-7), with empty interstitial voids that were previously occupied by acetic acid. In **3** there is no lattice water to transmit hydrogen bonding and the clusters are closer together maximising attractive dispersion forces. This close-packing could be responsible for the crystal retaining its crystallinity in spite of the removal of the relatively strong hydrogen bonds that previously held the structure together. The cavity that previously held lattice acetic acid is compressed and is too small to hold a molecule of this size (figure 2-8).

Removal of lattice acetic acid resolves the disorder in the positions of atoms O61/O62 and O71/O72. These can be modelled as single atoms O6 and O7 in both **2** and **3**, confirming that the lattice acetic acid is responsible for the disorder. C31/C32 is still disordered in **2** and C41/C42 is disordered in both **2** and **3**; this is unlikely to affect the Jahn-Teller axes on the Mn^{III} centres or indeed the quantum selection rules. The angles between the Jahn-Teller

axes and the crystallographic *c* axis in **2** and **3** are broadly similar to those observed previously, bearing in mind that these crystallographic data were collected at 100 K. [O12-O7, 34.13(6)° (**2**) and 36.38(4)° (**3**); O5-O6, 11.84(6)° (**2**) and 13.26(4)° (**3**)] (see table 2.3).

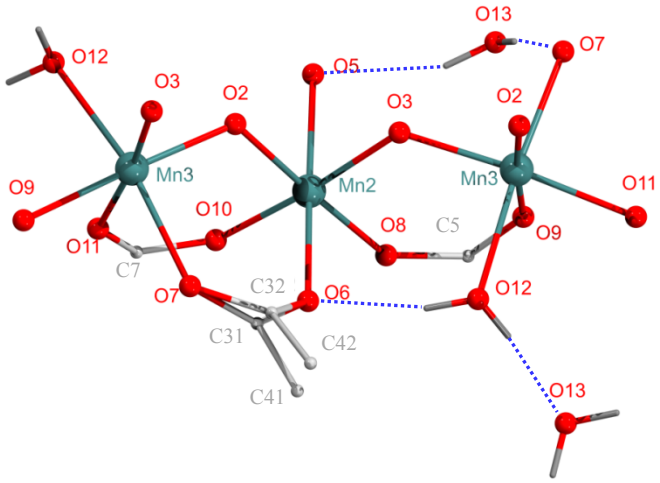

Figure 2-7: Hydrogen bonding arrangement in $[Mn_{12}O_{12}(O_2CMe)_{16}(H_2O)_4]\cdot 4H_2O$ (**2**). Disorder in the positions of C atoms in the acetate ligand O6/O7/C3/C4 is still observed but the removal of acetic acid removes the disorder in the positions of atoms O6 and O7. Water of crystallisation is shown as an acceptor from O12 and a donor to O5 and O7. Atom colours are as previously defined; H atoms except for those involved in hydrogen bonds are omitted for clarity.

It is impossible to distinguish between crystals of **2** and **3** visually. Elemental analysis suggests that the majority of crystals are species **2** with a small amount of **3** present. Thus, we cannot claim to have produced pure samples of axially symmetric $\{Mn_{12}\}$ complexes. However we have shown that full removal of the acetic acid of crystallisation certainly resolves disorder in the acetate ligands, producing species that have true, unbroken S_4 symmetry. We expect **2** and **3** to exhibit similar QTM dynamics[22, 117-119] to other fully axial analogues in the $\{Mn_{12}\}$ family: Mn_{12}-*t*BuAc and Mn_{12}-BrAc. HF-EPR and NMR measurements of **1** show severe broadening of signals compared with the axial species described, which show narrow non-overlapping signals.[22]

Further studies are planned encompassing measurement of dc magnetisation *vs.* field, HF-EPR and NMR of **2** and **3** in order to understand their quantum behaviour in the context of other members of the $\{Mn_{12}\}$ family. Additional benefits would be derived from refinement of the synthetic method used to produce species **2** and **3** in order to selectively produce pure samples of either material.

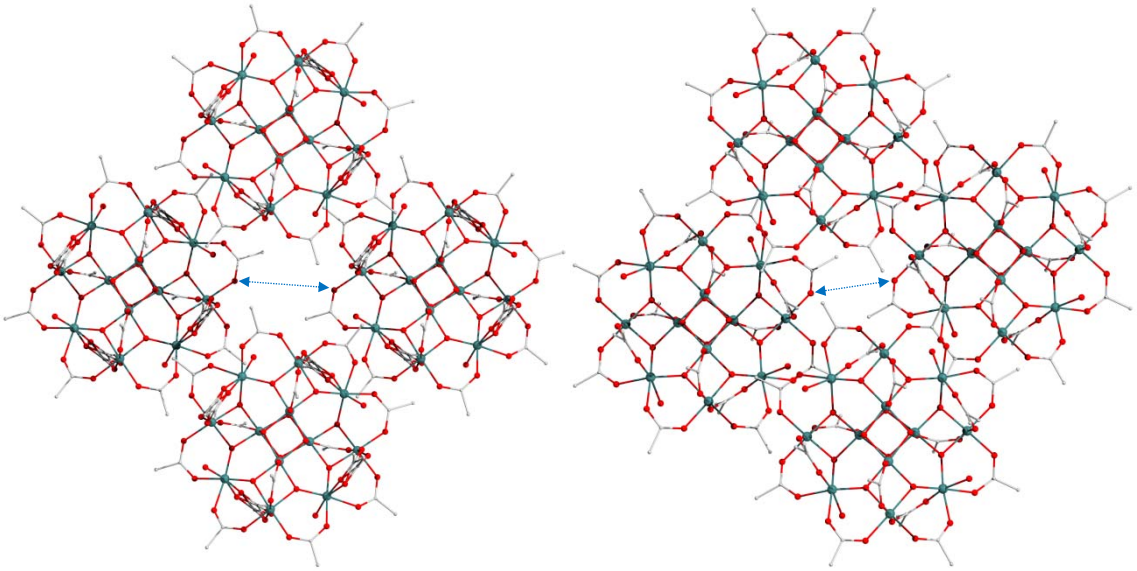

Figure 2-8: Comparison of interstitial cavity size for compound **1** (left) and $[Mn_{12}O_{12}(O_2CMe)_{16}(H_2O)_4]$ (**3**, right). All solvent of crystallisation is removed from the drawing of **1** for clarity. The marked cross-cavity distances are 5.8081(29) Å and 4.5114(30) Å respectively, showing a large reduction in size upon full desolvation. Consequently the $\{Mn_{12}\}$ clusters are significantly closer together in **3**.

2.2.4 Solvent replacement in a desolvated $\{Mn_{12}\}$ species

Further to the studies we performed concerning solvent removal, we attempted to 're-solvate' the desolvated species **2** and **3**. Song and co-workers have shown that single crystals of a 4*f* SMM can be dehydrated and subsequently rehydrated, retaining their crystallinity.[120] This transformation alters its low temperature magnetic properties. The selection of possible substitute solvents is narrowed by the constraint of the cavity size they are required to occupy. The void was previously occupied by acetic acid (CH_3CO_2H) and so we limited our choices to small molecules with no more than four non-hydrogen atoms.

We attempted to 're-solvate' portions of the bulk desolvated sample (a mixture of **2** and **3**) using water, methanol, ethanol, *n*-propyl alcohol, isopropyl alcohol and acetic acid. The crystals were exposed to vapour of each solvent under ambient pressure and temperature in a sealed vial. Methanol caused the crystals to decompose and most of the other solvents had no discernible effect (crystals measured subsequently were found to be **2**). Under these conditions only ethanol was able to be inserted into the structure, producing $[Mn_{12}O_{12}(O_2CCH_3)_{16}(CH_3CH_2OH)_4]\cdot CH_3CH_2OH$ (**4**). Only one crystal was found to have been transformed in this manner from a selection that was measured. It is possible that successful insertion of ethanol into the structure only occurs for crystals of **3**. Since there are relatively few crystals of **3** compared with **2** in the bulk desolvated sample, only those

few crystals could be converted to **4**. This is consistent with only one crystal of **4** being found in the sample after exposure to ethanol vapour. Furthermore, since all crystals measured after exposure to other solvents were species **2**, it might be the case that we did not select any crystals that were **3** and could have been converted to other species.

Similar to the previous analogues described, **4** crystallises in the tetragonal space group *I*-4. The cell volume has increased to V=3761(6) Å^3 compared with V=3595.64(8) Å^3, 3576.0(14) Å^3 and 3067.4(4) Å^3 for **1**, **2** and **3** respectively. This is largely due to an increase in the *a* distance from 17.1875(2) Å for **1** to 17.540(10) Å. In **4**, an ethanol ligand replaces the water ligand O12 that is present in **1**, **2** and **3**. Ethanol of crystallisation also occupies the interstitial void previously occupied by acetic acid in **1**. All non-hydrogen atoms except those belonging to the disordered ethanol of crystallisation were refined with ADPs. Part occupied atoms O13/O14/C11/C12 were refined isotropically. Hydrogen atoms were placed in calculated positions and allowed to ride on their parent atoms. The disordered lattice ethanol is situated on a two-fold rotation axis, but is also subject to further disorder in the orientation of the C-O bond relative to the C-C direction. The ethanol of crystallisation is comprised of atoms C11, C12 and either O13 or O14. The occupancies of C11 and C12 were restrained to be equivalent, refined to approximately 0.25 and then fixed at this value. The occupancies of O13/O14 were restrained to sum to 0.25; they refined to approximately 0.125 each and were subsequently fixed at this value. Thus, there is the equivalent of a half-occupied ethanol per site, and a total of one ethanol per cluster. Full crystallographic data are given in table 2.1.

Interestingly, for compound **4** the only significant intermolecular hydrogen bonding takes place between ethanol of crystallisation and a neighbouring cluster [O14---O6, 2.99(3) Å] (figure 2-9). There is also an intramolecular hydrogen bond between the coordinated ethanol and an acetate ligand [O12-H121---O6, 2.613(5) Å]. There is no water of crystallisation to preserve long-range crystallographic order as is observed in compounds **1** and **2**. In **3** where there is also no water of crystallisation, the previous packing arrangement is altered such that the clusters are closer together. Yet despite the lack of water of crystallisation in **4**, the $\{Mn_{12}\}$ clusters are actually further apart than in any of the other three complexes.

The disordered ethanol of crystallisation occupies approximately the same footprint as the acetic acid in **1**. Perhaps the key difference in **4** is the coordinated ethanol ligand

O12/C9/C10 that takes the place of the water present in the other 3 structures. It is conceivable that the steric bulk of having four such molecules (each with two extra carbon atoms compared with water) coordinated to each cluster forces the clusters apart.

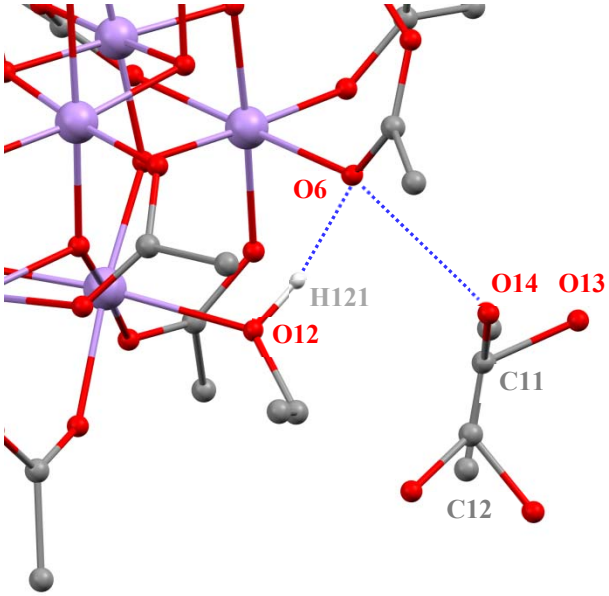

Figure 2-9: Intermolecular and intramolecular hydrogen bonding in **4**. The coordinated ethanol donates from O12 to O6 *via* H121 and the ethanol of crystallisation donates from O14 to O6. The ethanol of crystallisation is located on a two-fold rotation axis and also exhibits disorder in the position of the oxygen atom. Atoms are labelled for one orientation about the two-fold axis. Atom colours: Mn, purple; O, red; C, grey. H atoms except for that involved in intramolecular hydrogen bonding are omitted for clarity. It was not possible to place H atoms on the ethanol of crystallisation.

Mn-O bond distances around Mn2 and Mn3 show good agreement with those observed for the previous structures (see table 2.2), confirming that **4** has eight Mn^{III} centres with pseudo-aligned Jahn-Teller axes. The tilt angles for each of the Jahn-Teller axes are similar to those observed previously at 35.55(6)° and 9.20(6)° for Mn3 and Mn2 respectively. We expect this compound to exhibit slow relaxation properties commensurate with the original species **1** since the $\{Mn_{12}\}$ core is largely unaltered. However due to the presence of lattice solvent it is unclear whether or not the data will display the selection rules associated with S_4 symmetry. Such measurements are dependent on our ability to synthesise more crystals of this material.

2.2.5 Discussion of $\{Mn_{12}\}$ species

The joint X-ray and neutron study represents the first structural data collected for a single-molecule magnet, $[Mn_{12}O_{12}(O_2CMe)_{16}(H_2O)_4]\cdot 4H_2O\cdot 2MeCO_2H$ (commonly Mn_{12}-acetate, **1**), at the same temperature as magnetisation experiments were performed, 2 K. We have described a more complete model of the disorder and hydrogen-bonding network inherent

to the structure by using a combination of ultra-low temperature single-crystal X-ray and neutron diffraction experiments. We have found an additional hydrogen bond in the disordered region that contributes to a clear understanding of how the lattice solvent transmits disorder to the $\{Mn_{12}\}$ complex. A thorough comparison has been made between the structure measured at 2 K and the previously published data recorded at 83 K, revealing some interesting changes in the positions of each disordered component of the acetate ligands.

By synthesis of new desolvated species **2** $[Mn_{12}O_{12}(O_2CMe)_{16}(H_2O)_4]\cdot 4H_2O$ and **3** $[Mn_{12}O_{12}(O_2CMe)_{16}(H_2O)_4]$ (*via* single-crystal to single-crystal transformations), we have determined that disorder in the acetic acid of crystallisation is responsible for positional disorder in an acetate ligand in **1**. Upon removal of the acetic acid of crystallisation in **1**, the positional disorder in the acetate ligand O6/O7/C3/C4 is largely resolved. The extended network is created by a series of hydrogen bonds between clusters that take place through the water of crystallisation. This hydrogen-bonded network is preserved even in the absence of acetic acid of crystallisation (in **2**), however when solvent water is removed (in **3**) the network is modified such that $\{Mn_{12}\}$ clusters are significantly closer together. Further investigation into the ultra-low temperature quantum and magnetic properties of species **2** and **3** will be carried out in order that a comparison can be made with other axially symmetric members of the $\{Mn_{12}\}$ family, and with the original species **1**.

Successful solvent replacement has been achieved by insertion of ethanol into the cavity vacated by the removal of solvent of crystallisation from the original species **1**. New species $[Mn_{12}O_{12}(O_2CCH_3)_{16}(CH_3CH_2OH)_4]\cdot CH_3CH_2OH$ (**4**) is formed from **1** by sequential single-crystal to single-crystal transformations (desolvation then re-solvation) and crystallises in the same space group. It is unclear whether the intermediate desolvated species is **2** or **3**, but experimental evidence is more consistent with **4** forming from **3**. The $\{Mn_{12}\}$ core is retained with the coordinated water replaced by ethanol in addition to insertion of ethanol of crystallisation. We expect **4** to have similar magnetic properties to **1** but it has not yet been possible to isolate enough of the complex on which to perform magnetic measurements.

2.3 A high-symmetry {Mn_3} SMM

A series of Mn^{III}-based SMMs that each contain a $\{Mn^{III}_3O\}^{7+}$ oxo-centred triangle has been the subject of intense research over the last few years.[121] Each edge of the triangle is bridged by the –N–O– moiety of a doubly-deprotonated R-sao^{2-} ligand {$saoH_2$ = salicylaldoxime, see figure 2-10}. The R group can vary, and in doing so significant structural changes can be induced that affect the magnetic properties of the molecule. Using a bulky R group generally causes puckering of the (-Mn-O-N-)$_3$ ring favouring ferromagnetic exchange over antiferromagnetic exchange (see figure 2-11).[122] A great many SMMs have been reported that contain this basic unit (approximately eighty molecules at the time of writing). Some are based on a single $\{Mn^{III}_3O\}^{7+}$ triangle,[123] while others are based on two off-set, stacked triangles linked by two central oxime groups forming a {Mn_6} species.[124] For the {Mn_3} species, bulky ligands are used to cap one face of the triangle in order to prevent dimerisation. Another method of distorting the triangle in order to favour ferromagnetic exchange and enhance its SMM properties is to cap one face with a small tripodal ligand that constricts the geometry of the ring, *e.g.* ClO_4^- or ReO_4^-.

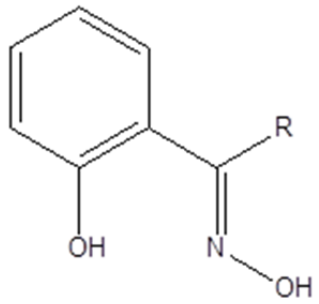

Figure 2-10: The R-substituted salicylaldoxime ligand.

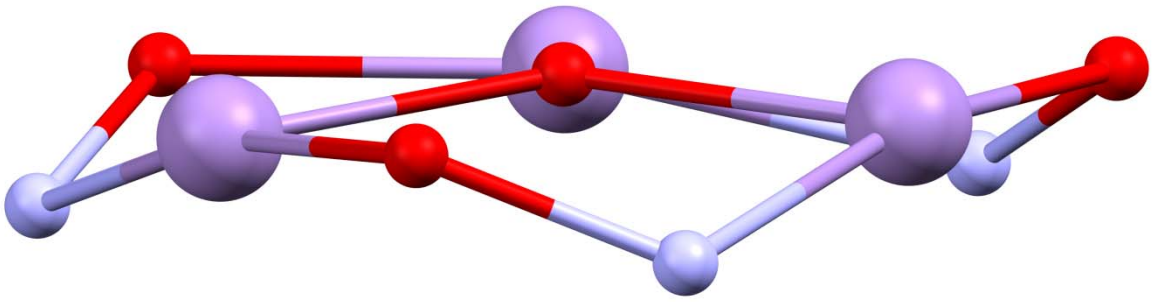

Figure 2-11: Puckering of the (-Mn-O-N-)$_3$ ring in {Mn_3} compounds. The example shown here is taken from our new ultra-low temperature (2 K) neutron structure determination of $[Mn^{III}_3O(Et\text{-}sao)_3(ClO_4)(MeOH)_3]$ {Et-$saoH_2$ = C_6H_4-1-$CH(C_2H_5)N(OH)$-2-OH} (**5**). Atom colours: Mn, purple; N, blue; O, red.

The molecule $[Mn^{III}_3O(Et\text{-}sao)_3(ClO_4)(MeOH)_3]$ {Et-saoH$_2$ = C_6H_4-1-$CH(C_2H_5)N(OH)$-2-OH} (**5**, structure shown in figure 2-12) was chosen for further structural studies since it exhibits strong single-molecule magnetic behaviour and crystallises in the rhombohedral space group *R*-3.[125] ClO_4^- caps one face of the triangle, exhibiting weak interactions to each of the three Mn^{III} ions. The other face is capped by 3 coordinated methanol ligands. There are complementary hydrogen bonds between the O-H of the methanol ligands and the phenolate oxygen atoms of the ethyl-salicylaldoxime ligands on neighbouring clusters, *i.e.* each molecule is hydrogen bonded to its three closest neighbours (figure 2-13). This produces a (6,3) net in the *ab* plane of alternating {Mn_3} clusters (figure 2-14); adjacent clusters point in opposite directions with the perchlorate ligand alternately pointing up and down (figure 2-15). The central triangles themselves are all approximately coplanar. It has previously been established by semi-quantitative magneto-structural correlations that Mn-O-N-Mn torsion angles above 31° should promote ferromagnetic exchange via this pathway and thus, encourage SMM behaviour (figure 2-16).[121, 122] From the crystal structure measured at 150 K, this torsion angle in **5** is approximately 42.1° (identical for all three due to the C_3 symmetry).

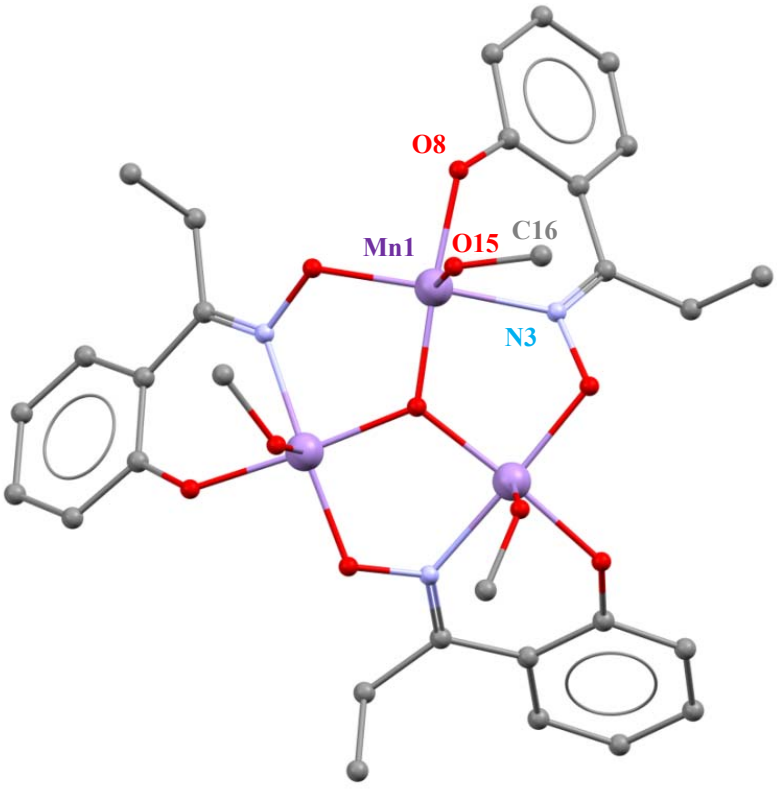

Figure 2-12: The structure of **5**. The perchlorate ligand occupies the lower face of the {Mn_3} triangle but is omitted for clarity. Atom colours as previously defined; C, grey. H atoms are omitted for clarity.

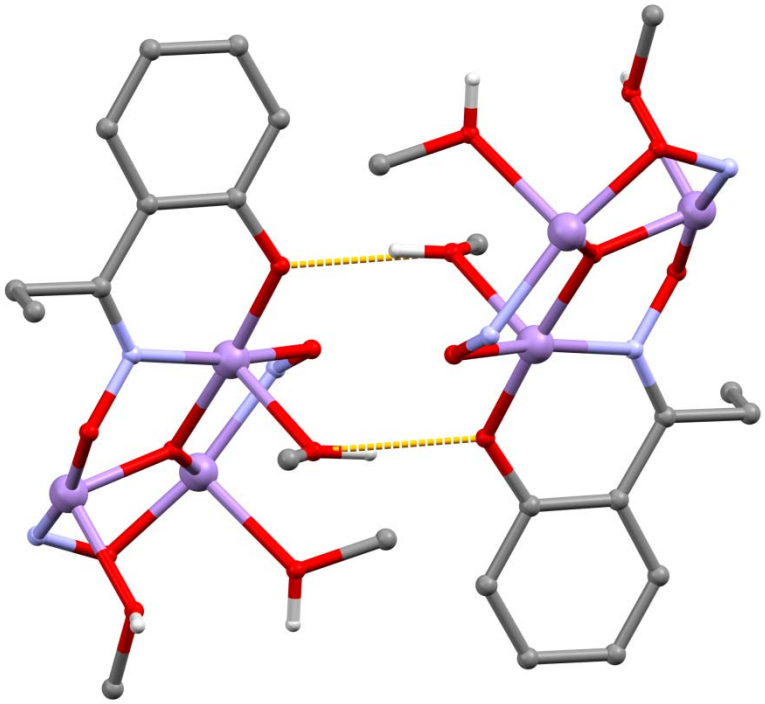

Figure 2-13: Complementary intermolecular hydrogen bonding in **5** from the O-H of the coordinated methanol to the phenolic oxygen atom of an Et-sao^{2-} ligand on a neighbouring molecule. Hydrogen atoms attached to carbon atoms are omitted for clarity. Atom colours are as previously defined; H, white.

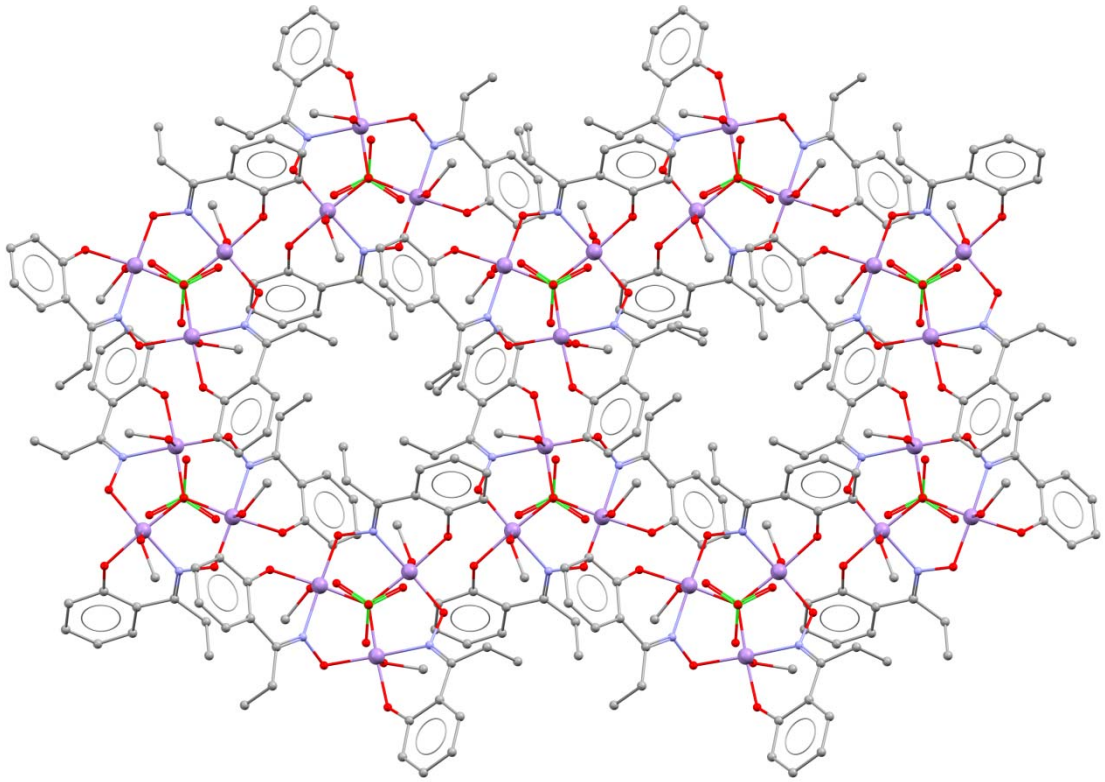

Figure 2-14: Crystal packing of **5** indicating the (6,3) net (molecules are arranged in a honeycomb-type structure with rings of 6, while each interacts with 3 others) in the *ab* plane of alternating {Mn_3} clusters; adjacent clusters point in opposite directions with the perchlorate ligand alternately pointing up and down. Atom colours are as previously defined; Cl, green. H atoms are omitted for clarity.

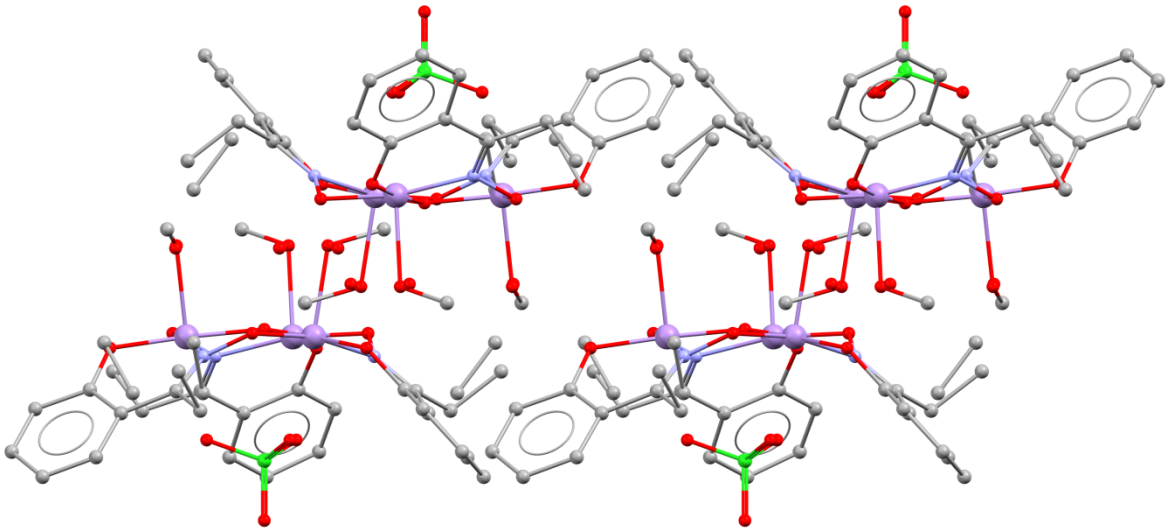

Figure 2-15: The bi-layer arrangement of **5** viewed along the crystallographic *a* axis. Atom colours are as previously defined; H atoms are omitted for clarity.

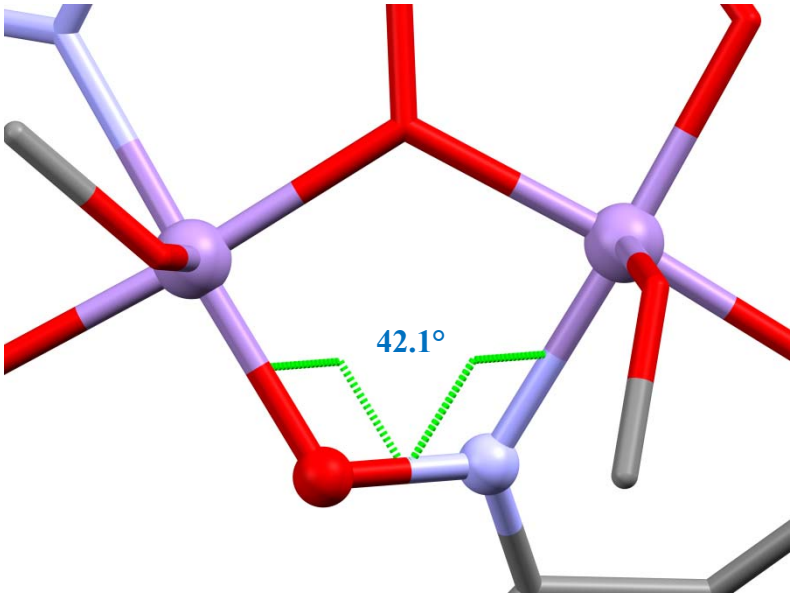

Figure 2-16: Mn-O-N-Mn torsion angle in **5**. Semi-quantitative magneto-structural correlations suggest that angles above approximately 31° should promote ferromagnetic exchange.[121, 122] Atom colours are as previously defined.

AC susceptibility measurements on **5** show a frequency-dependent out-of-phase signal at approximately 5 K.[125] Magnetisation measurements indicate an S=6 ground state with a significant anisotropy D. Fitting of the data with an axial zero field splitting (ZFS) and Zeeman Hamiltonian gave poor results, but suggest D=-0.95 cm^{-1}.[125] The accuracy of this value is questionable, according to the authors. SMM behaviour is confirmed by the observation of magnetisation *vs*. field hysteresis loops that are both temperature- and sweep-rate dependent. A detailed analysis of the hysteresis loops shows that the collective spin of each {Mn_3} cluster is weakly coupled antiferromagnetically to neighbouring

clusters. This acts as a bias that shifts the quantum tunnelling (QTM) resonances with respect to an isolated SMM.[125] The proposed mechanism for this coupling is through the complementary hydrogen bonds described above. Figure 1-5 shows magnetisation *vs*. field hysteresis loops for **5**. It is noted that there is no QTM step at zero field; this is indicative of intermolecular coupling.

2.3.1 Synthesis of $[Mn^{III}_3O(Et\text{-}sao)_3(ClO_4)(MeOH)_3]$ (5)

Synthesis of **5** was carried out by Dr Ross Inglis, University of Edinburgh, according to the published method.[19] $Mn^{II}(ClO_4)_2{\cdot}6H_2O$ (0.25 g, 0.98 mmol), Et-saoH_2 (0.17g, 1 mmol) and a 1.0 M aqueous solution of $NEt_4(OH)$ (2 mL) were dissolved in 25 mL of MeOH. After stirring for one hour, the resulting dark green solution was filtered and left for slow evaporation. Large black single crystals of **5** were obtained from the mother liquor after one week. Elemental analysis [%], calc. (found) for $C_{27.7}H_{34.4}ClMn_3N_3O_{14}$ ($[Mn_3O(Et\text{-}sao)_3(ClO_4)(H_2O)_{2.3}(CH_3OH)_{0.7}]$): C, 39.9 (39.8); H, 4.16 (4.07); N, 5.04 (4.98). These elemental analysis data were measured after ultra-low temperature structural data were collected for **5** and are consistent with the structural data (see below). The original published work does not refer to any disorder in the identity of the ligands.

2.3.2 Structural disorder at ultra-low temperature

The crystal structure of **5** was measured using X-ray and neutron radiation at ultra-low temperature. The X-ray structure was determined at 2 K using the XIPHOS facility at Durham University.[48] A crystal of approximate dimensions 0.25 x 0.25 x 0.25 mm was mounted on a graphite rod perpendicular to the incident beam. Neutron data were collected at 2 K and 30 K using the D19 monochromatic neutron diffraction instrument at ILL, Grenoble.[51] A crystal of approximate dimensions 3.5 x 3.5 x 2.0 mm was mounted on a vanadium rod and secured to the sample mount inside a two-stage Displex cryorefrigerator[126] equipped with an additional stage for cooling to 2 K.

Neutron Laue data were also measured at 5 K and 120 K using the Koala Quasi-Laue Diffractometer (QLD) at ANSTO, Sydney. A crystal of approximate dimensions 1.7 x 1.7 x 0.85 mm was held by a smear of Si grease on an Al foil support attached to the cold head of a Janis Research two-stage Gifford-McMahon cryorefrigerator. Data were collected for two crystals (approximately the same dimensions) and the data from both crystals were

combined after ensuring that the degree of disorder in each was similar. 10 Laue diffraction patterns, each accumulated over 38,000 seconds, were collected for each crystal in 10° intervals in rotation of the crystal perpendicular to the incident neutron beam. Data were observed to a minimum *d* spacing of 0.85 Å and 0.80 Å respectively for the first and second crystals. The Laue patterns were indexed using the program LAUEGEN of the Daresbury Laboratory Laue Suite[109, 127] and the reflections were integrated using the program INTEGRATE+ which uses a two-dimensional version of the minimum σ(I)/I algorithm described by Wilkinson *et al*.[111] Cell parameters at 5 K were taken from the 2 K neutron determination on D19; those at 120 K were taken from a previous 150 K structural determination.[125] The reflections were normalised to a common wavelength, using a curve derived by comparing equivalent reflections and multiple observations, and corrected for the different angles of incidence using the in-house program LAUE4.[128]

The difference in crystal size for each of the experiments reflects the requirement for much larger crystals in neutron diffraction compared to X-ray diffraction, and in particular for monochromatic neutron diffraction compared to neutron Laue diffraction. All samples used were from the same preparation of crystals and were not deuterated. Similar to the neutron experiment performed on Mn_{12}-acetate (**1**), the negative scattering density from hydrogen atoms was useful in accurately finding their positions from both sets of neutron data.

Broadly speaking, the X-ray structure we measured at 2 K is similar to the published structure at 150 K.[125] It crystallises in the same space group *R*-3 with a reduction in cell volume from 5279.7(2) $Å^3$ to 5115.1(3) $Å^3$. This reduction is probably caused by thermal contraction and is accompanied by a small reduction in the *c* length and larger reductions in *a* and *b*. However, a significant structural difference is noted between our new structure and the previous 150 K determination. For the sake of understanding this difference it is easier to consider the asymmetric unit of the structure. The single unique manganese Mn1 has one coordinated solvent molecule. In the previous determination this has been modelled as a fully occupied methanol molecule O15/C16 (as shown in figure 2-12). When we modelled it in this way for the 2 K data, the thermal ellipsoid on C16 was unusually large and it became apparent that it was not fully occupied. However oxygen atom O15 does appear to be fully occupied, indicating that the solvent can be modelled as part methanol and part water. O15 was split into two atoms O15 and O15A, with O15/C16 forming the methanol molecule and O15A forming the water molecule (figure 2-17). The

occupancies of these groups were restrained such that O15/C16 had the same occupancy, and that occupancy plus the occupancy of O15A were required to sum to unity. This resulted in a good refinement of all three atoms O15/C16/O15A, even when ADPs were included.

Atoms C13/C14 belonging to the ethyl substituent of the Et-sao^{2-} ligand showed some unusual elongation. We determined that these could be modelled over two positions, with the occupancies of each component restrained to sum to unity. These were denoted C13/C14 and C13A/C14A (figure 2-17). Again a good refinement was achieved, even when the atoms were modelled with ADPs.

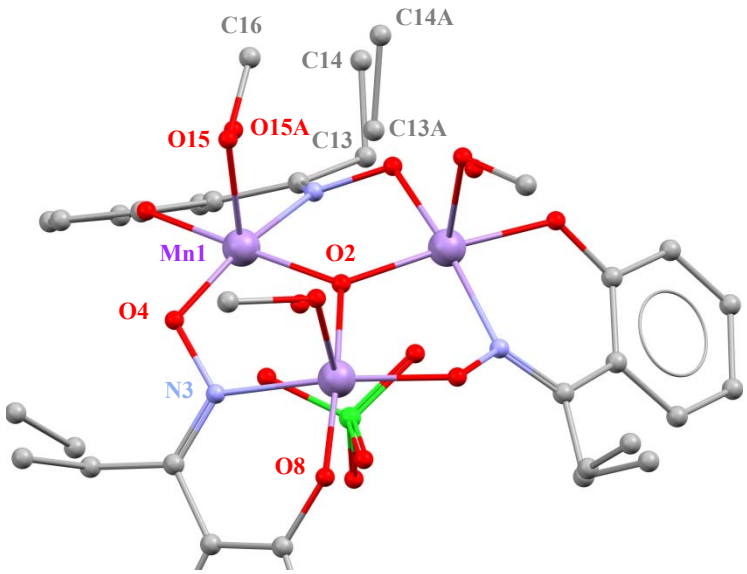

Figure 2-17: Crystal structure of **5** measured at 2 K using single-crystal X-ray diffraction, including both sites of the disordered ethyl substituents and methanol/water ligands. Atom labels are indicated for relevant atoms; the cluster has approximate C_3 symmetry. Atom colours are as previously defined. H atoms are omitted for clarity.

Interestingly it appears that both disordered regions in the cluster (coordinated solvent and Et-sao^{2-} ligand) are linked. We noticed that the distance between C16 of a coordinated methanol molecule and the terminal atom C14A of one of the sites for the ethyl substituent on an adjacent cluster is only 2.82(1) Å (figure 2-18). The Van der Waals radius of carbon is 1.70 Å and so the theoretical closest approach distance for two non-bonded carbon atoms is 3.40 Å. Clearly the ethyl substituent cannot be located in positions C13A/C14A when the identity of the nearest coordinated solvent on the adjacent cluster is methanol. Correspondingly the distance between C16 and C14, the other site for the terminal atom of the ethyl substituent is 3.419(8) Å. Furthermore the freely refined occupancies of O15/C16

and C13/C14 are very similar. We can explain the exact nature of the relationship in the disordered components as follows:

The identity of the coordinated solvent is either methanol or water. When it is water (atom O15A), the nearest ethyl substituent on the neighbouring cluster is in the position defined by atoms C13A/C14A. All three atoms are restrained to have the same occupancy. When the coordinated solvent is methanol (atoms O15/C16), the nearest ethyl substituent on the neighbouring cluster can no longer occupy the same positions (C13A/C14A) for steric reasons and must occupy the positions defined by atoms C13/C14. Again all four atoms here are restrained to have the same occupancy. Furthermore the occupancy of this component and that of the other component (atoms with an 'A') are restrained to sum to unity. In the crystal we measured at 2 K, the ratio between methanol and water is 0.644:0.356. However, there is strong evidence from other crystals that this ratio can vary significantly; one sample measured at 100 K on our own X-ray diffractometer showed the ratio to be 0.447:0.553.

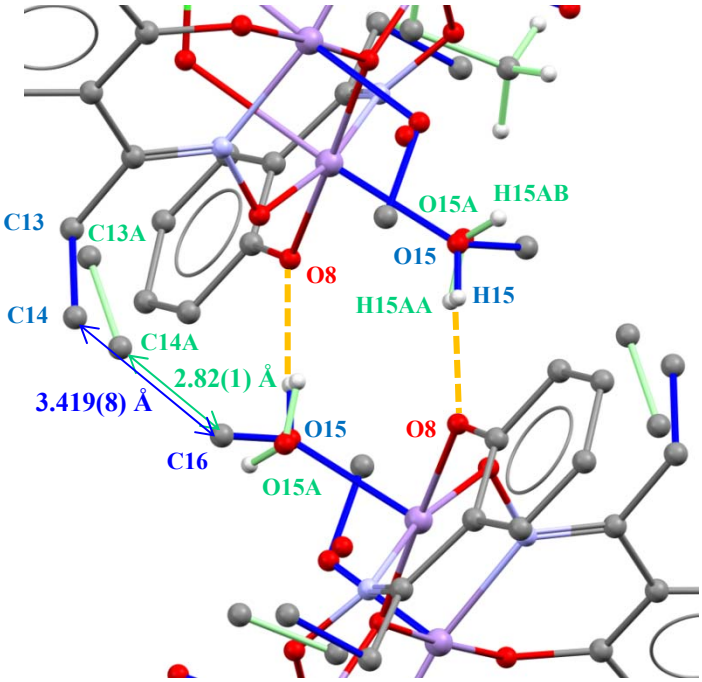

Figure 2-18: Intramolecular hydrogen bonding (shown in yellow) between two adjacent {Mn_3} clusters *via* complementary O-H---O pathways. The shortest distance (in Å) between the C atom of the methanol ligand (C16) and the terminal atom of the ethyl substituent (C14/C14A) is shown for both disorder components (blue = coordinated methanol; green = coordinated water). The sum of the Van der Waals radii (~3.4 Å) is greater than the distance for C16-C14A (2.82(1) Å), but approximately equal to the distance for C16-C14 (3.419(8) Å). Atom colours are as previously defined; H atoms except for those involved in hydrogen bonding are omitted for clarity.

Table 2.4: Crystallographic data for the various determinations of the structure of **5**. (i) X-ray, 2 K. (ii) Neutron, 2 K [D19]. (iii) Neutron, 30 K [D19]. (iv) Neutron, 5 K [KOALA]. (v) Neutron, 120 K [KOALA].

	5 (i)	**5 (ii)**	**5 (iii)**	**5 (iv)***	**5 (v)***
Formula	$C_{28.93}H_{36.86}ClMn_3N_3O_{14}$	$C_{30}H_{39}ClMn_3N_3O_{14}$	$C_{30}H_{39}ClMn_3N_3O_{14}$	$C_{27.96}H_{34.92}ClMn_3N_3O_{14}$	$C_{28.08}H_{35.17}ClMn_3N_3O_{14}$
CH_3OH : H_2O ratio	1.93 : 1.07	3.00 : 0.00	3.00 : 0.00	0.96:2.04	1.08:1.92
M_w	850.90	865.91	865.91	837.29	839.03
Crystal system	Trigonal	Trigonal	Trigonal	Trigonal	Trigonal
Space group	*R*-3	*R*-3	*R*-3	*R*-3	*R*-3
a [Å]	13.1815(5)	13.3400(19)	13.3390(19)	13.3400(19)	13.3784(3)
c [Å]	33.9935(12)	33.859(7)	33.860(7)	33.859(7)	34.0617(12)
V [Å^3]	5115.1(3)	5218.1(15)	5217.5(15)	5218.1(15)	5279.7(3)
Z	6	6	6	6	6
T [K]	2.0(1)	2.0(1)	30.0(1)	5.0(1)	120.0(1)
Radiation	X-ray	Neutron	Neutron	Neutron	Neutron
λ [Å]	0.71073	1.17017	1.17017	Laue	Laue
D_c [g cm^{-3}]	1.658	1.653	1.654	1.599	1.583
μ [mm^{-1}]	1.24	0.296	0.251	0.230	1.657
Meas./indep. refl.	12696/2256	17226/3972	18071/4019	26860/1951	28198/1940
R_{int}	0.0376	0.0750	0.0752	0.2469	0.2749
Obs. refl. [$I > 2\sigma(I)$]	2071	3679	3739	1416	1351
wR_2 [a]	0.0875	0.1136	0.1116	0.1195	0.1083
R_1 [b]	0.0361	0.0541	0.0536	0.0732	0.0683
Goodness of fit on F^2	1.24	2.561	2.575	1.861	1.667
$\Delta\rho_{max,min}$ [e Å^{-3} / fm Å^{-3}] [c]	0.54/-0.42	1.55/-1.31	1.69/-1.26	0.657/-0.663	0.487/-0.819

* Cell parameters for the neutron Laue data were taken from (iv) the 2 K D19 experiment and (v) a published 150 K study.[125] The CH_3OH:H_2O ratio for **5 (iv)** and **5 (v)** should be the same at both temperatures since the same crystals were used at each temperature and the datasets combined in the same way; however this is a refined value and subject to error.

[a] $wR_2 = \{\sum[w(F_O^2 - F_C^2)^2]/\sum[w(F_O^2)^2]\}^{1/2}$ on F^2; [b] $R_1 = \sum||F_O| - |F_C||/\sum|F_O|$; [c] Residual electron density (e Å^{-3}) is given for X-ray data and residual scattering length (fm Å^{-3}) is given for neutron data.

The structure derived from neutron Laue data at 5 K on Koala (full crystallographic data given in table 2.4) shows a similar effect; however, the ratio of coordinated methanol to water is quite different. The 2 K X-ray structure has approximately 64% methanol coordinated to the metal ions, while the 5 K neutron Laue structure has only 30% methanol. The occupancies of the two disordered components of the ligand ethyl substituent are again exactly related to those of the methanol and water ligands.

The neutron-derived structure at 2 K on D19, however, does not exhibit the same disorder seen in the X-ray determination at the same temperature. Three methanol molecules occupy one face of the triangle and the ethyl substituents on the ligands occupy only one site each. The anisotropic displacement parameters (ADPs) associated with all the atoms in the neutron-derived structure are extremely small, indicating no evidence of unresolved disorder. Indeed even hydrogen atoms attached to the carbon and oxygen atoms in question can be modelled with ADPs and show no evidence of disorder. We are confident that were such disorder to exist in the crystal measured, it would have been observable using this technique.

Unfortunately we do not have access to the raw data from the original 150 K structure determination and so we cannot determine for sure if the crystal that was measured of the original sample also exhibited the same disorder. What can be seen is that the thermal ellipsoids for atoms C13, C14 and C16 (both carbon atoms of the ligand ethyl substituent and the carbon atom of the coordinated methanol) show a degree of elongation not seen for neighbouring atoms. We see the same broadened ellipsoids when our 2 K X-ray data is modelled without taking account of the disorder. When the disorder is modelled, the ellipsoids for all atoms in both disorder components are smaller and comparable with their neighbours. While this is not conclusive evidence for disorder in the original published structure, it is at the very least consistent with this possibility.

A comparison can be made of the average size of the thermal ellipsoids for the structure of **5** as measured using each of the different techniques described above. ORTEP-style plots showing each structure drawn with thermal ellipsoids at the 50% probability level are given in figures 2-19 (2 K X-ray structure, published 150 K X-ray structure), 2-20 (2 K and 30 K monochromatic neutron structures) and 2-21 (5 K and 120 K neutron Laue structures). These plots were created using the Mercury software package[129] and rendered using POV-Ray.[130] All are shown at approximately the same scale.

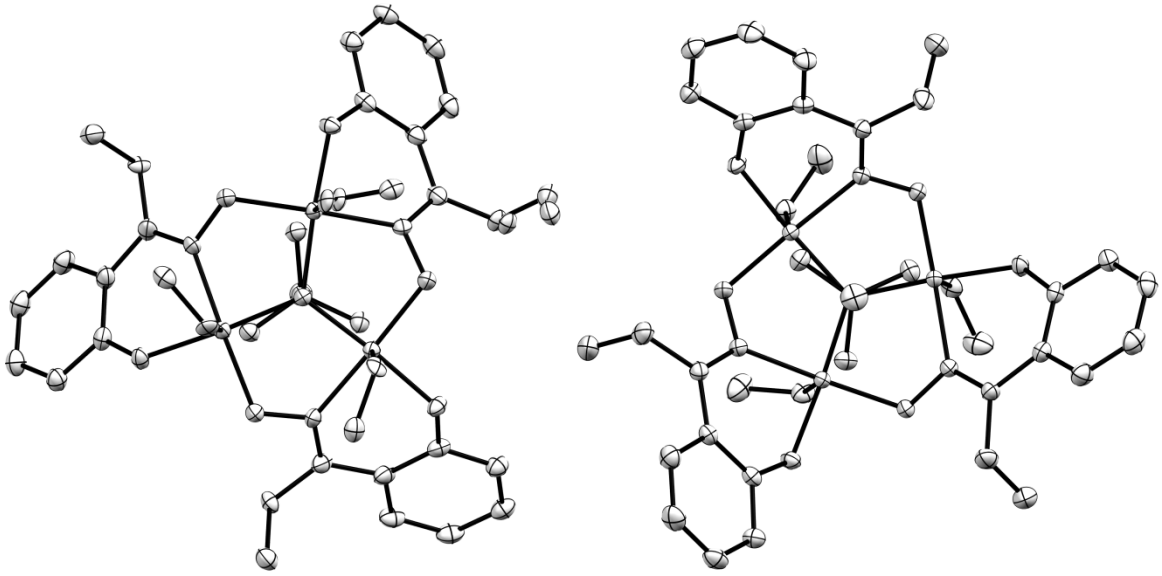

Figure 2-19: ORTEP-style plots of **5** at 2 K (left, X-ray data, XIPHOS) and 150 K (right, published data).[125] Ellipsoids are drawn at the 50% probability level. H atoms are omitted for these X-ray datasets since their thermal parameters are correlated with those of their parent atoms.

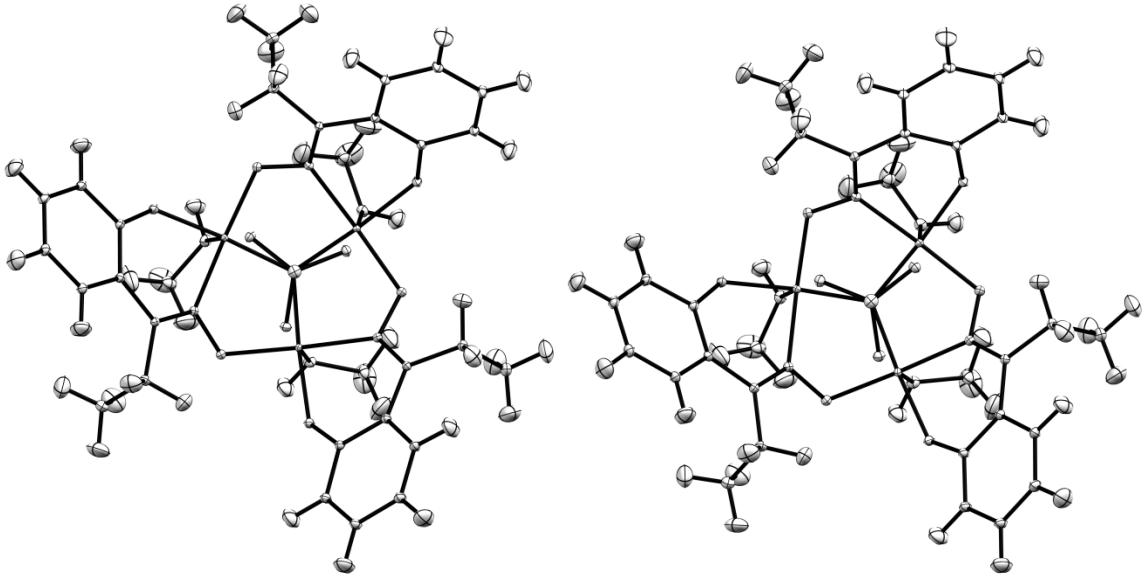

Figure 2-20: ORTEP-style plots of **5** at 2 K (left, monochromatic neutron data, D19) and 30 K (right, monochromatic neutron data, D19). Ellipsoids are drawn at the 50% probability level.

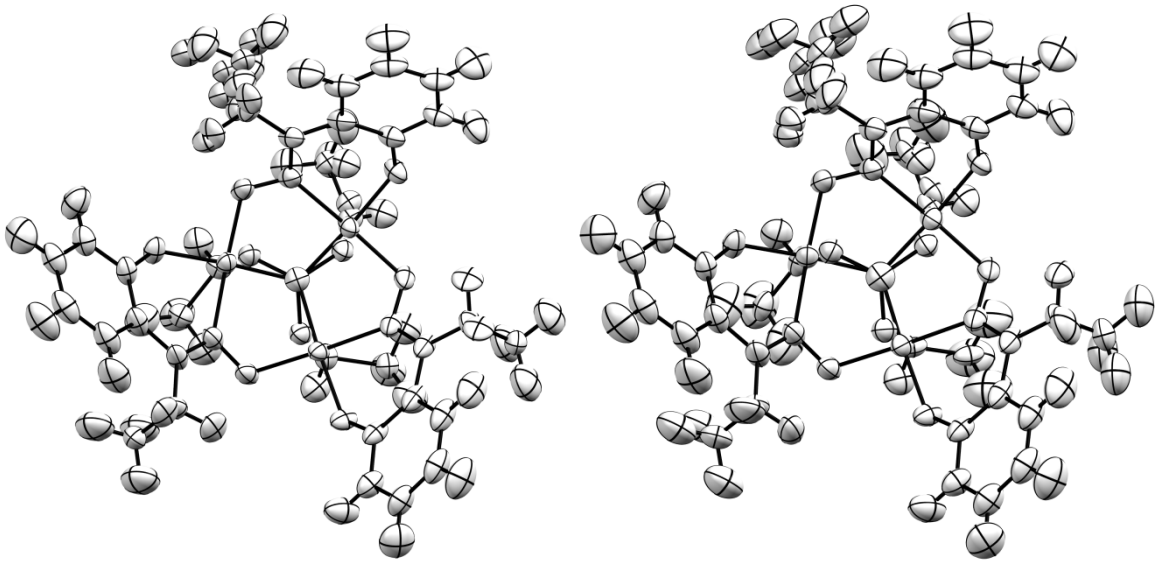

Figure 2-21: ORTEP-style plots of **5** at 5 K (left, neutron Laue data, KOALA) and 120 K (right, neutron Laue data, KOALA). Ellipsoids are drawn at the 50% probability level.

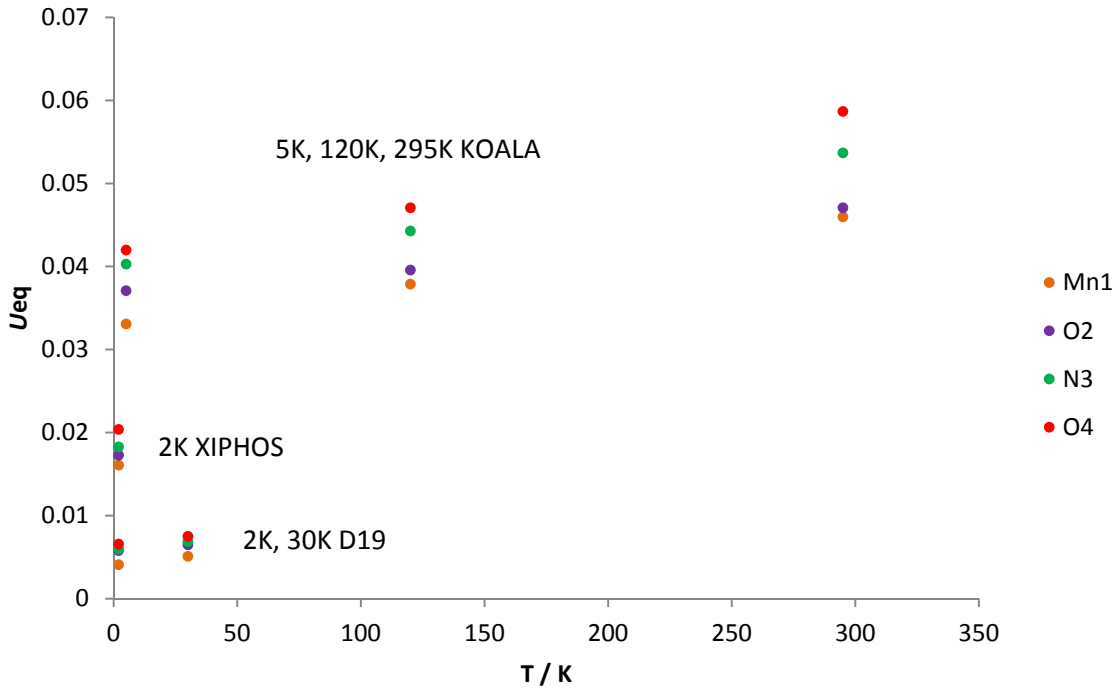

Figure 2-22: Equivalent isotropic thermal parameter U_{eq} *vs*. temperature for several atoms in **5**. Data are shown for the various datasets discussed herein.

Figure 2-22 shows a comparison of the equivalent isotropic thermal parameter U_{eq} for several atoms in **5** at various temperatures as measured by the techniques described herein. A clear trend can be seen within the thermal parameters for the three datasets collected using KOALA, and separately for the two datasets collected using D19; as expected, thermal motion decreases upon cooling. However data from D19 are inconsistent with data from KOALA; those collected on the latter instrument exhibit much larger thermal

parameters. This can be seen qualitatively by comparing figure 2-20 with figure 2-21. X-ray data (figure 2-19) are somewhere in the middle of the two extremes. It is not unusual to observe variation in thermal parameters from X-ray data *vs*. neutron data,[131, 132] however this does not account for the difference between the two types of neutron experiment (figure 2-20 *vs*. figure 2-21). The thermal parameters observed for the neutron Laue structure at 5 K are much larger than that expected from thermal motion at such a low temperature. It is unlikely that the sample temperature was incorrect, since the trend in thermal parameters for the three structures collected on Koala (295 K, 120 K, 5 K) is approximately linear. The size of the thermal ellipsoids can also be affected by systematic errors in the experiment or in the way the data are reduced. This possibility was investigated by altering the absorption correction and also by enlarging the size of the integration ellipses. The latter led to a 5% reduction in the size of the thermal ellipsoids; however, this does not come close to explaining the large increase in their size over what is expected. A further possibility is that the species measured in each experiment are not the same; the larger thermal parameters for every atom in the 5 K Laue structure could be attributed to a large scale disorder in the position of every atom in the $\{Mn_3\}$ cluster. The disorder in solvent ligand and ethyl substituent position described above could lead to inequivalence between clusters assumed to be equivalent by symmetry. In this case, the large thermal parameters would mask this disorder and it would not be reasonable to directly compare the structures of the two different species. Measurement of the structure of a non-disordered crystal of **5** by using the Laue technique would allow a direct comparison of its thermal parameters with those of the disordered structure measured using the same instrument.

2.3.3 Influence of structural disorder upon magnetic and quantum properties

The Mn-N-O-Mn torsion angle of 42.1° (figure 2-16) that is observed in the original 150 K structure is 42.7(2)° in the 2 K X-ray measurement, 42.4(1)° in the 2 K neutron measurement and 43.4(3)° in the 5 K neutron Laue measurement. All of these values are substantially greater than the 31° limit for ferromagnetic exchange via this pathway[122] and show good agreement with each other and so the single-molecule magnetic behaviour for an isolated cluster is not at all unexpected. However intermolecular antiferromagnetic exchange is thought to play a key role in the observed magnetic properties of the system. This is mediated by six O-H---O hydrogen bonds (one unique) between each cluster and its

neighbours (figure 2-18). The donor atom in this hydrogen bond is the oxygen atom of the coordinated solvent. In our X-ray structure at 2 K, the measured intermolecular contact distances (O15/O15A---O8) for this hydrogen bond are 2.66(2) Å (for methanol) and 2.81(3) Å (for water). H atom positions are not considered as these can be quite unreliable from X-ray measurements.[49] The analogous distance in the 2 K neutron structure is 2.715(2) Å. Clearly these distances are significantly different from each other. The strength of hydrogen bonding decreases with increasing distance and so the possible influence of antiferromagnetic exchange on the magnetic behaviour of the sample could be diminished in the case where the coordinated solvent is water.

The disorder also has strong implications for the quantum behaviour of the isolated cluster. The $\{Mn_3\}$ cluster has previously been assumed to possess crystallographic C_3 symmetry, as a consequence of the trigonal space group in which it crystallises. This is important as C_3 symmetry confers the quantum selection rule $\Delta m_s = 3$ upon quantum tunnelling steps (only every third step is observed) and implies a zero E term in the spin Hamiltonian.[133] Disorder in the identity of the coordinated solvent and in the position of the ethyl substituent of the ligand result in the existence of a number of possible isomers. One can easily envision four isomers, varying in the number (n) of coordinated solvents that are water from n=0 to n=3. However the reality is somewhat more complicated. The positional disorder of the ethyl substituent is entirely independent of the solvent disorder on the same cluster; in fact it is dependent on solvent disorder on a neighbouring cluster. Thus, we can introduce another variable p to describe the number of ethyl substituents that are positioned in accordance with a water solvent molecule on an adjacent cluster; p=0, 1, 2 or 3. n and p are entirely independent for a given cluster and therefore there are 16 possible combinations [np] with n=0-3 and p=0-3. Some of the combinations [np] only have a single isomer associated with them ([0p], [n0], [3p] and [n3]) while others could have more than one isomer, *e.g.* [11], depending on whether the Mn^{III} ion with a water attached is the same Mn^{III} ion that has a ligand positioned according to a water on the next cluster, or whether it is a different Mn^{III} ion. Other combinations [12], [21] and [22] can also have multiple isomers. However from all of the possible isomers, only the [00], [03], [30] and [33] isomers are axial, while all others possess a symmetry lower than C_3. The non-axial isomers are not subject to the quantum selection rule described above ($\Delta m_s = 3$) and are likely to possess a transverse anisotropy and consequently a non-zero E term. Figure 2-23 illustrates the various combinations that can exist.

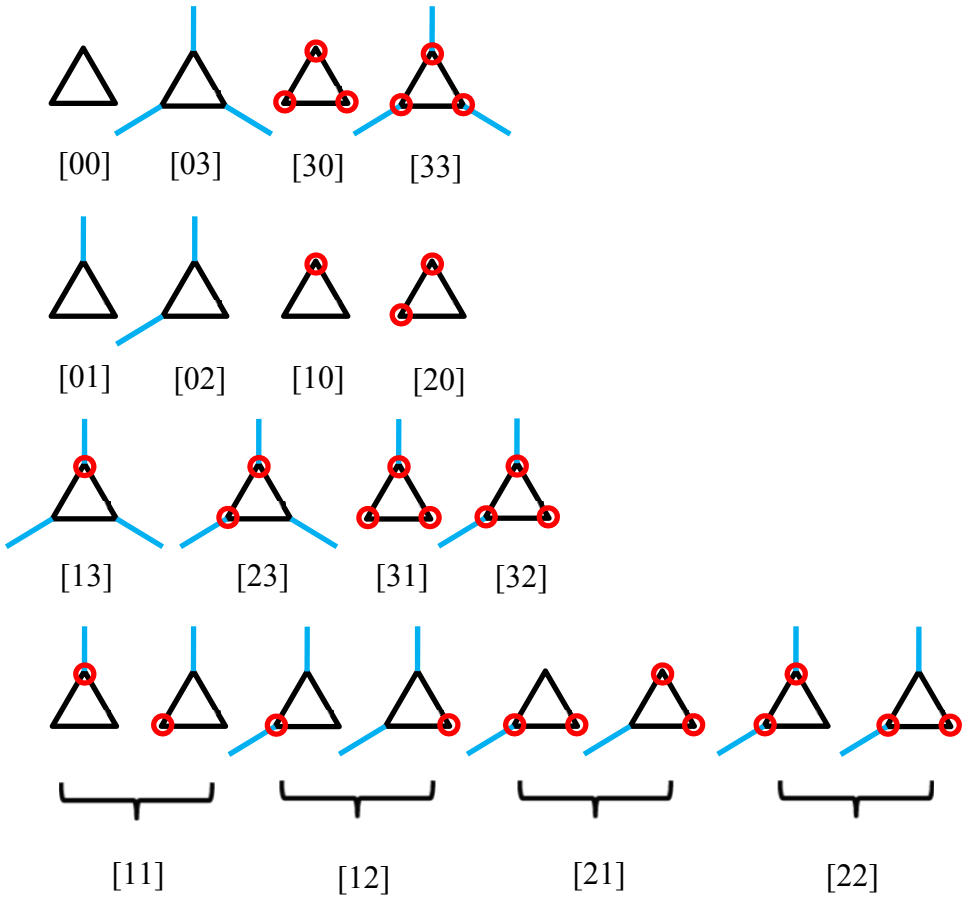

Figure 2-23: The simple black triangle represents the [00] species that contains 3 methanol ligands and 3 ethyl substituents that are each consistent with methanol ligands on the neighbouring clusters (atom positions C13/C14). For the other species, each blue line extending from a vertex of the triangle represents an ethyl substituent in positions C13A/C14A (*i.e.* consistent with a water ligand on the adjacent cluster); a red circle represents a water ligand in place of the methanol ligand coordinated to the cluster. The first row contains axial isomers, the second and third rows contain the non-axial [0*p*], [3*p*], [*n*0] and [*n*3] isomers and the fourth row contains non-axial combinations that have multiple isomers.

A difficult question to answer is which of these isomers actually exist in the crystal. This cannot be determined crystallographically; that only gives us the methanol:water ratio, and not the distribution of each across individual clusters. We can consider the measured physical and magnetic properties of **5** that are dependent on the symmetry. If only axial species [00], [03], [30] and [33] are present then we expect to see strict adherence to the selection rule $\Delta m_s = 3$ and no transverse anisotropy.

High-frequency and -field EPR (HF-EPR) measurements performed on single crystals of **5** by Inglis *et al*. are quite interesting in this regard.[123] The authors note that the appearance of multiple peaks for each cluster of fine-structure transitions suggests the presence of multiple species in the crystal. While there is strong agreement between the spectra and a spin Hamiltonian dependent on an S=6 ground state, the best simulation requires inclusion of transverse zero-field splitting terms; this suggests the presence of transverse anisotropy

and negates the possibility of solely axial species being present in the crystal. Both of these observations are consistent with the crystallographic information we have derived from the ultra-low temperature X-ray study and the neutron Laue study.

A similar effect has been observed for a family of $\{Ni_4\}$ SMMs; those that are solvated exhibit broad EPR signals compared with a non-solvated complex.[134] The broadening is thought to be caused by solvent and ligand disorder leading to additional distributions of microenvironments. We would like to be able to carry out further investigations on compound **5** in order to measure the HF-EPR characteristics of a crystal that does not exhibit any disorder. Unfortunately it appears that the abundance of such crystals is rarer than first thought and despite numerous attempts we have not been able to isolate another single crystal that does not exhibit disorder. In addition, the original non-disordered crystal measured at ILL was irreversibly damaged upon attempted re-measurement on XIPHOS.

2.4 Investigations of a $\{Mn_4\}$ SMM

There are several reported structures containing the cubane core $[Mn^{III}_3Mn^{IV}O_3X]^{6+}$, where X=F, Cl, Br. A brief survey of the Cambridge Structural Database[135] reveals nine unique $\{Mn_4\}$ species exhibiting this motif; seven with X=Cl, one with X=Br and one with X=F. They each feature three carboxylate ligands bridging from each of the Mn^{III} centres to the Mn^{IV}, and either one bidentate ligand (dibenzoylmethane) or two monodentate ligands (chloride or an *N*-heterocycle) coordinated to each Mn^{III} centre. Other cubanes exist with different species filling the X position, e.g. N_3^-, NCO^- and $MeCO_2^-$.[136]

Many of these cubane species exhibit a well-isolated S=9/2 ground state (due to ferromagnetic coupling between Mn^{III}-Mn^{III} pairs and antiferromagnetic coupling between Mn^{IV}-Mn^{III} pairs),[137] axial zero-field splitting[138] and slow relaxation of magnetisation.[136] One species $[Mn^{III}_3Mn^{IV}O_3Cl(O_2CEt)_3(py)_3]\cdot 4MeCN$ (**7**) crystallises in the trigonal space group *R*-3 with pairs of clusters facing each other in a dimer-like arrangement (figures 2-24, 2-25). There are hydrogen-bonding interactions between the clusters in each pair through six complementary C-H---Cl contacts and there is also a single Cl---Cl contact [distance 3.859(1) Å, sum of van der Waals' radii 3.50 Å]. These interactions favour a weak but noticeable antiferromagnetic coupling between two neighbouring clusters.[25] Thus, the ground state of the $\{Mn_4\}_2$ dimeric unit is S=0 yet quantum tunnelling (QTM)

steps are still observed in hysteresis loops of magnetisation *vs*. field. The key difference between the observed quantum tunnelling and that observed for similar non-exchange coupled $\{Mn_4\}$ species is the absence of a QTM step at zero field. Interestingly this is also observed for the $\{Mn_3\}$ species **5** discussed previously, but is not expected to be observed for isolated SMMs. The lack of a level crossing at zero field presents an interesting opportunity in the use of this species as a qubit for quantum computing.[139]

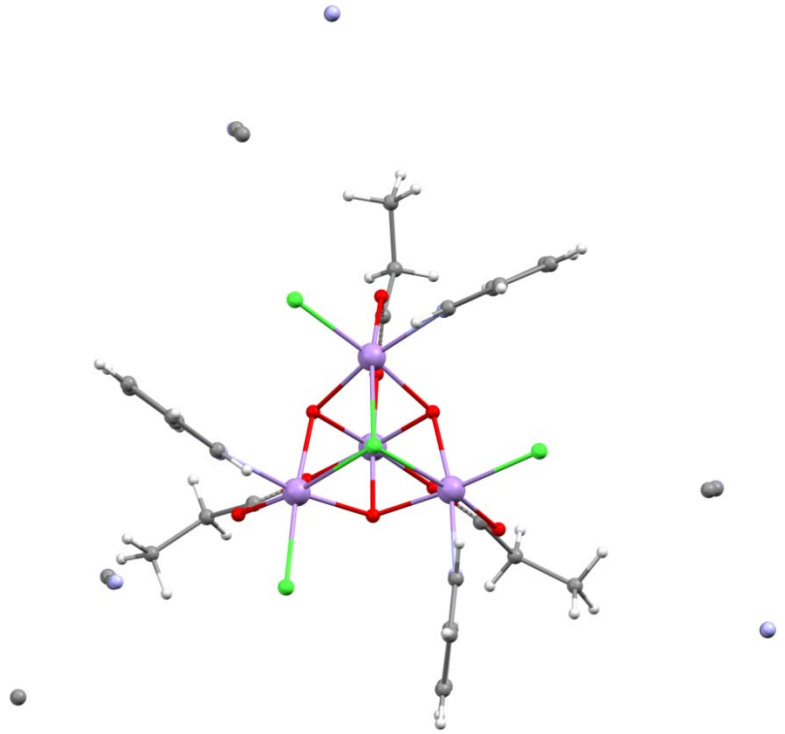

Figure 2-24: The crystal structure of **7** viewed down the three-fold axis. Acetonitriles of crystallisation are also shown (2 unique, one in a general position with a site multiplicity of 3 per cluster and one in a special position with only 1 per cluster for a total of 4 per cluster). Atom colours are as defined previously.

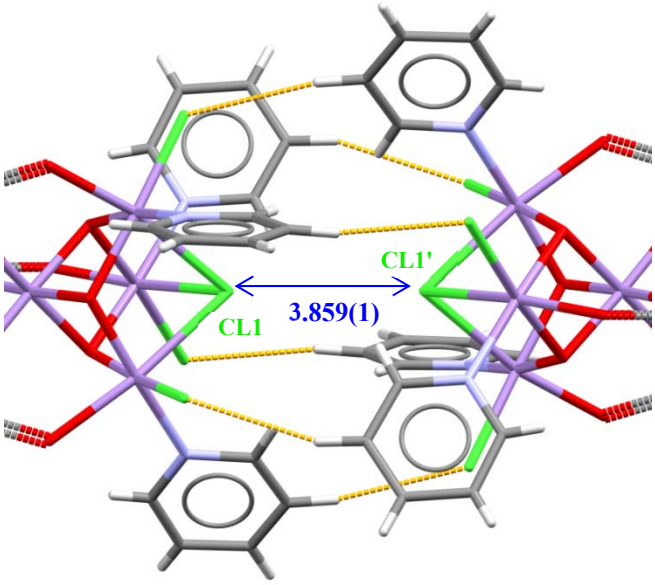

Figure 2-25: Intermolecular interactions between clusters in the dimeric structure of **7**. C-H---Cl contacts are shown in orange. The Cl-Cl' distance across the intermolecular bonding pathway is 3.859(1) Å. Atom colours are as previously defined.

2.4.1 Synthesis of {Mn_4} species and precursors

Some publications suggest using $Mn(O_2CMe)_2{\cdot}4H_2O$ as a starting material for synthesising the triangle precursor to the targeted {Mn_4} SMM;[138] we decided to attempt this method, as well as modification by using $Mn(O_2CEt)_2{\cdot}xH_2O$ and interestingly, Mn_{12}-acetate (**1**) instead. The results of these approaches are described here. The {Mn_3} triangle intermediates obtained from each of the different starting materials are denoted **6**, **6a** and **6b**.

2.4.1.1 Synthesis of tetrabutylammonium permanganate ($TBAMnO_4$)

This procedure is adapted from that described in the literature.[140, 141] Aqueous solutions of $KMnO_4$ (5.00 g, 31.6 mmol in 150 mL) and tetrabutylammonium bromide (9.12 g, 28.3 mmol in 50 mL) were mixed with stirring. The resulting precipitate was filtered on a sinter and washed with water (50 mL) and diethyl ether (300 mL) until dry. The compound was stored in the freezer under N_2 until required in order to slow its decay.

2.4.1.2 Synthesis of $Mn(O_2CEt)_2 \cdot xH_2O$

This procedure was adapted from that described in the literature.[142] To a stirred solution of $MnCl_2 \cdot 4H_2O$ (2.38 g, 12 mmol in 15 mL water) was added NaOH solution (0.96 g, 24 mmol in 5 mL water) forming a pale precipitate of $Mn(OH)_2$. To this reaction mixture was added excess propionic acid (2.00 g, 27 mmol in 10 mL water), quickly forming a clear colourless solution with a small amount of precipitate. After filtering to remove the precipitate, water was removed from the solution under vacuum to leave a pale pink viscous liquid. After several days a pale pink solid formed from this liquid, which was used without further analysis.

2.4.1.3 Synthesis of $[Mn_3O(O_2CEt)_6(py)_3](ClO_4)$ (6) from $Mn(O_2CEt)_2 \cdot xH_2O$

$Mn(O_2CEt)_2 \cdot xH_2O$ (2.00 g) formed from the previous procedure was dissolved in EtOH (20 mL) with stirring. To this solution were added propionic acid (12 mL) and pyridine (4 ml) followed by slow addition of tetrabutylammonium permanganate ($TBAMnO_4$, 1.14 g, 3.15 mmol) and then $NaClO_4$ (0.7 g, 5.6 mmol). The mixture was stored in the freezer overnight in order to produce a microcrystalline sample of **6**. Elemental analysis (%), calc (found) for $C_{33}H_{49}N_3ClMn_3O_{19}$ ($[Mn_3O(O_2CEt)_6(py)_3](ClO_4) \cdot 2H_2O$): C, 40.0 (39.6); H, 4.98 (4.72); N, 4.24 (4.31).

2.4.1.4 Synthesis of $[Mn_3O(O_2CEt)_6(py)_3](ClO_4)$ (6a) from $Mn(O_2CMe)_2 \cdot 4H_2O$

$Mn(O_2CMe)_2 \cdot 4H_2O$ (2.00 g, 8.2 mmol) was dissolved in EtOH (20 mL) with stirring. To this solution were added propionic acid (14 mL) and pyridine (4 mL) followed by slow addition of tetrabutylammonium permanganate ($TBAMnO_4$, 1.14 g, 3.15 mmol) and then $NaClO_4$ (0.7 g, 5.6 mmol). The mixture was stored at room temperature overnight in order to produce a microcrystalline sample of **6a**. A small portion was recrystallised in the minimum volume of acetone to produce small, needle-like crystals suitable for single-crystal X-ray structure determination. The structure of this crystal was found to be that of the expected $\{Mn_3\}$ triangle intermediate. Summary of crystallographic data for **6a**: monoclinic, *C*2/*c*, $C_{33}H_{45}ClMn_3N_3O_{17}$, a = 51.561(7) Å, b = 17.625(2) Å, c = 21.791(3) Å, β = 91.447(6) °, V = 19797(5) $Å^3$, Z = 20, T = 100(2) K, M_w = 955.57 g/mol, ρ = 1.528 g/cm^3, Mo K_α (λ=0.71073 Å), Refinement on F; R_1 = 0.0814 for 1308 parameters

and 14786 reflections with $I > 2\sigma$, and $wR_2 = 0.1449$ for all 20004 reflections. Elemental analysis (%), calc (found) for $C_{33}H_{48}N_3ClMn_3O_{18.5}$ ($[Mn_3O(O_2CEt)_6(py)_3](ClO_4)\cdot 1.5H_2O$): C, 40.3 (40.3); H, 4.92 (4.58); N, 4.27 (4.42).

2.4.1.5 Synthesis of $[Mn_3O(O_2CEt)_6(py)_3](ClO_4)$ (6b) from Mn_{12}-acetate (1)

$[Mn_{12}O_{12}(O_2CMe)_{16}(H_2O)_4]\cdot 2MeCO_2H\cdot 4H_2O$ (Mn_{12}-acetate, **1**) (2.00 g, 0.97 mmol) was synthesised as described previously in this chapter and dissolved in EtOH (20 mL) with stirring. To this solution were added propionic acid (14 mL) and pyridine (4 mL) followed by slow addition of tetrabutylammonium permanganate ($TBAMnO_4$, 1.14 g, 3.15 mmol) and then $NaClO_4$ (0.7 g, 5.6 mmol). The mixture was stored at room temperature overnight in order to produce large single crystals of **6b**; their identity was confirmed by single-crystal X-ray diffraction (full data given in table 2.5). Elemental analysis (%), calc (found) for $C_{33}H_{46}N_3ClMn_3O_{17.5}$ ($[Mn_3O(O_2CEt)_6(py)_3](ClO_4)\cdot 0.5H_2O$): C, 41.1 (41.0); H, 4.80 (4.69); N, 4.35 (4.41).

2.4.1.6 Synthesis of $[Mn_4O_3Cl_4(O_2CEt)_3(py)_3]\cdot 4MeCN$ (7)

The microcrystalline sample of **6a** produced from $Mn(O_2CMe)_2\cdot 4H_2O$ starting material was used in the synthesis of **7**. A stirred solution of **6a** (0.95 g, 1.00 mmol) in MeCN (50 mL) was treated with Me_3SiCl (0.70 mL, 5.5 mmol). The resulting solution was filtered on a sinter and the filtrate allowed to stand at 5 °C overnight in a sealed 100 mL conical flask. A few very small crystals of **7** were obtained and were washed with ethanol to remove any by-products. The identity of the crystals was confirmed by a basic X-ray structure determination (crystallographic data given in table 2.5). Insufficient sample was synthesised for elemental analysis.

2.4.1.7 Synthesis of $[Mn_4O_3Cl_7(O_2CEt)_3](C_5H_5NH)_3$ (8)

The microcrystalline sample of **6** produced from $Mn(O_2CEt)_2\cdot xH_2O$ starting material was used in the synthesis of **8**. A stirred solution of **6** (0.95 g, 1.00 mmol) in MeCN (50 mL) was treated with Me_3SiCl (0.70 mL, 5.5 mmol). Some small crystals of **8** were obtained directly from solution after several weeks and were washed with ethanol to remove any by-

products. The identity of the crystals was confirmed by an X-ray structure determination (full crystallographic data given in table 2.5). Insufficient sample was synthesised for elemental analysis.

2.4.2 Discussion of $\{Mn_3\}$ and $\{Mn_4\}$ species

2.4.2.1 The structure of {Mn3} triangle $[Mn_3O(O_2CEt)_6(py)_3](ClO_4)$ (6)

It proved possible to produce the $\{Mn_3\}$ triangle intermediate using either $Mn(O_2CEt)_2$, $Mn(O_2CMe)_2$ or Mn_{12}-acetate as the source of Mn in the reaction. For the latter two, where it was possible to crystallise the triangle and perform single-crystal X-ray analysis, we determined that both had the same unit cell and the same crystal packing despite the different starting material used. It was not possible to measure a crystal structure for the product obtained from $Mn(O_2CEt)_2$, however elemental analysis was consistent with it being the same $\{Mn_3\}$ species (a different number of adsorbed water molecules is estimated from elemental analysis for each of the preparations). The crystal structure presented here is that obtained from the Mn_{12}-acetate starting material, although both are identical. It should be noted that the quality of the data is distinctly average due to the large asymmetric unit and poor crystal quality. Its inclusion here is justified on the basis that there are no published data on this molecule in the Cambridge Structural Database.[135]

$[Mn_3O(O_2CEt)_6(py)_3](ClO_4)$ (**6b**) crystallises in the monoclinic space group *C*2/*c*. There are three crystallographically independent clusters, each with a single positive charge, and three perchlorate counter-ions, two of which are disordered on special positions (an inversion centre in one case; a two-fold rotation axis in the other). The unit cell is particularly large and contains twenty $\{Mn_3\}$ clusters and their counter-ions. There is some disorder in the positions of terminal carbon atoms in the propionate ligands. This has been dealt with by modelling each part-weight atom with isotropic displacement parameters and constraining the occupancies to sum to unity. The perchlorate anion located on the inversion centre was also modelled with isotropic displacement parameters. All other non-hydrogen atoms were modelled with ADPs. Thermal and similarity restraints were applied to 1,2 and 1,3 adjacent atoms in order to reduce the effects of libration. Bond distance and angle restraints were applied to some groups in order to restrain them to known geometries

(in particular one perchlorate group and some terminal C-C bond distances). Hydrogen atoms were placed in calculated positions and were not refined.

The cluster is similar to that of the related butyrate compound $[Mn_3O(O_2CCH_2Et)_6(py)_3](ClO_4)$ but with propionate ligands replacing the butyrate ligands (figure 2-26).[143] There is also a published structure of a similar propionate triangle with terminal 3-methylpyridine ligands instead of pyridine.[144] There are three Mn^{III} ions around a central oxide, with each Mn^{III} bridged to its neighbours by propionate ligands. The final position in the coordination sphere of each Mn^{III} is occupied by a terminal pyridine ligand. Each Mn^{III} experiences Jahn-Teller distortion but the three Jahn-Teller axes are not aligned. There are significant pi-pi stacking interactions (of both the face-to-face and offset face-to-face variety) due to stacked pyridine rings on neighbouring molecules (figure 2-27). Distances between rings are approximately 3.5 Å. Neither of the aforementioned analogous structures exhibits pi-pi stacking.

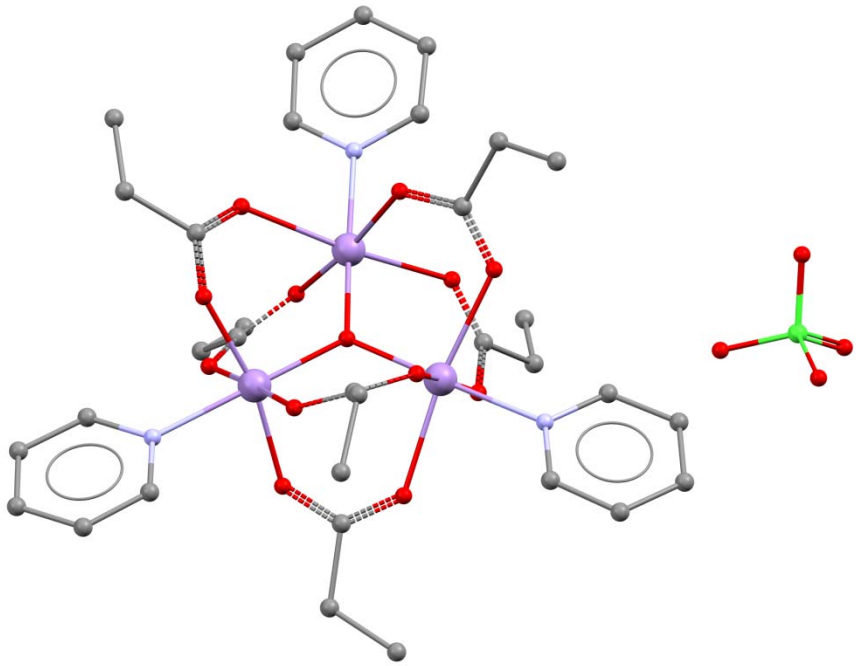

Figure 2-26: The structure of **6b** obtained from crystals synthesised using Mn_{12}-acetate (**1**) as a starting material. Atom colours are as previously defined; H atoms are omitted for clarity.

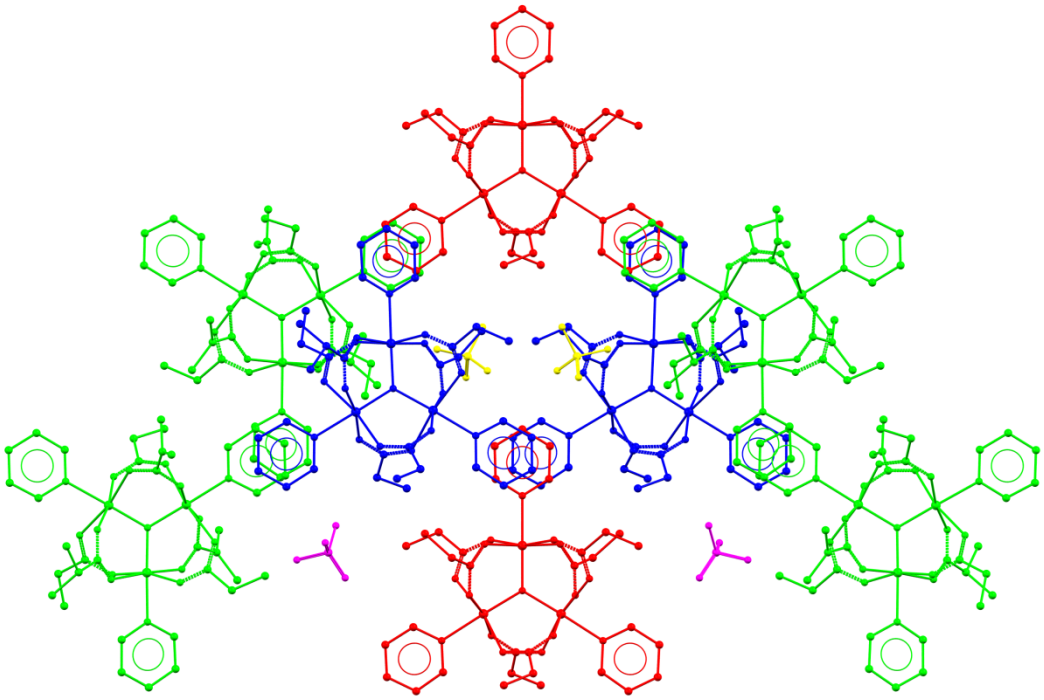

Figure 2-27: There are significant pi-pi stacking interactions in **6b** (face-to-face and offset face-to-face) through the pyridine rings coordinated to each cluster. This will aid crystallisation. Inter-ring distances are approximately 3.5 Å. The interstitial voids are occupied by perchlorate anions. Each colour represents symmetry-related molecules.

2.4.2.2 The structure of $[Mn_4O_3Cl_4(O_2CEt)_3(py)_3]\cdot 4MeCN$ (7)

The synthesis to produce species **7** yielded only sufficient product to carry out a basic structural determination by X-ray crystallography. We were able to confirm that the unit cell and the basic structure were the same as those published by Hendrickson *et al.*[138] However, due to the small crystal size and weak diffraction of the crystal, no data were observed beyond d = 1.09 Å; therefore this was a very basic structural determination with only isotropic displacement parameters refined and R_1 = 0.195. It was, however, sufficient to confirm that the structure is identical to that published. Unfortunately, despite strenuous efforts, the synthesis was only successful once and yielded only very small crystals. As such, it was not possible to carry out the planned ultra-low temperature neutron study on this compound. The published data on **7** are presented in the related reduced cell for consistency with an isostructural species; our data were solved and refined for the unit cell in a hexagonal setting.

7 is composed of a $[Mn^{III}_3Mn^{IV}O_3Cl]^{6+}$ cubane core with three bridging propionate ligands, three terminal pyridine ligands and three terminal chloride ligands (figures 2-24, 2-25). Acetonitrile of crystallisation fills the lattice voids. Each of the Mn^{III} ions possesses a Jahn-

Teller elongated axis (one unique). The previously published data indicate that this axis presents an angle of 41.84(6)° to the crystallographic three-fold axis. Our new data show good agreement with this.

2.4.2.3 The structure of $[Mn_4O_3Cl_7(O_2CEt)_3](C_5H_5NH)_3$ (8)

8 crystallises in the same trigonal/rhombohedral space group as **7** but structurally is quite different. The asymmetric unit of **8** contains two structurally analogous clusters (crystallographically unique). Refinement of both portions was performed in the same way. The crystal exhibited merohedral twinning with the twin law [0 1 0 1 0 0 0 0 -1]. All non-hydrogen atoms were refined anisotropically except for the second and third carbon atoms in each propionate ligand. Atoms in one of the pyridinium ions exhibited slightly elongated ADPs indicating that there might be some unresolved disorder in the orientation of the ring. The other pyridinium ion did not show this effect. All hydrogen atoms were placed in calculated positions and then allowed to ride on their parent atoms. The second and third carbon atoms in each propionate ligand were refined isotropically due to minor positional disorder. The terminal atoms were each split over two positions and the occupancies of each component restrained to sum to unity.

8 contains the same central $[Mn^{III}_3Mn^{IV}O_3Cl]^{6+}$ cubane core as **7**, and similarly each Mn^{III} is bridged to the Mn^{IV} via a propionate bridge (figure 2-28). However this is where the similarities end. Each Mn^{III} possesses a further two free positions in its coordination sphere. In **7** these are occupied by a chloride and a pyridine ligand on each Mn^{III}, making the complex neutral overall. In **8** both positions are occupied by chloride ligands, giving the complex a net -3 charge. This is balanced by three pyridinium cations (one unique) that surround each cluster according to the three-fold symmetry and each hydrogen-bond to two terminal chlorides and a μ_3-oxide in the cubane through the N-H donor. This subtle change dramatically alters the intermolecular contacts made by the cluster such that the dimer-like arrangement seen for **7** is not seen for **8**. The serendipitous nature of the synthesis of **8** is noted; this species was formed during attempts to synthesise crystals of **7** and is an unintended (yet nevertheless interesting) by-product.

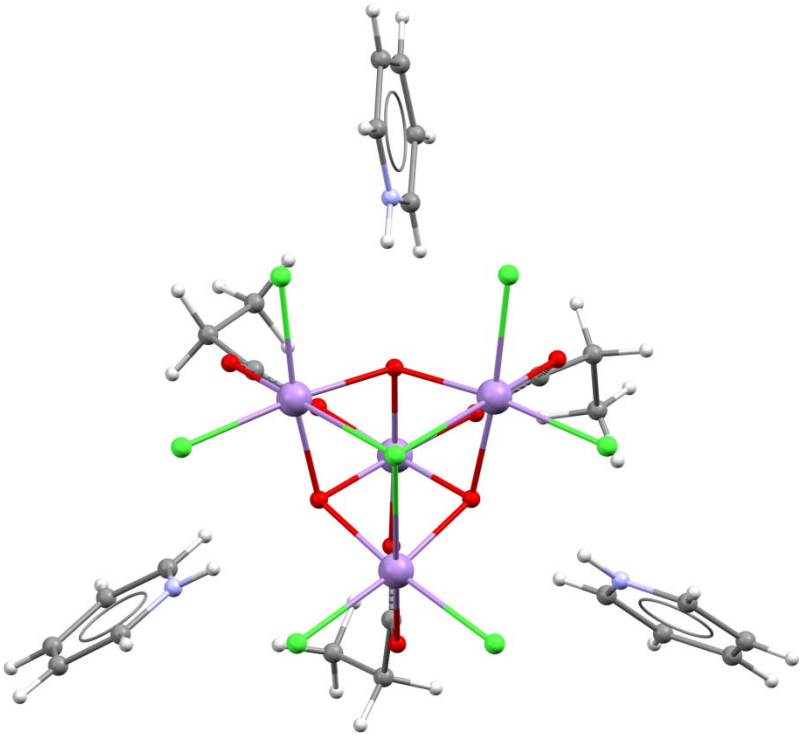

Figure 2-28 The crystal structure of **8** measured at 100 K as viewed down the three-fold axis. Each cluster is surrounded by three pyridinium cations. Atom colours are as previously defined.

There are still groups of two clusters facing each other along the -3 axis with the μ_3-chlorides facing each other as in **7**, however due to the altered structure the intermolecular distance between chlorides is increased from 3.859(1) Å (figure 2-21) to 6.001(3) Å (figure 2-29). In **7**, intermolecular interactions are thought to propagate *via* C-H---Cl contacts from the pyridine ligands on one cluster to the terminal chloride ligands on its neighbour. Because the pyridinium cations in **8** are not directly attached to the Mn^{III} centres and the intermolecular bonding pathway between Mn^{III} centres on adjacent clusters is therefore significantly longer, it is likely that the strength of any such intermolecular interactions will be greatly diminished when compared with the exchange bias observed in **7**.

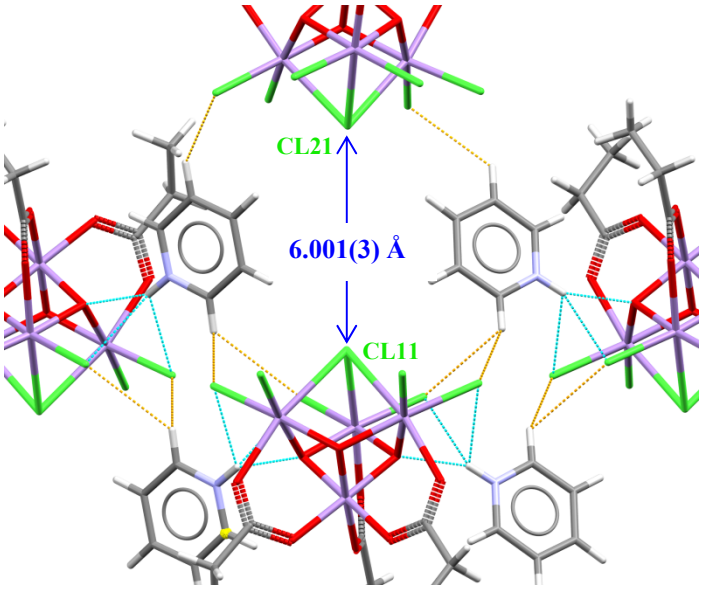

Figure 2-29: Possible intermolecular interactions in **8**, with C-H---Cl contacts shown in yellow and N-H---Cl/O contacts shown in blue. The analogous Cl-Cl' distance compared with **7** is shown [6.001(3) Å]. Atom colours are as previously defined.

Of course it is possible for interactions to take place through other pathways, such as the one shown in figure 2-30, that are not present in **7**. The Cl-Cl' distance in this case is 4.034(4) Å, however this is still not a direct pathway between neighbouring clusters and takes place *via* the lattice pyridinium ions.

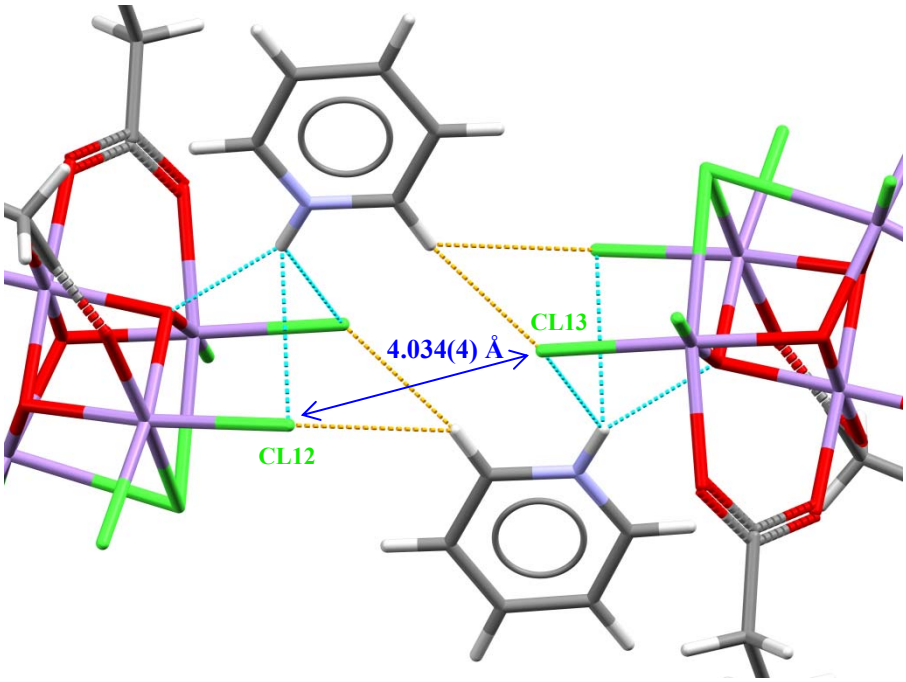

Figure 2-30: Alternative possible intermolecular bonding pathway in **8**. C-H---Cl contacts are again shown in yellow with N-H---Cl/O shown in blue. The closest Cl-Cl' distance is 4.034(4) Å.

Each of the three Mn^{III} ions possesses a Jahn-Teller elongated axis; by symmetry each makes an angle of approximately 41° with the crystallographic C_3 axis [40.72(8)°, 40.89(7)° for the two unique clusters]. This can be compared with 41.84(6)° for the similar compound **7**, indicating that the Jahn-Teller axes in **8** have marginally better alignment with the molecular easy axis than those in **7**. This is unlikely to make a significant difference to the magnetic properties of the cluster, assuming that the ground state of $S = 9/2$ is unchanged; rather it is the modification to the cluster's intermolecular interactions that will have a much greater impact on its properties.

Table 2.5 Crystallographic data for compounds **6b**, **7** and **8** measured at 100 K.

	6b	**7**	**8**
Formula	$C_{33}H_{45}ClMn_3N_3O_{17}$	$C_{32}H_{42}Cl_4Mn_4N_7O_9$	$C_{24}H_{33}Cl_7Mn_4N_3O_9$
M_w	955.97	1030.25	975.42
Crystal system	Monoclinic	Trigonal	Trigonal
Space group	*C*2/*c*	*R*-3	*R*-3
a [Å]	51.5199(16)	15.988(3)	17.2376(3)
b [Å]	17.6352(6)	15.988(3)	17.2376(3)
c [Å]	21.8119(7)	28.290(4)	44.4419(16)
α (°)	90	90	90
β (°)	91.372(2)	90	90
γ (°)	90	120	120
V [Å^3]	19811.8(11)	6262.5(17)	11436.1(5)
Z	20	6	12
T [K]	100(2)	100(2)	100(2)
Radiation	X-ray, Mo K_α	X-ray, Mo K_α	X-ray, Mo K_α
λ [Å]	0.71073	0.71073	0.71073
D_c [g cm^{-3}]	1.602	1.639	1.699
μ [mm^{-1}]	1.086	1.496	1.834
Meas./indep. refl.	68078/17448	15460/1108	134462/3879
R_{int}	0.065	0.074	0.124
Obs. refl. [$I > 2\sigma(I)$]	12469	809	3041
wR_2	0.0661	0.2262	0.0386
R_1	0.0596	0.1894	0.0347
Goodness of fit on F	1.0446	1.1150	1.1008
$\Delta\rho_{max,min}$ [e Å^{-3}]	2.87/-1.43	1.96/-4.08	0.34/-0.26

[a] $wR_2 = \{\sum[w(F_O - F_C)^2] / \sum[w(F_O)^2]\}^{1/2}$

[b] $R_1 = \sum||F_O| - |F_C|| / \sum|F_O|$

2.5 Conclusions

We have determined for the first time the ultra-low temperature crystal structure of the prototypical single-molecule magnet $[Mn_{12}O_{12}(O_2CMe)_{16}(H_2O)_4]\cdot 2MeCO_2H\cdot 4H_2O$ (Mn_{12}-acetate, **1**) by using single-crystal X-ray and neutron diffraction. We have contributed to a fuller understanding of the disorder and hydrogen bonding inherent to the structure. By carrying out single-crystal to single-crystal (SCSC) transformations to form two new desolvated $\{Mn_{12}\}$ species $[Mn_{12}O_{12}(O_2CMe)_{16}(H_2O)_4]\cdot 4H_2O$ (**2**) and $[Mn_{12}O_{12}(O_2CMe)_{16}(H_2O)_4]$ (**3**) we have determined that disorder in the acetic acid of crystallisation is responsible for positional disorder in an acetate ligand. These species differ in the number and identity of lattice solvent molecules present. We have also successfully inserted a different solvent into the new desolvated species, forming another new $\{Mn_{12}\}$ derivative $[Mn_{12}O_{12}(O_2CMe)_{16}(EtOH)_4]\cdot EtOH$ (**4**). Further work is required in order to reproduce this result and carry out magnetic measurements upon all three new species.

The ultra-low temperature crystal structure of another single-molecule magnet $[Mn_3O(Et\text{-}sao)_3(ClO_4)(MeOH)_x(H_2O)_{3-x}]$ (**5**) was also determined by using single-crystal X-ray and neutron diffraction. We found that there is disorder in the identity of the coordinated solvent (methanol or water) and in the position of the ethyl substituent of the Et-sao^{2-} ligand. The former impacts upon the latter due to steric constraints that result from the position of the carbon atom in the methanol group. The fractional distribution between the disordered parts varies between different crystals. Thus, we have developed a model encompassing a number of isomers that could be present in the crystal; some have C_3 axial symmetry but most do not. Our model is consistent with a previous HF-EPR study that indicates the presence of transverse anisotropy in this compound.

We report for the first time the crystal structure of the intermediate $[Mn_3O(O_2CEt)_6(py)_3](ClO_4)$ (**6**) formed during the synthesis of the interesting single-molecule magnet $[Mn_4O_3Cl_4(O_2CEt)_3(py)_3]\cdot 4MeCN$ (**7**). While it was not possible to produce good quality crystals of the latter sufficient for ultra-low temperature diffraction, we achieved for the first time the synthesis of a related compound $[Mn_4O_3Cl_7(O_2CEt)_3](C_5H_5NH)_3$ (**8**). **8** has a quite different packing arrangement to the previously known cubane **7** and does not form dimers. Further work will require magnetic measurements to be performed on **8** in order to compare its properties to those of **7**.

Chapter 3 Structures containing Ni^{II}

Synthetic and structural investigations of a $\{Ni_4\}$ SMM, its analogues and two $\{Ni_{10}\}$ clusters

3.1 Introduction to Ni^{II} SMMs

Ni^{II} has strong potential for use in SMMs due to its large Ising-type magnetic anisotropy. Indeed, there are several examples of SMMs based on Ni^{II} in the literature, including $\{Ni_4\}$,[145] $\{Ni_8\}$,[146] $\{Ni_{10}\}$,[84] $\{Ni_{12}\}$[147] and $\{Ni_{21}\}$[148] complexes, and even a heterometallic $\{Mn_2Ni_2\}$ complex.[149] The large anisotropy associated with Ni^{II} ions[150] should result in SMMs with high effective energy barriers to the reorientation of the magnetisation and hence, high blocking temperatures; however to date there are none that can compete with values recorded for many Mn^{III}-based SMMs (e.g. a $\{Mn_6\}$ cluster with a blocking temperature of ~4.5 K, effective barrier to reorientation of the magnetisation = 86.4 K.[91] For comparison, the effective barrier for the $\{Ni_4\}$ compound **9** described in this chapter is estimated to be only 12 K and so its blocking temperature will be much lower than that recorded for the $\{Mn_6\}$ cluster). Thus, much further research is required in order to understand the properties of Ni^{II}-based SMMs. We studied several polynuclear Ni^{II} complexes that exhibit slow magnetic relaxation.

3.2 $\{Ni_4\}$ cubanes

There are a number of $\{Ni_4O_4\}^{4+}$ cubanes, in which the four Ni^{II} ions are ferromagnetically coupled giving an S=4 ground state. If the molecular symmetry is high, e.g. S_4, then there are positive consequences for its quantum behaviour since certain quantum tunnelling resonances are forbidden.[133] $[Ni_4(thme)_4(MeCN)_4](NO_3)_4 \cdot 1.33NaNO_3$ [H_3thme = 1,1,1-tris(hydroxymethyl)ethane][151] and $[Ni_4(OMe)_4(sal)_4(MeOH)_4]$ (Hsal = salicylaldehyde)[152] exhibit an axial magnetic anisotropy and slow magnetic relaxation below 0.5 K and 0.3 K respectively. High-frequency and -field electron paramagnetic resonance (HF-EPR) measurements performed on several members of a family of cubanes $[Ni_4(hmp)_4(R\text{-}OH)_4Cl_4]$ (hmpH = 2-hydroxymethyl pyridine) show widely varying intermolecular exchange bias between the different compounds.[153-155] A recent study on $[Ni_4(hmp)_4(dmb)_4Cl_4]$ (dmb = 3,3'-dimethyl-1-butanol) indicated the presence of ferromagnetic ordering at approximately 300 mK.[156]

The magnetic properties of the SMM $[Ni_4(dea_4)Cl_4] \cdot 4MeCN \cdot 4.5H_2O$ (**9**) have also previously been investigated.[145] [deaH = diethanolamine, $HN(CH_2CH_2OH)_2$]. It has an S=4 ground state and a significant axial magnetoanisotropy, D = -0.75 cm^{-1}. Thus, the complex

should exhibit slow magnetic relaxation. Ac magnetic susceptibility measurements suggest that the complex does indeed exhibit slow relaxation of the magnetisation.[145]

9 displays hysteresis loops below 0.5 K that are small and round in shape, suggesting strong intermolecular interactions between neighbouring molecules and a fast relaxation rate. High Field Electron Paramagnetic Resonance (HF-EPR) measurements are consistent with an antiferromagnetic exchange bias of 0.63 T between adjacent molecules. Below 8 K, complex fine structure begins to develop in the spectra. Such features in similar systems have previously been shown to indicate entanglement, *i.e.* short-range antiferromagnetic correlations.[157, 158] These correlations only exist at low temperature and are destroyed by thermal fluctuations above 8 K.

Ni^{II} cubane SMMs consist of alternating Ni^{II} and O centres around a distorted cube with a chelating ligand capping each Ni^{II} vertex. It has long been known that nickel cubanes can exhibit ferromagnetic interactions through the bridging oxygen atoms.[151-155] This interaction is strongly dependent on the Ni-O-Ni bridging angle and Ni-Ni distances. A study by Halcrow *et al.* has shown experimentally that the crossover angle at which the superexchange interaction switches from ferromagnetic to antiferromagnetic is approximately 99°.[10] Below 99° the interaction is ferromagnetic, while above 99° it is antiferromagnetic. The same publication demonstrated that the Ni-(μ-O) bond distances have only a small effect on the observed *J* values compared with that caused by variation in Ni-O-Ni bridging angle.[10] This is in contrast to the findings published for a series of dinuclear Fe^{III} complexes, where it was indicated that the *J* value is dependent strongly on Fe-O distance.[159] All Ni^{II} ions in **9** are equivalent due to the molecular S_4 symmetry and each is coupled to the three others. Interactions across four of the six faces of the cubane are ferromagnetic with all Ni-O-Ni angles below 99° while the other two faces have angles above 99° and these interactions are antiferromagnetic. Thus, the system can be described with just two *J* values.

With these interesting properties in mind, it should be noted that the crystal structure of **9** has never been studied below 100 K. Molecular complexes in high symmetry space groups can undergo phase transitions at low temperature,[103, 160, 161] and so although the structure of **9** is known at 100 K, the structure below 8 K might be different. For example, if the crystallographic symmetry of **9** is lowered upon cooling, there could be more than one crystallographically unique $\{Ni_4\}$ cluster. In addition the dea^- ligand forms five-membered

rings with each Ni^{II} ion. Different conformations of these rings could freeze out at low temperatures. Since there are four dea^- ligands, there could be different $\{Ni_4\}$ environments depending on the arrangement of the conformations. Thus, it is not necessarily reasonable to interpret the low temperature magnetic properties of **9** based on the higher temperature structure. The structure of **9** at 1.7 K was studied using the single crystal neutron Laue diffractometer VIVALDI at ILL, in order to understand if there are any structural changes at this temperature that could be responsible for the observed HF-EPR spectra.

Additionally, analogues of **9** were investigated with two aims in mind: (a) increasing the average cluster separation distance should cause a reduction in the exchange bias field and serve to better isolate the individual clusters, and (b) increasing the axial anisotropy should enhance the energy barrier to relaxation of the magnetisation. Previously it has been established that use of heavy donor ligands in transition metal complexes can serve to increase the single-ion anisotropy.[162] Early magnetic susceptibility studies performed on hexahalorhenates and more recent HF-EPR studies performed on $[Mn^{II}(tpa)X_2]$ (tpa = tris-2-picolylamine; X = I, Br, Cl) and $[Tp^*Ni^{II}X]$ (Tp^{*-} = hydrotris(3,5-dimethylpyrazole)borate; X = I, Br, Cl) have shown that complexes with heavy halide ligands tend to exhibit larger axial zero-field splitting than the analogous complexes with smaller halides, often dramatically so.[163-165] A recent study performed on Cr^{II} and Cr^{III} complexes showed a similar effect.[162] Although these studies have been performed on mononuclear complexes, we are hopeful that polynuclear complexes will exhibit a similar trend even if the magnitude of the change is not as large. With this in mind we investigated analogues of **9** with the chloride ligand replaced by a bromide ligand. The bromide ligand has a larger size than chloride, but not as large as iodide, and so we were hopeful to achieve successful synthesis of the complex with a similar crystal packing arrangement and an increased anisotropy.

3.2.1 Synthesis of $\{Ni_4\}$ compounds

3.2.1.1 Ligands relevant to the synthesis of $\{Ni_4\}$ compounds

Several ligands were used during the synthesis and attempted synthesis of $\{Ni_4\}$ compounds. These are shown in figure 3-1.

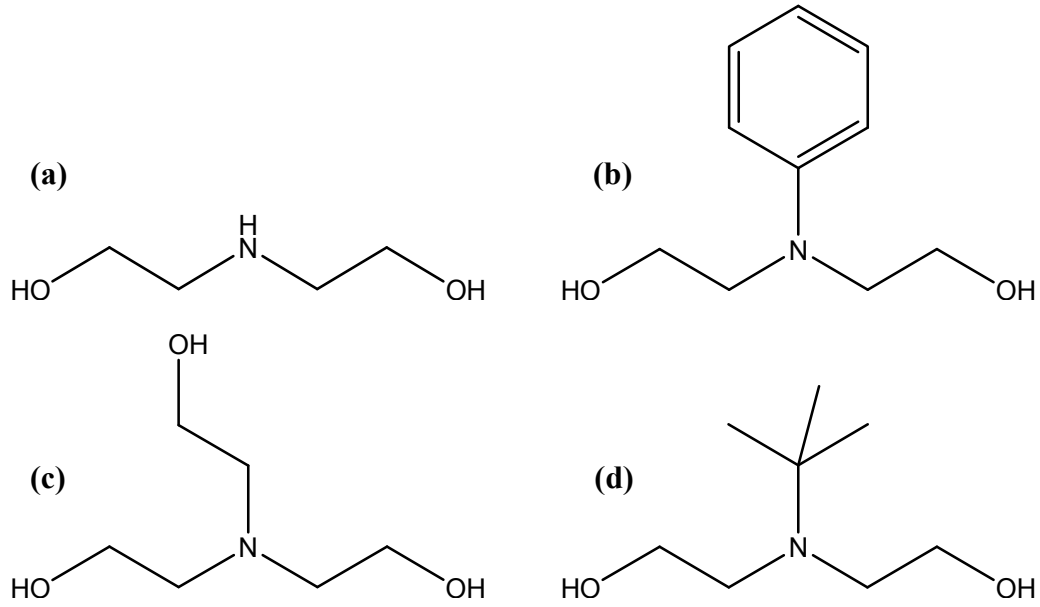

Figure 3-1: Ligands used in the synthesis of {Ni_4} compounds: (a) diethanolamine (deaH), (b) *N*-phenyl-diethanolamine (PhdeaH), (c) triethanolamine (teaH) and (d) *N*-tert-butyl-diethanolamine (tbdeaH).

3.2.1.2 Synthesis of $[Ni_4(dea)_4Cl_4]\cdot 4MeCN\cdot 0.6H_2O$ (9)

This procedure was carried out as per the published method,[145] which is detailed here so that a comparison can be made with the syntheses for related analogues of **9**. It is noted that the number of waters of crystallisation differs from the literature preparation; for our determination, we modelled all solvent explicitly whereas in the published structure the water of crystallisation was calculated using PLATON SQUEEZE.[166]

$NiCl_2\cdot 6H_2O$ (1.75 g, 8 mmol) was dissolved in MeOH (20 mL) and stirred for 5 minutes. To this solution was added tris (0.485 g, 4 mmol), diethanolamine (deaH, 0.421 g, 4 mmol) and NaOMe (0.432g, 8 mmol), ensuring that each reagent was fully dissolved before addition of the next. Stirring for 24 hours produced a green solution, which was filtered to remove a small amount of green precipitate. Portions of the filtrate were layered with MeCN in sealed tubes. After a week, large green single crystals of **9** formed. The crystals rapidly lose solvent when removed from the mother liquor. Analysis, calc. (found) for $C_{16}H_{46}Cl_4N_4Ni_4O_{11}$ ($Ni_4Cl_4(dea)_4\cdot 3H_2O$): C, 22.68 (22.88); H, 5.47 (5.13); N, 6.61 (6.52). The change in solvation from a single crystal to the powder sample used for microanalysis is attributed to loss of MeCN on drying and adsorption of moisture in the air to the surface of the sample.

The published synthesis contains an alternative method of producing the same compound, albeit in microcrystalline form. The method is similar to the first; tris is not used, and the quantity of diethanolamine is increased (0.842 g, 8 mmol). Upon repeating this method, large single crystals were obtained of the same species.

Infra-red spectra collected for **9** synthesised using both methods were identical. Selected data for an air-dried crystal: ν (cm^{-1}) = 3180, 2889, 1451, 1318, 1113, 1077, 1040, 990, 968, 907, 733.

3.2.1.3 Synthesis of $[Ni_4(dea)_4Cl_4]\cdot 0.8MeOH\cdot 0.2H_2O$ (10)

$NiCl_2\cdot 6H_2O$ (1.75 g, 8 mmol) was dissolved in MeOH (20 mL) and stirred for 5 minutes. To this solution was added deaH (0.842 g, 8 mmol) and NaOMe (0.432 g, 8 mmol), ensuring that each reagent was fully dissolved before addition of the next. Stirring for 24 hours produced a green solution, which was filtered to remove a small amount of green precipitate. Portions of the filtrate were layered with EtOH in sealed tubes. After a week small green single crystals of **10** formed. The crystals are relatively stable to solvent loss when removed from the mother liquor.

Selected infra-red data for an air-dried crystal of **10**: ν (cm^{-1}) = 3180, 2889, 1451, 1318, 1113, 1077, 1040, 990, 968, 907, 733. This is identical to the infra-red spectrum measured for the acetonitrile solvate, indicating that the major infra-red active modes are due to vibrations within the $\{Ni_4\}$ cluster rather than the solvent. Additionally, much of the solvent is lost upon drying in order to prepare the sample for measurement.

Analysis, calc (found) for $C_{16}H_{43.6}Cl_4N_4Ni_4O_{9.8}$ ($Ni_4Cl_4(dea)_4\cdot 1.8H_2O$): C, 23.28 (23.01); H, 5.32 (5.41); N, 6.79 (6.67).

3.2.1.4 Synthesis of $[Ni(tea)_2]Cl_2$ (11)

$NiCl_2\cdot 6H_2O$ (1.75 g, 8 mmol) was dissolved in MeOH (20 mL) and stirred for 5 minutes. To this solution was added triethanolamine (teaH, 1.192 g, 8 mmol) and NaOMe (0.432 g, 8 mmol), ensuring that each reagent was fully dissolved before addition of the next.

Stirring for 24 hours produced a blue solution, which was filtered to remove a small amount of green precipitate. Portions of the filtrate were layered with MeCN in sealed tubes. After a week small blue single crystals of **11** formed. The crystals are relatively stable to solvent loss when removed from the mother liquor. The structure of the crystals was determined by single-crystal X-ray diffraction at 100 K. No further analysis was carried out on **11** since its structure is already known[167] and not of particular interest to us.

3.2.1.5 Synthesis of $[Ni_4(dea)_4Br_4]\cdot 6MeCN$ (12)

$NiBr_2\cdot 2H_2O$ (2.04g, 8 mmol) was dissolved in MeOH (20 mL) and stirred for 5 minutes. To this solution was added deaH (0.842 g, 8 mmol) and NaOMe (0.432 g, 8 mmol), ensuring that each reagent was fully dissolved before addition of the next. Stirring for 24 hours produced a green solution, which was filtered to remove a small amount of green precipitate. Portions of the filtrate were layered with MeCN. After a week, a small number of large green single crystals of **12** formed in sealed tubes. There was not enough sample to perform elemental analysis; however it was possible to measure the crystal structure using single-crystal XRD at 30 K and 100 K. It was not possible to reproduce crystals of **12** in subsequent reactions. This is discussed later.

3.2.1.6 Synthesis of $[Ni_4(dea)_4Br_4]\cdot 0.7MeOH\cdot 0.6H_2O$ (13)

$NiBr_2\cdot 2H_2O$ (2.04g, 8 mmol) was dissolved in MeOH (20 mL) and stirred for 5 minutes. To this solution was added deaH (0.842 g, 8 mmol) and NaOMe (0.432 g, 8 mmol), ensuring that each reagent was fully dissolved before addition of the next. Stirring for 24 hours produced a green solution, which was filtered to remove a small amount of green precipitate. Portions of the filtrate were layered with either ethanol (EtOH), isopropyl-alcohol (IPA) or methyl *tert*-butyl ether (MTBE). After a week, small green single crystals of **13** formed in sealed tubes from all solvents. Selected infra-red data for an air-dried crystal of $[Ni_4(dea_4)Br_4]\cdot 0.7MeOH\cdot 0.6H_2O$ grown from MTBE (methyl *tert*-butyl ether): ν (cm^{-1}) = 3215, 2884 1450, 1314, 1112, 1074, 1037, 986, 907, 777, 685. Air dried crystals analyse as $[Ni_4Br_4(dea)_4]\cdot 0.7MeOH\cdot 1.8H_2O$, analysis (%) calc. (found): C, 19.55 (19.49); H, 4.56 (4.07); N, 5.46 (5.11). The difference in solvation between a single crystal and the powder used for elemental analysis is likely to be caused by adsorption of water onto the surface of the powdered sample.

A portion of the sample used for magnetic measurement was taken for elemental analysis and was also found to be $Ni_4Br_4(dea)_4 \cdot 0.7MeOH \cdot 1.6H_2O$, analysis (%) calc. (found): C, 19.62 (19.53); H, 4.53 (4.26); N, 5.48 (5.48).

3.2.1.7 Synthesis of $[Ni_4(dea)_4Br_2(H_2O)_2]Br_2$ (14)

$NiBr_2 \cdot 2H_2O$ (0.918 g, 3.6 mmol), diethanolamine (0.378 g, 3.60 mmol), NaOMe (0.240 g, 4.44 mmol) and MeCN (5 mL) were sealed in a 23 mL Teflon liner inside an autoclave. The contents were heated quickly to 150 °C for 12 hours and allowed to cool at 3 °C / hour. A mixture of small green crystals of **14**, small purple crystals of $[Ni(NH_3)_6]Br_2$ and green and white powders were formed directly from the solvothermal reaction. We are unsure of the mechanism of formation of ammonia from the reactants. Unfortunately the crystals cannot be separated from the by-products in order to perform elemental analysis.

3.2.1.8 Attempted synthesis of cubanes containing other N-substituted diethanolamine ligands

The standard reactions described in Section 3.2.1.2, both with tris and without tris, were carried out for $NiCl_2 \cdot 6H_2O$ and $NiBr_2 \cdot 2H_2O$ starting materials with *N*-phenyl-diethanolamine (hereafter PhdeaH) and *N*-tert-butyl-diethanolamine (hereafter tbdeaH). No crystals were obtained from these experiments; however other characterisation studies were performed on the solutions that were produced (see sections 3.2.3 and 3.2.6).

3.2.2 Structures containing the $[Ni_4(dea)_4Cl_4]$ cubane

3.2.2.1 $[Ni_4(dea)_4Cl_4] \cdot 4MeCN \cdot 0.6H_2O$ (9)

The crystal structure of **9** grown from the method where tris was not used was measured using X-ray and neutron radiation at low temperature, since this method gave larger and higher quality crystals than that where tris is used. The X-ray structure was determined at 30 K using a Bruker APEX II diffractometer equipped with an Oxford Cryosystems HELIX low temperature device. A crystal was carefully mounted on a glass fibre and

quickly placed under the cryo-stream to prevent solvent loss. The neutron structure was determined at 1.7 K using the Laue method on VIVALDI at ILL, Grenoble. This technique does not allow for absolute evaluation of cell dimensions, and so these were taken from the 30 K X-ray structure determination. A crystal was nudged from the mouth of the crystallisation vessel onto a bed of glass wool soaked with mother liquor. This was quickly sealed and cooled to 1.7 K for data collection. The structure of a crystal grown using tris was subsequently determined by XRD at 100 K to confirm that there were no differences in the $\{Ni_4\}$ clusters in the crystals grown from the two methods.

The X-ray- and neutron-derived structures are broadly similar in most respects. The neutron determination allows for accurate H atom location and refinement. Slightly different levels of acetonitrile solvation are found for the 30 K X-ray (4.44 acetonitriles per cluster) and 1.7 K neutron (4 acetonitriles per cluster) structures; as the crystal structure has channels between $\{Ni_4\}$ clusters, it is not unexpected that marginally different amounts of disordered solvent are found in these voids. It is possible that this is related to the method used to synthesize the crystals (*i.e.* tris or no tris used); it would be necessary to measure more crystals in order to prove such a link. The structural description, including distances and angles, in this section is taken from the 1.7 K neutron structure. This is in the same temperature regime as interesting magnetic properties occur and, as such, is the most relevant. It should be noted that the unusually large R_1 and wR_2 values obtained are characteristic of structures derived from neutron Laue diffraction. The structure was solved using 30 K X-ray data and then subsequently refined against the 1.7 K neutron data using the SHELXL package.[115] Full crystallographic data for the 1.7 K neutron structure are given in table 3.1.

The structure consists of a distorted cubane of Ni^{II} and O centres (figure 3-2). The four μ_3-O donors are derived from the alkoxide group of each dea^- ligand. The central amine group and the alcohol arm bind to just one metal ion and both remain protonated. A terminal chloride ligand fills the final site at each Ni^{II} centre. Table 3.2 lists bond distances made by Ni1 to the six atoms in its coordination sphere; table 3.3 lists the three unique bridging angles for superexchange within the $\{Ni_4\}$ cluster. The non-bridging alcohol arm of the dea^- ligand acts as an intramolecular hydrogen bond donor to a chloride ligand within the cluster [O71–H71 · · · $Cl1_{ii}$ = 3.044(4) Å; 166.6(8)° at 1.7 K] (symmetry operations relating equivalent atoms are indicated in the caption below figure 3-2).

Table 3.1: Crystallographic data for **9** collected at 1.7 K using the VIVALDI single-crystal neutron diffractometer.

Formula	$C_{24}H_{53.2}Cl_4N_8Ni_4O_{8.6}$
Moiety Formula	$[Ni_4(dea)_4Cl_4]\cdot 4MeCN\cdot 0.6H_2O$
FW (g mol^{-1})	968.11
Crystal system	Tetragonal
Space group	$I4_1/a$
a / Å	12.3203(6)
c / Å	28.8658(15)
V / Å^3	4381.5(4)
Z	4
T / K	1.7(1)
Radiation	Neutron Laue technique
D_c / Mg m^{-3}	1.468
Meas./indep. refl.	19709 / 2244
R_{int}	0.2875
Obs. refl. [$I > 2\sigma(I)$]	1876
wR_2 [a]	0.256
R_1 [b]	0.111
Goodness of fit on F^2	1.14
$\Delta\rho_{max,min}$ [fm Å^{-3}]	1.47/-1.25

[a] $wR_2 = \{\sum[w(F_O^2 - F_C^2)^2]/\sum[w(F_O^2)^2]\}^{1/2}$

[b] $R_1 = \sum||F_O| - |F_C||/\sum|F_O|$

9 crystallises in the tetragonal space group $I4_1/a$ with a total of four solvent acetonitrile molecules and one partially occupied water of crystallisation per cubane. The coordination geometry at each Ni^{II} centre is distorted octahedral. The cubane has crystallographic S_4 symmetry with the S_4 axis coincident with the crystallographic c axis. Each cluster also exhibits intermolecular hydrogen bonding to four neighbouring clusters through two complementary N–H · · · Cl contacts [N41–H41 · · · $Cl1_{ii}$' = 3.341(3) Å; 155.6(6)° at 1.7 K] (figure 3-3). Thus, each cluster is neighboured by four others in a distorted tetrahedral-like arrangement (figure 3-4), with the angles between the centroids of the clusters being 81° and 125°. This intermolecular hydrogen bonding bridges the two closest Ni^{II} centres on adjacent clusters. The Ni-Ni' intermolecular separation distance is 6.191(3) Å at 1.7 K. A comparison of distances and angles for hydrogen bonding at several temperatures is given in table 3.4.

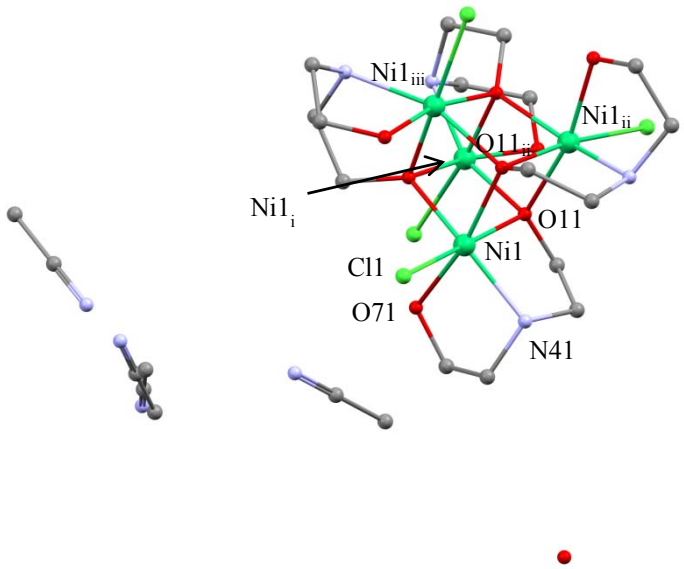

Figure 3-2: The neutron-derived molecular structure of **9** at 1.7 K including all solvent of crystallisation (Ni, mint green; N, blue; O, red; C, grey; Cl, bright green). H atoms are omitted for clarity. $Ni1_i$ = Ni1{¾+*y*,¼-*x*,¼-*z*}, $Ni1_{ii}$ = Ni1{-*x*, ½-*y*, *z*}, $Ni1_{iii}$ = Ni1{¼-*y*,¼+*x*,¼-*z*}.

The disordered solvent region contains three independent, part-occupied molecules of acetonitrile (figure 3-5). A further electron density peak in the region of one of the molecules was modelled as part-occupancy (0.15) water. One MeCN is in a general position (2); the other two (3, 4) are located near two-fold axes. All MeCN molecules were treated as freely-rotating rigid bodies and were given fixed occupancies of 0.5, 0.25 and 0.25 respectively.

Table 3.2: Bond distances made by Ni1 in **9**.

Distance*	1.7 K	30 K	100 K
Ni1—O11	2.046(4)	2.044(2)	2.035(2)
Ni1—$O11_i$	2.062(4)	2.061(2)	2.049(2)
Ni1—$O11_{ii}$	2.110(4)	2.105(2)	2.097(2)
Ni1—N41	2.110(3)	2.110(2)	2.099(2)
Ni1—O71	2.130(4)	2.129(2)	2.123(2)
Ni1—Cl1	2.407(3)	2.4052(8)	2.3955(7)

*$O11_i$ = O11{¾+y,¼-x,¼-z}, $O11_{ii}$ = O11{-x, ½-y, z}.

Table 3.3: Unique bridging angles (°) for superexchange in the cubane core of **9** at 1.7 K, 30 K and 100 K (original published data).[145]

Angle	1.7 K	30 K	100 K
Ni1 – O11 – $Ni1_{i}$	98.36(16)	98.21(9)	98.26(8)
Ni1 – O11 – $Ni1_{ii}$	100.19(17)	100.35(9)	100.39(8)
Ni1 – $O11_{ii}$ – $Ni1_{iii}$	96.37(16)	96.30(8)	96.28(7)

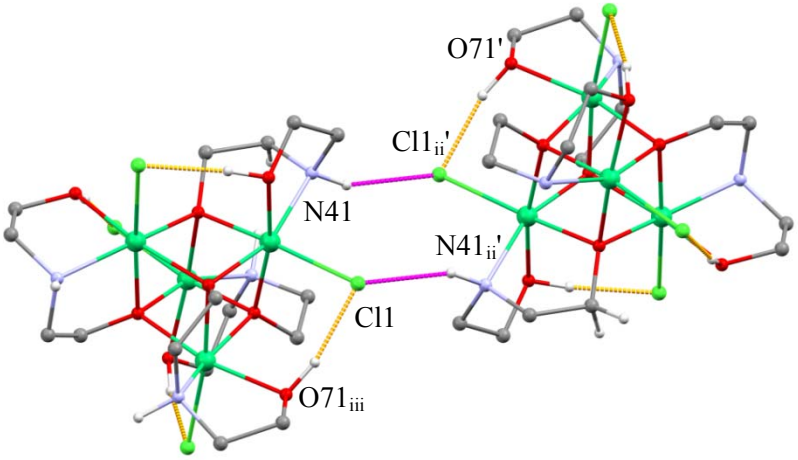

Figure 3-3: Intramolecular hydrogen bonding (yellow) through the O-H---Cl pathways within each cluster and intermolecular hydrogen bonding (purple) between two adjacent clusters through complementary N-H---Cl pathways. Solvent of crystallisation and H atoms (except those involved in H bonds as shown) are omitted for clarity. Atom colours are as previously defined, H atoms shown in white.

In the $\{Ni_4\}$ complex, all atoms (including H) were modelled with anisotropic displacement parameters (ADPs). C and N atoms in MeCN molecules 2 and 3 were also refined anisotropically, with molecule 4 being refined isotropically. The part-occupied water O atom was refined anisotropically. H atoms in the solvent region were modelled with common isotropic displacement parameters. Similarity and rigid bond restraints were applied to the ADPs in MeCN molecules 2 and 3. All C-H bond distances in the solvent region were restrained to be equal. No restraints were applied to the $\{Ni_4\}$ complex. Additionally a parameter was included for merohedral twinning with a scale factor of 0.0168.

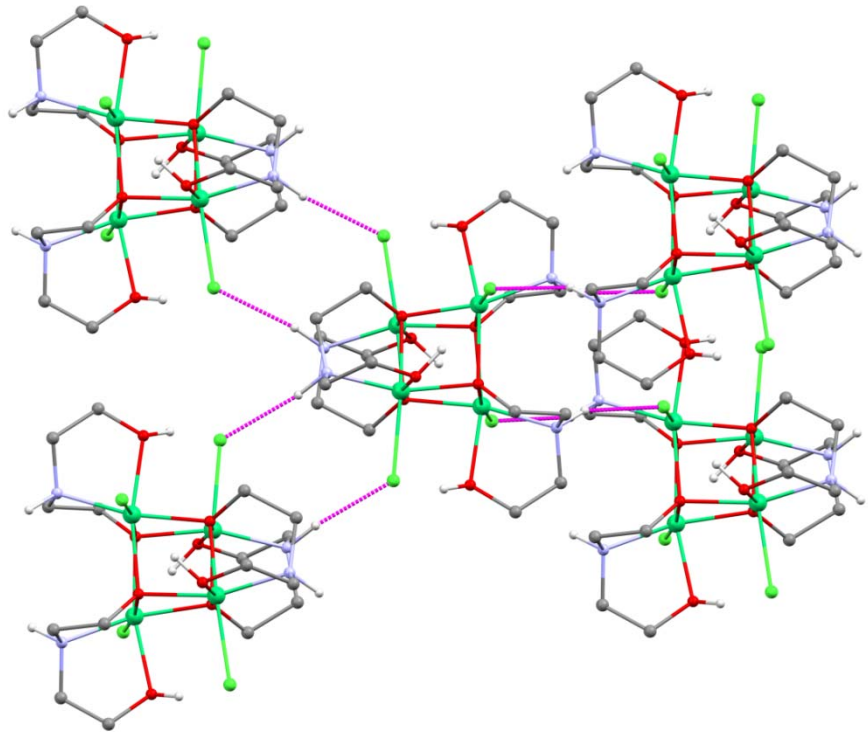

Figure 3-4: Intermolecular hydrogen bonding (purple) between one cluster and its four neighbours through N-H---Cl pathways. Solvent of crystallisation and H atoms in CH_2 groups are omitted for clarity. Atom colours are as previously defined.

Table 3.4: Intermolecular/intramolecular hydrogen bond distances and angles for **9** at 1.7 K, 30 K and 100 K (original published data).[145] Symmetry operations for atoms related by symmetry are as previously defined.

	Distance (Å)			Angle (°)		
Temperature (K)	1.7	30	100	1.7	30	100
O71—H711 · · · Cl_i	3.044(4)	3.046(2)	3.032(2)	166.8(8)	168(3)	170.4(1)
N41—H411 · · · $Cl1_{ii}$'	3.341(3)	3.341(2)	3.331(2)	155.6(6)	148.4(1)	155.3(1)
Ni1—$Ni1_{ii}$'	6.191(3)	6.1951(6)	6.1702(4)	-	-	-

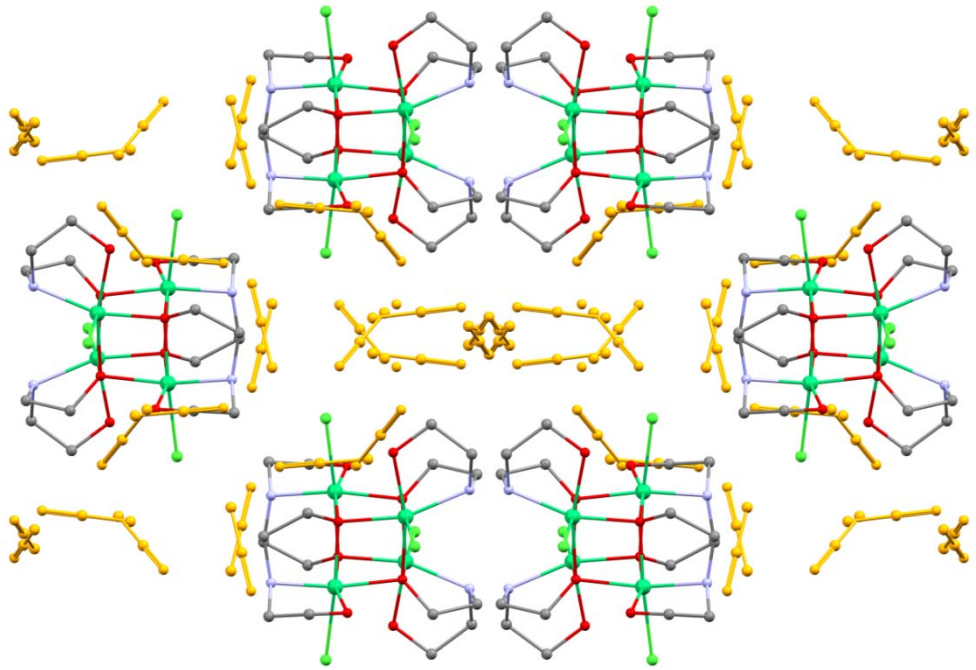

Figure 3-5: Crystal packing of **9** viewed along the crystallographic b axis. Solvent of crystallisation is highlighted in yellow to indicate the large interstitial voids present in the structure. Atom colours are as previously defined.

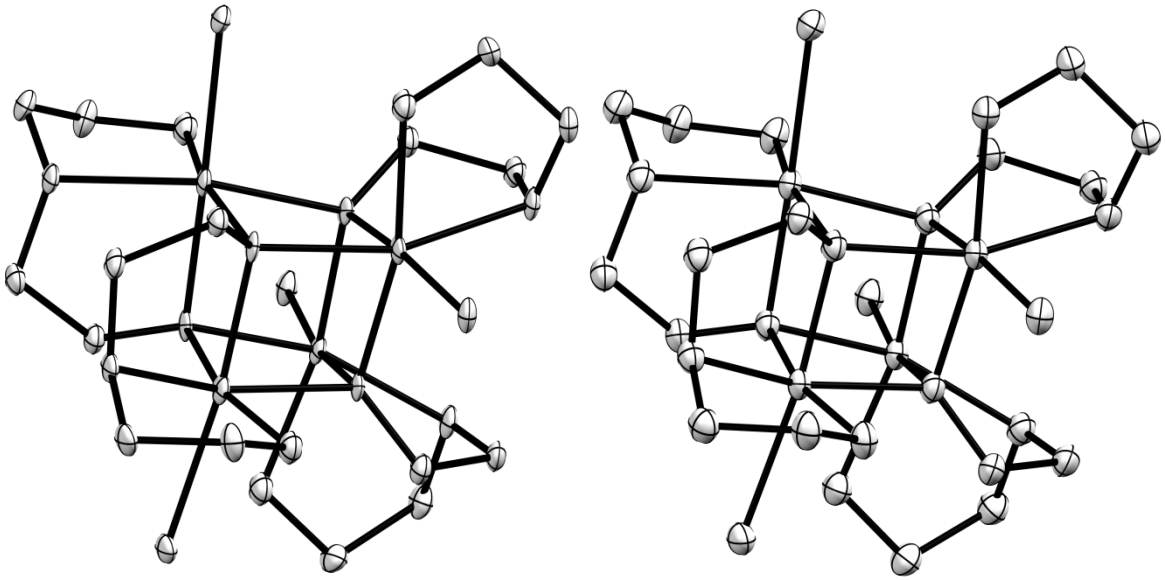

Figure 3-6: ORTEP-style plots for the structure of **9** at 1.7 K (left, neutron Laue diffraction) and 30 K (right, XRD). Ellipsoids are drawn at the 50% probability level. H atoms are omitted.

Figure 3-6 gives a comparison of the thermal ellipsoids for **9** at 1.7 K and 30 K measured by neutron and X-ray diffraction respectively. These plots are created using Mercury[129] and rendered using POV-Ray,[130] and are shown at approximately the same scale. The average equivalent isotropic displacement parameter for atoms in the 30 K structure is slightly larger than that for atoms in the 1.7 K structure; this is expected due to slightly increased thermal motion at 30 K. The ellipsoids in the 30 K X-ray structure have a regular

shape. Those in the 1.7 K neutron structure are unusually flat, particularly for the Ni and O atoms that make up the central cubane core. Due to the rigidity of the cubane enforced by the encapsulating ligands, the central atoms are not expected to exhibit this type of vibrational motion. This slight flattening could be attributed to incomplete data along the direction of the flattening; the data are only 80% complete for this experiment due to constraints on the experimental setup.

In summary, we have presented the first ultra-low temperature structural data for the $\{Ni_4\}$-based SMM **9** by using single-crystal neutron diffraction, as part of a wider study encompassing ultra-low temperature measurement of several SMMs. We note slightly increased D---A distances for both inter- and intra-molecular hydrogen bonds upon cooling from 100 K to 30 K (table 3.4); however, further cooling to 1.7 K has little effect. The D-H---A angle for these pathways at 100 K and 30 K is not especially reliable since hydrogen atom positions are not well-measured from X-ray diffraction experiments; the angle of 166.8(8)° measured by using neutron diffraction at 1.7 K is the most reliable measurement. Additionally the Ni1-Ni1$_{ii}$' distance (separation of two closest Ni^{II} ions through the direct hydrogen bonding pathway described above) also shows a small increase upon cooling from 100 K to 30 K, but no further change is noted upon cooling to 1.7 K. The small lengthening noted is unlikely to favour increased exchange bias between coupled clusters. Therefore, there is nothing particular to account for the entanglement observed in the HF-EPR spectra; the observed features are likely to be due to the intermolecular N–H---Cl interactions.

3.2.2.2 $[Ni_4(dea)_4Cl_4]\cdot 0.8MeOH\cdot 0.2H_2O$ (10)

After these crystals had been synthesised, a crystallographic communication was published by Yu *et al.*[168] containing the same methanol solvate synthesised by a different procedure. The data contained therein were collected at room temperature, and the communication presents only a brief structural description with no comparison to the acetonitrile solvate **9**. We measured the crystal structure of **10** at 100 K using a Bruker APEX II X-ray diffractometer equipped with an Oxford Cryosystems HELIX low temperature device. The crystals were not sufficiently large to use for a neutron diffraction study. Full crystallographic data are given in table 3.5.

The crystal of **10** chosen for this study was twinned and was integrated using two domains related by a 2-fold rotation about the *a** axis; however only reflections with a contribution from the major domain are included in the final refinement. The final twin scale factor was 0.40937(83). In the $\{Ni_4\}$ molecule all non-hydrogen atoms were refined with ADPs. The methanol of crystallisation was also refined anisotropically; however, the water of crystallisation was refined with an isotropic displacement parameter. H atoms attached to C and N were placed in calculated positions. H atoms were placed on the carbon atom of the methanol using the Sheldrick circular Fourier method. H atoms on other oxygen atoms were placed in such a way as to optimise hydrogen bonding. The partially occupied methanol and water of crystallisation occupy the same site in the ratio 0.8:0.2. This ratio was refined and then fixed towards the end of the refinement.

The cluster has a similar cubane structure to that of the acetonitrile solvate. The dea^- ligands are mono-deprotonated and bind to a Ni^{II} ion through the alcohol arm, the alkoxide arm and the amine (figure 3-7). This methanol solvate crystallises in the triclinic space group *P*-1. This means that each $\{Ni_4\}$ cluster contains four independent Ni^{II} centres, rather than just one as seen for the acetonitrile solvate, **9**. We have not been able to measure the low temperature magnetic properties of **10** so cannot report *S* or *D*. However, the cluster does not have the same S_4 symmetry and consequently will have a non-zero transverse anisotropy (*E* term in the spin Hamiltonian).[169] This is likely to reduce the effective energy barrier to relaxation, U_{eff}.

Considering all the Ni-O-Ni bridging angles in **10** (table 3.6), there are eight below the critical angle of approximately 99° and four above. This is consistent with the angles measured for **9** and thus, we expect that the superexchange interactions within **10** will be similar to those in **9**. Magnetisation studies were not performed on **10** because at the time it was synthesised, the SQUID magnetometer was not operational. Efforts are underway by another member of the research group to synthesise a fresh sample of **10** in order that such measurements can be performed. Magnetisation studies were performed on the analogous bromide species, **13**. These will be described in detail later in this chapter.

Table 3.5: Crystallographic data for **10** measured at 100 K.

Formula	$C_{16.8}H_{43.6}Cl_4N_4Ni_4O_9$
Moiety formula	$[Ni_4Cl_4(dea)_4].0.8MeOH.0.2H_2O$
FW / g mol^{-1}	822.40
Crystal system	Triclinic
Space group	*P*-1
α / °	91.708(1)
β / °	91.725(1)
γ / °	111.422(1)
a / Å	10.7404(4)
b / Å	11.4646(4)
c / Å	13.1649(4)
V / Å^3	1506.93(9)
Z	2
T / K	100
λ / Å	0.71073
D_c / Mg m^{-3}	1.812
μ / mm^{-1}	2.87
Meas./indep. refl.	29279 / 8552
R_{int}	0.0366
Obs. refl. [$I > 2\sigma(I)$]	7730
wR_2 [a]	0.100
R_1 [b]	0.035
Goodness of fit on F^2	1.02
$\Delta\rho_{max,min}$ [e Å^{-3}]	1.01/-0.72

[a] $wR_2 = \{\sum[w(F_O^2 - F_C^2)^2]/\sum[w(F_O^2)^2]\}^{1/2}$

[b] $R_1 = \sum||F_O| - |F_C||/\sum|F_O|$

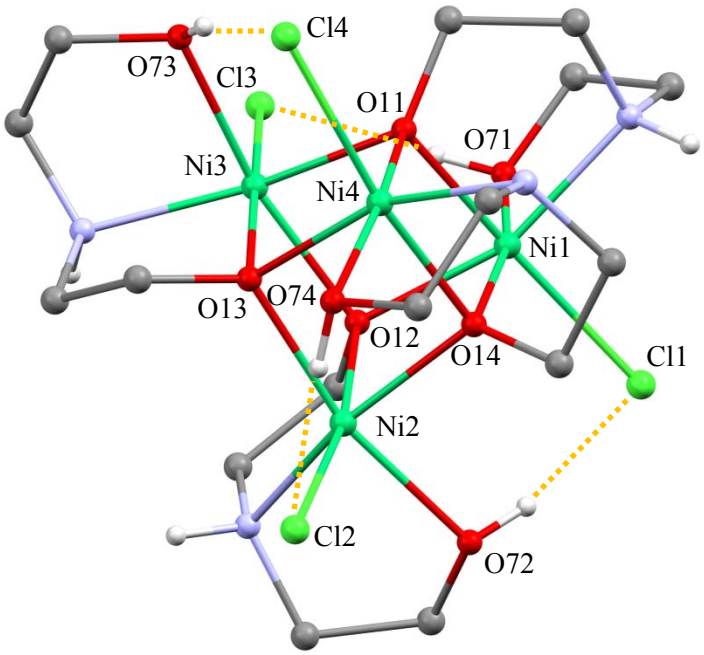

Figure 3-7: Molecular structure of **10** showing a single $\{Ni_4\}$ cluster. H atoms in CH_2 groups are omitted for clarity. Intramolecular hydrogen bonding O-H---Cl is shown in yellow. Atom colours are as previously defined. Ni, O and Cl atoms are labelled.

The $\{Ni_4\}$ cluster exhibits intramolecular hydrogen bonding from each alcohol arm of the dea^- ligand to a chloride ligand on the same cluster (figure 3-7). The extended hydrogen-bonded network structure of this low symmetry form is somewhat different to the tetragonal solvate, **9**. Each cluster is hydrogen bonded to only two others through two N-H · · · Cl contacts (through Ni2 and Ni4) (shown in figure 3-8). This leads to the formation of one-dimensional hydrogen-bonded chains of $\{Ni_4\}$ clusters. The other two N-H sites on each cluster (belonging to Ni1 and Ni3) do not hydrogen bond directly to adjacent clusters. The interstitial voids between 1D chains are filled with solvent of crystallisation, which hydrogen-bonds to the chains on either side *via* the two free N-H and Cl sites (belonging to Ni1 and Ni3) (see figures 3-9, 3-10). Details of inter- and intra-molecular hydrogen bonding are given in table 3.7.

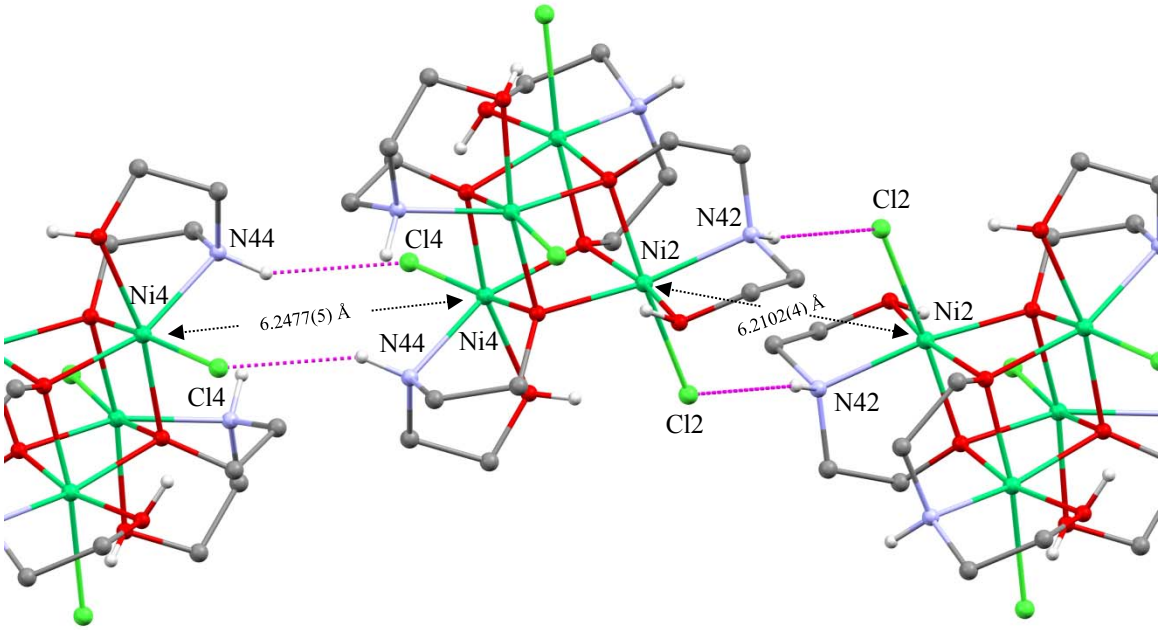

Figure 3-8: Direct intermolecular interactions (shown in pink) between $\{Ni_4\}$ clusters in **10**. Atom colours are as previously defined. H atoms in CH_2 groups are omitted for clarity. Direct interactions only take place through Ni2 and Ni4 (not Ni1 and Ni3); 1D hydrogen-bonded chains form as a result.

Table 3.6: Ni-O-Ni bridging angles for **10**.

Atoms	Angle (°)
Ni1 – O12 – Ni2	98.56(8)
Ni1 – O14 – Ni2	96.30(8)
Ni1 – O11 – Ni3	97.41(8)
Ni1 – O12 – Ni3	95.98(8)
Ni1 – O11 – Ni4	101.26(8)
Ni1 – O14 – Ni4	100.38(8)
Ni2 – O12 – Ni3	101.66(8)
Ni2 – O13 – Ni3	100.21(8)
Ni2 – O13 – Ni4	95.45(8)
Ni2 – O14 – Ni4	97.87(8)
Ni3 – O11 – Ni4	96.23(8)
Ni3 – O13 – Ni4	98.32(8)

The cluster separation along the chain is similar for both Ni2-Ni2' and Ni4-Ni4' [Ni2-Ni2', 6.2102(4) Å; Ni4-Ni4' 6.2477(5) Å] (see figure 3-8). The inter-chain separation for Ni^{II} centres hydrogen bonding through solvent of crystallisation is 7.6687(5) Å (Ni1-Ni2') or 8.0610(6) Å (Ni1-Ni3') (see figure 3-10). The part weight water of crystallisation donates

to two chloride ligands on adjacent clusters. Interstitial voids in **10** are smaller than those present in **9** (figure 3-11).

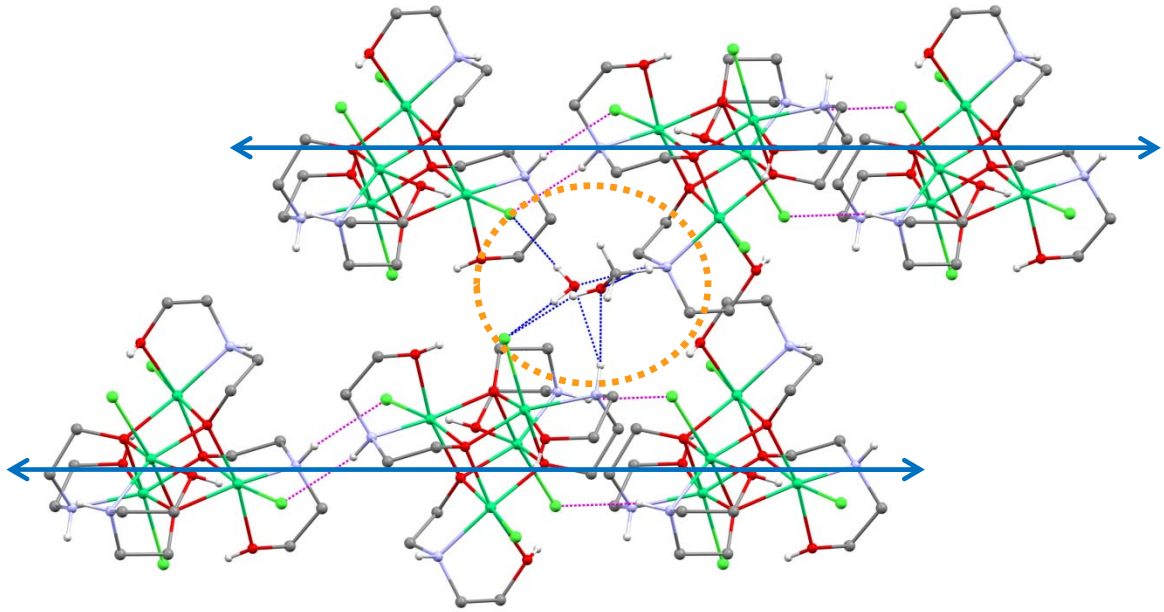

Figure 3-9: Neighbouring one-dimensional chains in **10** (directionality indicated by blue arrows) with methanol/water solvent of crystallisation filling the interstitial voids (circled in orange). Atom colours are as previously defined. H atoms in CH_2 groups are omitted for clarity. Direct intermolecular hydrogen bonding between clusters is shown in pink; hydrogen bonding between clusters and solvent of crystallisation is indicated in blue.

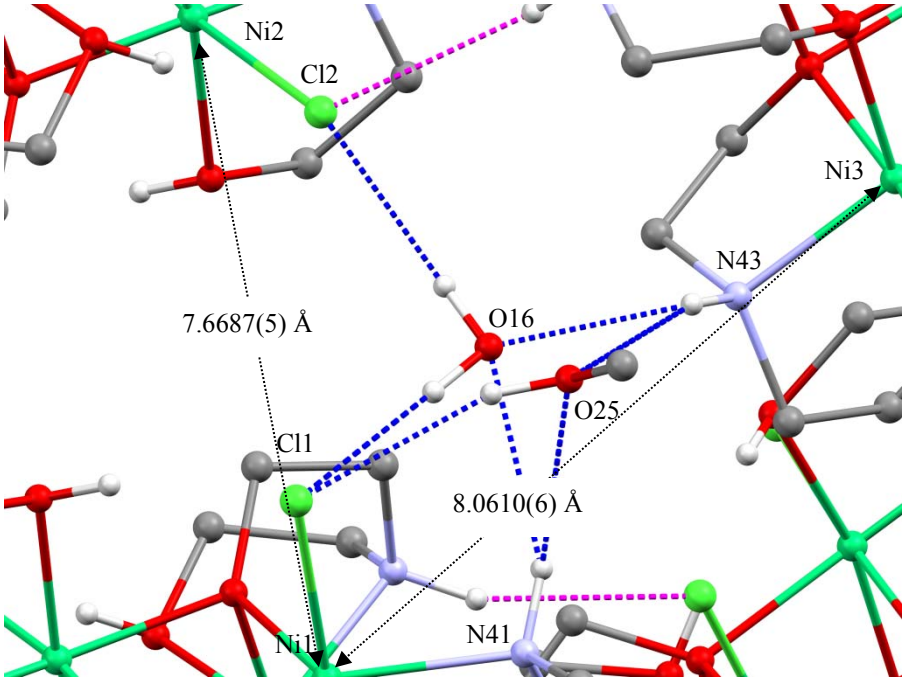

Figure 3-10: Enlarged image of the circled region in figure 3-9. Hydrogen bonding between 1D chains takes place through solvent of crystallisation as indicated in blue.

Table 3.7: Selected intermolecular/intramolecular hydrogen bond distances and angles for **10**.

Bond*	Distance (Å)	Angle (°)
O71—H711 · · · Cl3	2.999(2)	167.2(1)
N42—H42 · · · Cl2'	3.431(2)	156.4(1)
N44—H44 · · · Cl4'	3.403(2)	151.8(1)
N41—H411 · · · O25'	3.155(3)	134.7(1)
N41—H411 · · · O16'	3.27(2)	149.0(4)
N43—H431 · · · O25'	3.019(4)	160.9(1)
N43—H431 · · · O16'	2.95(2)	133.2(4)
O25—H251 · · ·Cl1	3.188(2)	161.6(2)
O16—H161 · · · Cl1'	2.99(2)	179(1)
O16—H162 · · · Cl2'	3.23(1)	179(1)

*Where ' is used, this denotes an atom on a neighbouring molecule.

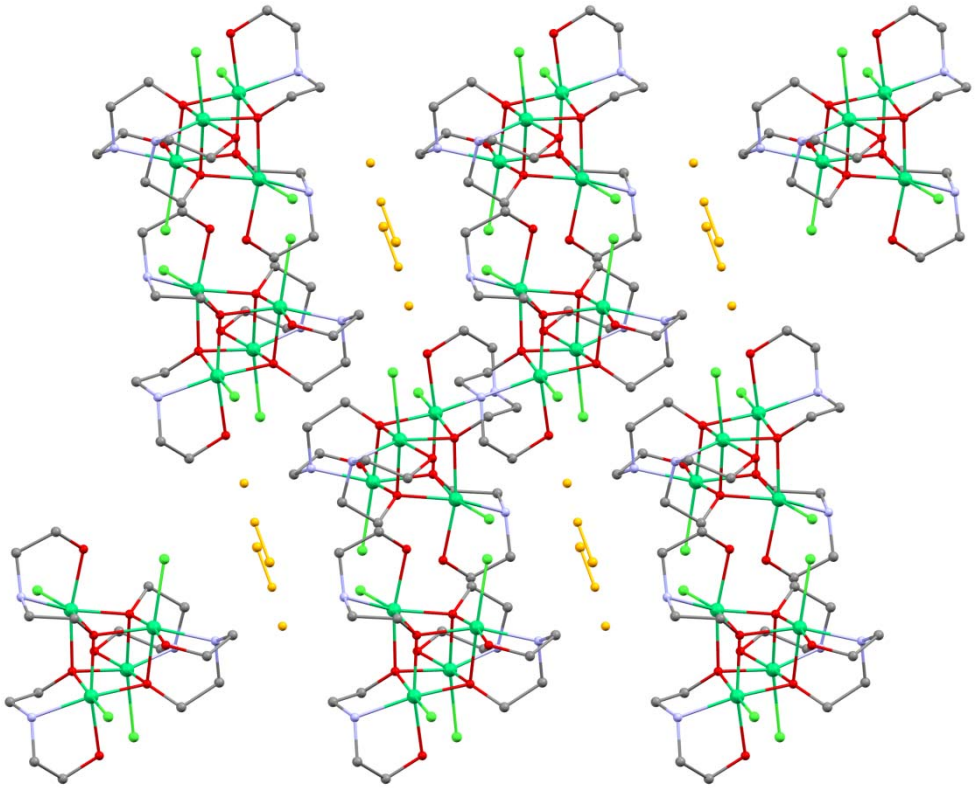

Figure 3-11: Crystal packing of **10** with solvent of crystallisation highlighted in yellow. Note that the interstitial void volume is not as great as for **9**.

3.2.3 Reaction products from using *N*-substituted diethanolamine ligands

High-frequency and -field EPR measurements on the original $\{Ni_4\}$ cubane, **9**, suggest the presence of intermolecular interactions between clusters. The crystallographic measurements carried out show that the predominant intermolecular bonding pathway is through N-H · · ·Cl contacts. One way of interrupting this is to use an *N*-substituted diethanolamine ligand with a larger group replacing the amino hydrogen atom. Ligands investigated previously within the research group include *N*-methyl-diethanolamine (mdeaH) and *N*-ethyl-diethanolamine (edeaH). There have been several reported SMMs that include these ligands: a tetranuclear star-type $\{Fe^{III}_4\}$ cluster,[170] a series of isostructural $\{Mn_5Ln_4\}$ clusters[171] and a $\{Dy_4\}$ butterfly[172] all contain mdea while a series of $\{Mn_{12}\}$ wheels[173, 174] and $\{Mn_6\}$ rods[175] contain either mdea or edea. Unfortunately previous unpublished work on Ni^{II} with these ligands within this research group only yielded monomeric products.[176]

Three further ligands were chosen for investigation: triethanolamine (teaH), *N*-tert-butyl-diethanolamine (tbdeaH) and *N*-phenyl-diethanolamine (PhdeaH). A search of the Cambridge Structural Database[135] yielded no transition metal $\{M_4O_4\}^{4+}$ cubanes containing tea, Phdea or tbdea. Many examples of complexes containing tea are found in the literature, including a $\{Mn_4\}$ butterfly,[177] a $\{Dy_4Fe_7\}$ complex[178] and $\{Fe_6\}/\{Fe_8\}$ disks encapsulating Li, Na and Cs.[179] The use of tbdea has been reported in several series of polynuclear clusters, most notably by Powell and co-workers; two out of three square-pyramidal μ_4-bridged Co^{II}_5 clusters exhibit behaviour consistent with single-molecule magnetism[180] while five members of a family of new octanuclear heterometallic 3*d*-4*f* complexes with a $\{Mn^{III}_4Ln^{III}_4\}$ "square in square" topology are also SMMs.[181] Polynuclear clusters including Phdea are much rarer with only one example reported in the CSD containing transition metals, again by Powell. No magnetic measurements were reported for $[Fe^{III}_7(\mu_3\text{-}O)_3(Phdea)_3(O_2CCMe_3)_6(O_2CCMe_3)_3(H_2O)_3]$.[182]

The use of teaH in our own experiments produced another monomeric compound, $[Ni(teaH)_2]Cl_2$ (**11**), that has previously been reported in the literature.[167] The teaH ligands remain fully protonated and coordinate to the Ni^{II} centre through two alcohol arms and the central amine (figure 3-12). The third alcohol arm does not coordinate to the metal. The remaining space in the lattice is filled by two Cl^- counter-ions per Ni^{II} complex. **11**

crystallises in the triclinic space group *P*-1 with two complexes per unit cell. The published data were collected at room temperature, and our data measured at 100 K show minor differences in the unit cell lengths and angles, but no major differences in the strong hydrogen bonding network that exists through the crystal structure. All six alcohol arms hydrogen bond to chloride ions in the lattice. Consequently each chloride ion acts as an acceptor for donors from three different clusters (figure 3-13).

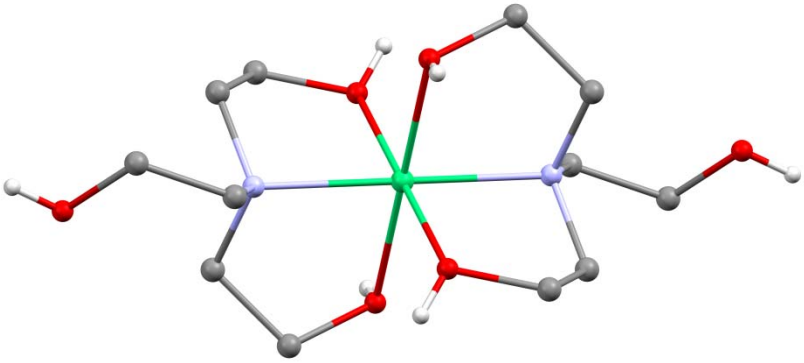

Figure 3-12: The Ni^{II}-based complex present in **11**. H atoms in CH_2 groups are omitted for clarity. Atom colours are as previously defined.

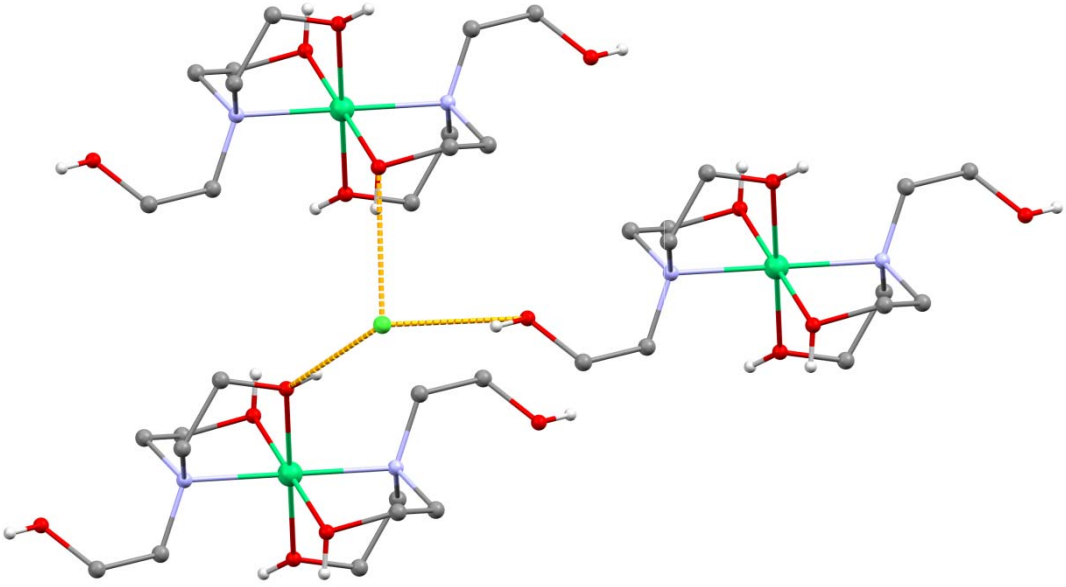

Figure 3-13: Lattice chloride ion hydrogen-bonding (yellow) from three monomeric Ni^{II} complexes. Each complex shares a total of six chloride ions with neighbouring clusters. H atoms in CH_2 groups are omitted for clarity. Atom colours are as previously defined.

A variety of solvent systems were used in order to encourage crystalline samples to grow from the reaction products of using PhdeaH and tbdeaH; however all of these were unsuccessful. Samples of the methanolic filtrate from reactions where PhdeaH was used (both with tris and without tris) were analysed by FAB^+ mass spectrometry. Although there

are many unassigned peaks in the spectra (likely due to by-products and leftover reactants in the filtrates) it was possible to assign several of the higher *m/z* peaks. A peak at *m/z* = 700.0 in the tris reaction was assigned as $[Ni_4Cl_3(Ph\text{-}NC_4H_8O_2)_2]^+$ (see figure 3-14); peaks at *m/z* = 642.7 and *m/z* = 604.7 in the non-tris reaction were assigned as $[Ni_3Cl_3(Ph\text{-}NC_4H_9O_2)_2]^+$ and $[Ni_3Cl_2(Ph\text{-}NC_4H_9O_2)(Ph\text{-}NC_4H_8O_2)]^+$ respectively (see figures 3-15, 3-16). Isotopic distributions for each peak show good agreement with calculated patterns.

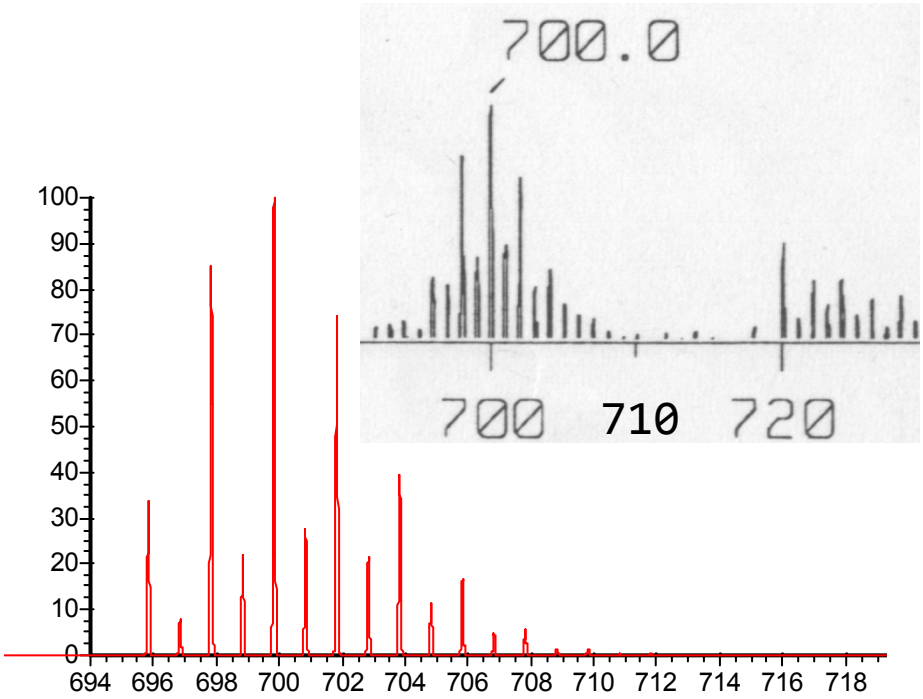

Figure 3-14: Simulated isotopic distribution for $[Ni_4Cl_3(Ph\text{-}NC_4H_8O_2)_2]^+$ with (inset) experimentally measured peak (tris reaction). The full mass spectrum is given in appendix E.

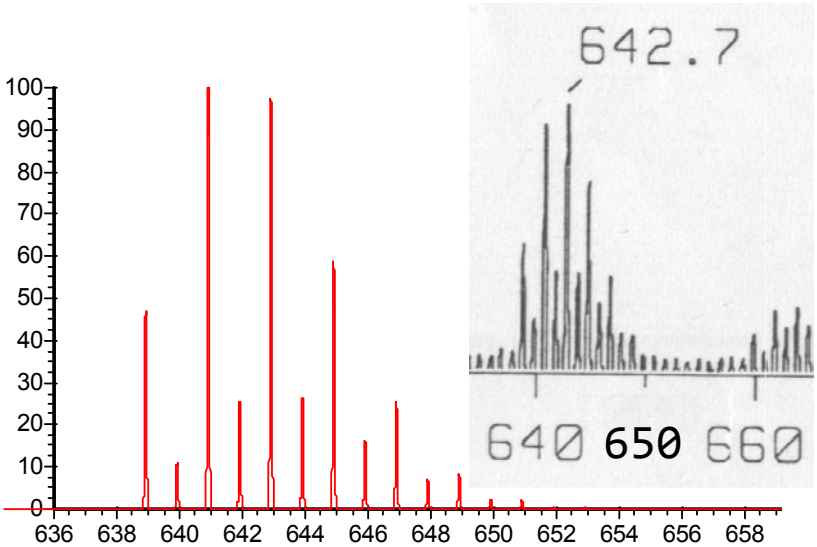

Figure 3-15: Simulated isotopic distribution for $[Ni_3Cl_3(Ph\text{-}NC_4H_9O_2)_2]^+$ with (inset) experimentally measured peak (non-tris reaction). The full mass spectrum is given in appendix E.

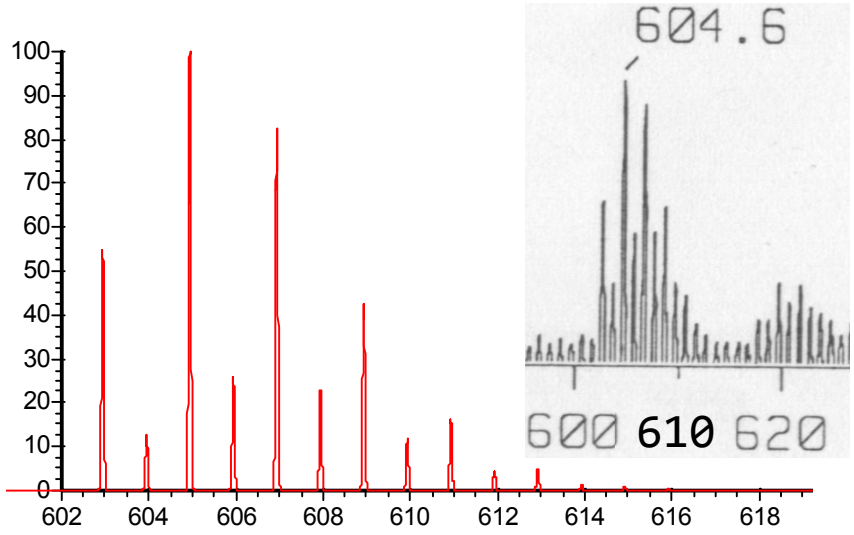

Figure 3-16: Simulated isotropic distribution for $[Ni_3Cl_2(Ph\text{-}NC_4H_9O_2)(Ph\text{-}NC_4H_8O_2)]^+$ with (inset) experimentally measured peak (non-tris reaction). The full mass spectrum is given in appendix E.

The mass spectra from the reaction products of tbdeaH did show some evidence of peaks at similarly high *m*/*z*, however these were dwarfed by very large peaks at low *m*/*z* (thought to be by-products and unreacted reagents).

No peaks are observed that correspond to the complete $\{Ni_4\}$ cubane structure for any of the reaction products. However this could be due to fragmentation that occurs during the analysis. The peaks that were observed for the PhdeaH reactions correlate well with particular fragments of the cubane. At the very least, the large *m*/*z* values recorded suggest that a complex of considerable molecular weight is formed during the reactions. Even if this was found not to be the expected cubane product, it could still be of considerable interest if a different polynuclear cluster. It is worth noting that no peaks are observed corresponding to fragments greater than the whole cubane (assuming *m*/*z* with *z*=1).

3.2.4 Structures containing the $[Ni_4(dea)_4Br_4]$ cubane

3.2.4.1 $[Ni_4(dea)_4Br_4]\cdot 6MeCN$ (12)

Synthesis of the tetragonal bromide analogue of the acetonitrile solvate **9** was achieved successfully; unfortunately it was only possible to produce a few crystals on one occasion. This was sufficient to carry out a detailed crystallographic study, however further studies including magnetic properties and elemental analysis were not possible. Further synthetic

experiments were performed in order to produce sufficient product for such studies but, despite employing a wide range of conditions (varying concentration and ratio of reagents, use of tris or no tris, identity of reaction solvent, level of hydration of $NiBr_2$ salt and ratio of reaction filtrate to acetonitrile for liquid-liquid diffusion), no more reactions were successful. Indeed, the solvothermal reaction that produced species **14** was part of an unsuccessful strategy to synthesise **12**.

The crystal structure of **12** was measured at 100 K and 30 K using a Bruker APEX II X-ray diffractometer equipped with an Oxford Cryosystems HELIX low temperature device. A crystal was carefully mounted on a glass fibre and quickly placed under the cryo-stream to prevent solvent loss. The structure is broadly similar to the original chloride cubane, **9**, in most respects. The solvent region was modelled slightly differently; this is not unexpected since this region is quite disordered. Full crystallographic data are given in table 3.8.

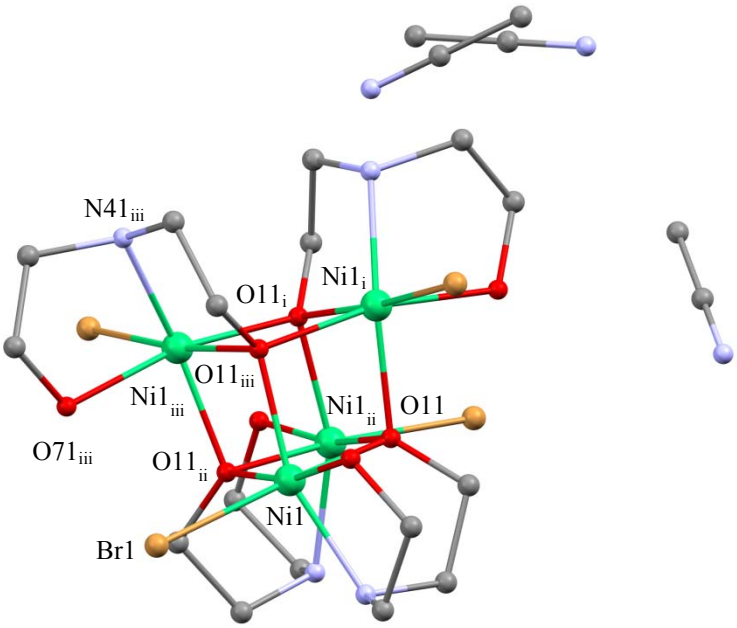

Figure 3-17: Crystal structure of **12** with its associated MeCN of crystallisation in three positions. (Ni, mint green; N, blue; O, red; C, grey; Br, light brown). H atoms are omitted for clarity. $Ni1_i$ = Ni1 {*y*-¼,½-*x*,¼-*z*}, $Ni1_{ii}$ = Ni1 {-*x*,½-*y*,*z*}, $Ni1_{iii}$ = Ni1 {*y*-¼,¼+*x*,¼-*z*}.

The structure of the cubane **12** (figure 3-17) is almost identical to that of **9**, the major difference being that a bromide ligand now fills the final coordination site at each Ni^{II} centre instead of a chloride ligand. The dea^- ligands remain mono-deprotonated and bond to the Ni^{II} through the alcohol arm, the alkoxide arm and the amine. The bridging angles between the four Ni^{II} centres (table 3.9) are similar to those observed at the same temperature for **9**. There are eight below 99° and four above this angle. However, the M-L

distances (table 3.10) are different to those observed for **9**. All distances are shortened in the bromide analogue **12**, save for the M-X distance (X=Cl, Br) which is considerably lengthened due to the larger size of the bromide ligand compared with the chloride ligand. The intramolecular hydrogen bond from the alcohol arm to a bromide ligand within the cluster is lengthened from 3.046(2) Å to 3.146(2) Å while the angle is similar [166(3)° *vs* 168(3)°] (see table 3.11, figure 3-18).

Table 3.8: Crystallographic data for **12** measured at 30 K.

Formula	$C_{28}H_{58}Br_4N_{10}Ni_4O_8$
Moiety formula	$[Ni_4(dea)_4Br_4]\cdot 6MeCN$
FW (g mol^{-1})	1217.32
Crystal system	Tetragonal
Space group	$I4_1/a$
a / Å	12.2449(5)
c / Å	29.5504(14)
V / Å^3	4430.7(3)
Z	4
T / K	30(2)
λ / Å	0.71073
D_c / Mg m^{-3}	1.825
μ [mm^{-1}]	5.335
Meas./indep. refl.	20481 / 2439
R_{int}	0.0439
Obs. refl. [$I > 2\sigma(I)$]	2138
wR_2 [a]	0.0828
R_1 [b]	0.0376
Goodness of fit on F^2	1.059
$\Delta\rho_{max,min}$ [e Å^{-3}]	0.80/-1.00

[a] $wR_2 = \{\sum[w(F_O^2 - F_C^2)^2]/\sum[w(F_O^2)^2]\}^{1/2}$

[b] $R_1 = \sum||F_O| - |F_C||/\sum|F_O|$

Table 3.9: Bridging angles in the cubane cores of **9** and **12** at 30 K.

Atoms*	Angle in **9** (°)	Angle in **12** (°)
Ni1 – O11 – $Ni1_i$	98.21(9)	98.53(9)
Ni1 – O11 – $Ni1_{ii}$	100.35(9)	100.32(10)
Ni1 – $O11_{ii}$ – $Ni1_{iii}$	96.30(8)	96.44(9)

* $Ni1_i$ = Ni1 {y-¼,½-x,¼-z}, $Ni1_{ii}$ = Ni1 {-x,½-y,z}, $Ni1_{iii}$ = Ni1 {y-¼,¼+x,¼-z}. $O1_i$ = O1 {y-¼,½-x,¼-z}, $O1_{ii}$ = O1 {-x,½-y,z}, $O1_{iii}$ = O1 {y-¼,¼+x,¼-z}.

Table 3.10: Comparison of bond distances made by Ni1 in **9** and **12** at 30 K. X=Cl, Br.

Bond*	Distance in **9** (X=Cl) (Å)	Distance in **12** (X=Br) (Å)
Ni1—O11	2.044(2)	2.035(2)
Ni1—$O11_i$	2.062(2)	2.050(2)
Ni1—$O11_{ii}$	2.105(2)	2.101(2)
Ni1—N41	2.110(2)	2.095(3)
Ni1—O71	2.129(2)	2.119(2)
Ni1—X1	2.4052(8)	2.5494(5)

* Symmetry operations relating equivalent atoms are as previously defined.

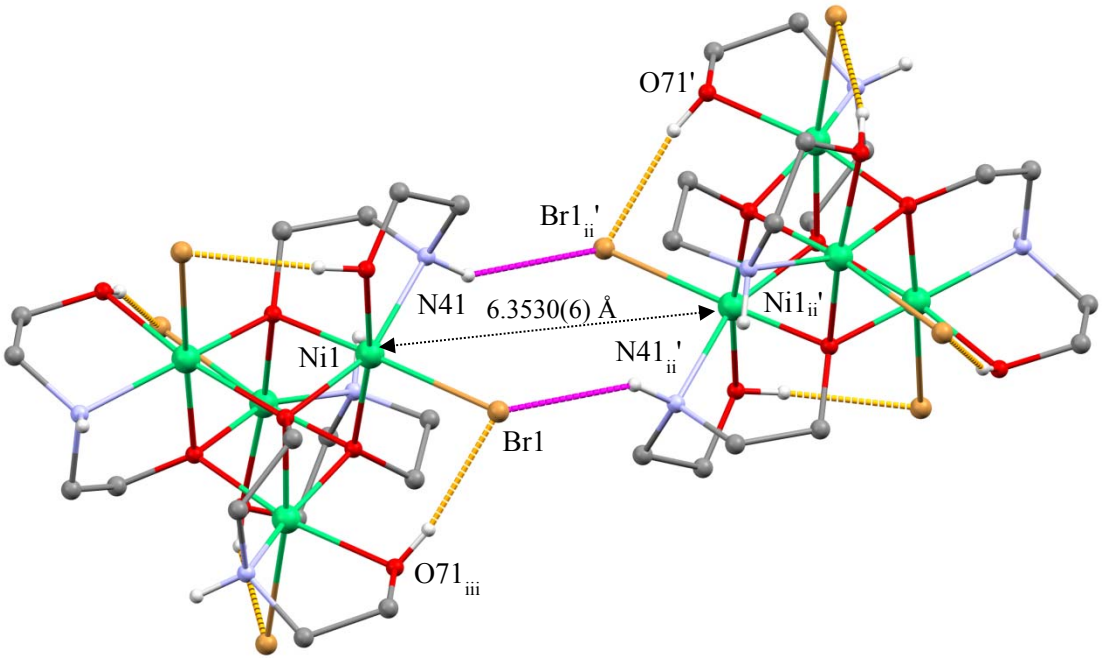

Figure 3-18: Intramolecular hydrogen bonding (yellow) through the O-H---Br pathways within each cluster and intermolecular hydrogen bonding (purple) between two adjacent clusters through complementary N-H---Br pathways. Solvent of crystallisation and H atoms (except those involved in H bonds as shown) are omitted for clarity. Atom colours are as previously defined, H atoms shown in white. Symmetry operations relating equivalent atoms are as previously defined.

Table 3.11: Selected intermolecular/intramolecular hydrogen bond distances and angles for **12** at 30 K.

Bond	Distance (Å)	Angle (°)
O71—H711 · · · $Br1_{i}$	3.146(2)	166(3)
N41—H411 · · · $Br1_{ii}$'	3.440(3)	148.8(2)
Ni1—$Ni1_{ii}$'	6.3530(6)	-

The cluster also exhibits intermolecular hydrogen bonding to four neighbouring clusters through two complementary N–H · · · Br contacts [N41–H41 · · · $Br1_{ii}$' = 3.440(3) Å; 148.8(2)°] (symmetry operations relating equivalent atoms are as previously defined) in a distorted tetrahedral-like arrangement (figure 3-19). This distance is again approximately 0.1 Å longer than the analogous distance in **9** [3.440(3) Å *vs*. 3.341(2) Å] and the angle is similar [148.8(2)° *vs*. 148.4(1)°]. The Ni-Ni' separation distance is 6.3530(6) Å in **12**, a small but significant increase over that measured for **9** [6.191(3) Å]. The pseudo-tetrahedral distortion in this complex is slightly more pronounced, with the angles between the centroids of adjacent clusters being 79° and 126° (compared with 81° and 125° for **9**).

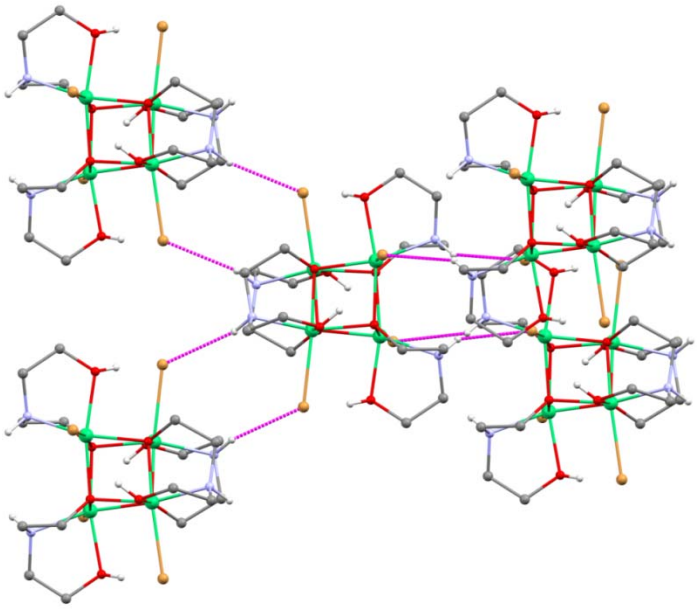

Figure 3-19: Intermolecular hydrogen bonding (purple) between one cluster and its four neighbours through N-H---Br pathways in a distorted pseudo-tetrahedral geometry. Solvent of crystallisation and H atoms in CH_2 groups are omitted for clarity. Atom colours are as previously defined.

The disordered solvent region (figure 3-20) contains two independent molecules of acetonitrile. One MeCN is in a general position (2) and the other (3) is located near a two-fold axis. Both MeCN molecules were treated as freely rotating rigid bodies and were given occupancies of 1.0 and 0.5 respectively. All non-hydrogen atoms in the $\{Ni_4\}$ complex and MeCN molecule 2 were refined with anisotropic displacement parameters.

The atoms in MeCN molecule 3 were given a common isotropic displacement parameter. H atoms were placed in calculated positions on the C and N atoms of the $\{Ni_4\}$ complex. Thereafter they were allowed to ride on their parent atoms with an isotropic displacement parameter equal to 1.2 times that of the equivalent isotropic displacement parameter (U_{eq}) of their parent atoms. The hydroxyl H atom attached to O71 was located in a difference map and refined subject to the restraint that the O-H distance was 0.85(1) Å. The hydrogen atoms of the methyl groups of the acetonitriles of solvation were located in a Fourier synthesis performed about the locus of possible hydrogen atom positions; the whole methyl group was then treated as a rotating rigid body.

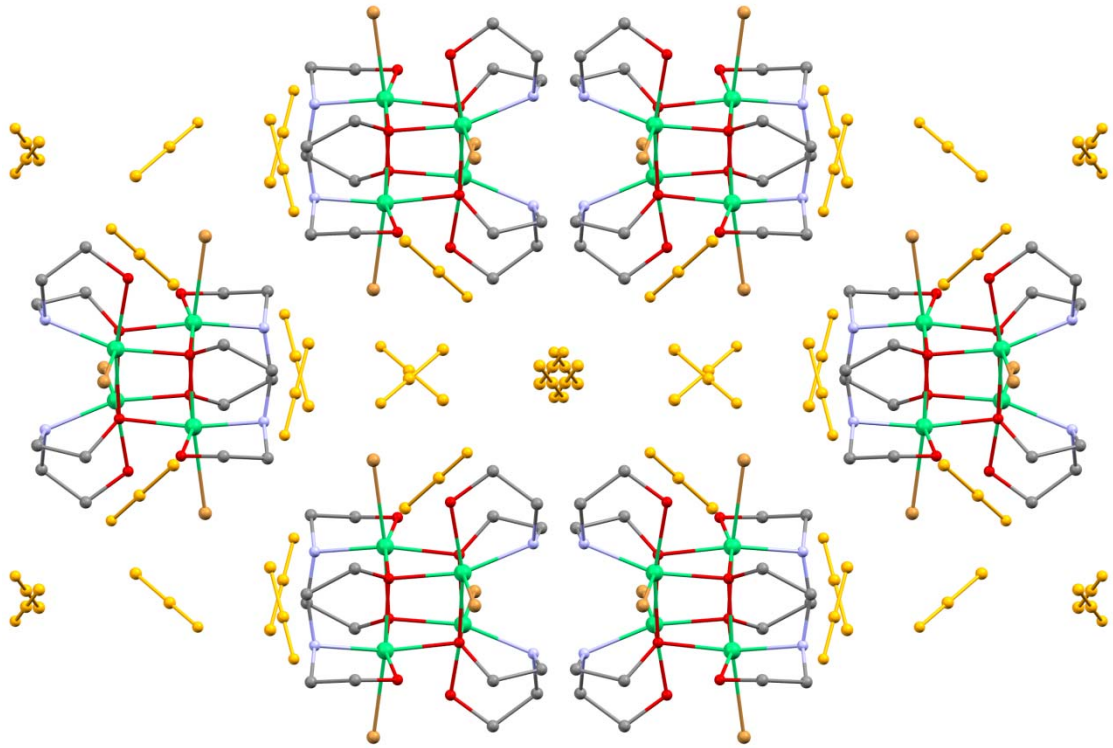

Figure 3-20: Crystal packing of **12** viewed along the crystallographic *b* axis. Solvent of crystallisation is highlighted in yellow to indicate the large interstitial voids present in the structure. H atoms are omitted for clarity. Atom colours are as previously defined.

3.2.4.2 $[Ni_4(dea)_4Br_4]\cdot 0.7MeOH\cdot 0.6H_2O$ (13)

Crystallographic data were measured at 100 K and 30 K using a Bruker APEX II X-ray diffractometer equipped with an Oxford Cryosystems HELIX low temperature device. A crystal was carefully mounted on a glass fibre and cooled under the cryo-stream. These crystals do not lose solvent so quickly when removed from the mother liquor compared with the acetonitrile solvates **9** and **12**. The unit cell and basic structure were found to be

similar to the methanol solvate of the chloride cubane (**10**) and so a direct comparison is possible. Distances and angles quoted here are from the 100 K structure so that they can be compared with the chloride analogue. Full crystallographic data are given in table 3.12.

Crystals can be successfully grown from layering the methanol (MeOH) filtrate with ethanol (EtOH), iso-propyl-alcohol (IPA) or methyl tert-butyl ether (MTBE). Crystallographic measurements were carried out on samples obtained from all three solvent systems and found to be identical. The data presented here at 100 K were collected on a crystal grown from MeOH/MTBE, while the data at 30 K were collected using a crystal grown from MeOH/IPA. Magnetic data are also presented for a sample grown from MeOH/IPA.

All non-H atoms in the cluster and solvents of crystallisation were refined with ADPs. Analysis of intermolecular contacts suggested that the methanol molecule and the two water molecules form two separate disorder components; thus, the occupancies of the two components were constrained to sum to unity. H atoms attached to N and C were placed in calculated positions. H atoms attached to O atoms and the methanol of crystallisation (O25, C15) were located in a difference map and allowed to refine subject to restraints on the O-H and C-H distances (0.85(1) Å and 0.99(1) Å respectively) and on the O-C-H, H-C-H and C-O-H angles (109(1)°). H atoms attached to one of the waters of crystallisation (O16) were placed on the basis of two hydrogen bonds formed with H411 and H431. A similar analysis on the geometry about O26 (the other water of crystallisation) does not allow H atoms to be placed, and so these H atoms are left unplaced. As some atoms of the dea^- ligands adopted prolate ADPs, rigid bond and body restraints were applied to all C, N and O atoms in order to alleviate this.

The structure of the cubane (figure 3-21) and its extended hydrogen-bonded network are essentially the same as the chloride analogue, **10**. The same formation of one-dimensional hydrogen-bonded chains of $\{Ni_4\}$ clusters is observed here, with direct interactions between Ni2 and Ni4 atoms in clusters through N—H · · ·Br contacts (figure 3-22). The other two N-H sites on each cluster (belonging to Ni1 and Ni3) do not hydrogen bond directly to adjacent clusters. The interstitial voids between 1D chains are filled with solvent of crystallisation, which hydrogen-bonds to the chains on either side *via* the two free N-H and Br sites (see figures 3-23, 3-24). There are small differences in the occupancies of the

solvent of crystallisation (highlighted in figure 3-25) but these do not affect the clusters in any appreciable way.

Table 3.12: Crystallographic data for **13** measured at 100 K by using XRD.

Formula	$C_{16.71}H_{43.42}Br_4N_4Ni_4O_{9.29}$
Moiety formula	$[Ni_4(dea)_4Br_4]\cdot 0.7MeOH\cdot 0.6H_2O$
FW / g mol^{-1}	1003.58
Crystal system	Triclinic
Space group	*P*-1
α / °	92.4480(10)
β / °	90.9710(10)
γ / °	110.4330(10)
a / Å	10.9905(2)
b / Å	11.5994(2)
c / Å	13.3222(2)
V / Å^3	1589.12(5)
Z	2
T / K	100
λ / Å	0.71073
D_c / Mg m^{-3}	2.097
μ / mm^{-1}	7.410
Meas./indep. refl.	21461 / 6929
R_{int}	0.035
Obs. refl. [$I > 2\sigma(I)$]	5338
R_1 [a]	0.0497
wR_2 [b]	0.0902
Goodness of fit on F^2	0.9476
$\Delta\rho_{max,min}$ [e Å^{-3}]	1.56/-1.14

[a] $wR_2 = \{\sum[w(F_O^2 - F_C^2)^2]/\sum[w(F_O^2)^2]\}^{1/2}$

[b] $R_1 = \sum||F_O| - |F_C||/\sum|F_O|$

Similar to **10**, the cluster does not have S_4 crystallographic symmetry, meaning that the spin Hamiltonian will have a non-zero *E* term (see earlier discussion on the analogous chloride complex **10**). The cluster separation along the chain is lengthened to 6.3929(8), 6.4570(8) Å from 6.2102(4), 6.2477(5) Å for Ni2-Ni2' and Ni4-Ni4' distances. The inter-chain separation for interaction through the solvent of crystallisation is also increased to

8.3189(9) Å from 8.0610 Å (Ni1-Ni3'), however the Ni1-Ni2' distance is essentially unchanged [7.6389(9) Å *vs*. 7.6687(5) Å]. The noted increases are clear consequences of increasing the size of the halide. Details of inter- and intra-molecular hydrogen bonding are given in table 3.13.

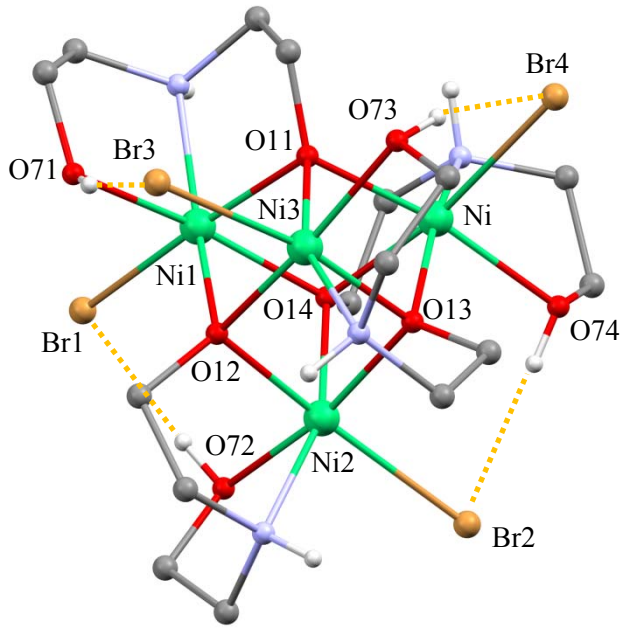

Figure 3-21: Molecular structure of **13** showing a single $\{Ni_4\}$ cluster. H atoms in CH_2 groups are omitted for clarity. Intramolecular hydrogen bonding O-H---Br is shown in yellow. Atom colours are as previously defined.

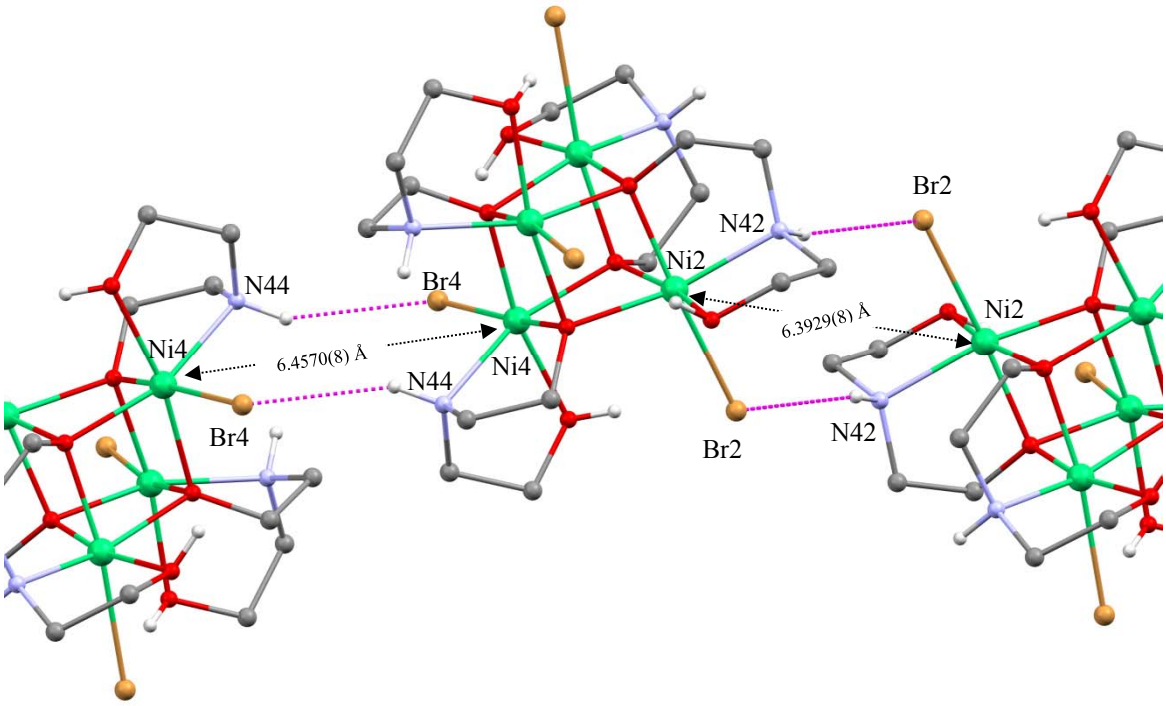

Figure 3-22: Direct intermolecular interactions (shown in pink) between $\{Ni_4\}$ clusters in **13**. Atom colours are as previously defined. H atoms in CH_2 groups are omitted for clarity. Direct interactions only take place through Ni2 and Ni4 (not Ni1 and Ni3); 1D hydrogen-bonded chains form as a result.

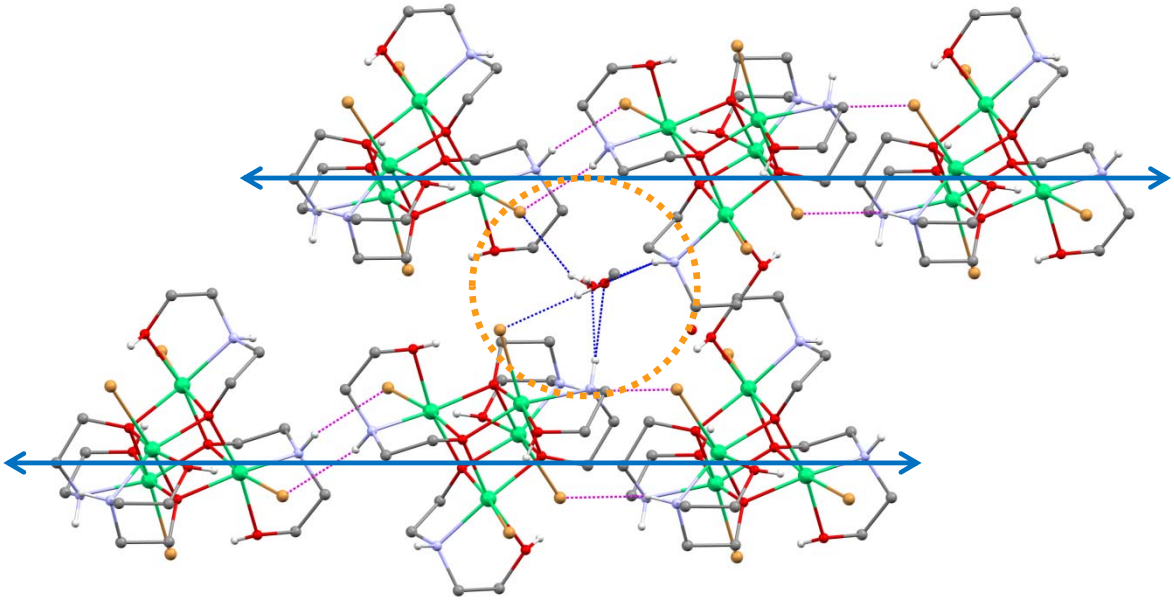

Figure 3-23: Neighbouring one-dimensional chains in **13** (directionality indicated by blue arrows) with methanol/water solvent of crystallisation filling the interstitial voids (circled in orange). Atom colours are as previously defined. H atoms in CH_2 groups are omitted for clarity. Direct intermolecular hydrogen bonding between clusters is shown in pink; hydrogen bonding between clusters and solvent of crystallisation is indicated in blue.

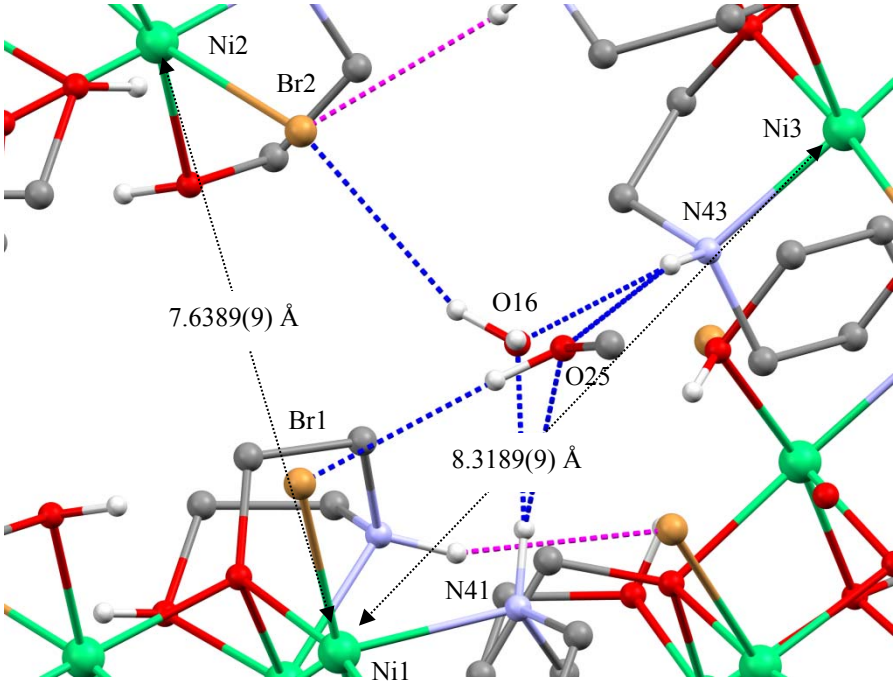

Figure 3-24: Enlarged image of the circled region in figure 3-23. Hydrogen bonding between 1D chains takes place through solvent of crystallisation as indicated in blue.

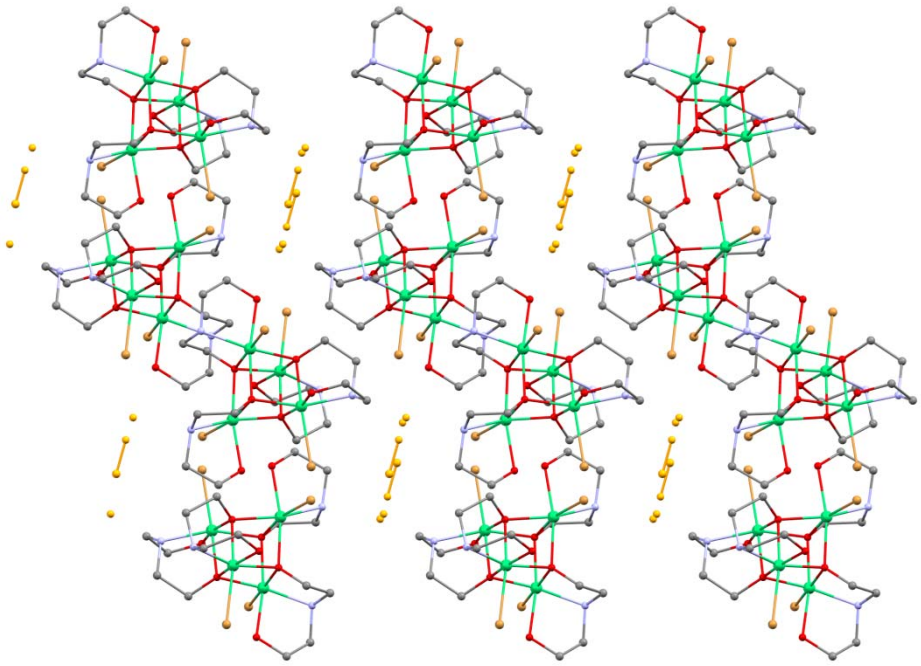

Figure 3-25: Crystal packing of **13** with solvent of crystallisation highlighted in yellow. The interstitial void spaces present in this structure are much smaller than those in **12**.

Table 3.13: Selected intermolecular/intramolecular hydrogen bond distances and angles for **13**.

Bond	Distance (Å)	Angle (°)
O71—H711 · · · Br3	3.134(4)	166(6)
N41—H411 · · · O25	3.260(8)	134.8(3)
N41—H411 · · · O16	3.05(2)	151.8(6)
N43—H431 · · · O25'	3.047(9)	161.4(3)
N43—H431 · · · O16'	2.85(2)	140.5(6)
O25—H251 · · ·Br1	3.412(7)	170(6)
O16—H162 · · · Br2	3.60(2)	160(1)

Considering all the Ni-O-Ni bridging angles in **13** (table 3.14), there are eight below the critical angle of approximately 99° and four above. This is consistent with the angles measured for **9**, **10** and **12**. Magnetic measurements were performed on **13** using a Quantum Design MPMS XL SQUID magnetometer. A number of single crystals grown by the method described previously were collected and lightly ground to a powder. The powder was dried under vacuum before preparation for measurement on the magnetometer. A small mass of powder (21.75 mg, 20.9 mmol) was immobilised in eicosane and placed in a gelatin capsule.

Table 3.14: Bridging angles in the cubane core of **13**.

Atoms	Angle (°)
Ni1 – O12 – Ni2	98.8(1)
Ni1 – O14 – Ni2	96.4(1)
Ni1 – O11 – Ni3	97.8(1)
Ni1 – O12 – Ni3	96.5(1)
Ni1 – O11 – Ni4	101.1(1)
Ni1 – O14 – Ni4	100.5(1)
Ni2 – O12 – Ni3	101.5(1)
Ni2 – O13 – Ni3	100.1(2)
Ni2 – O13 – Ni4	95.2(1)
Ni2 – O14 – Ni4	98.3(1)
Ni3 – O11 – Ni4	96.6(1)
Ni3 – O13 – Ni4	98.3(2)

Magnetisation increases with field (figure 3-26) but does not quite saturate with a field of 5 T. However the curve is clearly beginning to level off and we estimate that the magnetisation would saturate between 8.0-8.5 Nβ, suggesting that the ground state can be assigned as $S = 4$. This is consistent with measurements performed on **9**.[145]

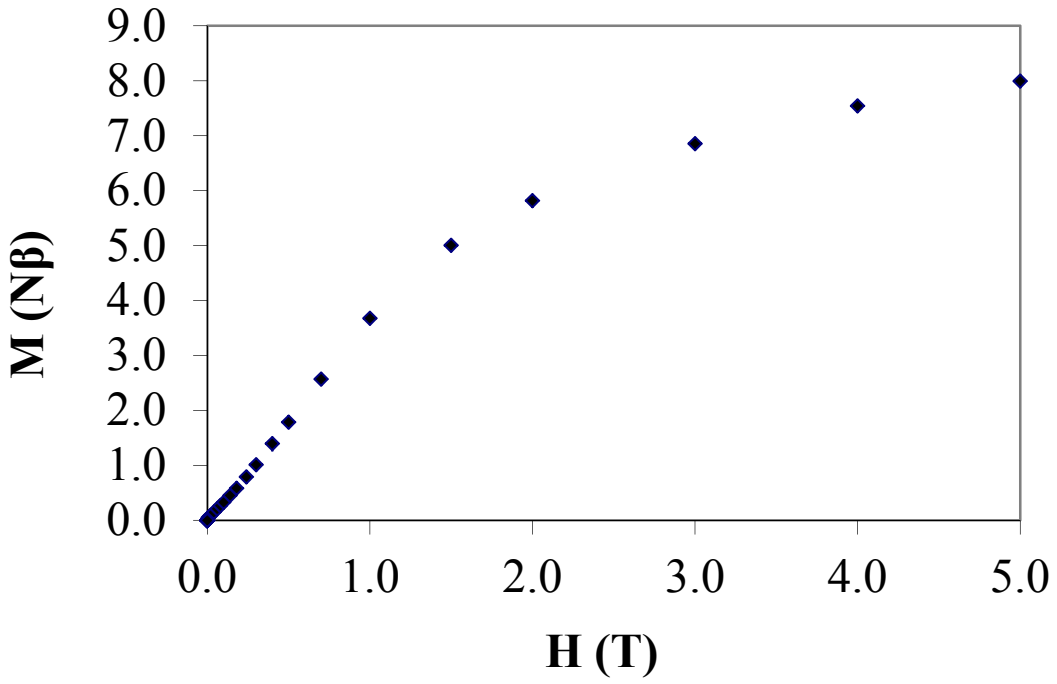

Figure 3-26: Plot of *M vs. H* for **13**.

A plot of χT *vs.* T (figure 3-27) indicates ferromagnetic behaviour with χT rising to a maximum value of 10.87 cm^3 mol^{-1} K at 12 K. Below 12 K, χT falls away quickly; this is fairly common for SMMs and could be due to a large zero-field splitting (ZFS) and/or intermolecular interactions. For the purposes of fitting, the system was described using one *J* parameter for the interactions around the side faces (angles less than 99°), and another for the interactions on the top and bottom faces of the cubane (angles greater than 99°). Although interactions that are deemed equivalent in this way are not strictly the same (due to the lack of S_4 symmetry), the model is much simplified compared to using six *J*s and is still a good approximation. To simplify the model further we linked parameters J_1 and J_2 by a coefficient of -0.25 (determined by the ratio of J_1 and J_2 in the published data for **9**). Thus, the magnetic data can be reproduced using a 2*J* model and were fitted to the spin Hamiltonian shown in equation 3.1 in the temperature range 300 K to 12 K, within MAGMUN-4.1.[183] All parameters used for the fit are given in the caption for figure 3-27 below. The data are consistent with a *g* value of 2.30 for four uncoupled Ni^{II} ions. This is significantly higher than the value of g = 2.15 reported for **9** from a fitting of the magnetisation data; however HF-EPR measurements performed on **9** gave a best-fit value of g = 2.275.[145] J_1 and J_2 are 13.663 cm^{-1} and -3.416 cm^{-1} respectively giving a large ferromagnetic interaction and a smaller antiferromagnetic interaction. Given that our spin Hamiltonian (equation 3.1) uses '-*J*', whereas that used for **9** uses '-2*J*', these values are quite consistent with J_1 and J_2 = 7.29 cm^{-1} and -2.08 cm^{-1} obtained for **9**. A significant negative value for θ (-1.5 K) indicate strong antiferromagnetic intermolecular exchange.

$$\hat{H} = -J_1\left(\hat{S}_1\hat{S}_2 + \hat{S}_1\hat{S}_3 + \hat{S}_2\hat{S}_4 + \hat{S}_3\hat{S}_4\right) - J_2(\hat{S}_1\hat{S}_4 + \hat{S}_2\hat{S}_3) \qquad (3.1)$$

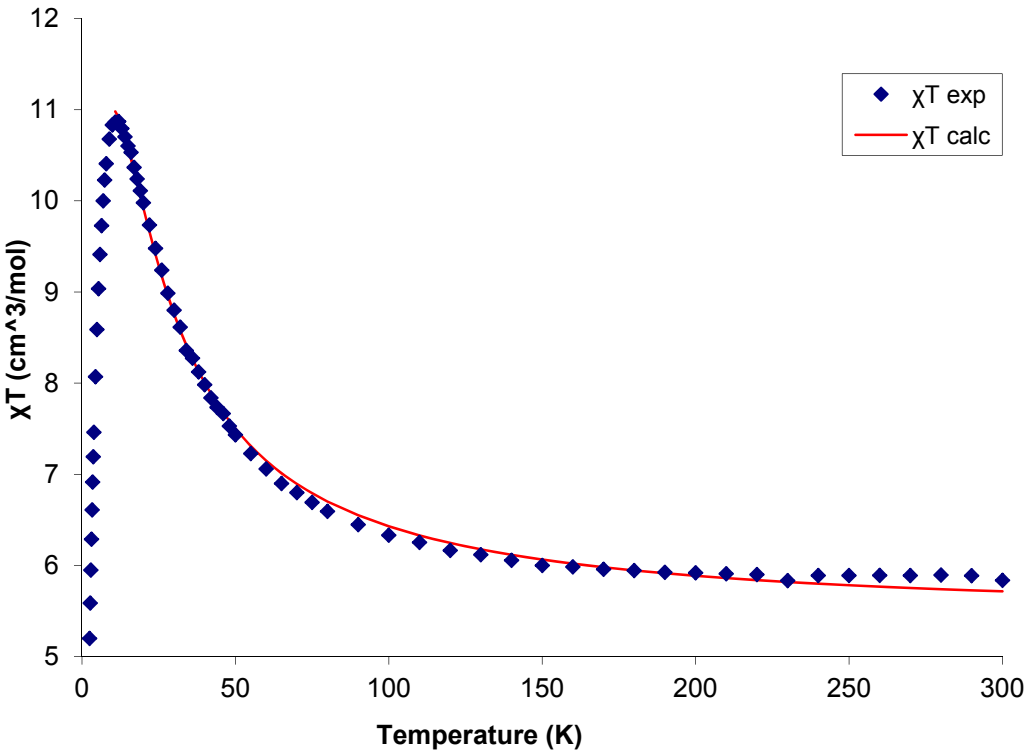

Figure 3-27: Fitting of χT *vs.* T for **13** in the temperature range 300 K to 12 K. Measured data is shown to 2.5 K.. R*100 = 0.95545, g = 2.2986 ± 0.01523, J_1 = 13.663 ± 0.64182 cm^{-1}, J_2 = -0.25J_1, TIP (temperature-independent paramagnetism) = 0.00018 cm^3 mol^{-1}, ρ = 0.003 (ρ is the fraction of monomeric impurity in the sample; 0.003 is equivalent to 0.3%), θ = -1.5 K.

The ac susceptibility data are particularly interesting when compared with data collected for the original compound **9**. Data were collected for **13** in the temperature range 1.8 – 8 K for a selection of oscillation frequencies. Below 3 K, the out-of-phase component of the ac susceptibility (figure 3-28) shows a frequency-dependent increase, similar to that observed for **9**. High-frequency ac magnetic susceptibility data for **9** indicate that χ" rises to a maximum of approximately 1 cm^3 mol^{-1};[145] although no high-frequency data are available for **13**, the behaviour of χ" between 3 K and 1.8 K is entirely consistent with **9**, suggesting that the lower temperature behaviour might be comparable. Above 3 K, the behaviour of the species diverges. **9** displays no further maxima in χ", while **13** displays a frequency-dependent peak with a maximum at 4-6 K of 0.065-0.085 cm^3 mol^{-1}. The frequency-dependent data can be fitted to an Arrhenius-like expression in order to derive the size of the effective energy barrier to relaxation, $U_{eff,}$ and pre-exponential factor, τ_0, for the relaxation process. The energy barrier quoted as U_{eff}/k_B was found to be 119 K and τ_0 is 7.2 x 10^{-14} s. Pre-exponential factors (τ_0) for an SMM are typically much larger than 10^{-12} s,[184, 185] and the energy barrier is normally smaller for Ni^{II} systems (for **9** it is estimated to be 12 K based on S=4, D=-0.75 cm^{-1}).[145] The maximum value of χ" indicates that only a

small fraction of molecules are undergoing this relaxation process. (χ' *vs.* T is shown in figure 3-29 to illustrate the relative signal heights; note the scale on the vertical axis). It is estimated from the relative heights that only approximately 8% of the sample undergoes this process. The characteristics of this relaxation process are not consistent with those of typical SMM-like behaviour, and it is therefore suggested that some other physical phenomenon could be responsible.

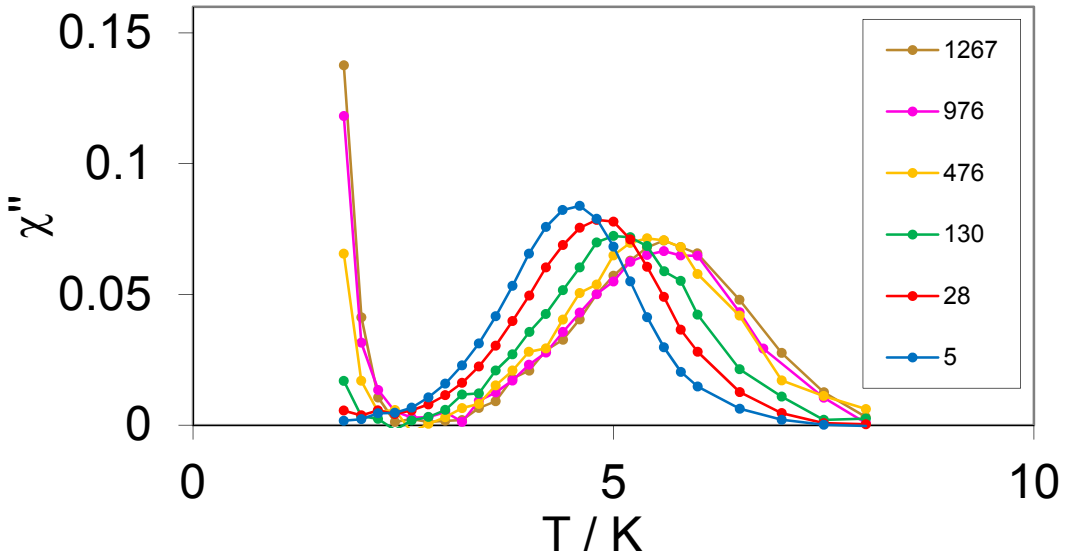

Figure 3-28: Out-of-phase ac magnetic susceptibility (χ'') *vs.* T for **13**. Oscillation frequencies are given in the legend (measured in Hz).

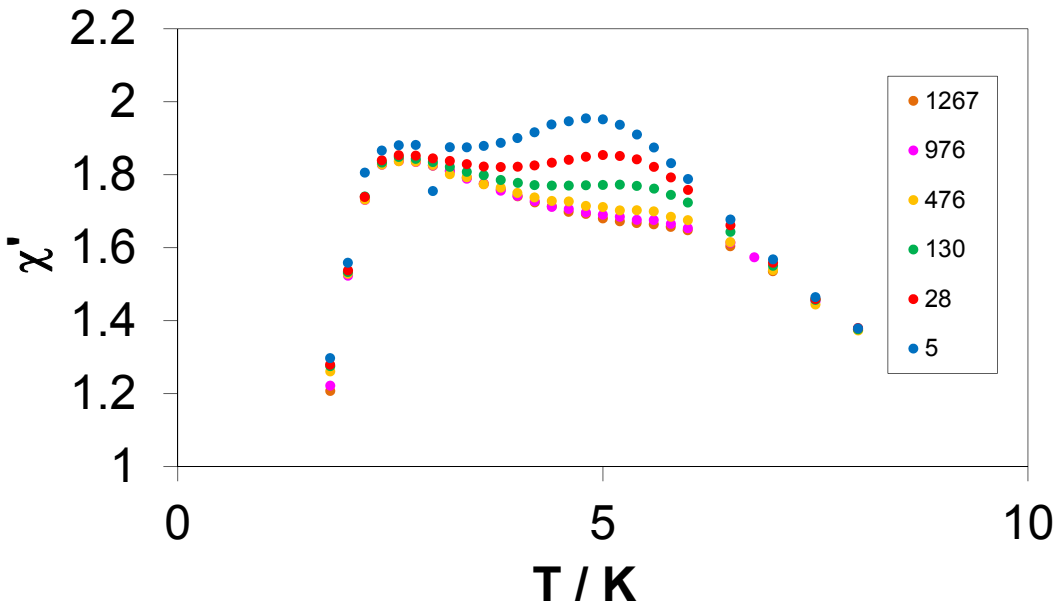

Figure 3-29: In-phase ac magnetic susceptibility (χ') *vs.* T for **13**. Oscillation frequencies are given in the legend (measured in Hz).

Single-chain magnets (SCMs) can be composed of one-dimensional hydrogen-bonded networks of coupled SMMs. The association of the SMMs into chains has been shown in a number of cases to modulate the intrinsic behaviour of the individual SMM units. Studies performed by Lecren and co-workers[186] on a series of antiferromagnetically coupled $\{Mn_4\}$ SMMs showed a marked increase in the effective energy barrier to relaxation accompanied by a decrease in the pre-exponential term of the Arrhenius expression by several orders of magnitude compared with isolated $\{Mn_4\}$ units. The isolated species $[Mn_4(hmp)_6(CH_3CO_2)_2(H_2O)_2](ClO_4)_2{\cdot}4H_2O$ (hmpH = 2-hydroxymethylpyridine) exhibits slow magnetic relaxation with U_{eff}/k_B = 11.9 K, τ_0 = 6 x 10^{-8} s. The analogous chain compound, $\{[Mn_4(hmp)_6(CH_3CO_2)_2](ClO_4)_2{\cdot}H_2O\}_n$ has U_{eff}/k_B = 37.3 K and τ_0 = 9.5 x 10^{-11} s. Although the units are antiferromagnetically coupled, defects in the structure create chains of finite length. Hence, chains with odd numbers of units will have net spin and can exhibit slow magnetic relaxation. The trend is borne out with other members of the $\{Mn_4\}$ family[187] and indeed with many other species.[188]

13 contains chains of strongly hydrogen-bonded $\{Ni_4\}$ clusters with weaker hydrogen-bonds between chains through solvent of crystallisation. It is therefore possible to draw certain parallels between our data and those mentioned above concerning SCMs. We observe an energy barrier higher than that typically associated with Ni^{II} SMMs and a pre-exponential Arrhenius term several orders of magnitude smaller. The structural defects required for such a system, *i.e.* those that cause chains to break down into short chains of finite length, could have occurred when the sample was dried under vacuum prior to measurement; removal of solvent of crystallisation would likely destroy long-range crystalline order since this is mediated in part by hydrogen-bonding through the solvent. Another possibility is that **13** is exhibiting spin glass behaviour; this is often associated with an extremely fast pre-exponential term.[6, 189]

Further work is in progress to allow confirmation of these results and to examine the effect upon the magnetic properties of the system of preparing the sample without drying under vacuum.

3.2.5 Structures containing the $[Ni_4(dea)_4Br_2(H_2O)_2]$ cubane

3.2.5.1 $[Ni_4(dea)_4Br_2(H_2O)_2]Br_2$ (14)

The species $[Ni_4(dea)_4Br_2(H_2O)_2]Br_2$ is produced solvothermally alongside a monomeric by-product $[Ni(NH_3)_6]Br_2$ that has previously been studied for its unusual hydrogen atom disorder and consequent rotational tunnelling behaviour.[190, 191] Crystallographic data were measured at 100 K using a Bruker APEX II X-ray diffractometer equipped with an Oxford Cryosystems HELIX low temperature device. A crystal was carefully mounted on a glass fibre and cooled under the cryo-stream. Full crystallographic data are given in table 3.15.

Unfortunately the crystals were produced in low yield (fewer than a dozen crystals) alongside a large amount of green and white powders and purple crystals of $[Ni(NH_3)_6]Br_2$; it was impossible to separate a sufficient amount of pure sample for elemental analysis. It is possible that refinement of the method could improve the yield and selectivity for producing crystals of **14**, by changing heating/cooling rates, reaction temperature and reaction time.

This species differs from the $\{Ni_4\}$ cubanes described previously in that two of the bromide ligands are replaced with water ligands giving the complex a +2 charge. Two bromide anions are located in the lattice (one is disordered about two sites), allowing some interesting intermolecular hydrogen bonding to be observed. The molecular structure is shown in figure 3-30.

The core of the cubane is similar to that identified previously. Ni-O-Ni bridging angles are similar also, with eight angles below 99° and four angles above 99° (table 3.16). The dea^- ligands are mono-deprotonated and exhibit binding to the Ni^{II} centres through the alcohol arm, the alkoxide arm and the amine. The alkoxide arms each bridge three Ni^{II} centres and form part of the $\{Ni_4O_4\}$ core. The structure crystallises in the triclinic space group *P*-1, with the asymmetric unit containing one whole cluster and associated anions. Again, there are four independent Ni^{II} centres and the cluster does not possess S_4 symmetry as is seen for the original acetonitrile solvate. In fact the symmetry is even lower than the pseudo-S_4 symmetry displayed by the methanol solvates **10** and **13** due to the asymmetry in the identity of the coordinated terminal ligands (Cl^- or Br^- *vs*. mixed Br^-/H_2O).

Table 3.15: Crystallographic data for **14**.

Formula	$C_{16}H_{44}Br_4N_4Ni_4O_{10}$
Moiety formula	$[Ni_4(dea)_4Br_2(H_2O)_2]Br_2$
FW / g mol^{-1}	1007.00
Crystal system	Triclinic
Space group	*P*-1
α / °	73.706(4)
β / °	86.467(4)
γ / °	62.953(3)
a / Å	10.5191(9)
b / Å	10.9949(10)
c / Å	16.7187(12)
V / Å^3	1648.1(2)
Z	2
T / K	100(2)
λ / Å	0.71073
D_c / Mg m^{-3}	2.029
μ / mm^{-1}	7.147
Meas./indep. refl.	12623 / 5728
R_{int}	0.049
Obs. refl. [$I > 2\sigma(I)$]	4100
wR_2 [a]	0.0410
R_1 [b]	0.0459
Goodness of fit on *F*	1.1489
$\Delta\rho_{max,min}$ [e Å^{-3}]	1.25/-0.68

[a] $wR_2 = \{\sum[w(F_o - F_c)^2]/\sum[w(F_o)^2]\}^{1/2}$

[b] $R_1 = \sum||F_o| - |F_c||/\sum|F_o|$

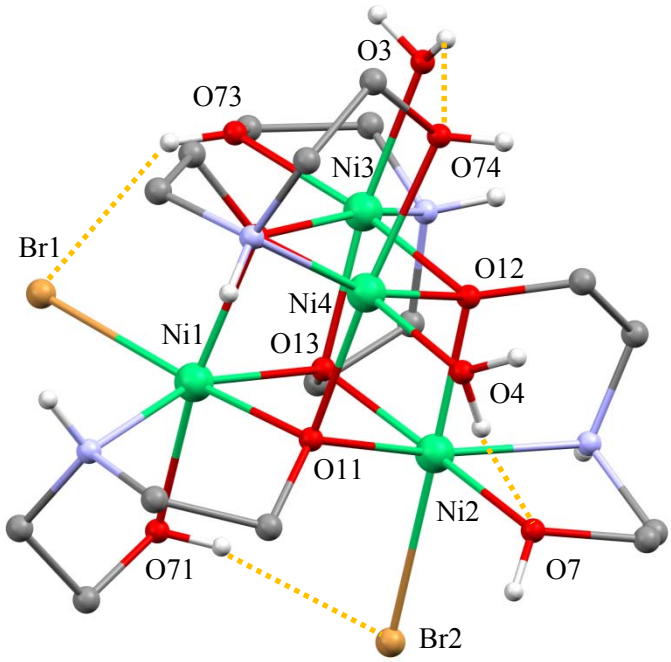

Figure 3-30: Molecular structure of **14** showing a single $\{Ni_4\}$ cluster. H atoms in CH_2 groups are omitted for clarity. Intramolecular hydrogen bonding O-H---Br and O-H---O is shown in yellow. Atom colours are as previously defined. Ni, O and Br atoms are labelled.

Each $\{Ni_4\}$ cluster exhibits both inter- and intra-molecular hydrogen bonding. Within the cluster there are two O-H---Br hydrogen bonds (from the alcohol arms of dea$^-$ ligands) and two O-H---O hydrogen bonds (from coordinated water molecules to alcohol oxygen atoms) across four faces of the cubane (indicated in figure 3-30). Direct intermolecular hydrogen bonding from N41-H411---Br1' and the reverse N41'-H411'---Br1 causes adjacent clusters to form dimeric pairs (figure 3-31). A similar arrangement is seen for the $\{Mn_4\}_2$ dimer described in Chapter 2 and results in modification of the quantum tunnelling steps observed in hysteresis loops of magnetisation *vs*. field for that compound.[25] Indirect intermolecular hydrogen bonding takes place through lattice anions Br3 (figure 3-32) and Br41/Br42 (figure 3-33) between neighbouring dimeric pairs. The overall effect is to create a three-dimensional hydrogen-bonded network of $\{Ni_4\}_2$ dimers linked through the lattice bromide anions. There is no solvent of crystallisation as observed in the other $\{Ni_4\}$ cubanes. It has been suggested by Hill *et al.* that solvent of crystallisation can cause HF-EPR spectra of an SMM to be more complex since the presence of such solvent often induces disorder in the crystal and a lowering of the local symmetry.[117, 192] However the disorder in Br41/Br42 might present similar problems. Full details of inter- and intra-molecular hydrogen bonding are given in table 3.17.

Table 3.16: Bridging angles in the cubane core of **14**.

Atoms	Angle (°)
Ni1 – O11 – Ni2	98.3(2)
Ni1 – O13 – Ni2	96.7(2)
Ni1 – O13 – Ni3	97.0(2)
Ni1 – O14 – Ni3	95.2(2)
Ni1 – O11 – Ni4	100.3(2)
Ni1 – O14 – Ni4	100.7(2)
Ni2 – O12 – Ni3	99.8(2)
Ni2 – O13 – Ni3	101.0(2)
Ni2 – O11 – Ni4	95.6(2)
Ni2 – O12 – Ni4	96.9(2)
Ni3 – O12 – Ni4	95.6(2)
Ni3 – O14 – Ni4	97.8(2)

Table 3.17: Selected inter- and intra-molecular hydrogen bond distances and angles for **14**.

Bond	Distance (Å)	Angle (°)
O71—H711 · · · Br2	3.188(4)	164.3(3)
O73—H731 · · · Br1	3.159(5)	138.8(4)
O3—H32 · · · O74	3.047(7)	126.4(4)
O4—H41 · · · O72	2.957(7)	147.1(3)
N41—H411 · · · Br1'	3.475(4)	143.5(4)
O74—H741 · · · Br3'	3.215(5)	148.4(4)
O72—H721 · · · Br3'	3.279(5)	147.1(3)
N43—H431 · · · Br3'	3.463(5)	145.4(4)
N42—H421 · · · Br42'	3.268(7)	140.6(4)
N44—H441 · · · Br42'	3.095(9)	141.4(4)
O3—H31 · · · Br41'	3.930(8)	133.1(4)
O4—H42 · · · Br3'	3.524(6)	137.4(4)

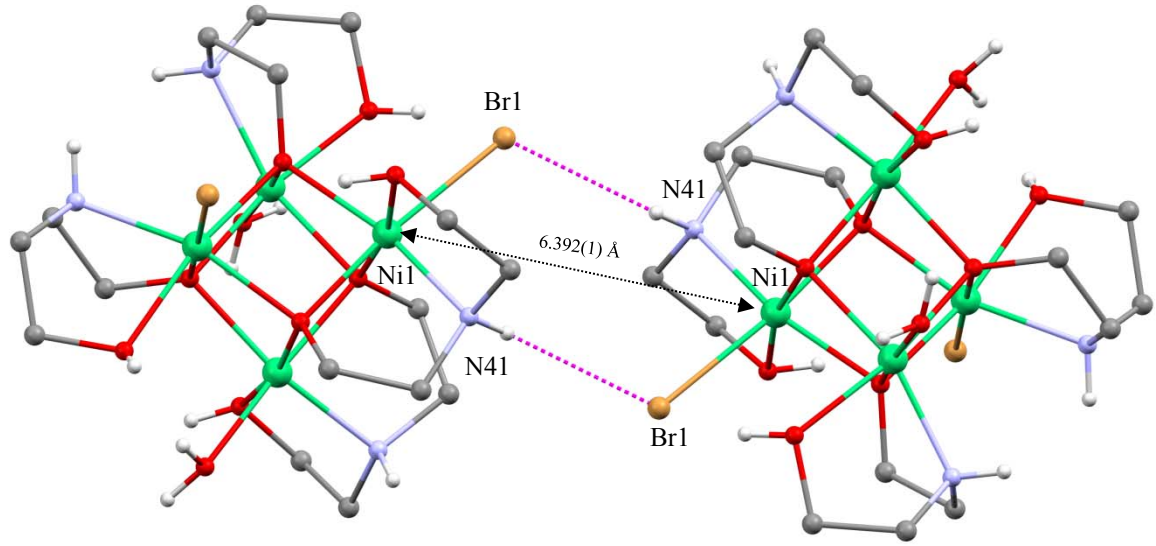

Figure 3-31: Direct intermolecular interactions (shown in pink) between $\{Ni_4\}$ clusters in **14**. Atom colours are as previously defined. H atoms in CH_2 groups are omitted for clarity. Direct interactions (via the Ni-N-H---Br-Ni pathway) only take place between Ni1 and Ni1' on adjacent clusters, forming dimers of directly hydrogen-bonded clusters. Other hydrogen-bonding interactions take place through lattice anions Br3 and Br41/Br42.

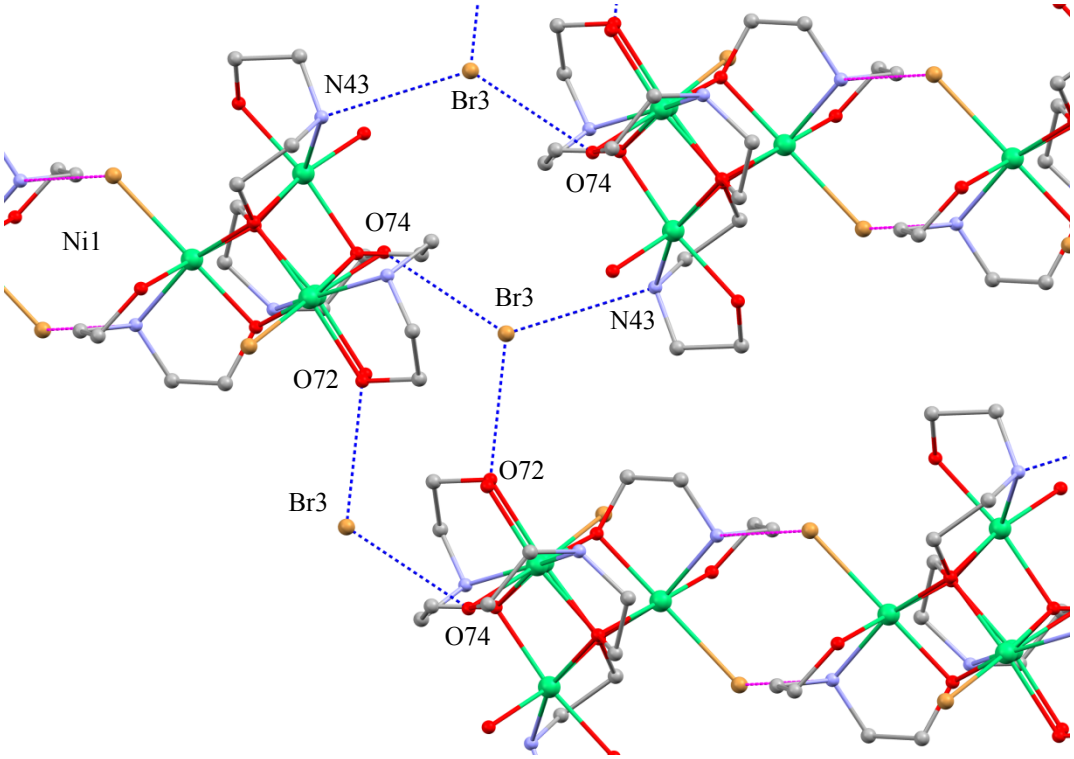

Figure 3-32: Extended network of $\{Ni_4\}$ clusters in **14**. 'Direct' intermolecular interactions forming dimeric pairs of clusters are shown in pink (see also figure 3-31); indirect intermolecular interactions through lattice anion Br3 are shown in blue. Atom colours are as previously defined; H atoms are omitted for clarity.

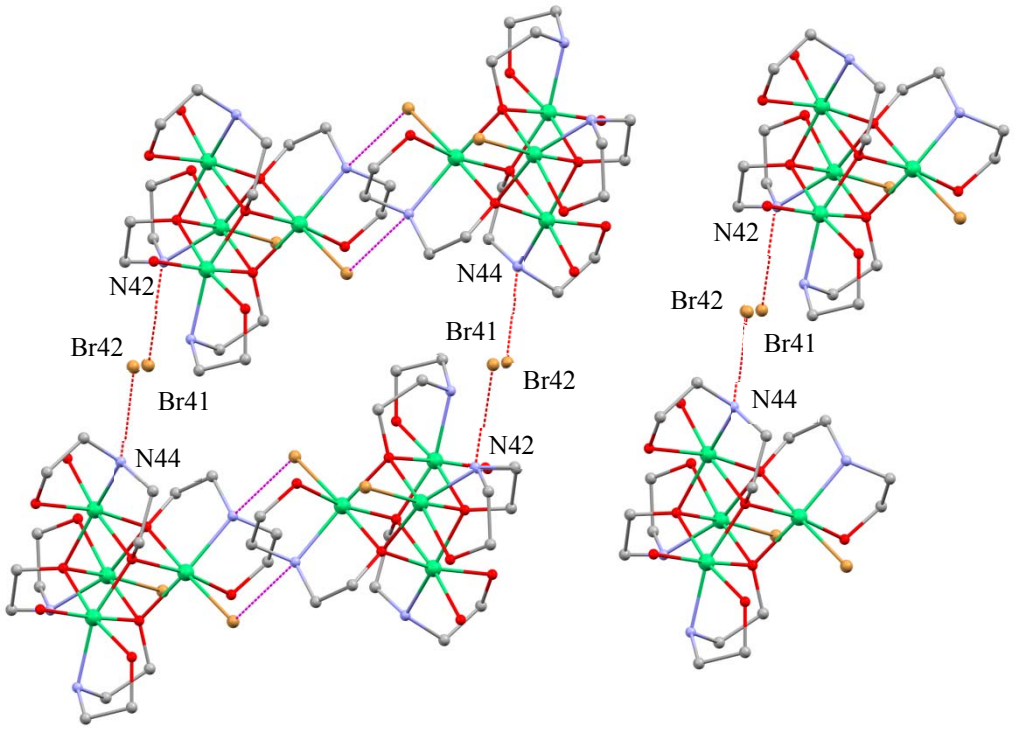

Figure 3-33: Direct complementary hydrogen bonds (pink) between neighbouring clusters (also see figure 3-31) and indirect hydrogen bonds (red) through lattice anions Br41/Br42 (one bromide anion disordered over two sites in a known ratio). H atoms are omitted for clarity. Atom colours are as previously defined.

3.2.6 Reaction products from using *N*-substituted diethanolamine ligands

N-substituted diethanolamine ligands were used in the same way as for the nickel chloride reactions in order to disrupt the N-H · · ·Br interaction that exists between clusters in the acetonitrile solvate. This modification should promote better SMM character by minimising undesirable antiferromagnetic intermolecular exchange.[193-195] The same ligands used previously for the syntheses starting from $NiCl_2{\cdot}6H_2O$ were used again: PhdeaH, tbdeaH and teaH. Crystals were not obtained from these reactions despite the use of a wide range of solvent systems designed to promote crystallisation. FAB^+ mass spectrometry was used again to indicate if any polynuclear species were present in the reaction filtrates. The spectra obtained for PhdeaH and tbdeaH reactions were dominated by strong, low *m*/*z* peaks. However, the spectrum obtained from the teaH reaction gave several higher *m*/*z* peaks. A peak at *m*/*z* = 753.9 was assigned as $[Ni_4Br(NC_6H_{13}O_3)_3]^+$ (see figure 3-34, present in both tris and non-tris filtrates) and a peak at *m*/*z* = 605.2 was assigned as $[Ni_4Br(NC_6H_{12}O_3)_2]^+$ (see figure 3-35, present only in non-tris filtrate). Isotopic distributions for both peaks showed good agreement with calculated patterns.

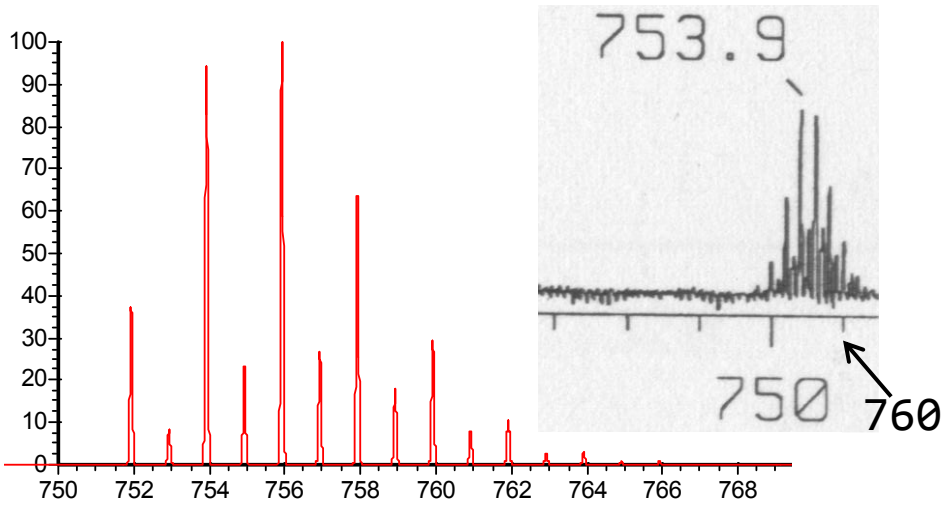

Figure 3-34: Simulated isotopic distribution for $[Ni_4Br(NC_6H_{13}O_3)_3]^+$ with (inset) experimentally measured peak (tris reaction). The full mass spectrum is given in appendix E.

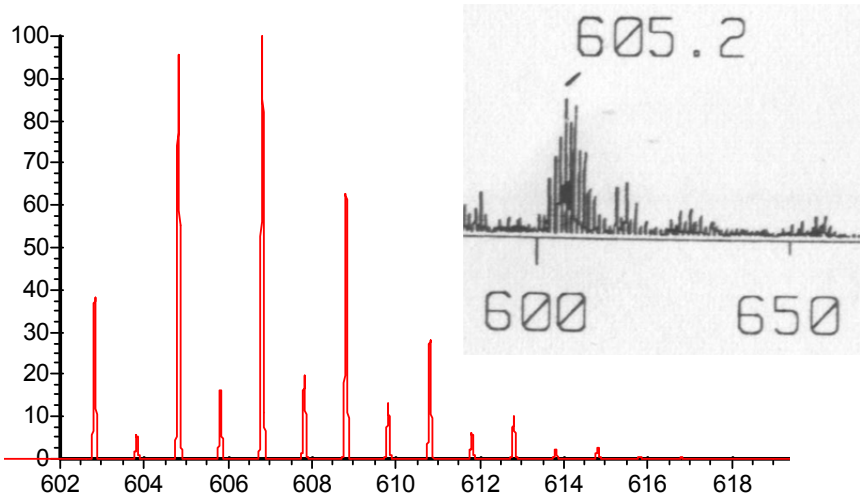

Figure 3-35: Simulated isotopic distribution for $[Ni_4Br(NC_6H_{12}O_3)_2]^+$ with (inset) experimentally measured peak (non-tris reaction). The full mass spectrum is given in appendix E.

No peaks are observed that correspond to the complete $\{Ni_4\}$ cubane structure for any of the reaction products. However this could be due to fragmentation that occurs during the analysis. The peaks that were observed for the teaH reactions correlate well with particular fragments on the cubane. At the very least, the large *m*/*z* values recorded suggest that a complex of considerable molecular weight is formed during the reactions. Even if this was found not to be the expected cubane product, it could still be of considerable interest if found to be a different polynuclear cluster. It is worth noting that no peaks are observed corresponding to fragments greater than the whole cubane, assuming *m*/*z* where *z*=1.

3.3 $\{Ni_{10}\}$ pyramids

A family of clusters based on a central $\{Ni_{10}\}$ unit was also studied with the aim of probing their low-temperature structures. The inorganic core of these structures is a highly regular $\{Ni^{II}_{10}\}$ supertetrahedron centred on a μ_6-oxide (figure 3-36). There are 4 Ni^{II} vertices and the other Ni^{II} ions each bisect an edge. The triangular $\{Ni_6\}$ faces are each held together by a fully deprotonated μ_6-tris-alkoxide ligand (figure 3-37). The remaining coordination sites of each of the vertex Ni^{II} ions are filled by a chelating diketonate ligand and either a terminal bonded solvent or a carboxylate that bridges along an edge. The remaining sites on the edge Ni^{II} ions are occupied by solvent or diketonate.

The first species to be discovered, $[Ni_{10}(O)(thme)_4(dbm)_4(PhCO_2)_2(EtOH)_6]$ (**15**) (H_3thme = 1,1,1-trishydroxymethylethane, Hdbm = dibenzoylmethane, HO_2CPh = benzoic acid), was found to exhibit magnetic characteristics inconsistent with simple SMM behaviour.[84, 196] Only a very small frequency-dependence was observed in out-of-phase ac magnetic susceptibility despite the observation of slow magnetic relaxation at temperatures up to 20 K. The system does not have the anisotropy barrier normally associated with such behaviour. **15** possesses a magnetic spectrum with a dense band-like group of states at low energy, well-separated from all other levels.[196] Its unusual magnetic behaviour is thought to arise from a form of resonant phonon trapping that occurs due to a dense band of low-energy states in its magnetic spectrum.[197]

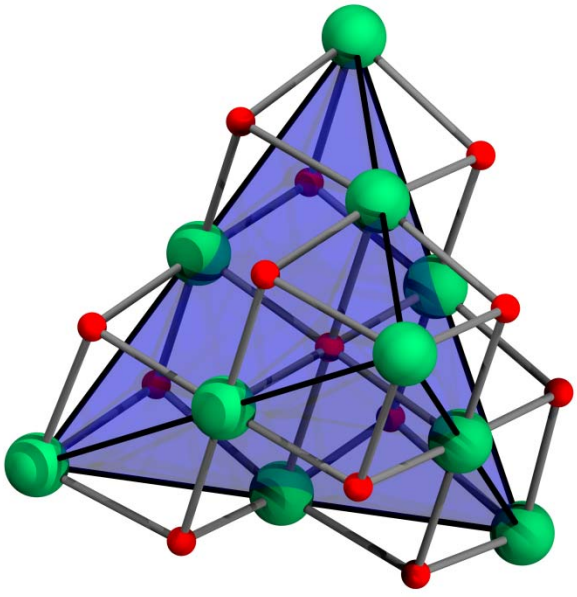

Figure 3-36: The supertetrahedral core of **17** composed of four $\{Ni_6\}$ faces. Structural data is used from the Cambridge Structural Database.[135]

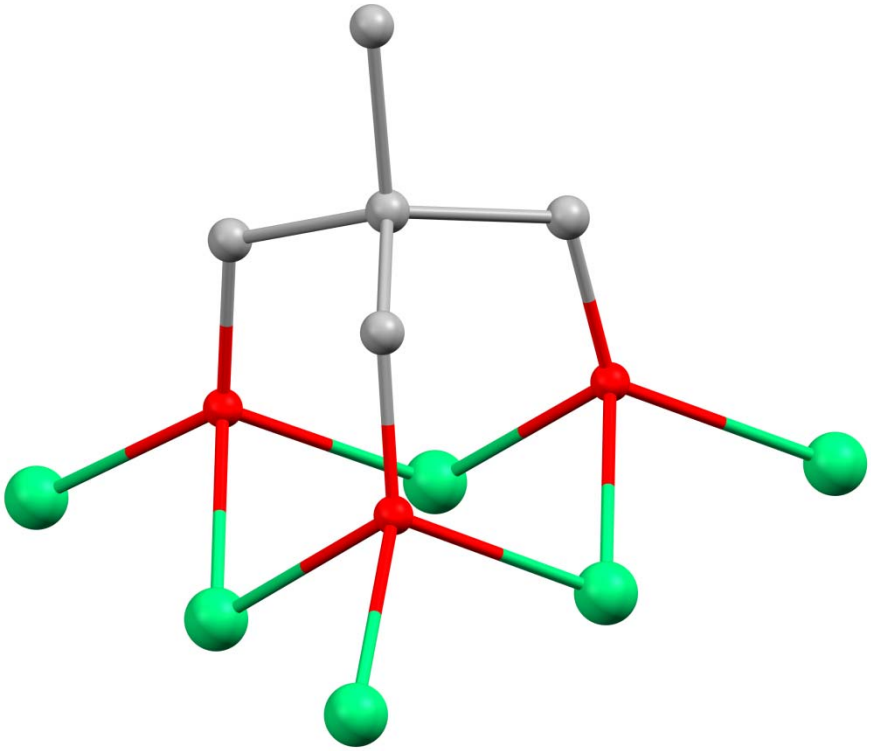

Figure 3-37: The μ_6-binding mode of tris-alkoxide ligand cht^{3-} (H_3cht = *cis*,*cis*-1,3,5-cyclohexanetriol) in **17**. A similar μ_6-mode is observed for $thme^{3-}$ (H_3thme = 1,1,1-trishydroxymethylethane). Structural data is used from the Cambridge Structural Database.[135]

Another member of the family, $[Ni_{10}(O)(thme)_4(dbm)_4(AdCO_2)_2(EtOH)_6]$ ($AdCO_2H$ = 1-adamantane carboxylic acid) (**16**), does not exhibit the same magnetic properties as **15** despite possessing the same inorganic core and arrangement of Ni^{II} centres. Furthermore, various examples of $\{Ni_{10}\}$ species that exhibit each type of behaviour (slow relaxation *vs*. no slow relaxation) have been synthesised, with no apparent relation between the structure and its properties. Analogues of $\{Ni_{10}\}$ exist with H_3thme or H_3cht (*cis*,*cis*-1,3,5-cyclohexanetriol) as the tripodal alcohol, with Hdbm (dibenzoylmethane) or Hdpm (dipivaloylmethane) as the diketone and a range of carboxylic acids including $AdCO_2H$, $PhCO_2H$ or AcOH (acetic acid).

Intermolecular exchange has previously been excluded as a possible cause for the difference in behaviour based on crystal structures measured at 100 K: intermolecular close contacts do not vary significantly between those species that do and those that do not exhibit the behaviour. Each cluster is extremely well isolated from its neighbours by organic ligands. The space group and crystal packing of different members of the family varies significantly; molecular symmetry can introduce certain selection rules for QTM behaviour in SMMs at low temperature. However the behaviour observed in $\{Ni_{10}\}$ species

is not thought to be caused by the same effects as in SMMs. Since the magnetic behaviour is only observed at low temperature, certainly below the temperature at which previous structural data was collected, we planned an ultra-low temperature neutron study on two examples of $\{Ni_{10}\}$ species in order to determine if there is a structural transition that could be responsible for the differences in behaviour. The utility of a neutron experiment in this instance is that it provides the opportunity to reach ultra-low temperatures that cannot normally be achieved on X-ray diffractometers (excluding the new XIPHOS diffractometer).[48] The non-magnetic example to be studied was **16** described above, while the magnetic example was a different species, $[Ni_{10}(O)(cht)_4(dpm)_4(O_2CMe)_2(H_2O)_2]$ (**17**).

3.3.1 Synthesis of $\{Ni_{10}\}$ compounds

Various modifications, including altering reagent concentration, solvent volume, hold temperature and cooling rate, were made to the original solvothermal procedures[84, 198] in order to optimise growth of large single crystals as required for neutron diffraction. The procedures reported below yielded the best crystals in terms of size and quality. The only notable difference between our procedures and those published is the change in cooling rate for **17** from 3 °C per hour to 0.6 °C per hour.

3.3.1.1 Ligands used in the synthesis of $\{Ni_{10}\}$ compounds

Various ligands were used in the synthesis of $\{Ni_{10}\}$ compounds. These are shown in figure 3-38.

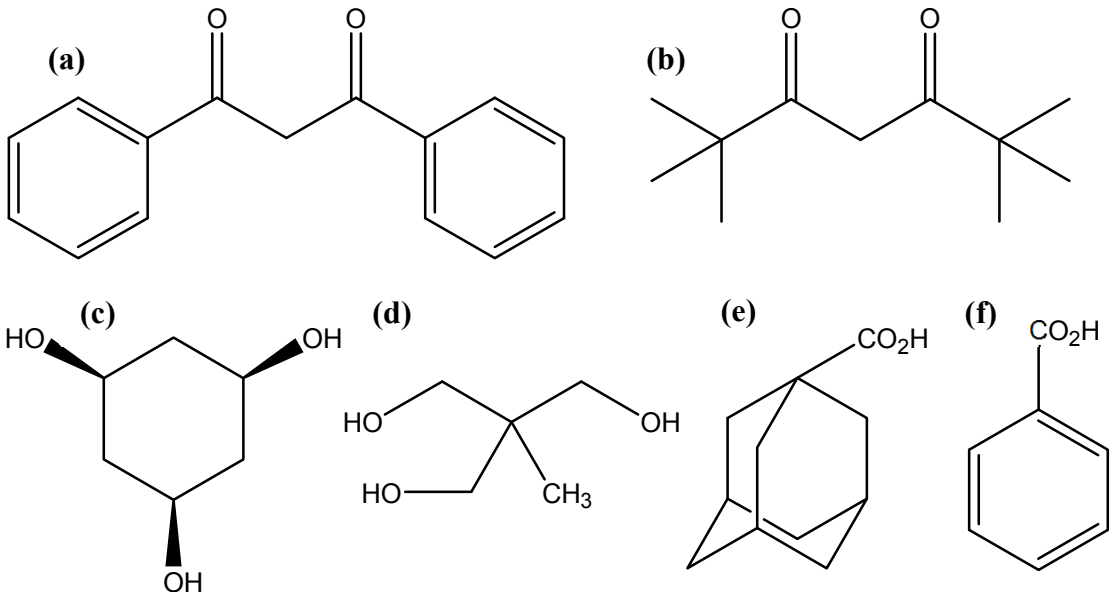

Figure 3-38 Ligands used in the synthesis of $\{Ni_{10}\}$ compounds: (a) dibenzoylmethane (Hdbm), (b) dipivaloylmethane (Hdpm), (c) *cis*,*cis*-1,3,5-cyclohexanetriol (H_3cht), (d) 1,1,1-trishydroxymethylethane (H_3thme), (e) 1-adamantane carboxylic acid ($AdCO_2H$) and (f) benzoic acid ($PhCO_2H$).

3.3.1.2 Synthesis of $Ni(dpm)_2 \cdot 0.7H_2O$

Synthesis of this precursor was carried out following the published method.[199] $Ni(NO_3)_2 \cdot 6H_2O$ (5.81 g, 20.0 mmol) was dissolved in a 50% ethanol/water mixture (50 mL). To this solution was added a solution of Hdpm (7.37 g, 40.0 mmol) dissolved in a 95% ethanol/water mixture (20 mL). Subsequent slow addition of sodium hydroxide (1.60 g, 40.0 mmol) in a 50% ethanol/water mixture (50 mL) with stirring caused a green precipitate to form during 10 minutes. After drying lightly on a sinter, the powder was dried in an oven overnight at 110 °C producing a dry purple powder of $Ni(dpm)_2 \cdot 0.7H_2O$ (7.82 g, 17.9 mmol, 89.5%). Analysis, calc. (found) for $C_{22}H_{39.4}NiO_{4.7}$ ($Ni(dpm)_2 \cdot 0.7H_2O$): C, 60.35 (60.28); H, 9.07 (8.89).

3.3.1.3 Synthesis of $Ni(dbm)_2 \cdot 0.4H_2O$

Synthesis of this precursor was carried out following the published method.[200] $Ni(O_2CMe)_2 \cdot 4H_2O$ (2.49 g, 10.0 mmol) was dissolved in a 90% ethanol/water mixture (150 mL) and heated to 60 °C. A solution of Hdbm (4.49 g, 20.0 mmol) in a 90% ethanol/water mixture (150 mL) was added to the first solution and the reaction mixture was then stirred while cooling for one hour. The resulting light green precipitate was dried lightly on a sinter, followed by drying in an oven overnight at 110 °C to produce a dry

yellow powder of $Ni(dbm)_2 \cdot 0.4H_2O$ (4.36 g, 8.5 mmol, 85%). Analysis, calc. (found) for $C_{30}H_{22.8}NiO_{4.4}$ ($Ni(dbm)_2 \cdot 0.4H_2O$): C, 70.32 (70.28); H, 4.48 (4.36).

3.3.1.4 Synthesis of $[Ni_{10}(O)(cht)_4(dpm)_4(O_2CMe)_2(H_2O)_2]$ (17)

$Ni(dpm)_2 \cdot 0.7H_2O$ (0.25 g, 0.57 mmol), H_3cht (0.036 g, 0.22 mmol), $Ni(OAc)_2.4H_2O$ (0.013 g, 0.05 mmol) and MeCN (9 mL) were sealed inside a 23 mL Teflon liner in an autoclave. The reaction mixture was heated from ambient temperature to 150 °C at 2 °C per minute. The temperature was maintained at 150 °C for 12 hours before cooling to 20 °C at 0.6 °C per hour. Crystals of **17** formed directly from the solvothermal reaction. The identity of the crystals was confirmed by single crystal X-ray diffraction.

3.3.1.5 Synthesis of $[Ni_{10}(O)(thme)_4(dbm)_4(AdCO_2)_2(EtOH)_6]$ (16)

$Ni(dbm)_2.0.4H_2O$ (0.25 g, 0.49 mmol), H_3thme (0.056 g, 0.46 mmol), $AdCO_2H$ (0.083 g, 0.46 mmol) and EtOH (9 mL) were sealed inside a 23 mL Teflon liner in an autoclave. The reaction mixture was heated from ambient temperature to 150 °C at 2 °C per minute. The temperature was maintained at 150 °C for 12 hours before cooling to 20 °C at 3 °C per hour. Large crystals of **16** formed directly from the solvothermal reaction. The identity of the product was confirmed by single-crystal X-ray diffraction.

3.3.2 Experiments on $\{Ni_{10}\}$ compounds

For molecular crystals with large unit cell volume and small crystal volume it is appropriate to use neutron Laue diffraction to accurately determine the crystal structure. Since the single-crystal neutron diffractometer VIVALDI at ILL was shut down at the time we wished to carry out measurements on **16** and **17** we applied for, and were subsequently granted, time to use the KOALA diffractometer at ANSTO, Sydney. This diffractometer works on the same principles as VIVALDI but has greater flux at the sample position. The minimum achievable temperature is slightly higher than on VIVALDI, but this is not a problem for the samples in question since the onset of slow magnetic relaxation occurs at temperatures of up to 20 K. The aim of the experiment was therefore to determine the ultra-low temperature crystal structures of **16** and **17** in order to determine if there are any

unusual structural changes in one or the other that could contribute to the observed difference in magnetic properties.

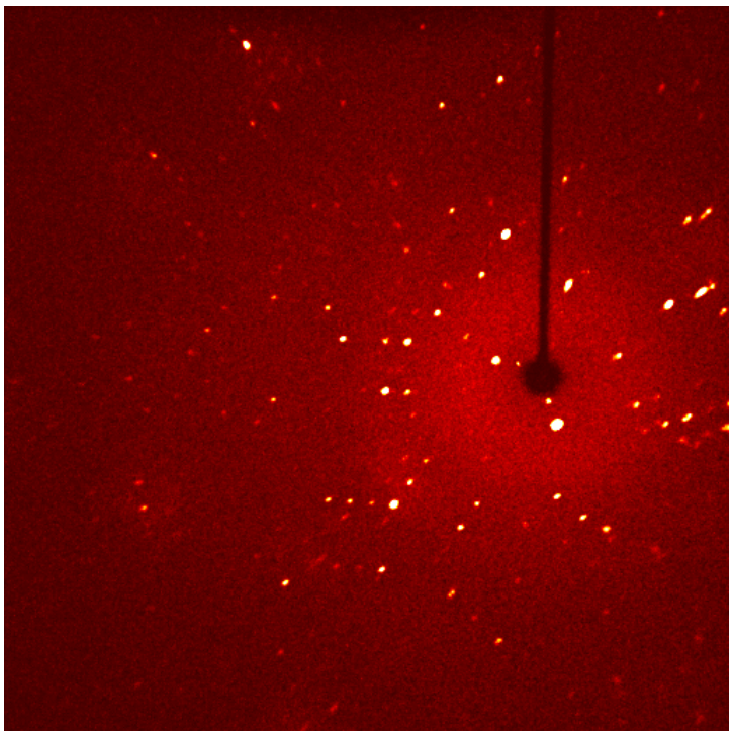

Figure 3-39: Sample X-ray diffraction image from **16**.

From the single-crystal X-ray diffraction patterns for **16** and **17** it appeared that the crystals were of sufficiently good quality for neutron diffraction. A typical X-ray diffraction image from **16** is shown in figure 3-39. Unfortunately the crystals degraded a little in transit and, as Laue diffraction is somewhat sensitive to crystal quality, we were not able to extract usable data from the Laue patterns obtained.

A future experiment is planned to measure the structure of **16** and **17** at 2 K using the XIPHOS X-ray diffractometer at Durham University. This system uses a Displex to cool to 2 K under vacuum. We are unsure whether problems will be encountered with exposing these crystals to vacuum. Another possibility is to further optimise the growth of high quality single-crystals and carefully consider how they are to be transported to the experiment in order to minimise degradation.

3.4 Conclusions

The synthesis of **9** previously reported[145] was repeated in order to grow large single crystals suitable for neutron diffraction. We also obtained crystals of the same material from the second method described in the original publication (without tris), which originally yielded only a microcrystalline powder.

We determined that the ultra-low temperature (1.7 K) structure of **9** is broadly similar to the 100 K structure. Alongside the other studies described in this work, this is one of the first ultra-low temperature crystal structure determinations of an SMM. We expanded upon the nature of the disordered solvent present in the structure of **9** and were able to identify three part-occupied acetonitrile molecules and one part-occupied water molecule in the interstitial voids. Each cluster is neighboured by four others in a distorted tetrahedral-like arrangement. The analogous bromide form of **9** was synthesised, **12**, and found to pack in a similar manner, albeit with small differences in the solvent of crystallisation. It has not been possible to synthesise a sufficient amount of **12** to measure its magnetic measurements.

Methanol solvates of both structures **9** and **12** were synthesised (**10** and **13** respectively). These crystallise in a lower symmetry space group with very different packing of clusters. Each cluster is hydrogen-bonded to two others forming one-dimensional hydrogen-bonded chains. Solvent of crystallisation that fills the voids between chains acts as a bridge to hydrogen bond adjacent chains together. A study of the low temperature magnetic properties and relaxation characteristics of **13** was carried out using a SQUID magnetometer. Initial analysis shows that **13** exhibits a similar low-temperature (sub-3 K) slow relaxation process to that observed in **9**. Additionally there is a higher temperature slow relaxation process in **13** with a frequency-dependent maximum in the out-of-phase ac magnetic susceptibility at 4-6 K. This relaxation process has a higher energy barrier and a much smaller pre-exponential term, $\tau_{0,}$ than is typically associated with single-molecule magnets; these characteristics are closer to those usually seen for single-chain magnets, or even spin glasses. Further investigations will focus on probing the properties of **13** further in order to gain insight into the process or processes responsible for the higher temperature peak in the frequency-dependent ac magnetic susceptibility data. It will also prove useful to collect magnetic data on **10**, the chloride analogue of **13**, and also on **12**, the bromide

analogue of **9**. This should enable us to make a proper comparison between species and directly observe the effect of changing the halide upon the magnetic properties.

A similar new structure $[Ni_4(dea)_4Br_2(H_2O)_2]Br_2$ (**14**) was synthesised solvothermally as part of efforts to synthesise more crystals of **12**. This is again based on a central $\{Ni_4O_4\}$ core with diethanolamine ligands but two of the bromide ligands are replaced with water leaving a positively-charged complex. The clusters hydrogen-bond directly to form dimeric units that are further linked by indirect hydrogen-bonds through bromide anions that fill the interstitial voids. Unfortunately the sample was not pure and more work is required to synthesise a sample suitable for magnetic study.

Attempting to form cubanes with *N*-substituted diethanolamine ligands was partially successful. Mass spectrometry of the reaction filtrates indicated that some polynuclear species may be present in solution but it did not prove possible to crystallise any species. In particular, mass spectrometry was consistent with fragments of a $[Ni_4Cl_4(Phdea)_4]$ cubane and a $[Ni_4Br_4(tea)_4]$ cubane formed from the relevant reactions. This is the first evidence for $\{M_4O_4\}^{4+}$ cubane formation using the substituted diethanolamine ligands *N*-phenyldiethanolamine (PhdeaH) and triethanolamine (teaH). Mass spectrometry was not carried out on the precipitates from any reactions since they were not soluble in any of a wide range of solvents.

No changes occurred in the structure of **9** at ultra-low temperature that might account for the fine structure observed in the HF-EPR spectra, *e.g.* significantly enhanced intermolecular interactions. These features are not consistent with isolated molecules, indicating that some short-range correlations are beginning to occur, likely through the already-known hydrogen-bonding pathways N–H---Cl.

We attempted to investigate two species based on a $\{Ni^{II}_{10}\}$ supertetrahedron: **16** and **17**. Some members of this family exhibit interesting magnetic characteristics that are inconsistent with simple SMM behaviour; namely, slow magnetic relaxation up to 20 K but with only a very small frequency-dependence in the ac magnetic susceptibility data.[84, 196, 197] **17** exhibits such behaviour while **16** does not. We wished to measure the ultra-low temperature crystal structures of both species in order to determine if there is a structural change occurring in either of the complexes that could be responsible for their unusual behaviour. Unfortunately the neutron Laue diffraction experiments were not successful

since the crystals degraded in transit. It is hoped that the complexes can be measured at 2 K using the XIPHOS diffractometer at the University of Durham.[48]

Chapter 4 A cobalt (II)-based SMM

Ultra-low temperature investigations of structural and magnetic properties pertaining to a $\{Co_4\}$ cubane SMM

4.1 Background to Co^{II} SMMs

Although SMMs based on Mn^{III} ions are by far the most ubiquitous type, many examples have been reported that contain Co^{II} ions. Whereas most SMMs are described as being in the strong exchange limit, polynuclear clusters based on Co^{II} are in the weak exchange limit and consequently the magnetic anisotropy can be of the same order of magnitude or larger than the exchange coupling.[201] Co^{II} SMMs can have a large Ising-type anisotropy; however, strong spin-orbit coupling means that there is a large orbital contribution to the magnetic moment and a description of the system in terms of S and D is not valid.[86, 201] S is not a good quantum number for Co^{II} SMMs and so an effective spin S' is often used instead. Examples of SMMs incorporating Co^{II} include $\{Co_4\}$ cubanes,[202-205] $\{Co_4\}$ squares,[206] $\{Co_5\}$ square pyramids,[180] $\{Co_7\}$ discs[207-209] and $\{Co_{12}\}$[210] systems as well as $\{Co^{II}Ln^{III}\}$ systems.[211, 212] Quantum tunnelling of the magnetisation (QTM) has been shown to short-cut the energy barrier; in fact QTM is often more efficient for Co^{II}-based SMMs than for SMMs based on other metal ions.[201]

The first reported Co^{II}-based SMM was a $\{Co_4\}$ cubane, $[Co_4(hmp)_4(MeOH)_4Cl_4]$ (hmpH = 2-hydroxymethylpyridine).[202] Magnetic susceptibility data are consistent with four ferromagnetically-coupled effective $S' = ½$ spins. Hysteresis is observed below 1.2 K. We chose to study another high-symmetry $\{Co_4\}$ cubane, described below.

4.2 Co_4-citrate

The SMM $(C(NH_2)_3)_8[Co_4(cit)_4]\cdot 4H_2O$ (hereafter **18** or Co_4-citrate; H_4cit = citric acid = $(HO_2CCH_2)_2C(OH)CO_2H$, structure shown in figure 4-1) was first synthesised by Hudson *et al*. in 2006 and was initially reported to have a non-magnetic ground state.[213] Subsequent work carried out by Galloway *et al*. showed characteristic SMM behaviour including frequency-dependent out-of-phase ac magnetic susceptibility and low temperature hysteresis.[203] The data are consistent with a magnetic ground state and low-lying excited states. Unfortunately the large orbital contribution of Co^{II} makes a quantitative analysis of the dc magnetic susceptibility data difficult since temperature affects the population of different states. In order to address this problem it was proposed to investigate the energy level structure of the complex at low temperature using inelastic neutron scattering (INS). In addition to these measurements, powder and single-crystal neutron diffraction and

single-crystal X-ray diffraction were used to investigate the ultra-low temperature structure of **18** in order to observe any structural changes that might occur.

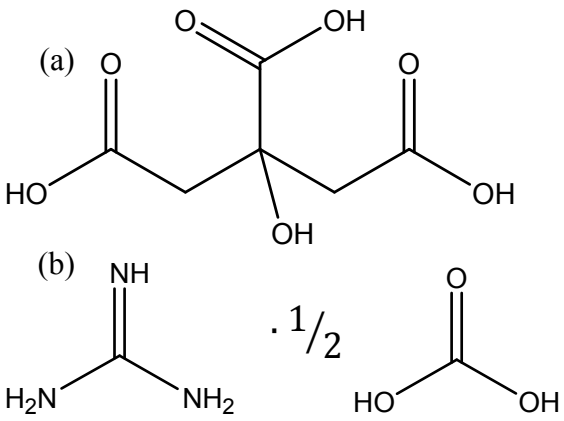

Figure 4-1: Structures of (a) citric acid, and (b) guanidine carbonate used to form **18**.

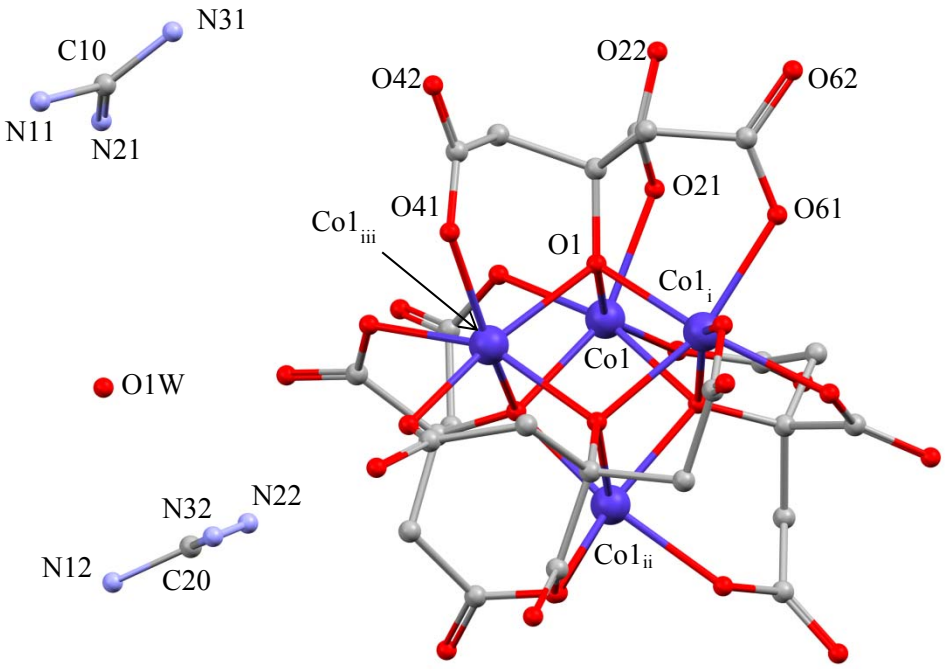

Figure 4-2: A single {Co_4} cluster with the two unique guanidinium cations and single unique solvent water (Co, dark blue; N, light blue; O, red; C, grey). H atoms are omitted for clarity.

The structure consists of a distorted cubane of Co^{II} and O centres (figure 4-2). The four μ_3-O donors are derived from the alkoxide group of each citrate ligand. The three acid moieties of each ligand are also deprotonated and bind to just one metal centre each (figure 4-3). Each cluster is associated with 8 guanidinium cations (2 unique) and 4 waters of crystallisation (1 unique) which fill the interstitial voids between clusters; the negatively-charged cluster acts as a hydrogen bond acceptor to a total of 20 guanidinium cations and 8

solvent water molecules (figure 4-4). This creates an extensive hydrogen-bonded network throughout the structure, with each cubane making around 40 hydrogen bonds in total.

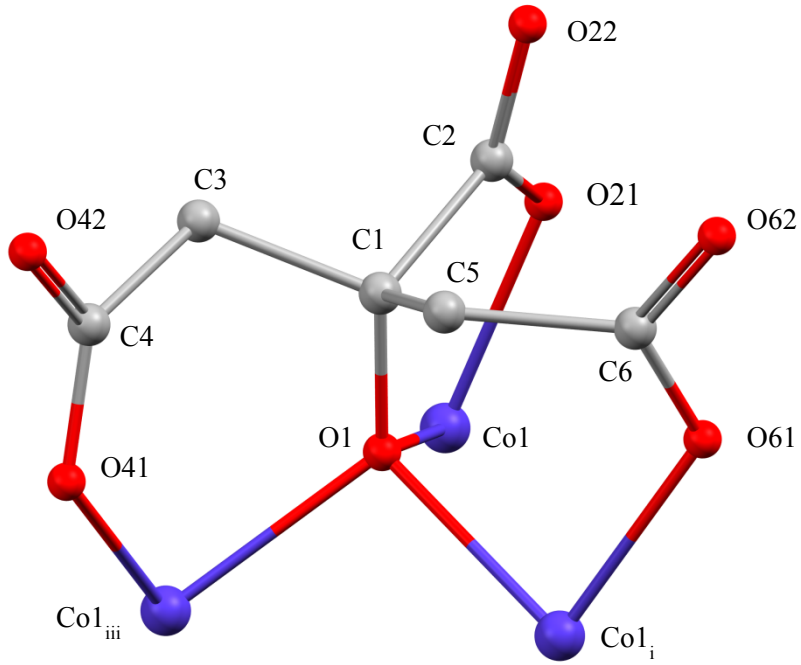

Figure 4-3: Binding motif exhibited by citrate^{4-} ligand in **18**; the alkoxide group bridges three Co^{II} centres and each carboxylate group binds to one of these ions. Atom colours as previously defined; H atoms omitted for clarity.

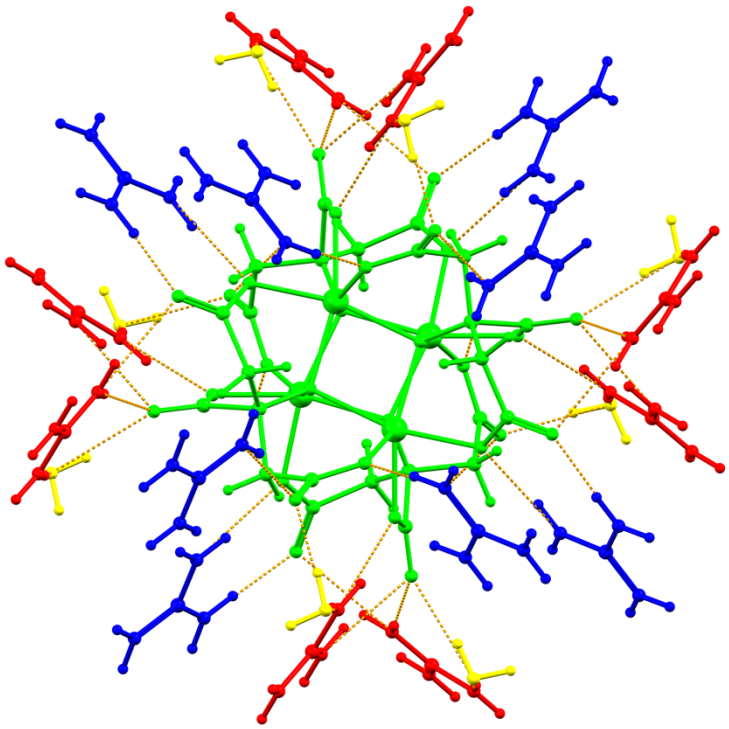

Figure 4-4: Hydrogen bonding (gold) around a single cluster (shown in green). Donation is from solvent water molecules (yellow) and two sets of crystallographically inequivalent guanidinium cations (red and blue). H atoms are omitted for clarity.

4.2.1 Synthesis of $(C(NH_2)_3)_8[Co_4(cit)_4]\cdot 4H_2O$ (18)

Synthesis was carried out based on the published procedure by Galloway *et al*.[203]

To a solution of citric acid monohydrate (0.55 g, 2.9 mmol) in water (50 mL) was added a solution of $Co(NO_3)_2\cdot 6H_2O$ (0.76 g, 2.6 mmol) in water (50 mL) followed by a solution of guanidine carbonate $[NH_2C(=NH)NH_2\cdot 0.5H_2CO_3]$ (1.87 g, 20.8 mmol) in water (50 mL) without stirring. The solution was left to stand overnight, producing purple crystals of $(C(NH_2)_3)_8[Co_4(cit)_4]\cdot 4H_2O$ (0.81 g, 0.53 mmol, 81% based on available Co) Selected IR data for an air dried crystal of **18**: ν (cm^{-1}) = 3338m, 3148m, 1657s, 1538s, 1379s, 1233m, 1082w, 923m, 847m, 652m. Air-dried crystals analyse as $C_{32}N_{24}H_{72}Co_4O_{32}$ ($(C(NH_2)_3)_8[Co_4(cit)_4]\cdot 4H_2O$), analysis (%) calc. (found): C, 24.94 (24.81); H, 4.71 (4.71); N, 21.82 (21.62). Crystal growth was optimised by using clean, unscratched 250 mL glass beakers; tests on a range of crystallisation vessels showed that these were most conducive to growth of large, high-quality single crystals.

4.2.2 Synthesis of a deuterated analogue of 18 (19)

In order to produce a sample suitable for INS and neutron powder diffraction it was necessary to use deuterated materials. This is due to the large incoherent scattering cross-section of hydrogen to neutrons. This was achieved by H-D exchange of commercially-available starting materials: guanidine carbonate (structure shown in figure 4-1) and citric acid-d_4 (wherein the two CH_2 groups are replaced by CD_2). A quantity of guanidine carbonate was fully dissolved in D_2O then the solvent was removed under vacuum at an elevated temperature. The transformation from $[C(NH_2)_3^+]_2[CO_2^{2-}]$ to $[C(ND_2)_3^+]_2[CO_2^{2-}]$ was tracked using IR spectroscopy. The characteristic broad absorption for N-H stretching modes observed at approximately 2700 – 3400 cm^{-1} was completely removed and replaced by a similarly broad absorption band at approximately 2000 – 2600 cm^{-1}; this is consistent with the replacement of hydrogen with deuterium, as the heavier mass of deuterium will shift the absorption to lower wavenumber compared with hydrogen.[71] Although the transformation appeared to be complete after just a single treatment, this procedure was repeated three times to ensure that all material was converted to the deuterated form (figure 4-5 shows the IR spectra of both the starting material and the fully deuterated material). Citric acid-d_4 is commercially available; however the acid and alcohol groups still contain hydrogen atoms rather than deuterium. Therefore, it was necessary to carry out a similar

procedure to that described above in order to prepare the fully deuterated analogue of citric acid. As citric acid-d_4 is expensive, initial tests were performed using fully hydrogenous citric acid in order to determine that the -OH and -CO_2H groups would be fully replaced by -OD and -CO_2D. The transformation was again tracked using IR spectroscopy. The characteristic broad absorption for O-H stretching modes observed at approximately 2700 – 3400 cm^{-1} was removed and replaced by a similarly broad absorption band at 1900 – 2600 cm^{-1}; this is consistent with replacement of hydrogen by deuterium. Having confirmed that the transformation was successful, the procedure was repeated using the citric acid-d_4 that would subsequently be used in the reaction to synthesise **19** (IR spectra are shown in figure 4-6 for comparison). $Co(NO_3)_2{\cdot}6H_2O$ was used without any special treatment as the H_2O of crystallisation will fully exchange with the very large excess of D_2O upon dissolution.

To a solution of citric acid-d_8 (synthesised by the procedure described above from commercially available citric acid-d_4) (0.39 g, 1.9 mmol) in D_2O (25 mL) was added a solution of $Co(NO_3)_2{\cdot}6H_2O$ (0.55 g, 1.9 mmol) in D_2O (25 mL) followed by a solution of deuterated guanidine carbonate ($[ND_2C(=ND)ND_2{\cdot}0.5D_2CO_3]$, synthesised as described above) (0.94 g, 10.4 mmol) in D_2O (25 mL) without stirring. The solution was left to stand overnight, producing purple microcrystals of $(C(ND_xH_{2-x})_3)_8[Co_4(d_4\text{-cit})_4]{\cdot}yD_2O{\cdot}(4\text{-}y)H_2O$ (**19**) (0.458 g, ~0.28 mmol, 59% based on available Co). The infra-red spectrum of a small portion of the solid product was measured in order to confirm that the material was deuterated (figure 4-7). Most of the broad absorption at 3000-3500 cm^{-1} was again shifted to approximately 2400 cm^{-1}. However this time there is a small residual absorption peak at approximately 3300 cm^{-1}, thought to be caused by some water of crystallisation in the sample. Measurements subsequently performed on this sample (neutron diffraction and inelastic neutron scattering) also indicated the presence of some non-deuterated species in the sample. This will be discussed in more detail later. It is not possible to recrystallise samples of this material since it is insoluble in all common solvents; thus, it was not possible to exchange water in **19** with D_2O.

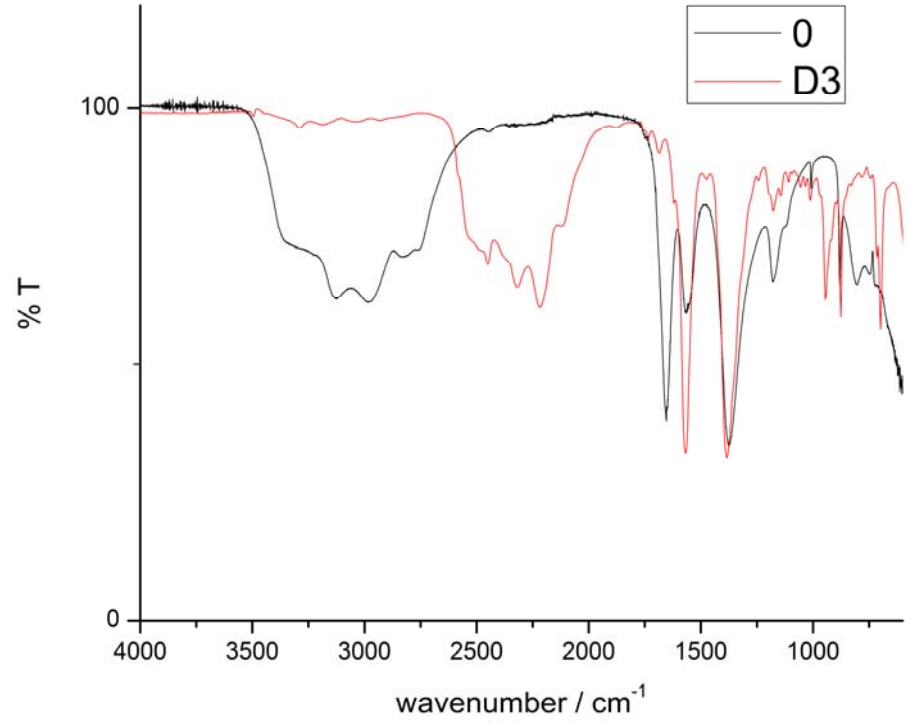

Figure 4-5: The infrared spectrum of guanidine carbonate before (black, 0) and after (red, D3) deuteration.

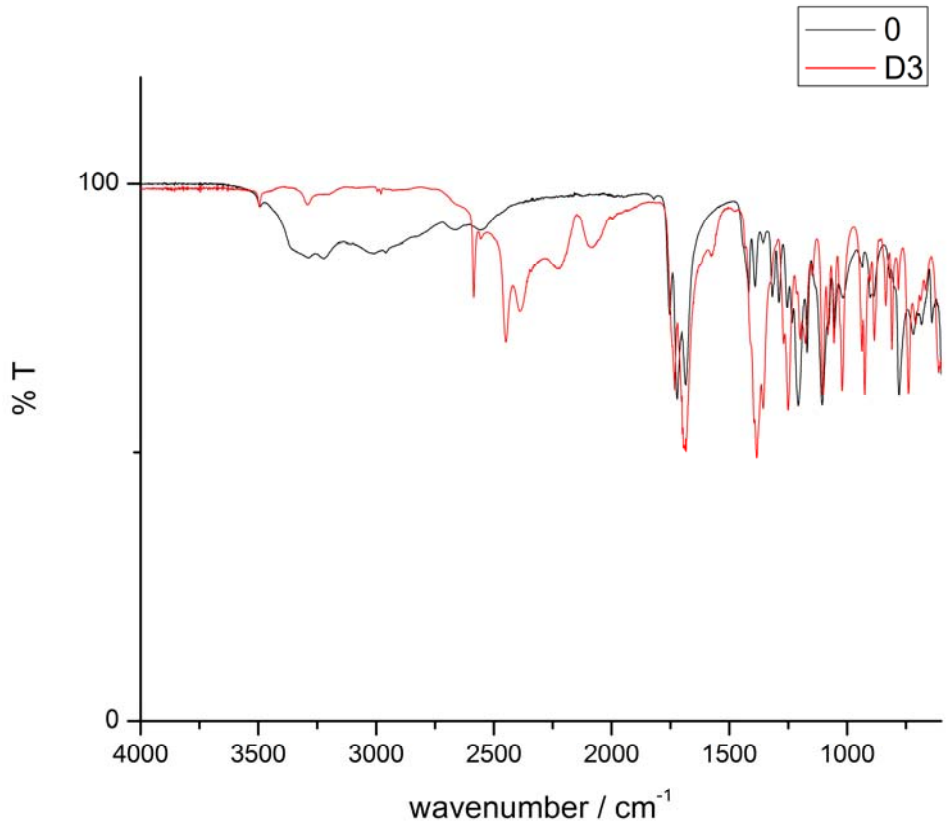

Figure 4-6: The infrared spectrum of citric acid-d_4 before (black, 0) and after (red, D3) deuteration.

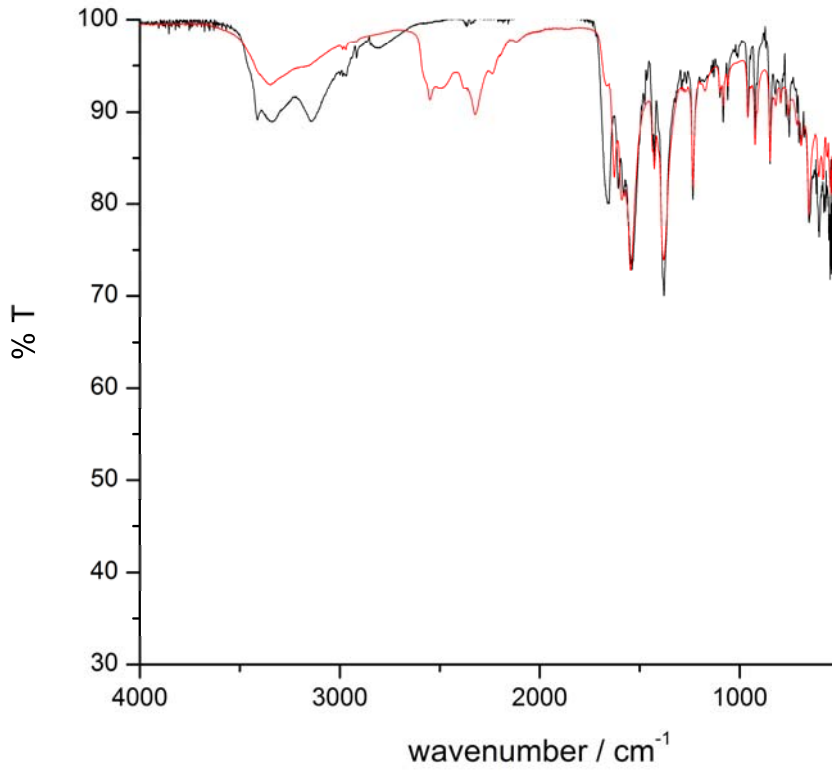

Figure 4-7: The infrared spectrum of **18** (black, before deuteration) and **19** (red, after deuteration).

The two structures, **18** and **19**, described herein are identical except for the substitution of deuterium for hydrogen in the second complex. They crystallise in the same space group and exhibit the same crystal packing arrangement. Visually the crystals are rather similar, though the average size of the deuterated crystals is smaller.

4.2.3 Structural studies of Co_4-citrate

4.2.3.1 Single-crystal X-ray diffraction at 2 K

Ultra-low temperature (2 K) structural data were collected for **18** using both X-ray and neutron radiation. The X-ray crystal structure was determined using the XIPHOS single-crystal X-ray diffractometer (Mo K_α radiation, λ = 0.71073 Å) at Durham University. A crystal of **18**, of approximate dimensions 0.10 x 0.20 x 0.35 mm, was mounted on a graphite rod perpendicular to the incident beam and cooled to 2 K. Data were integrated using SAINT[106] and empirical absorption corrections using equivalent reflections were performed with the program SADABS.[107] It was not necessary to apply a masking routine[214] to filter out reflections potentially affected by powder diffraction from the two cylindrical beryllium shrouds, since diffraction from the crystal was particularly strong.

The structure was solved using SHELXS[115] and refined using least squares minimisation implemented within the Crystals software package.[114] All non-hydrogen atoms were modelled with ADPs. Hydrogen atoms were placed in calculated positions, except for those attached to the guanidinium cations and water of crystallisation. These were found in a Fourier difference map. All hydrogen atoms were allowed to ride on their parent atoms. Full crystallographic data are given in table 4.1.

4.2.3.2 Single-crystal X-ray diffraction at 30 K

Single-crystal X-ray data were collected at 30 K using a Bruker APEX II diffractometer equipped with an Oxford Cryosystems HELIX low temperature device. Crystal mounting was straightforward since this sample does not lose solvent quickly outside of its mother liquor. A crystal of **18**, of approximate size 0.15 x 0.15 x 0.15 mm, was mounted on a glass fibre secured to the goniometer. Data were integrated using SAINT[106] and empirical absorption corrections using equivalent reflections were performed with the program SADABS.[107]

The structure was solved using SIR92[215] and refined using SHELXL-97.[115] All non-hydrogen atoms were modelled with ADPs except for the low-occupancy water molecule O2W (see note on this molecule below). Hydrogen atoms on the water molecule O1W were located in a difference map. The geometry of the molecule was then idealised and the whole molecule treated as a freely-rotating rigid group. Other hydrogen atoms were placed in calculated positions and allowed to ride on their parent atoms. Full crystallographic data are given in table 4.1.

A small residual electron density peak (1.39 e $Å^{-3}$) was modelled as a part occupied ($1/8^{th}$) water of crystallisation. The volume of the void that this atom occupies was calculated to be 30 $Å^3$ using PLATON SQUEEZE,[166] large enough to contain a water molecule. This molecule was not observed for either of the ultra-low temperature structures (X-ray or neutron), which were measured using different crystals.

4.2.3.3 Single-crystal Neutron Laue diffraction at 2 K

Single-crystal neutron Laue data were collected using the VIVALDI single-crystal neutron diffractometer at ILL, Grenoble.[53, 108] A single crystal of **18**, of approximate size 0.50 x 0.30 x 0.10 mm, was mounted on a vanadium rod and secured to the sample mount placed perpendicular to the incident beam. 6 Laue patterns were collected for equally-spaced sample orientations, from 0° to 50° around the vertical rotation axis (ϕ). Cell parameters were taken from X-ray data at 2 K and the Laue patterns were indexed using LAUEGEN. Background-corrected integrated intensities were extracted using ARGONNE_BOXES. Normalisation to a common wavelength was performed over the wavelength range 0.9-2.8 Å using LAUENORM. LAUEGEN[109] and LAUENORM[110] are part of the Daresbury Laue Suite, while ARGONNE_BOXES is an in-house two-dimensional adaptation of the three-dimensional minimum σ(I)/I routine.[111] Neutron Laue data were also measured at room temperature for comparison since some unusual splitting was observed in the diffraction spots below 100 K. Nevertheless, it did prove possible to process the data collected at both temperatures successfully and good structure refinements were achieved for each.

The crystal chosen for the neutron experiment was slightly larger than for the X-ray experiment since this gives the best chance of collecting good quality data; however for a neutron Laue experiment it is possible to use a sub-1 mm^3 crystal due to the high flux compared with a monochromatic experiment. The neutron sample was not deuterated; for single-crystal measurements the large incoherent scattering cross section of hydrogen to neutrons does not normally adversely affect the measured data. Indeed, for single-crystal neutron data the negative scattering density for hydrogen can aid precise determination of hydrogen atom positions – and equally where they are not located.

The structure from the ultra-low temperature X-ray experiment was used as a starting point for the neutron refinement, but with all hydrogen atoms removed first. Refinement was performed using SHELXL-97[115] and all hydrogen atoms were located with negative scattering density in the Fourier difference map. All atoms (including hydrogen) were refined with ADPs. Thermal similarity restraints were applied to several sets of hydrogen atoms. Full crystallographic data are given in table 4.1.

4.2.3.4 Neutron Powder Diffraction at 2 K

Neutron data were also collected on a deuterated polycrystalline sample of **19** using the High Resolution Neutron Powder Diffractometer (HRPD) at ISIS, Oxfordshire.[55] As stated previously in the synthetic details for **19**, we are not entirely confident in the level of deuteration achieved. This experiment was performed prior to the single-crystal experiment on VIVALDI since there was some doubt as to whether or not it would be possible to collect a high-quality data set on such a small non-deuterated single-crystal of **18**.

2.4031 g of **19** (microcrystalline) were sealed inside a vanadium can (height, 20 mm; radius 5.5 mm) and cooled to 2 K inside the cryostat on the HRPD beam line. Data were collected over a period of two days. The data measured on all the detector banks were integrated and then corrected for absorption by the sample and by the vanadium can.

A joint 2 K X-ray single-crystal – 2 K neutron powder Rietveld refinement was performed in TOPAS-Academic,[216] using the 2 K X-ray structure described above and the neutron powder data from HRPD. Both guanidinium cations and the water/deuterium oxide were treated as rigid bodies. O1W was modelled as two separate molecules; one hydrogenous and one deuterated. The occupancies of these two components were restrained to sum to unity. Corrective terms were applied to the data in order to account for differences in the thermal parameters in neutron diffraction compared to X-ray diffraction.[131] The key parameters for the neutron refinement are given in table 4.2. The CIF produced from the refinement is included on the enclosed CD.

Table 4.1: Crystallographic data for the various determinations of the structure of **18**. (i) X-ray, 2 K. (ii) X-ray, 30 K. (iii) Neutron, 2 K. (iv) Neutron, RT. Data were collected using a different crystal for each experiment.

	18 (i)	**18 (ii)**	**18 (iii)**	**18 (iv)**
Formula	$C_{32}H_{72}Co_4N_{24}O_{32}$	$C_{32}H_{72.25}Co_4N_{24}O_{32.125}$	$C_{32}H_{72}Co_4N_{24}O_{32}$	$C_{32}H_{72}Co_4N_{24}O_{32}$
M_w	1540.80	1543.11	1540.80	1540.80
Crystal system	Tetragonal	Tetragonal	Tetragonal	Tetragonal
Space group	$P4_2/n$	$P4_2/n$	$P4_2/n$	$P4_2/n$
a [Å]	16.1149(6)	16.0956(10)	16.1149(6)	16.13685(15)
c [Å]	11.5251(4)	11.5050(7)	11.5251(4)	11.5028(2)
V [Å^3]	2992.95(19)	2980.6(3)	2992.95(19)	2995.31(7)
Z	2	2	2	2
T [K]	2.00(5)	30(2)	2.0(1)	295(2)
Radiation	X-ray	X-ray	Neutron	Neutron
λ [Å]	0.71073	0.71073	Laue	Laue
D_c [g cm^{-3}]	1.710	1.719	1.710	1.709
μ [mm^{-1}]	1.200	1.206	1.647	1.645
Meas./indep. refl.	19380/3052	12980/3258	10139/1830	22006/1296
R_{int}	0.031	0.069	0.4349	0.9543
Obs. refl. [$I > 2\sigma(I)$]	2478	2473	1063	691
wR_2 [a]	0.0405	0.1200	0.1369	0.0753
R_1 [b]	0.0365	0.0508	0.0787	0.0535
Goodness of fit on F/F^2	1.0739	1.048	1.312	0.956
$\Delta\rho_{max,min}$ [e Å^{-3}]	1.00/-0.34	0.782/-0.508	1.146/-0.801	0.530/-0.452

[a] $wR_2 = \left\{\sum \frac{[w(F_O^2 - F_C^2)^2]}{\sum[w(F_O^2)^2]}\right\}^{\frac{1}{2}}$ on F^2, $wR_2 = \left\{\sum \frac{[w(F_O - F_C)^2]}{\sum[w(F_O^2)^2]}\right\}^{\frac{1}{2}}$ on F; [b] $R_1 = \frac{\Sigma||F_O| - |F_C||}{\Sigma|F_O|}$

Cell parameters for **18 (iii)** are taken from the 2 K X-ray experiment; those for **18 (iv)** were taken from the previous 100 K structural determination and refined in order to index the unit cell successfully since data were not already available at room temperature. Data for **18 (i)** were refined on F; the other datasets were refined on F^2.

Table 4.2: Rietveld refinement data for **19**.

Formula	$C_{32}D_{65.16}H_{6.84}Co_4N_{24}O_{32}$
Moiety formula	$(C(ND_2)_3)_8[Co_4(d_4\text{-cit})_4]\cdot 3.42H_2O\cdot 0.58D_2O$
M_w	1606.34
Crystal system	Tetragonal
Space group	$P4_2/n$
a [Å]	16.13685(15)
c [Å]	11.50281(20)
Z	2
T [K]	2.0(1)
Radiation	Neutron time of flight
R_{exp}	0.98784 %
R_{wp}	0.97958 %
Goodness of fit	0.99163

4.2.3.5 Analysis of ultra-low temperature X-ray and neutron diffraction data

The structure obtained from the two X-ray measurements (2 K, 30 K) was found to be largely similar to previous determinations at higher temperatures. This structural description is given in full in the introductory section for this compound. A second water molecule O2W was modelled (without hydrogen atoms) in the 30 K structure on the basis of a small residual electron density peak in the Fourier difference map. Its occupancy factor is only $1/8^{th}$ however, and it was not observed in the 2 K structure. Each study was carried out using a different crystal and it is possible that additional water could be observed in some crystals but not in others. A water of crystallisation O1W acts as a hydrogen bond donor to carboxylate groups in the $\{Co_4\}$ clusters and as an acceptor from the guanidinium cations in the lattice (figure 4-8). Hydrogen bonding distances and angles do not show great variation between the datasets collected (table 4.3).

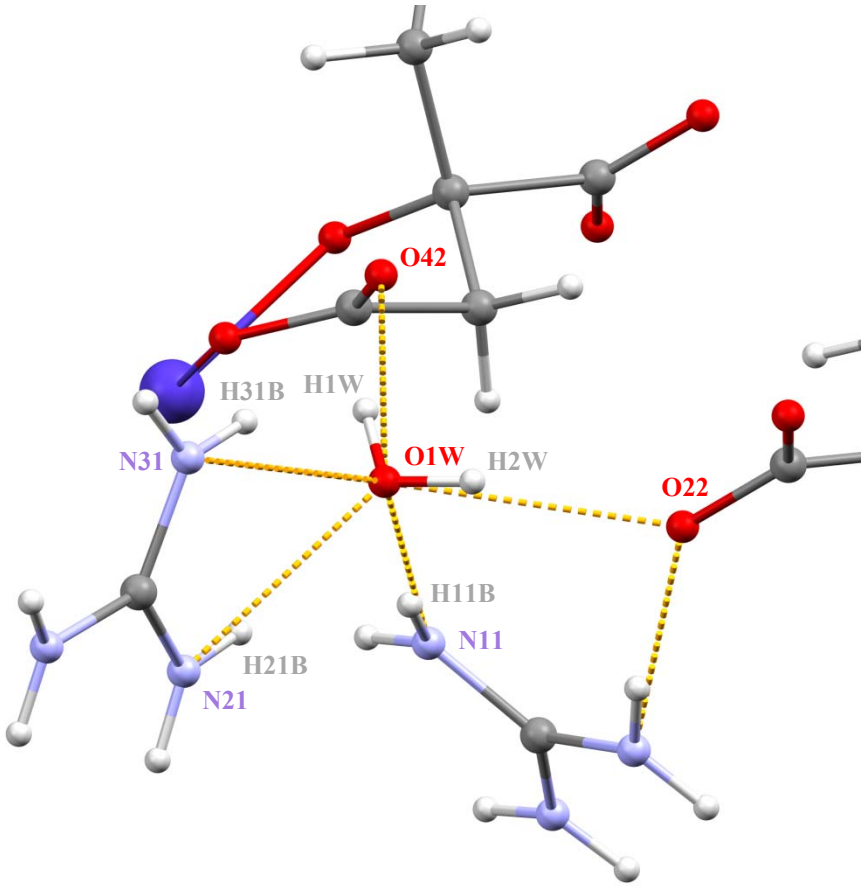

Figure 4-8 Hydrogen bonding (yellow) around O1W in **18** from the 2 K X-ray structure. O1W acts as a hydrogen bond donor to O42 and O22 (*via* H1W and H2W respectively), and as an acceptor from N11, N21 and N31 (*via* H11B, H21B and H31B respectively). Atom colours as previously defined, H atoms are shown in white.

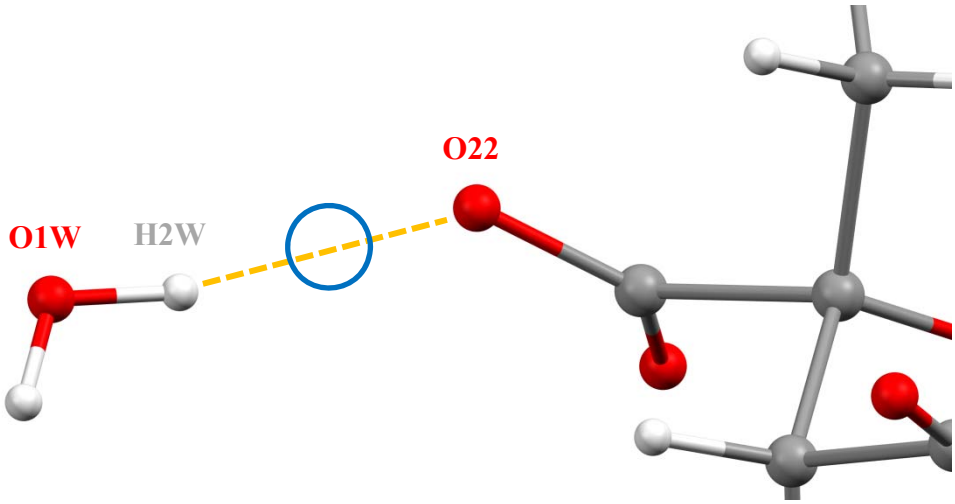

Figure 4-9 Hydrogen bonding from O1W to O22 *via* H2W (yellow). A Fourier difference map in the 2 K X-ray refinement reveals an electron density peak at a distance of approximately 0.88 Å from O22 in a reasonable geometry for a hydrogen bond donation from O22 to O1W (approximate location circled in blue). Atom colours as previously defined.

Table 4.3: Selected bond distances and angles for **18** (Å / °). (i) X-ray, 2 K. (ii) X-ray, 30 K. (iii) Neutron, 2 K. (iv) Neutron, RT.

H-bond pathway	**18 (i)**	**18 (ii)**	**18 (iii)**	**18 (iv)**
O1W–H1W---O42	2.721(3) / 156.7(1)	2.718(4) / 161.1(2)	2.71(1) / 163(1)	2.74(2) / 164(2)
O1W–H2W---O22	2.784(3) / 161.8(1)	2.774(4) / 159.9(2)	2.78(1) / 160(1)	2.76(2) / 159(2)
N11–H11B---O1W	3.039(3) / 171.5(1)	3.035(5) / 174.2(2)	3.03(1) / 174(1)	3.04(2) / 178(2)
N21–H21B---O1W	2.867(3) / 155.4(1)	2.868(4) / 154.2(2)	2.87(1) / 154(1)	2.88(2) / 157(2)
N31–H31B---O1W	3.070(3) / 142.4(1)	3.071(5) / 142.5(2)	3.07(1) / 138(1)	3.10(2) / 141(2)

One hydrogen bonding pathway from O1W to O22 *via* H2W (figure 4-9) showed an unusual peak in a Fourier difference map calculated from the 2 K X-ray data. Some unresolved electron density was observed at approximately 0.88 Å from O22 in a sensible geometry to be the hydrogen atom in a carboxylic acid group (the approximate location of this peak is circled in figure 4-9). It would also be reasonable for a hydrogen bond to exist from O22 to O1W if a hydrogen atom were located at that position. If O1W acts as a hydrogen bond acceptor from O22, then H2W cannot be located in the position shown in figure 4-9. Hence, it must be located in a different position (giving a different orientation for the water molecule O1W) or O1W-H1W is actually a free hydroxide in the lattice. There is no evidence for a second orientation for O1W. The latter possibility would assist in re-balancing the charge of the structure (protonation of the carboxylate removes a negative charge from the cluster). However there are relatively few structures of this type in the Cambridge Structural Database that have free hydroxides in the lattice, and even fewer where it has been possible to find hydrogen atoms for lattice water and hydroxides.[135] Furthermore, the bond lengths C2-O21 and C2-O22 are 1.258(3) Å and 1.248(3) Å respectively. A C-O bond is longer than a C=O bond; 1.248(3) Å is firmly in the typical range for a double bond, and so this does not support the argument for O22 having a bonded hydrogen atom. Neutron data are particularly useful for determining accurate hydrogen atom positions. Thus, it was hoped that the neutron powder data and the higher-quality single-crystal neutron data would be able to clear up this uncertainty.

The high-resolution neutron powder data collected at 2 K allowed a joint X-ray/neutron refinement also using the single-crystal X-ray data at 2 K. Although the quality of the neutron structure obtained is only mediocre, it was possible to refine atomic positions for all atoms and anisotropic displacement parameters for all non-hydrogen atoms. The structure is closely comparable to that obtained from the ultra-low temperature X-ray data. Similarly, some residual negative scattering density was observed in the Fourier difference map between H2W/D2W and O22. In addition, the isotropic displacement parameter for

D11B (bonded to N11 and mediates a hydrogen bond from N11 to O1W, see figure 4-8) is unusually large. This could indicate a lower occupancy for the deuterium in this position, and therefore some of the time it could be bonded to O1W creating a sensible second orientation for the D_2O molecule. It was possible to obtain a better fit between the observed and calculated patterns by including water of crystallisation as well as D_2O. They occupy the same site and so their occupancies were restrained to sum to unity. The refined D_2O:H_2O ratio was 0.144:0.856, indicating that the majority of the crystallised solvent is actually water. This is consistent with the measured IR spectrum (figure 4-7) that indicated some residual water in the structure. It is possible that the D_2O used for the reaction contained some water or that water from the $Co(NO_3)_2{\cdot}6H_2O$ starting material has been incorporated into the structure. It is also possible that atmospheric water has quickly exchanged with D_2O after synthesis.

The single-crystal neutron experiment yielded good quality data at 2 K and at ambient temperature. It was possible to refine all atoms, including hydrogen atoms, with anisotropic displacement parameters. No disorder was observed and it was not necessary to apply thermal similarity restraints to the refinement at 2 K. These were applied to some hydrogen atoms in the room temperature data set. The high R_{int} values are typical of neutron Laue experiments; more important is to consider the goodness of fit, *S*, in order to evaluate the quality of the data. Unlike a typical refinement using X-ray data where a weighting scheme is chosen to give a goodness of fit close to 1, standard weights are applied to the neutron data that are consistent with our confidence in the data. This allows evaluation of *S* as a measure of the quality of the data. Importantly we were able to determine the positions of hydrogen atoms on the water of crystallisation O1W. O1W acts as an acceptor to hydrogen bonds from N11, N21 and N31 (*via* H11B, H21B and H31B respectively) on symmetry-related guanidinium cations (as shown in figure 4-8), and as a donor to O42 and O22 (*via* H1W and H2W respectively) on neighbouring $\{Co_4\}$ clusters (also shown in figure 4-8).

Therefore, it is necessary to consider the contradictions posed by the different studies. Both the 2 K X-ray data and 2 K neutron powder data offer evidence that there might be some disorder in hydrogen atom positions, and indeed in the chemical identity of some molecules in the structure (*i.e.* water *vs*. hydroxide; carboxylate *vs*. carboxylic acid). On the other hand, the 2 K single crystal neutron data and the 30 K X-ray data are consistent with the published structure (as described earlier in this chapter) and show no evidence of

such disorder. X-ray data are often not particularly useful for determining accurate hydrogen atom positions. And there is nothing to suggest a lengthened C-O bond in the ligand that should result from protonation of the oxygen. The Rietveld refinement carried out using the neutron powder diffraction data is a good fit and the structure obtained again shows residual density close to O22; however, the C2-O22 bond is similar to that seen in the X-ray data, showing no evidence of bond lengthening. The single-crystal neutron data collected at ultra-low temperature are of high quality and offer no evidence to support the suggestion of disordered hydrogen atoms. As we have discussed previously, neutron data are particularly useful for determining hydrogen atom positions, and single-crystal measurements even more so than powder experiments. Thus, while we cannot say with complete certainty that the structural model suggested by the single-crystal neutron data is correct, it is more likely to be so. Another possibility is that by measuring different crystals with each technique, we have observed disorder in some and not in others. This would be similar to the case presented for the $\{Mn_3\}$ complex (**5**) in chapter 2. If sufficient neutron beam time could be obtained, it might be possible to measure a series of crystals grown from different reactions in order to observe any differences in the structure of each.

A published study concerning proton migration in the urea-phosphoric acid system found that multiple-temperature X-ray diffraction and neutron diffraction showed a difference in the magnitude of the proton shift depending on the technique used.[217] It is noted here that neutron diffraction probes the structure (measuring nuclear density), and X-ray diffraction probes bonding within the structure (measuring electron density).

The thermal ellipsoids of atoms in **18** as measured by the various techniques described above can be compared. ORTEP-style plots are shown in figures 4-10 and 4-11. The figures were created in Mercury[129] and rendered using POV-Ray.[130] All are shown at approximately the same scale. The thermal ellipsoids (and the equivalent isotropic displacement parameter, U_{eq}) are slightly smaller at 2 K than at 30 K for the X-ray diffraction data. This is consistent with reduced thermal motion upon cooling. A similar effect is seen for the neutron Laue data at 2 K compared with 295 K. Thermal ellipsoids (and U_{eq}) for the neutron data at 2 K are larger than those for the X-ray data at the same temperature, though not to the same degree seen in compound **5**. Since the difference for this compound is much smaller, it might be possible to adjust certain parameters in the integration and data reduction procedure to give consistent values; in particular, the splitting of spots that was noted above could have contributed to a slight inaccuracy in

recorded intensities. Some flattening is observed in the thermal ellipsoids of the neutron structure at 2 K, similar to that observed in **9** at 1.7 K. Again, this could be caused by incomplete data in the direction of the flattening. The data are only 79% complete for this experiment at 2 K.

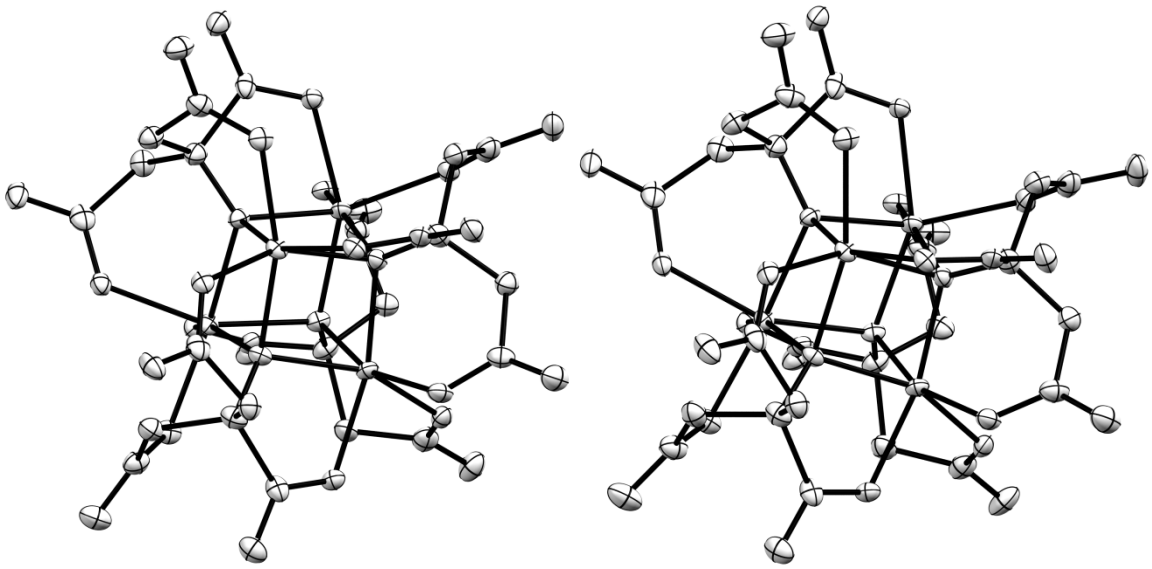

Figure 4-10: ORTEP-style plots of the structure of **18** at 2 K (left, XRD) and 30 K (right, XRD). Thermal ellipsoids are drawn at the 50% probability level. H atoms are omitted for these X-ray structures since their thermal parameters are correlated with those of their parent atoms.

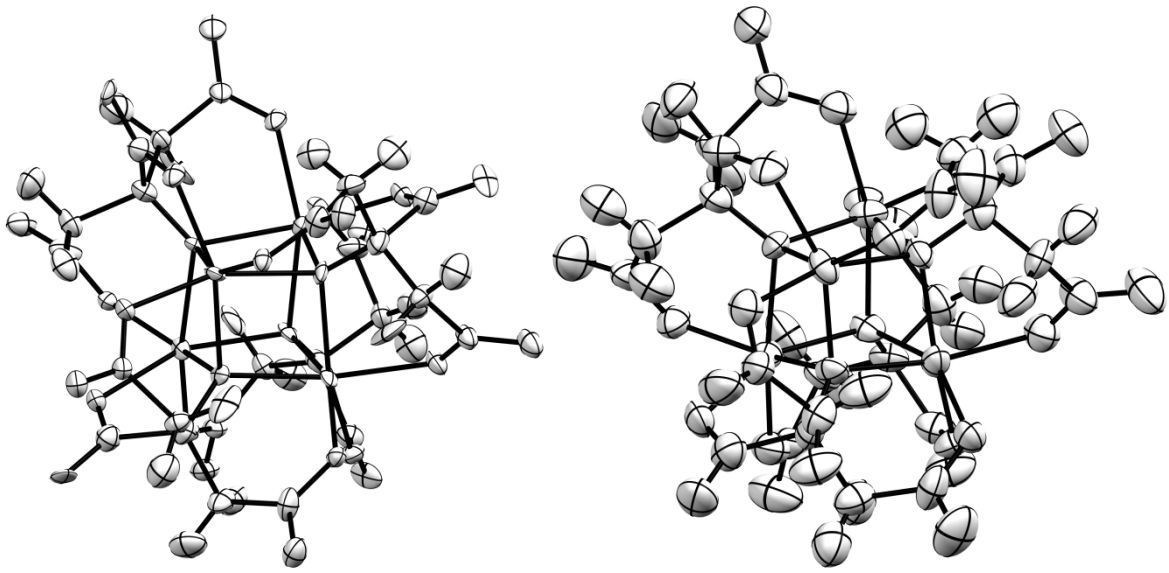

Figure 4-11: ORTEP-style plots of the structure of **18** at 2 K (left, neutron diffraction) and room temperature (right, neutron diffraction). Thermal ellipsoids are drawn at the 50% probability level. H atoms are included for these neutron structures since their thermal parameters are refined independently.

4.2.4 Inelastic/Polarised Neutron Scattering (INS/PNS)

INS/PNS measurements were performed in order to gain insight into the energy level structure of **18**/**19** at low temperature. A previous INS study on a fully-deuterated Co^{II}-based cluster $[Co_4(H_2O)_2(PW_9O_{34})_2]^{10-}$ was able to determine the energy splittings in the ground state resulting from anisotropic exchange coupling.[219] Other similar studies have been performed on two dimetallic Co^{II} complexes[220] and a $\{Co^{II}_3\}$ moiety encapsulated in a polyoxometalate anion.[221] Three neutron spectrometers were used for our studies: IN5[222] and D7[67, 223] at ILL, Grenoble and FOCUS[65, 224, 225] at PSI, Switzerland. IN5 and FOCUS are cold neutron time-of-flight (tof) instruments while D7 is a diffuse scattering spectrometer offering neutron polarisation analysis. Data analysis for the experiment on IN5 was carried out by Dr Grégory Chaboussant; data analysis for the experiments on D7 and FOCUS was carried out by Dr Stefan Ochsenbein.

The first INS experiment on **19** was carried out on IN5 and was intended to directly measure the exchange splitting and determine the exchange interaction parameters, by using a magnetic field of a few Tesla; the ground state, the energy level structure and the origin of effective quantum tunnelling of the magnetisation (QTM) below 2 K are still unknown despite the discovery of this single-molecule magnet several years prior. 1.8 g of the deuterated polycrystalline sample (**19**) was encapsulated in a hollow cylindrical aluminium can with a cadmium shield placed on top. A 2.5 T cryomagnet was used to apply the magnetic field and cool the sample. Various configurations were used including variation of wavelength and chopper speed to probe regions of different energy. Spurious peaks were observed due to the cryomagnet. High energy scattering was found to increase with increasing momentum transfer (Q) suggesting that this is not magnetic in origin;[226] however, at lower energies some scattering was observed that is field- and temperature-dependent and thus, is clearly associated with the magnetic nature of the material.[227]

Unfortunately it was later determined that the height calibration for the sample position in the spectrometer was incorrect, and that only a very small amount of the sample was actually exposed to the neutron beam. The effect of this would be poor resolution and a much lower signal-to-noise ratio than expected if the full sample was in the beam. Thus, the scattering contribution from the cryomagnet is much more significant and it is difficult to separate magnetic scattering from spurious peaks. This error was only determined

around the time of the latter experiment on D7, and so both subsequent experiments described below were planned based on the incorrectly weak spectra recorded at the time.

In order to probe the weak, possibly magnetic scattering observed on IN5, another INS experiment was carried out on FOCUS at PSI, Switzerland. Using λ_i = 3.2 Å a broad peak was observed at 4-5 meV energy transfer (figure 4-12). A smaller peak was seen at approximately 2.5 meV (**II**) and also a shoulder on the elastic line (~ 1.4 meV, **I**) (figure 4-12, peaks are labelled in figure 4-14).

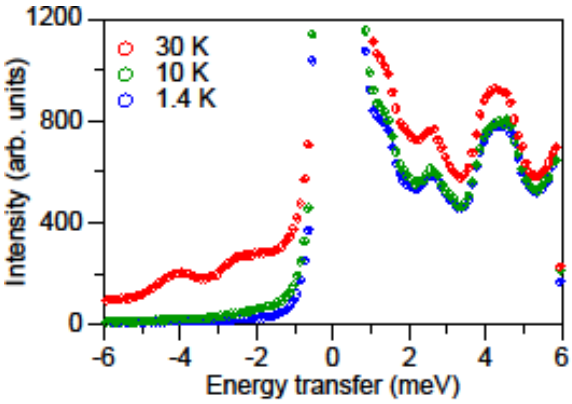

Figure 4-12: INS spectra of **19** measured on FOCUS with initial wavelength λ_i = 3.2 Å at temperatures of 1.4, 10 and 30 K, summed over all scattering angles.

However, the intensities of these three peaks all increase with increasing temperature and increasing Q indicating that these are non-magnetic excitations. Corrections were applied to take account of these scattering modes and it became clear that the broad high-energy peak was indeed non-magnetic, but there are some magnetic components to the two lower energy peaks at 1.4 meV (**I**) and 2.5 meV (**II**) (figure 4-13).

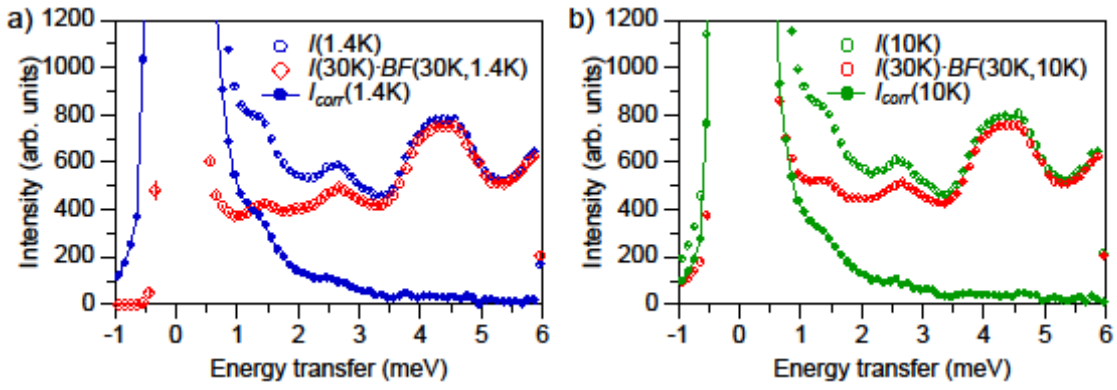

Figure 4-13: Bose-correction of FOCUS INS data for **19**. (a) the 30 K spectrum multiplied by the Bose-factor (*BF*(30K,1.4K)) is subtracted from the 1.4 K data. (b) the 30 K spectrum multiplied by the Bose-factor (*BF*(30K,10K)) is subtracted from the 10 K data. $\boldsymbol{BF(T_2,T_1) = \frac{1-\exp(-\hbar\omega_2/kT_2)}{1-\exp(-\hbar\omega_1/kT_1)}}$.

The data were fitted to the Hamiltonian shown in equation 4.1 using the MAGPACK modelling software package[228] and the exchange coefficients J^z = 0.56 meV and J^{xy} = 0.28 meV were obtained (figure 4-14).

$$\mathcal{H} = 2J^z \sum_{i<j} \hat{S}_i^z \hat{S}_j^z - 2J^{xy} \sum_{i<j} \left(\hat{S}_i^x \hat{S}_j^x + \hat{S}_i^y \hat{S}_j^y \right) \qquad (4.1)$$

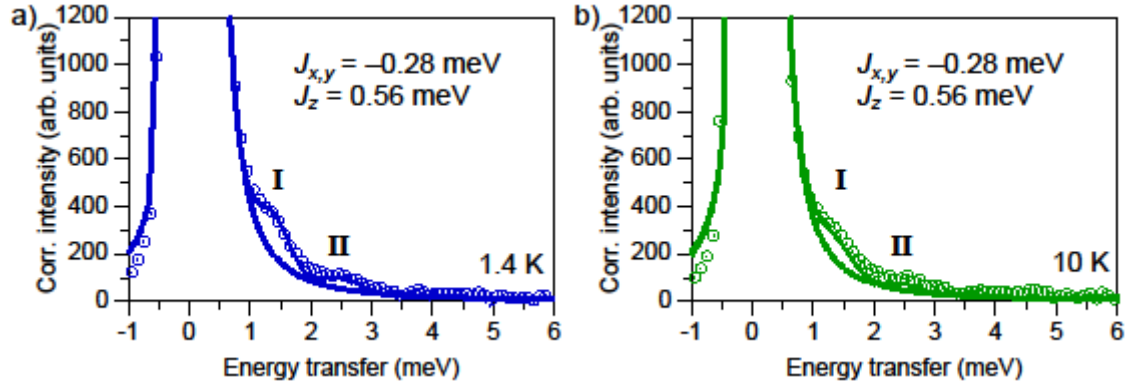

Figure 4-14: Corrected INS spectra of **19** from FOCUS including background fit (dotted lines) and calculated spectra (solid lines) based on the fit to equation 4.1 from MAGPACK using the parameters given. (a) 1.4 K, (b) 10 K.

The agreement with the experimental data is generally good and the consequent energy difference between m_s = ±2 states and the lowest m_s = 0 state is 1.68 meV or 19.5 K, close to the anisotropy barrier of 21 K determined from ac susceptibility experiments. Figure 4-15 shows a rudimentary energy level schematic derived from *J* values obtained from the MAGPACK calculations. Calculated and experimentally observed magnetisation *vs*. field plots are shown in figure 4-16; it can be seen that the proposed model provides reasonable agreement with the experimental data, although it does not reproduce the inflection from 1.5-5 T.

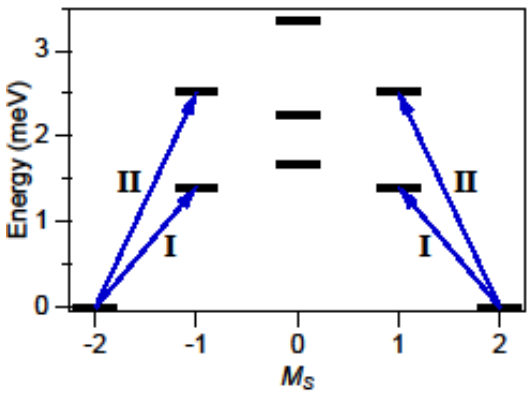

Figure 4-15: Calculated energy levels for **19** from the fit to equation 4.1 (giving parameters $\boldsymbol{J^z}$ = 0.56 meV and $\boldsymbol{J^{xy}}$ = -0.28 meV) as a function of the cluster magnetic quantum number m_s. The observed transitions are also indicated.

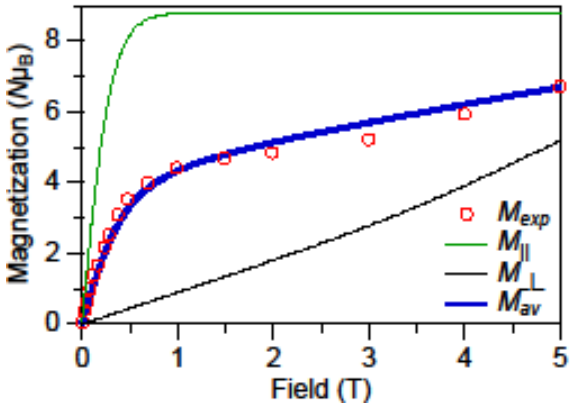

Figure 4-16: Experimental and calculated magnetisation for **19**. The calculated components of the magnetisation parallel and perpendicular to the field are shown independently in green and black respectively; the average of these contributions is shown in blue and shows reasonable agreement with the experimentally observed data, although it does not reproduce the inflection from 1.5-5 T.

In order to investigate the magnetic properties of the system in further detail, a sample was analysed using the polarised neutron spectrometer D7 at ILL, Grenoble. It was hoped this would enable the magnetic transitions to be observed in the absence of the large phononic signals observed on FOCUS.

4.45 g of **19** was placed in a hollow aluminium cylinder on the D7 spectrometer. An incident neutron wavelength of λ_i = 3.12 Å was selected with a pyrolytic graphite monochromator. Inelastic scattering measurements were performed with a Fermi chopper in the beam before the sample position in order to create a time-of-flight (TOF) effect. One-dimensional polarisation analysis can be performed in this configuration in order to differentiate spin-flipped (*sf*) and non-spin-flipped (*nsf*) scattered neutrons. Magnetic excitations appear in both *sf* and *nsf* channels while non-magnetic excitations only appear in the *nsf* channel.[67] Figure 4-17 shows INS spectra recorded at 1.5 K, 25 K and 50 K.

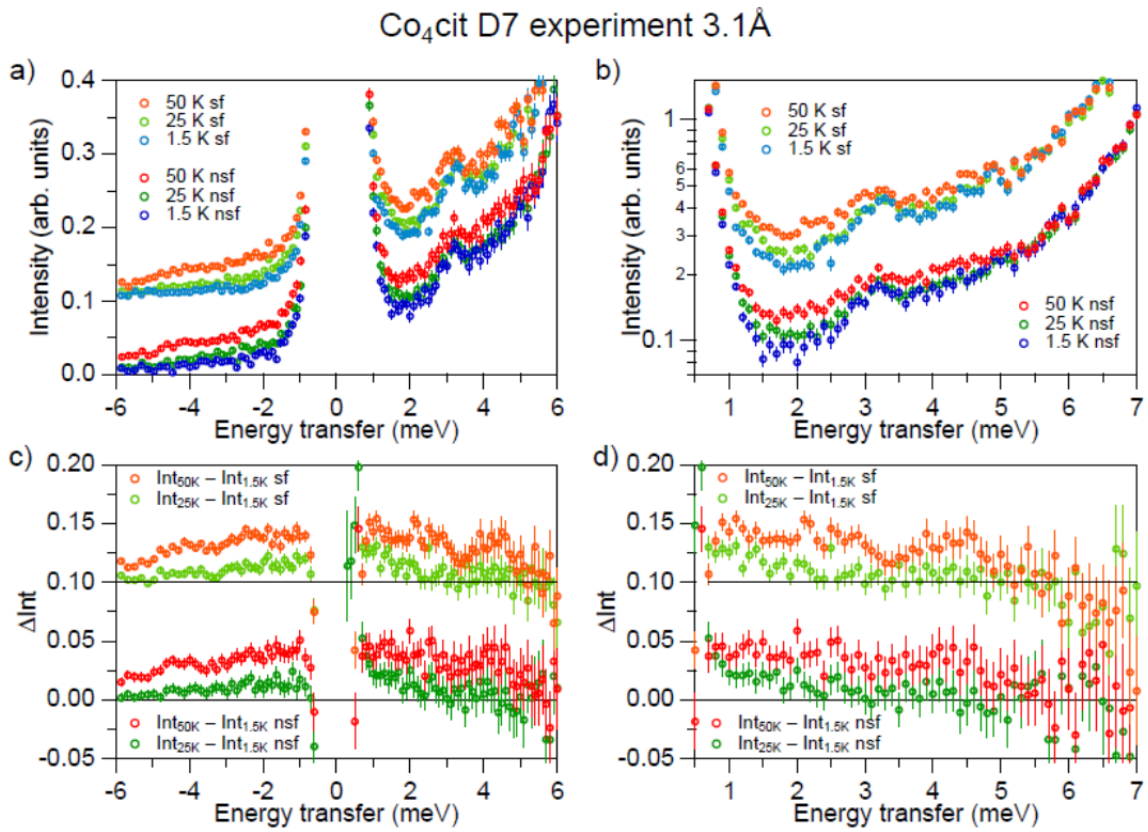

Figure 4-17: (a) INS spectra of **19** measured on D7 with λ_i = 3.12 Å. Spin-flipped spectra are offset for clarity. (b) as (a) with only neutron energy loss side shown in semi-log plot. (c) Difference spectra (higher temperature spectra – 1.5 K spectra). (d) as (c) with only neutron energy loss side shown.

It can be seen in figure 4-17(a) that most features appear in both *sf* and *nsf* channels, indicating that they correspond to magnetic excitations. The largest inelastic peak is at 3.2 meV. The intensity of this peak decreases with increasing temperature although it can still be seen in the higher temperature spectra. This experiment was performed only recently and it has not yet been possible to achieve a satisfactory simulation of the spectra and their temperature dependence. Interestingly we did not observe on D7 the large phononic signals seen on FOCUS (there are no significant peaks in the *nsf* spectra only). It is possible that those signals were artefacts of the experimental setup on FOCUS.

Elastic scattering measurements were also carried out using polarised neutrons on D7. With the Fermi chopper removed, polarisation analysis can be performed in three dimensions allowing the coherent, spin incoherent and magnetic scattering components to be separated. Figure 4-18 shows the 1.5 K scattering intensity as a function of momentum transfer (Q). (a) shows the components on an absolute scale; (b) shows only magnetic scattering.

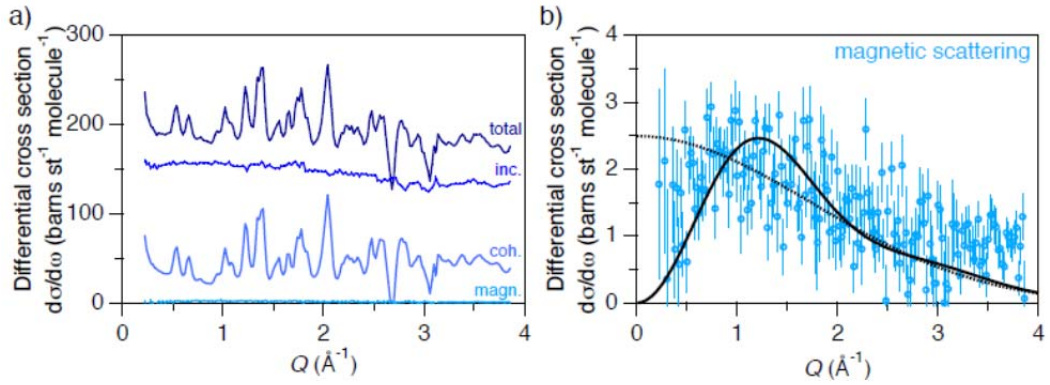

Figure 4-18: (a) Differential neutron scattering cross-section *vs*. Q; individual contributions are shown (incoherent, inc; coherent, coh; magnetic, magn). (b) Magnetic scattering including calculated curves (dotted, scaled square of magnetic form factor; solid, based on equation 4.2 – see text).

It is clear that the magnetic contribution to the total scattering is weak. Hence, the polarisation analysis is useful since it enables that contribution to be observed without the other scattering components. The incoherent scattering cross-section comes largely from hydrogen atoms in the sample; the average value of 145 barns st^{-1} $molecule^{-1}$ indicates that a significant number of hydrogen atoms exist in the sample. The ratio of hydrogen to deuterium can be varied to obtain a good fit to this value and is calculated to be approximately 21/51 (for the 72 H/D atoms in the compound). This is consistent with indications from the IR spectrum of **19** (figure 4-7) that some hydrogen is present post-deuteration. It is unlikely that any of the CD_2 groups has exchanged with hydrogen to form CH_2. Thus, the H atoms must be present in either the guanidinium cations or water of crystallisation. High-resolution neutron powder diffraction data are consistent with approximately 3.4 H_2O molecules per cluster (6.8 H atoms) and no deuteration in the guanidinium cations; this falls short of the 21 H atoms estimated from the experiment on D7. We considered whether or not the H/D ratio is stable over time; the latest INS experiment was carried out almost two and a half years after the diffraction experiment. Figure 4-19 shows a comparison of the IR spectrum of **19** immediately after it was synthesised with the IR spectrum measured almost three years later. There are no significant differences between the spectra, indicating that that the H/D ratio is stable over time.

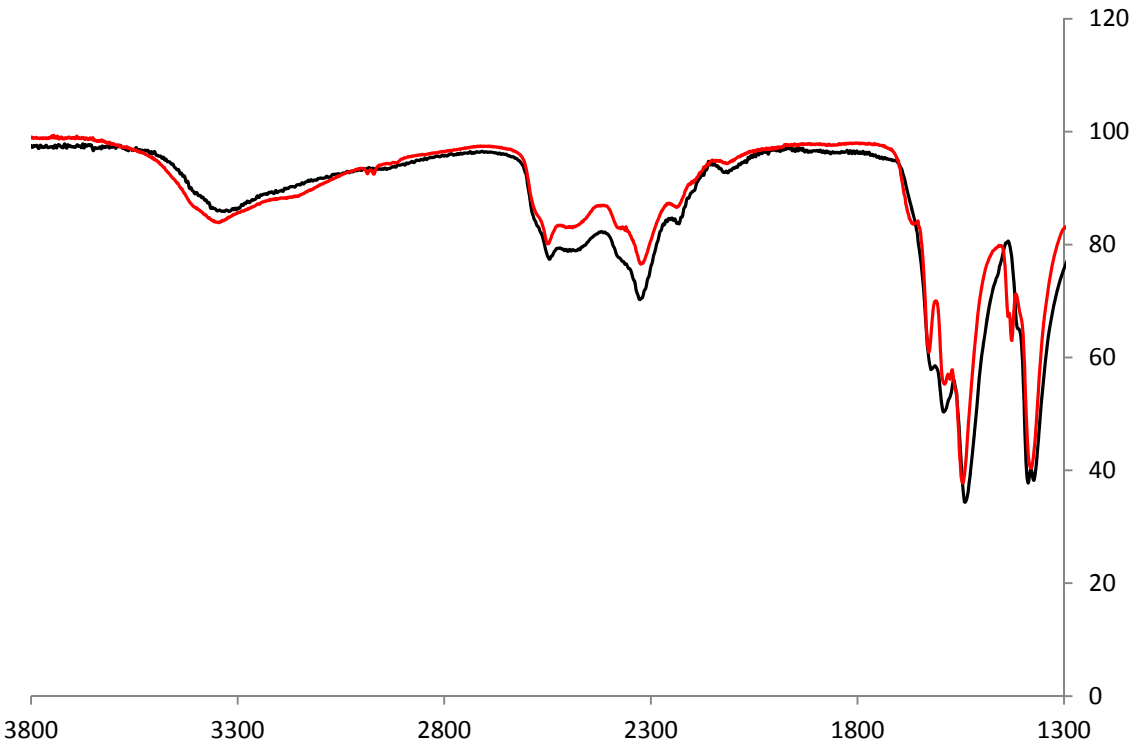

Figure 4-19: Comparison of the IR spectrum of **19** immediately after it was synthesised (red) with the IR spectrum measured almost three years later for the same compound (black).

Due to the weakness of the magnetic scattering, it is inherently noisy. A broad maximum at around 1 – 1.5 $Å^{-1}$ is observed (figure 4-18). The dotted line in part (b) of figure 4-18 is the scaled square of the magnetic form factor $F(Q)$ for Co^{II}; the solid line was calculated using equation 4.2 (R=3.219 Å, R'=3.171 Å are the Co^{II}-Co^{II} distances in **18**).[229]

$$\frac{d\sigma}{d\omega} \propto F(Q)^2 \left[\left(1 - \frac{\sin QR}{QR}\right) + 2\left(1 - \frac{\sin QR'}{QR'}\right)\right] \qquad (4.2)$$

This equation is a simplification, as in principle the magnetic scattering contains information on the correlation between the Co^{II} spins. Unfortunately the noise does not allow a more detailed analysis.

4.3 Conclusions

We have studied the ultra-low temperature (2 K) structure of $(C(NH_2)_3)_8[Co_4(cit)_4]\cdot 4H_2O$ (**18** and deuterated analogue **19**) using a combination of high-resolution powder neutron diffraction, single-crystal X-ray diffraction and single-crystal neutron diffraction. The former two techniques indicated that there might be some disorder in the position of

hydrogen atoms involved in hydrogen-bonding between the $\{Co_4\}$ clusters, water of crystallisation and lattice guanidinium cations. However, a slightly higher temperature (30 K) single-crystal X-ray study and the ultra-low temperature single-crystal neutron data both are consistent with the originally reported structure and show no evidence of this disorder. There is no evidence in any of the studies for a longer C-O bond in the citrate^{4-} ligand that should be observed if the oxygen atom O22 is protonated. Taking into account this observation in addition to the accuracy of neutrons for detecting hydrogen atom positions, it is more likely that the neutron-derived single-crystal structure is correct. It is also possible that some crystals display disorder and others do not, similar to the case presented for the $\{Mn_3\}$ complex (**5**) in chapter 2. The best way to resolve this would be to measure a series of crystals grown from different reactions by using single-crystal neutron diffraction and observe any differences. Unfortunately neutron beam time is difficult to obtain and the length of time required for such a study is unlikely to be awarded.

We have carried out a series of inelastic and polarised neutron scattering (INS/PNS) measurements using the IN5 and D7 spectrometers at ILL, Grenoble and using the FOCUS spectrometer at PSI, Switzerland. The initial experiment on IN5 was not particularly successful due to an incorrect sample height calibration. The subsequent experiment on FOCUS revealed strong phononic scattering in addition to weak magnetic scattering. The final experiment on D7 was designed to separate the magnetic components of the scattering from the non-magnetic components by using polarised neutrons. Interestingly the large phononic signals observed on FOCUS were not present in the spectra obtained from D7. One-dimensional polarisation analysis showed many features in the spectra that are almost all caused by magnetic excitations. Elastic scattering was also carried out on D7 in order to enable three-dimensional polarisation analysis to be performed. This allowed separation of the coherent, spin incoherent and magnetic scattering components. The spin incoherent scattering component allows determination of the amount of hydrogen in the sample; the H/D ratio is estimated as 21/51. Due to the high level of noise in the magnetic scattering signal, it was not possible to perform a detailed analysis of the magnetic scattering that would yield information about the exchange interaction between Co^{II} spins in the cluster.

References

1. O. Kahn, *Molecular Magnetism*, VCH Publishers, 1942.
2. F. E. Mabbs and D. J. Machin, *Magnetism and Transition Metal Complexes*, Dover Publications, Inc., 2008.
3. R. L. Carlin, *Magnetochemistry*, Springer-Verlag, 1935.
4. D. Jiles, *Introduction to Magnetism and Magnetic Materials*, Taylor & Francis Group, Florida, 1998.
5. R. S. Drago, *Physical Methods for Chemists*, Saunders College Publishing, Surfside, Gainsville, FL, 1992.
6. D. Gatteschi, R. Sessoli and J. Villain, *Molecular Nanomagnets*, OUP, Oxford, 2006.
7. J. B. Goodenough, *Phys. Rev.*, 1955, **100**, 564.
8. J. B. Goodenough, *J. Phys. Chem. Solids*, 1958, **6**, 287.
9. J. Kanamori, *J. Phys. Chem. Solids*, 1959, **10**, 87.
10. M. A. Halcrow, J. S. Sun, J. C. Huffman and G. Christou, *Inorg. Chem.*, 1995, **34**, 4167.
11. R. E. Fontana Jr., S. R. Hetzler and G. Decad, *Tape Based Magnetic Recording: Technology Landscape Comparisons with Hard Disk Drive and Flash Roadmaps; IBM Areal Density Comparison Paper*, 2011.
12. G. Aromi and E. K. Brechin, in *Single-Molecule Magnets and Related Phenomena*, ed. R. E. P. Winpenny, Springer, 2006.
13. R. Sessoli, H. L. Tsai, A. R. Schake, S. Y. Wang, J. B. Vincent, K. Folting, D. Gatteschi, G. Christou and D. N. Hendrickson, *J. Am. Chem. Soc.*, 1993, **115**, 1804.
14. R. Sessoli, D. Gatteschi, A. Caneschi and M. A. Novak, *Nature*, 1993, **365**, 141.
15. J. D. Rinehart, M. Fang, W. J. Evans and J. R. Long, *J. Am. Chem. Soc.*, 2011, **133**, 14236.
16. J. D. Rinehart, M. Fang, W. J. Evans and J. R. Long, *Nat. Chem.*, 2011, **3**, 538.
17. R. Bagai and G. Christou, *Chem. Soc. Rev.*, 2009, **38**, 1011.
18. D. Martien, *Introduction to AC Susceptibility*, Quantum Design, 2004.
19. R. Inglis, G. S. Papaefstathiou, W. Wernsdorfer and E. K. Brechin, *Aust. J. Chem.*, 2009, **62**, 1108.
20. M. Evangelisti, J. Bartolome and F. Luis, *Solid State Commun.*, 1999, **112**, 687.
21. M. Evangelisti and J. Bartolomé, *J. Magn. Magn. Mater.*, 2000, **221**, 99.
22. N. E. Chakov, S.-C. Lee, A. G. Harter, P. L. Kuhns, A. P. Reyes, S. O. Hill, N. S. Dalal, W. Wernsdorfer, K. A. Abboud and G. Christou, *J. Am. Chem. Soc.*, 2006, **128**, 6975.
23. M. Soler, W. Wernsdorfer, K. A. Abboud, J. C. Huffman, E. R. Davidson, D. N. Hendrickson and G. Christou, *J. Am. Chem. Soc.*, 2003, **125**, 3576.
24. J. R. Long, in *Chemistry of Nanostructured Materials*, ed. P. Yang, World Scientific Publishing, Hong Kong, 2003.
25. W. Wernsdorfer, N. Aliaga-Alcalde, D. N. Hendrickson and G. Christou, *Nature*, 2002, **416**, 406.
26. F. Troiani and M. Affronte, *Chem. Soc. Rev.*, 2011, **40**, 3119.
27. N. Domingo, E. Bellido and D. Ruiz-Molina, *Chem. Soc. Rev.*, 2012, **41**, 258.
28. M. del Carmen Giménez-López, F. Moro, A. La Torre, C. J. Gómez-García, P. D. Brown, J. van Slageren and A. N. Khlobystov, *Nat. Commun.*, 2011, **2**, 407.
29. E. M. Chudnovsky and J. Tejada, *Macroscopic Tunneling of the Magnetic Moment*, Cambridge University Press, Cambridge, 1998.

30. S. Hill, S. Datta, J. Liu, R. Inglis, C. J. Milios, P. L. Feng, J. J. Henderson, E. del Barco, E. K. Brechin and D. N. Hendrickson, *Dalton Trans.*, 2010, **39**, 4693.
31. G. Christou, D. Gatteschi, D. N. Hendrickson and R. Sessoli, *MRS Bull.*, 2000, **25**, 66.
32. P. C. Riedi, in *Electron Paramagnetic Resonance*, eds. B. C. Gilbert, M. J. Davies and D. M. Murphy, The Royal Society of Chemistry, 2007, vol. 20, p. 256.
33. J. van Slageren, Frequency Domain Magnetic Resonance Spectroscopy on Molecular Magnets, http://www.pi1.physik.uni-stuttgart.de/Praesentationen/Daten/253/253.pdf, Accessed 17th January, 2013.
34. A. Caneschi, D. Gatteschi, R. Sessoli, A. L. Barra, L. C. Brunel and M. Guillot, *J. Am. Chem. Soc.*, 1991, **113**, 5873.
35. K. Park, T. Baruah, N. Bernstein and M. R. Pederson, *Phys. Rev. B*, 2004, **69**, 144426.
36. A. Cornia, R. Sessoli, L. Sorace, D. Gatteschi, A. L. Barra and C. Daiguebonne, *Phys. Rev. Lett.*, 2002, **89**, 257201.
37. R. Amigó, E. Del Barco, L. Casas, E. Molins, J. Tejada, I. B. Rutel, B. Mommouton, N. S. Dalal and J. S. Brooks, *Phys. Rev. B*, 2002, **65**, 172403.
38. W. Clegg, *Crystal Structure Determination*, OUP, 1998.
39. W. Clegg, A. J. Blake, R. O. Gould and P. Main, *Crystal Structure Analysis: Principles and Practice*, OUP, 2002.
40. J. P. Glusker, M. Lewis and M. Rossi, *Crystal Structure Analysis for Chemists and Biologists*, John Wiley & Sons, USA, 1994.
41. C. Giacovazzo, H. L. Monaco, D. Viterbo, F. Scordari, G. Gilli, G. Zanotti and M. Catti, *Fundamentals of Crystallography*, OUP, 1992.
42. S. M. Gruner, X-ray Detectors II: Film, Image Plates & Phosphors, http://neutrons.ornl.gov/conf/NXS2008/Presentations/Sol%20M.%20Gruner%20-%20Detectors%20II.pdf, Accessed 20th April, 2013.
43. Y. Amemiya, *Meth. Enzymology*, 1997, **276**, 233.
44. G. Oszlanyi and A. Suto, *Acta Cryst.*, 2004, **A60**, 134.
45. L. Palatinus and G. Chapuis, *J. Appl. Cryst.*, 2007, **40**, 786.
46. L. Palatinus and A. van der Lee, *J. Appl. Cryst.*, 2008, **41**, 975.
47. G. Oszlanyi and A. Suto, *Acta Cryst.*, 2005, **A61**, 147.
48. M. R. Probert, C. M. Robertson, J. A. Coome, J. A. K. Howard, B. C. Michell and A. E. Goeta, *J. Appl. Cryst.*, 2010, **43**, 1415.
49. C. C. Wilson, *Single Crystal Neutron Diffraction From Molecular Materials*, World Scientific, 2000.
50. A. J. Edwards, *Aust. J. Chem.*, 2011, **64**, 869.
51. S. A. Mason, V. T. Forsyth, J. A. K. Howard, M. G. Davidson, W. Fuller and D. A. Myles, in *Opportunities For Neutron Scattering In The 3rd Millennium*, ed. J. Dianoux, Institut Laue Langevin, Grenoble, 2001, p. 332.
52. S. A. Mason, S. Capelli and V. T. Forsyth, Thermal neutron diffractometer for single-crystal and fibre diffraction D19, http://www.ill.eu/instruments-support/instruments-groups/instruments/d19/description/instrument-layout, Accessed 21st January, 2013.
53. C. Wilkinson, J. A. Cowan, D. A. A. Myles, F. Cipriani and G. J. McIntyre, *Neutron News*, 2002, **13**, 37.
54. G. J. McIntyre, M.-H. Lemée-Cailleau and C. Wilkinson, *Physica B: Condensed Matter*, 2006, **385–386, Part 2**, 1055-1058.
55. W. I. F. David, W. T. A. Harrison and M. W. Johnson, The High Resolution Powder Diffractometer, HRPD, At The Pulsed Neutron Source ISIS, Regensburg, 1986.

56. J. K. Cockcroft and S. Jacques, Production of Spallation Neutrons, http://pd.chem.ucl.ac.uk/pdnn/inst3/pulsed.htm, Accessed 21st January, 2013.
57. STFC, HRPD User Manual, http://www.isis.stfc.ac.uk/instruments/hrpd/documents/hrpd-manual6735.pdf, Accessed 21st January, 2013.
58. R. A. Young, *The Rietveld Method*, OUP, 1993.
59. H. M. Rietveld, *J. Appl. Cryst.*, 1969, **2**, 65.
60. R. Snellings, L. Machiels, G. Mertens and J. Elsen, *Geologica Belgica*, 2010, **13/3**, 183.
61. R. Caciuffo, G. Amoretti, A. Murani, R. Sessoli, A. Caneschi and D. Gatteschi, *Phys. Rev. Lett.*, 1998, **81**, 4744.
62. J. M. Clemente-Juan, H. Andres, J. J. Borrás-Almenar, E. Coronado, H. U. Güdel, M. Aebersold, G. Kearly, H. Büttner and M. Zolliker, *J. Am. Chem. Soc.*, 1999, **121**, 10021.
63. G. Chaboussant, S. T. Ochsenbein, A. Sieber, H. U. Güdel, H. Mutka, A. Müller and B. Barbara, *Europhys. Lett.*, 2004, **66**, 423.
64. H. Schober, A. J. Dianoux, J. C. Cook and F. Mezei, *Physica B: Condensed Matter*, 2000, **276–278**, 164.
65. C. Beck, S. Janssen, B. Groß and R. Hempelmann, *Scripta Materialia*, 2001, **44**, 2309.
66. S. F. Parker, in *Encyclopedia of Spectroscopy and Spectrometry (2nd ed.)*, ed. J. C. Lindon, Academic Press, Oxford, 2010, p. 1035.
67. O. Schärpf and H. Capellmann, *phys. stat. sol. (a)*, 1993, **135**, 359.
68. B. Roessli and P. Böni, in *Scattering: Scattering and inverse scattering in Pure and Applied Science*, eds. E. R. Pike and P. C. Sabatier, Academic Press, London, 2001, p. 1242.
69. F. Siebert and P. Hildebrandt, *Vibrational Spectroscopy in Life Science*, Wiley-VCH, Weinheim, 2007.
70. P. R. Griffiths and J. A. De Haseth, *Fourier Transform Infrared Spectroscopy*, Wiley Interscience, Hoboken, NJ, 2007.
71. W. J. Jones, *Trans. Faraday. Soc.*, 1959, **55**, 524.
72. M. McElfresh, *Fundamentals of Magnetism and Magnetic Measurements*, Quantum Design, 1994.
73. Rebecca H. Laye and Eric J. L. McInnes, *Eur. J. Inorg. Chem.*, 2004, **2004**, 2811.
74. M. I. Khan, Q. Chen, D. P. Goshorn, H. Hope, S. Parkin and J. Zubieta, *J. Am. Chem. Soc.*, 1992, **114**, 3341.
75. M. I. Khan, Q. Chen, D. P. Goshorn and J. Zubieta, *Inorg. Chem.*, 1993, **32**, 672.
76. M. I. Khan, Q. Chen, H. Hope, S. Parkin, C. J. O'Connor and J. Zubieta, *Inorg. Chem.*, 1993, **32**, 2929.
77. M. I. Khan, Q. Chen, J. Zubieta and D. P. Goshorn, *Inorg. Chem.*, 1992, **31**, 1556.
78. M. I. Khan, Y.-S. Lee, C. J. O'Connor and J. Zubieta, *J. Am. Chem. Soc.*, 1994, **116**, 5001.
79. M. Eshel, A. Bino, I. Felner, D. C. Johnston, M. Luban and L. L. Miller, *Inorg. Chem.*, 2000, **39**, 1376.
80. E. J. L. McInnes, C. Anson, A. K. Powell, A. J. Thomson, S. Poussereau and R. Sessoli, *Chem. Commun.*, 2001, 89.
81. S. Konar and A. Clearfield, *Inorg. Chem.*, 2008, **47**, 3489.
82. R. C. Finn and J. Zubieta, *J. Cluster Sci.*, 2000, **11**, 461.
83. S. O. H. Gutschke, D. J. Price, A. K. Powell and P. T. Wood, *Angew. Chem. Int. Ed.*, 1999, **38**, 1088.

84. R. Shaw, I. S. Tidmarsh, R. H. Laye, B. Breeze, M. Helliwell, E. K. Brechin, S. L. Heath, M. Murrie, S. Ochsenbein, H.-U. Gudel and E. J. L. McInnes, *Chem. Commun.*, 2004, 1418.
85. P. Langan, R. Robinson, P. J. Brown, D. Argyriou, D. Hendrickson and G. Christou, *Acta Cryst.*, 2001, **C57**, 909.
86. G. Aromi, E. J. L. McInnes and R. E. P. Winpenny, in *Molecular Cluster Magnets*, ed. R. E. P. Winpenny, World Scientific Publishing Co. Pte. Ltd., Singapore, 2011.
87. A. J. Tasiopoulos, A. Vinslava, W. Wernsdorfer, K. A. Abboud and G. Christou, *Angew. Chem. Int. Ed.*, 2004, **43**, 2117.
88. J. Yoo, E. M. Rumberger, D. N. Hendrickson, A. Yamaguchi, H. Ishimoto, E. Brechin and G. Christou, *J. Appl. Phys.*, 2002, **91**, 7155.
89. E. K. Brechin, J. Yoo, M. Nakano, J. C. Huffman, D. N. Hendrickson and G. Christou, *Chem. Commun.*, 1999, 783.
90. M. Hołyńska, D. Premužić, I.-R. Jeon, W. Wernsdorfer, R. Clérac and S. Dehnen, *Chem. Eur. J.*, 2011, **17**, 9605.
91. C. J. Milios, A. Vinslava, W. Wernsdorfer, S. Moggach, S. Parsons, S. P. Perlepes, G. Christou and E. K. Brechin, *J. Am. Chem. Soc.*, 2007, **129**, 2754.
92. I. Mirebeau, M. Hennion, H. Casalta, H. Andres, H. U. Güdel, A. V. Irodova and A. Caneschi, *Phys. Rev. Lett.*, 1999, **83**, 628.
93. J. R. Friedman, M. P. Sarachik, J. Tejada and R. Ziolo, *Phys. Rev. Lett.*, 1996, **76**, 3830.
94. A. Cornia, A. C. Fabretti, R. Sessoli, L. Sorace, D. Gatteschi, A.-L. Barra, C. Daiguebonne and T. Roisnel, *Acta Cryst.*, 2002, **C58**, m371.
95. L. Thomas, F. Lionti, R. Ballou, D. Gatteschi, R. Sessoli and B. Barbara, *Nature*, 1996, **383**, 145.
96. W. Wernsdorfer, M. Murugesu and G. Christou, *Phys. Rev. Lett.*, 2006, **96**, 057208.
97. S. Takahashi, R. S. Edwards, J. M. North, S. Hill and N. S. Dalal, *Phys. Rev. B*, 2004, **70**, 094429.
98. H. De Raedt, S. Miyashita, K. Michielsen and M. Machida, *Phys. Rev. B*, 2004, **70**, 064401.
99. N. Kirchner, J. van Slageren, B. Tsukerblat, O. Waldmann and M. Dressel, *Phys. Rev. B*, 2008, **78**, 094426.
100. O. Waldmann, G. Carver, C. Dobe, A. Sieber, H. U. Güdel and H. Mutka, *J. Am. Chem. Soc.*, 2007, **129**, 1526.
101. P. Parois, S. A. Moggach, J. Sanchez-Benitez, K. V. Kamenev, A. R. Lennie, J. E. Warren, E. K. Brechin, S. Parsons and M. Murrie, *Chem. Commun.*, 2010, **46**, 1881.
102. J.-F. Bardeau, A. Bulou, W. T. Klooster, T. F. Koetzle, S. Johnson, B. Scott, B. I. Swanson and J. Eckert, *Acta Cryst.*, 1996, **B52**, 854.
103. D.-H. Wu, L. Jin and Y. Zhang, *Inorg. Chem. Commun.*, 2012, **23**, 117.
104. B. A. Zakharov, E. A. Losev, B. A. Kolesov, V. A. Drebushchak and E. V. Boldyreva, *Acta Cryst.*, 2012, **B68**, 287.
105. T. Lis, *Acta Cryst.*, 1980, **B36**, 2042.
106. Bruker, *SAINT*, 2007, Bruker AXS Inc., Madison, Wisconsin, USA.
107. G. M. Sheldrick, *SADABS*, 1996, University of Göttingen, Germany.
108. G. J. McIntyre, M.-H. Lemée-Cailleau and C. Wilkinson, *Physica B: Condensed Matter*, 2006, **385-386**, 1055.
109. J. W. Campbell, Q. Hao, M. M. Harding, N. D. Nguti and C. Wilkinson, *J. Appl. Cryst.*, 1998, **31**, 496.
110. J. W. Campbell, J. Habash, J. R. Helliwell and K. Moffat, in *Information Quarterly for Protein Crystallography No. 18*, SERC Daresbury Laboratory, Warrington, England, 1986, p. 23.

111. C. Wilkinson, H. W. Khamis, S. R. F. D. and G. J. McIntyre, *J. Appl. Cryst.*, 1988, **21**, 471.
112. Nonius, *COLLECT*, 1998, Nonius BV, Delft, The Netherlands.
113. Z. Otwinowski and W. Minor, *Macromolecular Crystallography, Part A*, Academic Press, New York, 1997.
114. P. W. Betteridge, J. R. Carruthers, R. I. Cooper, K. Prout and D. J. Watkin, *J. Appl. Cryst.*, 2003, **36**, 1487.
115. G. M. Sheldrick, *Acta Cryst.*, 2008, **A64**, 112.
116. J. Larionova, R. Clerac, B. Boury, J. Le Bideau, L. Lecren and S. Willemin, *J. Mater. Chem.*, 2003, **13**, 795.
117. S. Hill, N. Anderson, A. Wilson, S. Takahashi, K. Petukhov, N. E. Chakov, M. Murugesu, J. M. North, E. d. Barco, A. D. Kent, N. S. Dalal and G. Christou, *Polyhedron*, 2005, **24**, 2284.
118. S. Hill, N. Anderson, A. Wilson, S. Takahashi, N. E. Chakov, M. Murugesu, J. M. North, N. S. Dalal and G. Christou, *J. Appl. Phys.*, 2005, **97**, 10M510.
119. G. Redler, C. Lampropoulos, S. Datta, C. Koo, T. C. Stamatatos, N. E. Chakov, G. Christou and S. Hill, *Phys. Rev. B*, 2009, **80**, 094408.
120. Y.-m. Song, F. Luo, M.-b. Luo, Z.-w. Liao, G.-m. Sun, X.-z. Tian, Y. Zhu, Z.-J. Yuan, S.-j. Liu, W.-y. Xu and X.-f. Feng, *Chem. Commun.*, 2012, **48**, 1006.
121. R. Inglis, C. J. Milios, L. F. Jones, S. Piligkos and E. K. Brechin, *Chem. Commun.*, 2012, **48**, 181.
122. C. J. Milios, R. Inglis, A. Vinslava, R. Bagai, W. Wernsdorfer, S. Parsons, S. P. Perlepes, G. Christou and E. K. Brechin, *J. Am. Chem. Soc.*, 2007, **129**, 12505.
123. R. Inglis, S. M. Taylor, L. F. Jones, G. S. Papaefstathiou, S. P. Perlepes, S. Datta, S. Hill, W. Wernsdorfer and E. K. Brechin, *Dalton Trans.*, 2009, 9157.
124. R. Inglis, L. F. Jones, C. J. Milios, S. Datta, A. Collins, S. Parsons, W. Wernsdorfer, S. Hill, S. P. Perlepes, S. Piligkos and E. K. Brechin, *Dalton Trans.*, 2009, 3403.
125. R. Inglis, L. F. Jones, G. Karotsis, A. Collins, S. Parsons, S. P. Perlepes, W. Wernsdorfer and E. K. Brechin, *Chem. Commun.*, 2008, 5924.
126. J. M. Archer and M. S. Lehmann, *J. Appl. Cryst.*, 1986, **19**, 456.
127. J. W. Campbell, *J. Appl. Cryst.*, 1995, **28**, 228.
128. R. O. Piltz, *Acta Cryst.*, 2011, **A67**, C155.
129. C. F. Macrae, P. R. Edgington, P. McCabe, E. Pidcock, G. P. Shields, R. Taylor, M. Towler and J. van de Streek, *J. Appl. Cryst.*, 2006, **39**, 453-457.
130. *Persistence of Vision Raytracer v3.6*, 2004, Williamstown, Victoria, Australia.
131. R. H. Blessing, *Acta Cryst.*, 1995, **B51**, 816.
132. J. M. Cole, A. E. Goeta, J. A. K. Howard and G. J. McIntyre, *Acta Cryst.*, 2002, **B58**, 690.
133. J. J. Henderson, C. Koo, P. L. Feng, E. Del Barco, S. Hill, I. S. Tupitsyn, P. C. E. Stamp and D. N. Hendrickson, *Phys. Rev. Lett.*, 2009, **103**, 017202.
134. J. Lawrence, E.-C. Yang, R. Edwards, M. M. Olmstead, C. Ramsey, N. S. Dalal, P. K. Gantzel, S. Hill and D. N. Hendrickson, *Inorg. Chem.*, 2008, **47**, 1965.
135. F. R. Allen, *Acta Cryst.*, 2002, **B58**, 380-388.
136. S. M. J. Aubin, M. W. Wemple, D. M. Adams, H.-L. Tsai, G. Christou and D. N. Hendrickson, *J. Am. Chem. Soc.*, 1996, **118**, 7746.
137. M. W. Wemple, H. L. Tsai, K. Folting, D. N. Hendrickson and G. Christou, *Inorg. Chem.*, 1993, **32**, 2025.
138. D. N. Hendrickson, G. Christou, E. A. Schmitt, E. Libby, J. S. Bashkin, S. Wang, H. L. Tsai, J. B. Vincent and P. D. W. Boyd, *J. Am. Chem. Soc.*, 1992, **114**, 2455-2471.
139. M. N. Leuenberger and D. Loss, *Nature*, 2001, **410**, 789.

140. T. Sala and M. V. Sargent, *J. Chem. Soc., Chem. Commun.*, 1978, 253.
141. J. B. Vincent, H. R. Chang, K. Folting, J. C. Huffman, G. Christou and D. N. Hendrickson, *J. Am. Chem. Soc.*, 1987, **109**, 5703.
142. T. Lis, *Acta Cryst.*, 1977, **B33**, 2964.
143. J. Li, S. Yang, F. Zhang, Z. Tang, S. Ma, Q. Shi, Q. Wu and Z. Huang, *Inorg. Chim. Acta*, 1999, **294**, 109.
144. J. An, Z.-D. Chen, J. Bian, X.-L. Jin, S.-X. Wang and G.-X. Xu, *Inorg. Chim. Acta*, 1999, **287**, 82.
145. A. Ferguson, J. Lawrence, A. Parkin, J. Sanchez-Benitez, K. V. Kamenev, E. K. Brechin, W. Wernsdorfer, S. Hill and M. Murrie, *Dalton Trans.*, 2008, 6409.
146. A. Bell, G. Aromi, S. J. Teat, W. Wernsdorfer and R. E. P. Winpenny, *Chem. Commun.*, 2005, 2808.
147. A. J. Blake, C. M. Grant, S. Parsons, J. M. Rawson and R. E. P. Winpenny, *J. Chem. Soc., Chem. Commun.*, 1994, 2363.
148. S. T. Ochsenbein, M. Murrie, E. Rusanov, H. Stoeckli-Evans, C. Sekine and H. U. Güdel, *Inorg. Chem.*, 2002, **41**, 5133.
149. H. Oshio, M. Nihei, S. Koizumi, T. Shiga, H. Nojiri, M. Nakano, N. Shirakawa and M. Akatsu, *J. Am. Chem. Soc.*, 2005, **127**, 4568.
150. G. Rogez, J.-N. Rebilly, A.-L. Barra, L. Sorace, G. Blondin, N. Kirchner, M. Duran, J. van Slageren, S. Parsons, L. Ricard, A. Marvilliers and T. Mallah, *Angew. Chem. Int. Ed.*, 2005, **44**, 1876.
151. M. Moragues-Cánovas, M. Helliwell, L. Ricard, É. Rivière, W. Wernsdorfer, E. Brechin and T. Mallah, *Eur. J. Inorg. Chem.*, 2004, **2004**, 2219.
152. M. Nakano, G.-E. Matsubayashi, T. Muramatsu, T. C. Kobayashi, K. Amaya, J. Yoo, G. Christou and D. N. Hendrickson, *Mol. Cryst. Liq. Cryst.*, 2002, **376**, 405.
153. R. S. Edwards, S. Maccagnano, E. C. Yang, S. Hill, W. Wernsdorfer, D. Hendrickson and G. Christou, *J. Appl. Phys.*, 2003, **93**, 7807.
154. E.-C. Yang, W. Wernsdorfer, S. Hill, R. S. Edwards, M. Nakano, S. Maccagnano, L. N. Zakharov, A. L. Rheingold, G. Christou and D. N. Hendrickson, *Polyhedron*, 2003, **22**, 1727.
155. C. Kirman, J. Lawrence, S. Hill, E. C. Yang and D. N. Hendrickson, *J. Appl. Phys.*, 2005, **97**, 10M501.
156. C. C. Beedle, J. J. Henderson, P.-C. Ho, T. Sayles, M. Nakano, J. R. O'Brien, K. J. Heroux, E. del Barco, M. B. Maple and D. N. Hendrickson, *Inorg. Chem.*, 2010, **49**, 5780.
157. S. Hill and A. Wilson, *J. Low Temp. Phys.*, 2006, **142**, 267.
158. S. Hill, R. S. Edwards, N. Aliaga-Alcalde and G. Christou, *Science*, 2003, **302**, 1015.
159. A. Elmali, Y. Elerman, I. Svoboda and H. Fuess, *J. Mol. Struct.*, 2000, **516**, 43.
160. K. D. M. Harris, I. Gameson and J. M. Thomas, *J. Chem. Soc., Faraday Trans.*, 1990, **86**, 3135.
161. M. K. Saha, F. R. Fronczek, L. H. Rees and I. Bernal, *Inorg. Chem. Commun.*, 2003, **6**, 983.
162. H. I. Karunadasa, K. D. Arquero, L. A. Berben and J. R. Long, *Inorg. Chem.*, 2010, **49**, 4738.
163. R. H. Busey and E. Sonder, *J. Chem. Phys.*, 1962, **36**, 93.
164. C. Duboc, T. Phoeung, S. Zein, J. Pécaut, M.-N. Collomb and F. Neese, *Inorg. Chem.*, 2007, **46**, 4905.
165. P. J. Desrochers, J. Telser, S. A. Zvyagin, A. Ozarowski, J. Krzystek and D. A. Vicic, *Inorg. Chem.*, 2006, **45**, 8930.
166. A. L. Spek, *J. Appl. Cryst.*, 2003, **36**, 7.

167. H. Icbudak, V. T. Yilmaz, R. A. Howie, O. Andac and H. Olmez, *Acta Cryst.*, 1995, **C51**, 1759.
168. Y. Yu, Y. Guo, L. Lv and D. Li, *Acta Cryst.*, 2010, **E66**, m861.
169. A. Wilson, E.-C. Yang, D. N. Hendrickson and S. Hill, *Polyhedron*, 2007, **26**, 2065.
170. R. W. Saalfrank, A. Scheurer, I. Bernt, F. W. Heinemann, A. V. Postnikov, V. Schunemann, A. X. Trautwein, M. S. Alam, H. Rupp and P. Muller, *Dalton Trans.*, 2006, 2865.
171. V. Mereacre, A. M. Ako, R. Clérac, W. Wernsdorfer, I. J. Hewitt, C. E. Anson and A. K. Powell, *Chem. Eur. J.*, 2008, **14**, 3577.
172. G. Abbas, Y. Lan, G. E. Kostakis, W. Wernsdorfer, C. E. Anson and A. K. Powell, *Inorg. Chem.*, 2010, **49**, 8067.
173. S. J. Shah, C. M. Ramsey, K. J. Heroux, A. G. DiPasquale, N. S. Dalal, A. L. Rheingold, E. del Barco and D. N. Hendrickson, *Inorg. Chem.*, 2008, **47**, 9569.
174. E. M. Rumberger, L. N. Zakharov, A. L. Rheingold and D. N. Hendrickson, *Inorg. Chem.*, 2004, **43**, 6531.
175. K. J. Heroux, S. J. Shah, J. R. O'Brien, M. Nakano, A. G. DiPasquale and D. N. Hendrickson, *Inorg. Chim. Acta*, 2010, **364**, 46.
176. A. Whyte and M. Murrie, unpublished work.
177. L. M. Wittick, L. F. Jones, P. Jensen, B. Moubaraki, L. Spiccia, K. J. Berry and K. S. Murray, *Dalton Trans.*, 2006, 1534.
178. V. Mereacre, D. Prodius, Y. Lan, C. Turta, C. E. Anson and A. K. Powell, *Chem. Eur. J.*, 2011, **17**, 123.
179. R. W. Saalfrank, I. Bernt, E. Uller and F. Hampel, *Angew. Chem. Int. Ed.*, 1997, **36**, 2482.
180. F. Klöwer, Y. Lan, J. Nehrkorn, O. Waldmann, C. E. Anson and A. K. Powell, *Chem.Eur. J.*, 2009, **15**, 7413.
181. V. Mereacre, M. N. Akhtar, Y. Lan, A. M. Ako, R. Clérac, C. E. Anson and A. K. Powell, *Dalton Trans.*, 2010, **39**, 4918.
182. A. M. Ako, O. Waldmann, V. Mereacre, F. Klöwer, I. J. Hewitt, C. E. Anson, H. U. Güdel and A. K. Powell, *Inorg. Chem.*, 2007, **46**, 756.
183. MAGMUN-4.1 is available free of charge. It has been developed by Dr. Zhiqiang Xu (Memorial University) and Kathy He in collaboration with Prof. L.K. Thompson (lthomp@mun.ca), and Dr. O. Waldmann (oliver.waldmann@iac.unibe.ch) and is available from the authors free of charge.
184. V. Mougel, L. Chatelain, J. Pécaut, R. Caciuffo, E. Colineau, J.-C. Griveau and M. Mazzanti, *Nat. Chem.*, 2012, **4**, 1011.
185. J. Ruiz, A. J. Mota, A. Rodriguez-Dieguez, S. Titos, J. M. Herrera, E. Ruiz, E. Cremades, J. P. Costes and E. Colacio, *Chem. Commun.*, 2012, **48**, 7916.
186. L. Lecren, O. Roubeau, Y.-G. Li, X. F. Le Goff, H. Miyasaka, F. Richard, W. Wernsdorfer, C. Coulon and R. Clerac, *Dalton Trans.*, 2008, 755.
187. L. Lecren, O. Roubeau, C. Coulon, Y.-G. Li, X. F. Le Goff, W. Wernsdorfer, H. Miyasaka and R. Clérac, *J. Am. Chem. Soc.*, 2005, **127**, 17353.
188. I.-R. Jeon and R. Clerac, *Dalton Trans.*, 2012, **41**, 9569.
189. D. Gatteschi, in *Organic Conductors, Superconductors and Magnets: From Synthesis to Molecular Electronics*, eds. L. Ouahab and E. Yagubskii, Kluwer Academic Publishers, Dordrecht, The Netherlands, 2003, p. 186.
190. W. Press and M. Prager, *J. Chem. Phys.*, 1977, **67**, 5752.
191. P. Schiebel, A. Hoser, W. Prandl, G. Heger, W. Paulus and P. Schweiss, *J. Phys.: Condens. Matter*, 1994, **6**, 10989.
192. S. Hill, R. S. Edwards, J. M. North, K. Park and N. S. Dalal, *Polyhedron*

Proceedings of the 8th International Conference on Molecule-Based Magnets (ICMM 2002), 2003, **22**, 1889-1896.
193. K. J. Cho, D. W. Ryu, H. Y. Kwak, J. W. Lee, W. R. Lee, K. S. Lim, E. K. Koh, Y. W. Kwon and C. S. Hong, *Chem. Commun.*, 2012, **48**, 7404.
194. R. Bagai, W. Wernsdorfer, K. A. Abboud and G. Christou, *J. Am. Chem. Soc.*, 2007, **129**, 12918.
195. W. Wernsdorfer, N. Aliaga-Alcalde, R. Tiron, D. N. Hendrickson and G. Christou, *J. Magn. Magn. Mater.*, 2004, **272-276**, 1037.
196. S. Carretta, P. Santini, G. Amoretti, M. Affronte, A. Candini, A. Ghirri, I. S. Tidmarsh, R. H. Laye, R. Shaw and E. J. L. McInnes, *Phys. Rev. Lett.*, 2006, **97**, 207201.
197. S. Carretta, P. Santini, G. Amoretti, M. Affronte, A. Candini, A. Ghirri, I. S. Tidmarsh, R. H. Laye, R. Shaw and E. J. L. McInnes, *Solid State Sciences*, 2009, **11**, 778.
198. J. R. Hawkett, Ph. D, University of Manchester, 2010.
199. M. J. Collins and H. F. Henneike, *Inorg. Chem.*, 1973, **12**, 2983.
200. D. V. Soldatov, A. T. Henegouwen, G. D. Enright, C. I. Ratcliffe and J. A. Ripmeester, *Inorg. Chem.*, 2001, **40**, 1626.
201. M. Murrie, *Chem. Soc. Rev.*, 2010, **39**, 1986.
202. E. Yang, D. Hendrickson, W. Wernsdorfer, M. Nakano, L. Zakharov, R. Sommer, A. Rheingold, M. Ledezma-Gairaud and G. Christou, *J. Appl. Phys.*, 2002, **91**, 7382.
203. K. Galloway, A. Whyte, W. Wernsdorfer, J. Sanchez-Benitez, K. Kamenev, A. Parkin, R. Peacock and M. Murrie, *Inorg. Chem.*, 2008, **47**, 7438.
204. J. Liu, S. Datta, E. Bolin, J. Lawrence, C. Beedle, E. Yang, P. Goy, D. Hendrickson and S. Hill, *Polyhedron*, 2009, **28**, 1922.
205. B. Moubaraki, K. S. Murray, T. A. Hudson and R. Robson, *Eur. J. Inorg. Chem.*, 2008, **29**, 4525.
206. D.-H. Wu, D. Guo, Y. Song, W. Huang, C. Duan, Q. Meng and O. Sato, *Inorg. Chem.*, 2009, **48**, 854.
207. Y.-Z. Zhang, W. Wernsdorfer, F. Pan, Z.-M. Wang and S. Gao, *Chem. Commun.*, 2006, 3302.
208. X.-T. Wang, B.-W. Wang, Z.-M. Wang, W. Zhang and S. Gao, *Inorg. Chim. Acta*, 2008, **361**, 3895.
209. A. Ferguson, A. Parkin, J. Sanchez-Benitez, K. Kamenev, W. Wernsdorfer and M. Murrie, *Chem. Commun.*, 2007, 3473.
210. M.-H. Zeng, M.-X. Yao, H. Liang, W.-X. Zhang and X.-M. Chen, *Angew. Chem. Int. Ed.*, 2007, **46**, 1832.
211. V. Chandrasekhar, B. M. Pandian, R. Azhakar, J. J. Vittal and R. Clérac, *Inorg. Chem.*, 2007, **46**, 5140.
212. V. Chandrasekhar, B. M. Pandian, J. J. Vittal and R. Clérac, *Inorg. Chem.*, 2009, **48**, 1148.
213. T. A. Hudson, K. J. Berry, B. Moubaraki, K. S. Murray and R. Robson, *Inorg. Chem.*, 2006, **45**, 3549.
214. J. A. Coome, A. E. Goeta, J. A. K. Howard and M. R. Probert, *J. Appl. Cryst.*, 2012, **45(2)**, 292.
215. A. Altomore, G. Cascarano, C. Giacovazzo, A. Guagliardi, M. C. Burla, G. Polidori and M. Camalli, *J. Appl. Cryst.*, 1994, **27**, 435.
216. A. A. Coelho, *TOPAS-Academic V5*, 2012, Coelho Software, Brisbane, Australia.
217. A. Parkin, S. M. Harte, A. E. Goeta and C. C. Wilson, *New J. Chem.*, 2004, **28**, 718.
218. J. M. Cole, H.-B. Bürgi and G. J. McIntyre, *Phys. Rev. B*, 2011, **83**, 224202.

219. H. Andres, J. M. Clemente-Juan, M. Aebersold, H. U. Güdel, E. Coronado, H. Büttner, G. Kearly, J. Melero and R. Burriel, *J. Am. Chem. Soc.*, 1999, **121**, 10028.
220. A. B. Boeer, A.-L. Barra, L. F. Chibotaru, D. Collison, E. J. L. McInnes, R. A. Mole, G. G. Simeoni, G. A. Timco, L. Ungur, T. Unruh and R. E. P. Winpenny, *Angew. Chem. Int. Ed.*, 2011, **50**, 4007-4011.
221. J. M. Clemente-Juan, E. Coronado, A. Gaita-Ariño, C. Giménez-Saiz, G. Chaboussant, H.-U. Güdel, R. Burriel and H. Mutka, *Chem. Eur. J.*, 2002, **8**, 5701.
222. J. Ollivier, H. Casalta, H. Schober, J. C. Cook, P. Malbert, M. Locatelli, C. Gomez, S. Jenkins, I. J. Sutton and M. Thomas, *Appl. Phys. A*, 2002, **74 [Suppl.]**, S305.
223. J. R. Stewart, P. P. Deen, K. H. Andersen, H. Schober, J.-F. Barthelemy, J. M. Hillier, A. P. Murani, T. Hayes and B. Lindenau, *J. Appl. Cryst.*, 2009, **42**, 69.
224. J. Mesot, S. Janssen, L. Holitzner and R. Hempelmann, *J. Neutr. Res.*, 1996, **3**, 293.
225. S. Janssen, J. Mesot, L. Holitzner, A. Furrer and R. Hempelmann, *Physica B: Condensed Matter*, 1997, **234-236**, 1174.
226. O. Waldmann, *Phys. Rev. B*, 2003, **68**, 174406.
227. J. Nehrkorn, S. Mukherjee, S. Stuiber, H. Mutka, T. Strässle, G. Christou and O. Waldmann, *Phys. Rev. B*, 2012, **86**, 134417.
228. J. J. Borrás-Almenar, J. M. Clemente-Juan, E. Coronado and B. S. Tsukerblat, *J. Comput. Chem.*, 2001, **22**, 985.
229. G. L. Squires, *Introduction to the Theory of Neutron Scattering*, Dover Publications, Inc., Mineola, NY, 1978.
230. A. R. Farrell, J. A. Coome, M. R. Probert, A. E. Goeta, J. A. K. Howard, M.-H. Lemée-Cailleau, S. Parsons and M. Murrie, *CrystEngComm*, 2013, **15**, 3423.
231. V. A. Milway, F. Tuna, A. R. Farrell, L. E. Sharp, S. Parsons and M. Murrie, *Angew. Chem. Int. Ed.*, 2013, **52**, 1949.

Appendix A: Experiments carried out

Routine 100 K and 30 K X-ray diffraction experiments were all performed by me and are not included in this list. Unless otherwise noted, I attended all of the experiments listed.

$[Mn_{12}O_{12}(O_2CMe)_{16}(H_2O)_4]\cdot 2MeCO_2H\cdot 4H_2O$ (1)

Single-crystal X-ray diffraction	XIPHOS at Durham	May 2011
Single-crystal neutron diffraction	VIVALDI at ILL	May 2011

$[Mn_3O(Et\text{-}sao)_3(ClO_4)(MeOH)_x(H_2O)_{3-x}]$ (5)

Single-crystal neutron diffraction	D19 at ILL	June 2012
Single-crystal neutron diffraction	KOALA at ANSTO	April 2012

- Did not attend experiment, but did carry out structure solution and refinement.

$[Ni_4(dea)_4Cl_4]\cdot 4MeCN\cdot 0.6H_2O$ (9)

Single-crystal neutron diffraction	VIVALDI at ILL	September 2010
High-pressure X-ray diffraction	I19 at DIAMOND	April 2010

- This experiment was not successful and so the results are not included here.

$(C(NH_2)_3)_8[Co_4(cit)_4]\cdot 4H_2O$ (18) and deuterated analogue (19)

Inelastic neutron scattering	IN5 at ILL	June 2010

- Data treatment carried out by Dr Grégory Chaboussant

Neutron powder diffraction	HRPD at ISIS	July 2010
Single-crystal neutron diffraction	VIVALDI at ILL	July/September 2011
Polarised neutron diffraction	D7 at ILL	December 2012

- Data treatment carried out by Dr Stefan T. Ochsenbein

Appendix B: Conference presentations

I attended and presented a poster entitled 'The Low Temperature Structure of a Ni_4 SMM at 1.7 K by using single-crystal neutron diffraction' at the following conferences and meetings.

Universities of Scotland Inorganic Chemistry Conference (USIC)
July 21st – 22nd 2011, University of Glasgow

European Conference on Molecular Magnetism (ECMM)
November 22nd – 25th 2011, Paris

Scottish Dalton Meeting
April 11th 2012, University of Strathclyde

Appendix C: X-ray crystal structures

During my Ph.D., I collected and analysed single-crystal X-ray data for other members of the research group. Several of these are discussed in a published article (see Appendix D). The most interesting of the others are presented here briefly.

A series of heterometallic $\{Ln^{III}Mn^{III}\}$ one-dimensional chains (Ln = Gd [**20**], Nd [**21**], Eu [**22**]) was synthesised by Dr Victoria Milway. The chains consist of alternating Ln^{III} and Mn^{III} ions and are described by the formulae $([MnLn(H_2btp)(NO_3)(H_2O)_3]\cdot NO_3\cdot 2H_2O)_n$ (**20**, **21**) and $([MnEu(H_2btp)(NO_3)_2(H_2O)]\cdot 0.71MeOH)_n$ (**22**). Each Mn^{III} is enclosed by a bis-tris propane ligand {2,2'-(propane-1,3-diyldiimino)bis[2-(hydroxymethyl)-propane-1,3-diol]} (H_6btp, figures C-1, C-2). Four of the arms are deprotonated and bridge the Mn^{III} and Ln^{III} ions.

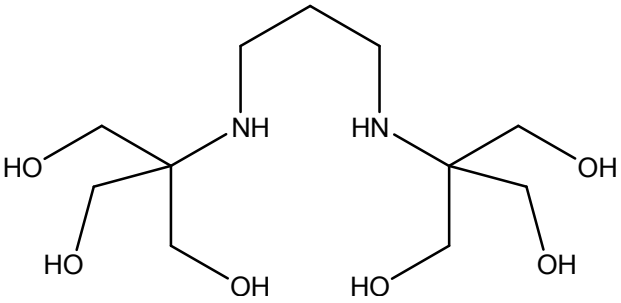

Figure C-1: The bis-tris propane ligand.

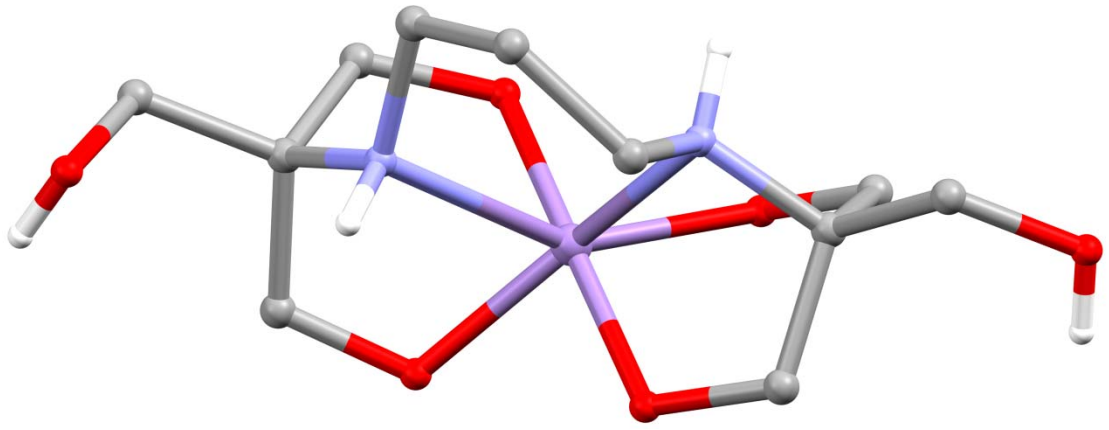

Figure C-2: The binding mode of the bis-tris propane ligand in **20**, **21** and **22**. The ligand is four times deprotonated in each of these species. Atom colours: Mn, purple; O, red; N, blue; C, grey; H, white. H atoms in CH_2 groups are omitted for clarity.

The structures of **20** and **21** are very similar (see figure C-3); both crystallise in the acentric orthorhombic space group $P2_12_12_1$ with approximately the same unit cell parameters and are essentially isostructural. Each lanthanide has a nitrate ligand and three water ligands coordinated to it, and additionally there are two waters of crystallisation and one nitrate in the lattice.

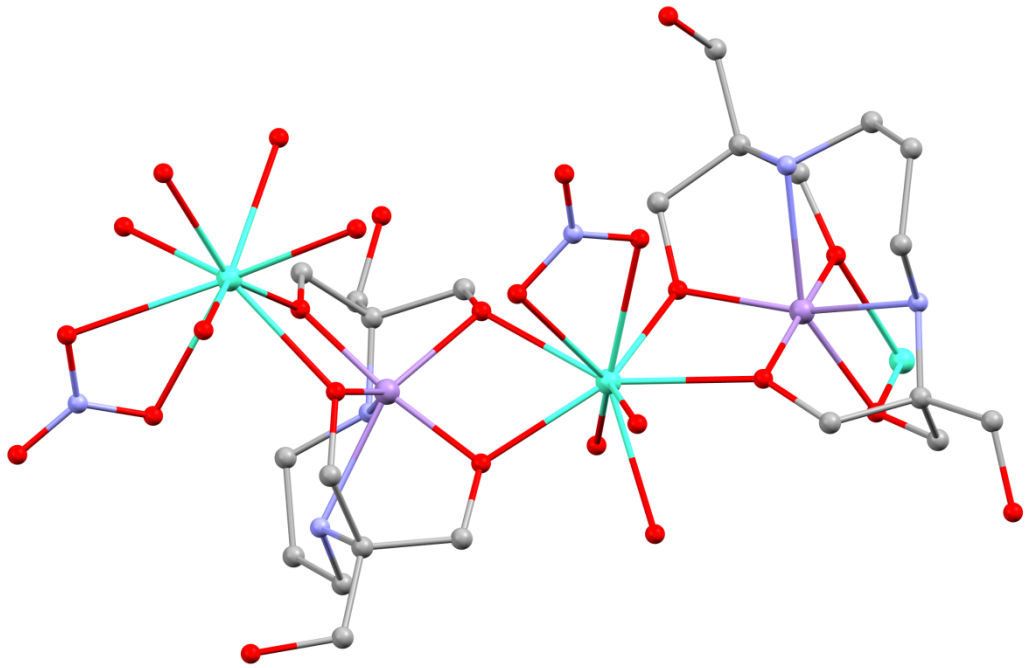

Figure C-3: A section of the one-dimensional chain structure of **20** (essentially isostructural with **21**). Atom colours as previously defined; Gd, turquoise. H atoms are omitted for clarity.

Both structures are well-ordered with low values for R_1 and wR_2 (full crystallographic data given in table C.1). All non-hydrogen atoms are refined anisotropically in both **20** and **21**. H atoms in CH_2 groups were placed in calculated positions. All other H atoms were found in a Fourier difference map. All H atoms were allowed to ride on their parent atoms. Refinement of the Flack parameter for each structure reveals that the absolute configurations are not the same. **20** and **21** form helical chains with different handedness to each other, *i.e.* one is the inverted form of the other. It is not yet known whether the handedness of **20** and **21** is fixed for crystals of the same species or if different crystals from the same reaction or other repeated reactions will contain the opposite enantiomer. **22**, on the other hand, crystallises in the centric orthorhombic space group *Pcab*, an alternative setting of the more common *Pbca*. The unit cell of **22** is approximately twice as large as that of **20** and **21**. The structure of **22** is shown in figure C-4. The Eu^{III} has two nitrate ligands and only a single water ligand, while there is a part-weight methanol of crystallisation in the lattice. Part of the H_2btp^{4-} ligand is disordered over two positions. The

occupancies of each fragment were constrained to sum to unity and refined. The occupancy of the methanol of crystallisation was also allowed to refine. H atoms in CH_2 groups were placed in calculated positions. All other H atoms were found in a Fourier difference map. All H atoms were allowed to ride on their parent atoms. Due to the centricity of the space group, **22** cannot exist solely as left-handed or right-handed helices; the inversion symmetry means that there is an equal number of each in the crystal.

Table C.1: Crystallographic data for compounds **20**, **21** and **22** measured at 100 K.

	20	**21**	**22**
Formula	$C_{11}H_{32}GdMnN_4O_{17}$	$C_{11}H_{32}MnN_4NdO_{17}$	$C_{11.71}H_{26.85}EuMnN_4O_{13.71}$
M_w	704.57	691.56	650.03
Crystal system	Orthorhombic	Orthorhombic	Orthorhombic
Space group	$P2_12_12_1$	$P2_12_12_1$	*Pcab*
a [Å]	11.9338(3)	12.0314(3)	11.9477(5)
b [Å]	12.6981(3)	12.6212(5)	17.9916(8)
c [Å]	14.7886(2)	14.9152(5)	20.8709(8)
V [Å^3]	2241.01(8)	2264.88(13)	4486.4(3)
Z	4	4	8
T [K]	100(2)	100(2)	100(2)
Radiation	X-ray, Mo K_α	X-ray, Mo K_α	X-ray, Mo K_α
λ [Å]	0.71073	0.71073	0.71073
D_c [g cm^{-3}]	2.088	2.028	1.925
μ [mm^{-1}]	3.587	2.914	3.405
Meas./indep. refl.	40001/4093	20784/4146	23717/4097
R_{int}	0.056	0.050	0.094
Obs. refl. [$I > 2\sigma(I)$]	3996	3973	2571
wR_2	0.0318	0.0491	0.0969
R_1	0.0169	0.0278	0.0905
Goodness of fit on F^2	0.9454	0.9449	0.9718
Flack parameter	0.013(8)	0.006(13)	-
$\Delta\rho_{max,min}$ [e Å^{-3}]	0.54/-0.61	0.36/-0.29	2.11/-1.75

[a] $wR_2 = \{\sum[w(F_O^2 - F_C^2)^2]/\sum[w(F_O^2)^2]\}^{1/2}$

[b] $R_1 = \sum||F_O| - |F_C||/\sum|F_O|$

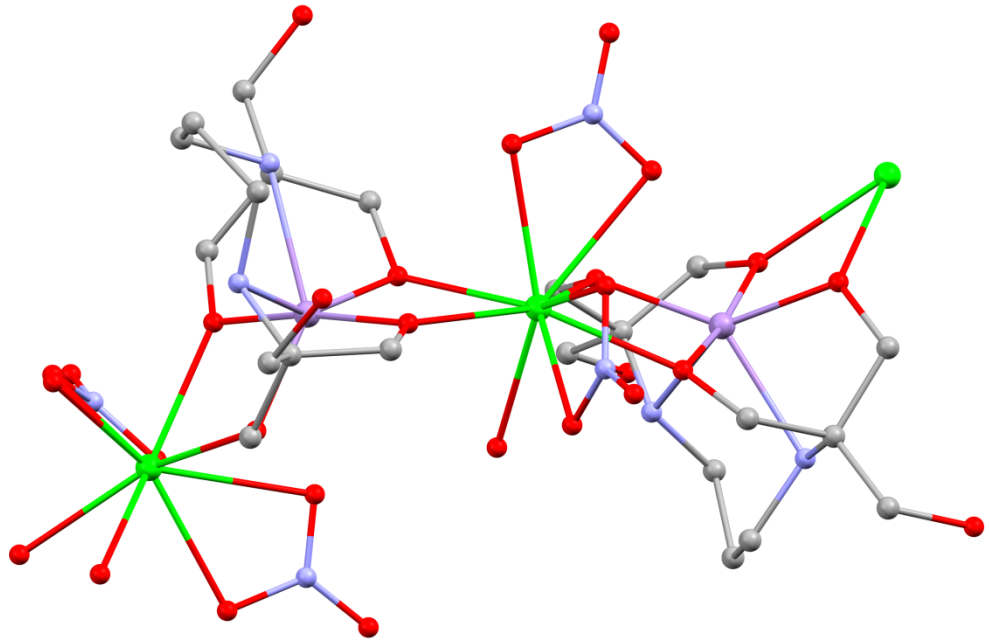

Figure C-4: A section of the one-dimensional chain structure of **22** (disorder in ligand is not shown). Atom colours as defined previously; Eu, green. H atoms are omitted for clarity.

Appendix D: Authored manuscripts

The work on Mn_{12}-acetate (**1**) and desolvated products **2** and **3** is the subject of a published manuscript entitled 'Ultra-low temperature structure determination of a Mn_{12} single-molecule magnet and the interplay between lattice solvent and structural disorder'.[230] I also contributed to a manuscript entitled 'Directed Synthesis of $\{Mn_{18}Cu_6\}$ Heterometallic Complexes';[231] I carried out X-ray crystallography including data collection, structure solution, refinement and final publication of all three structures described therein.

Appendix E: Mass spectra

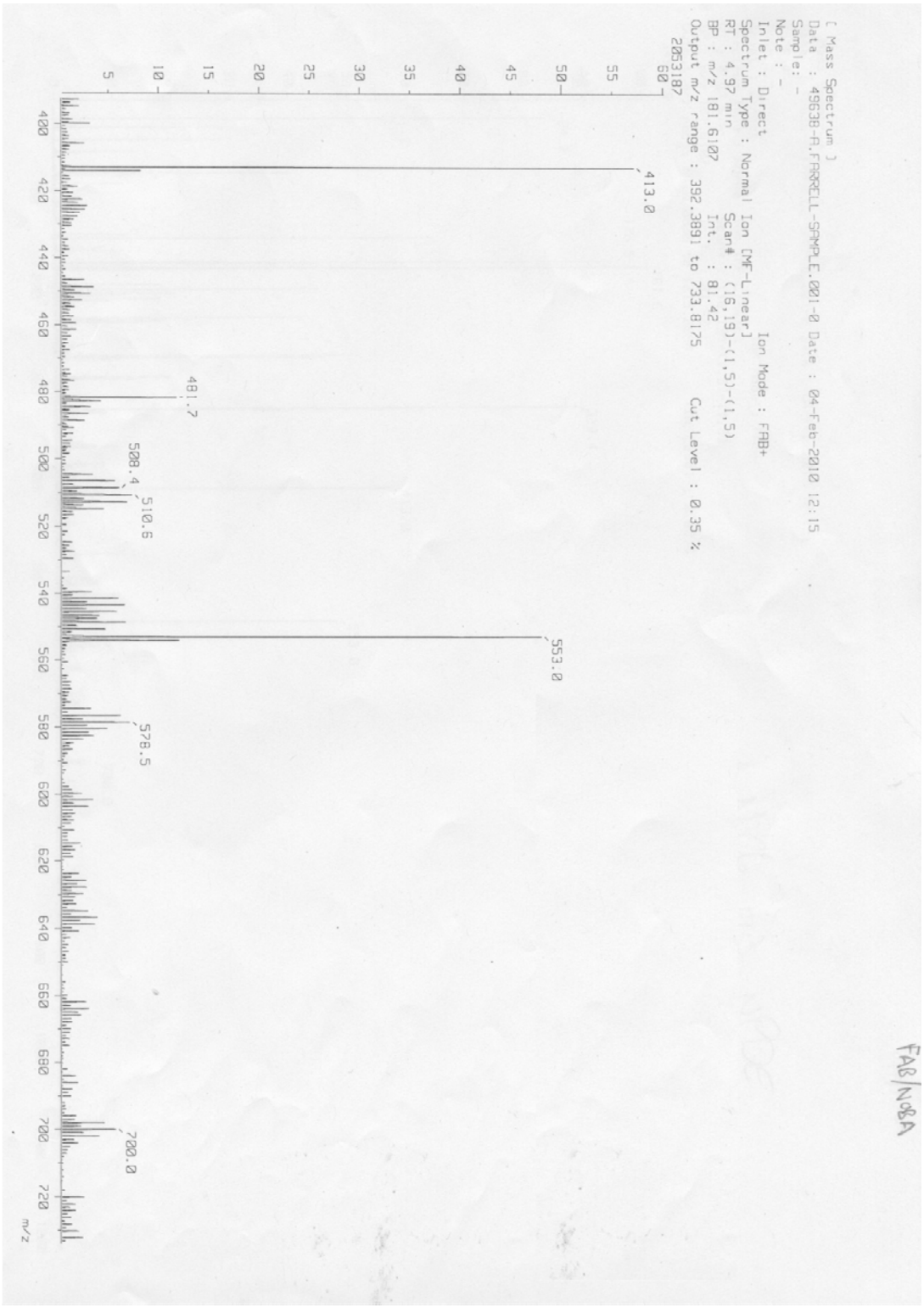

Figure E-1: The mass spectrum for the filtrate obtained from the reaction of $NiCl_2 \cdot 6H_2O$, *N*-phenyldiethanolamine, tris and NaOMe in MeOH.

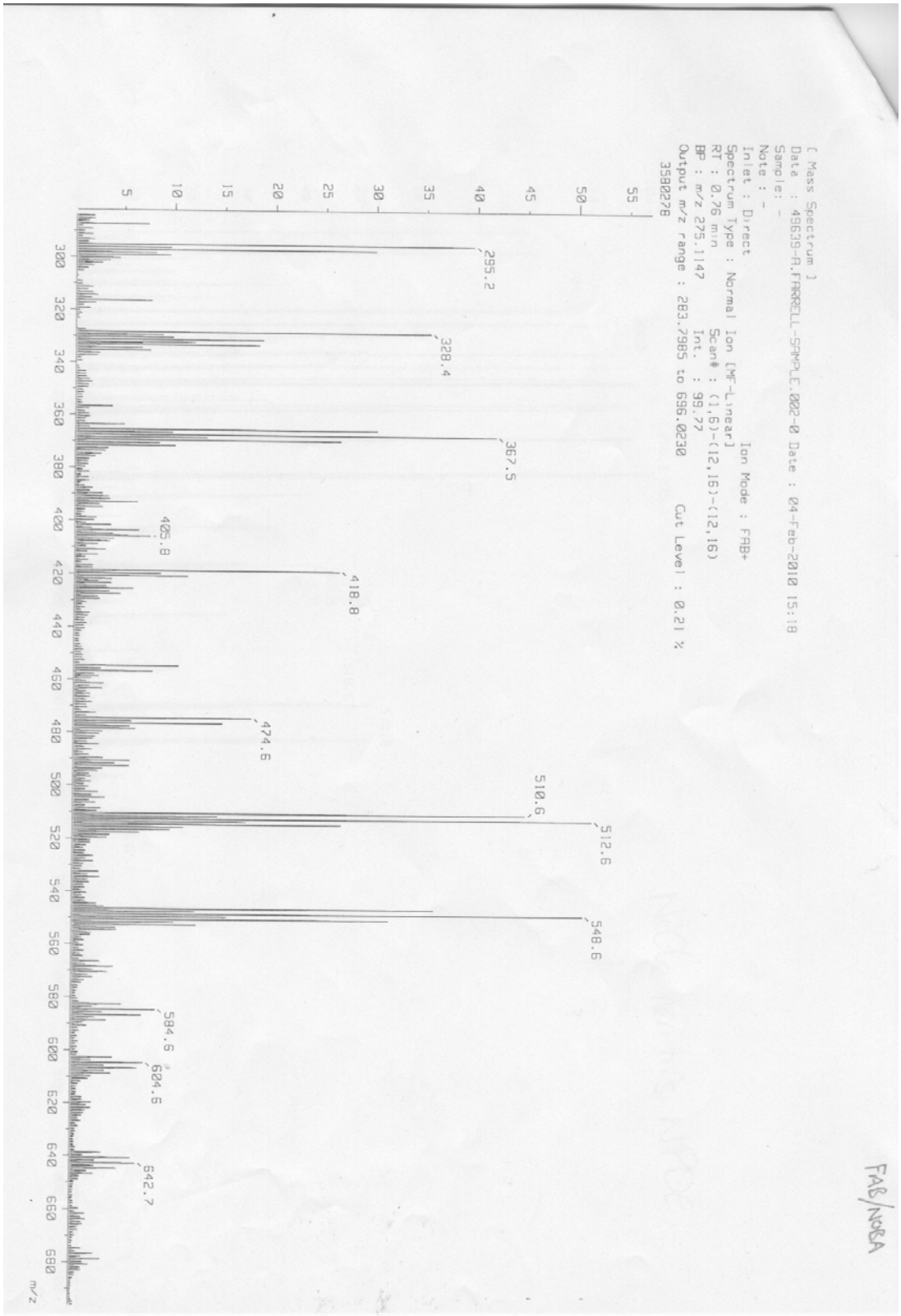

Figure E-2: The mass spectrum for the filtrate obtained from the reaction of $NiCl_2 \cdot 6H_2O$, *N*-phenyldiethanolamine and NaOMe in MeOH.

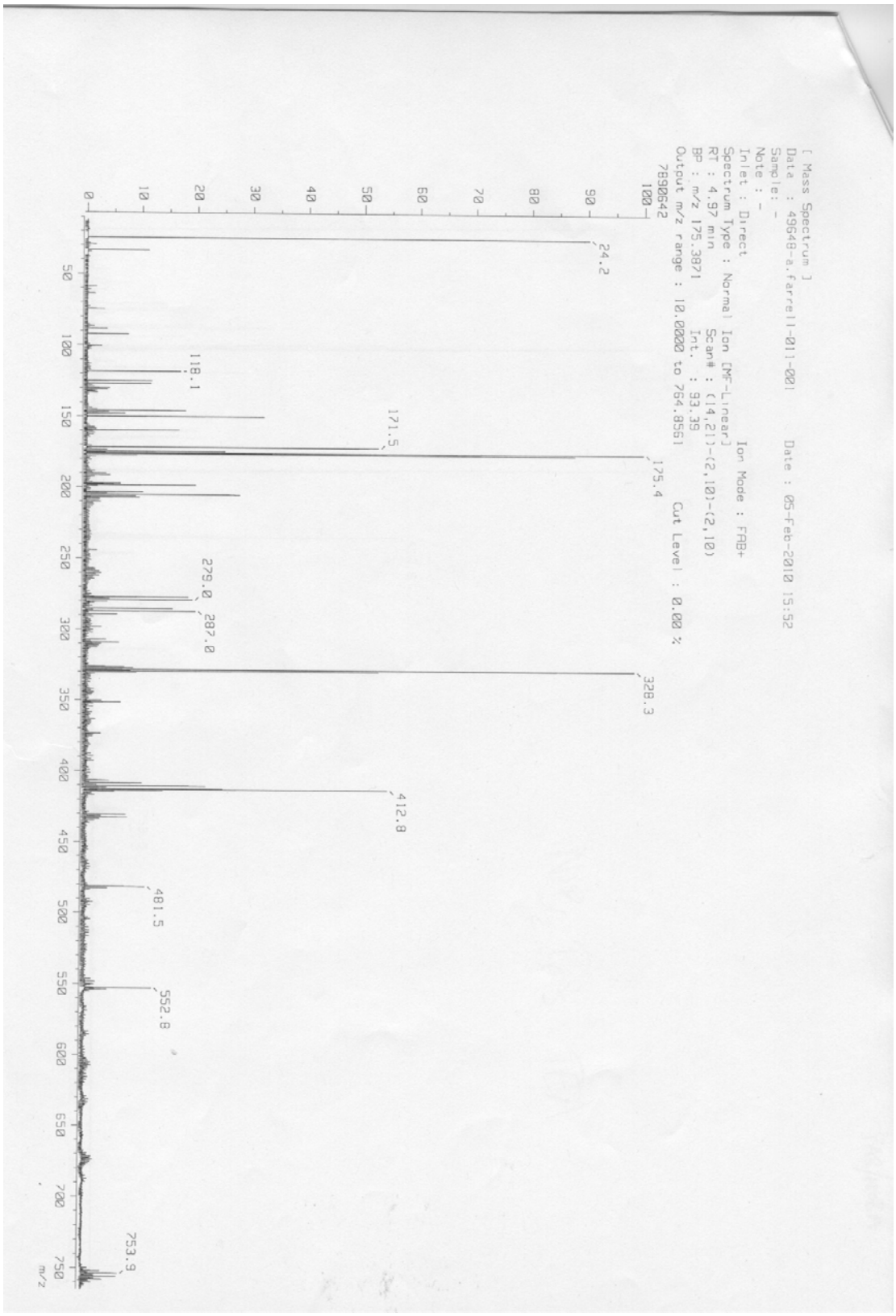

Figure E-3: The mass spectrum for the filtrate obtained from the reaction of $NiBr_2 \cdot 2H_2O$, triethanolamine, tris and NaOMe in MeOH.

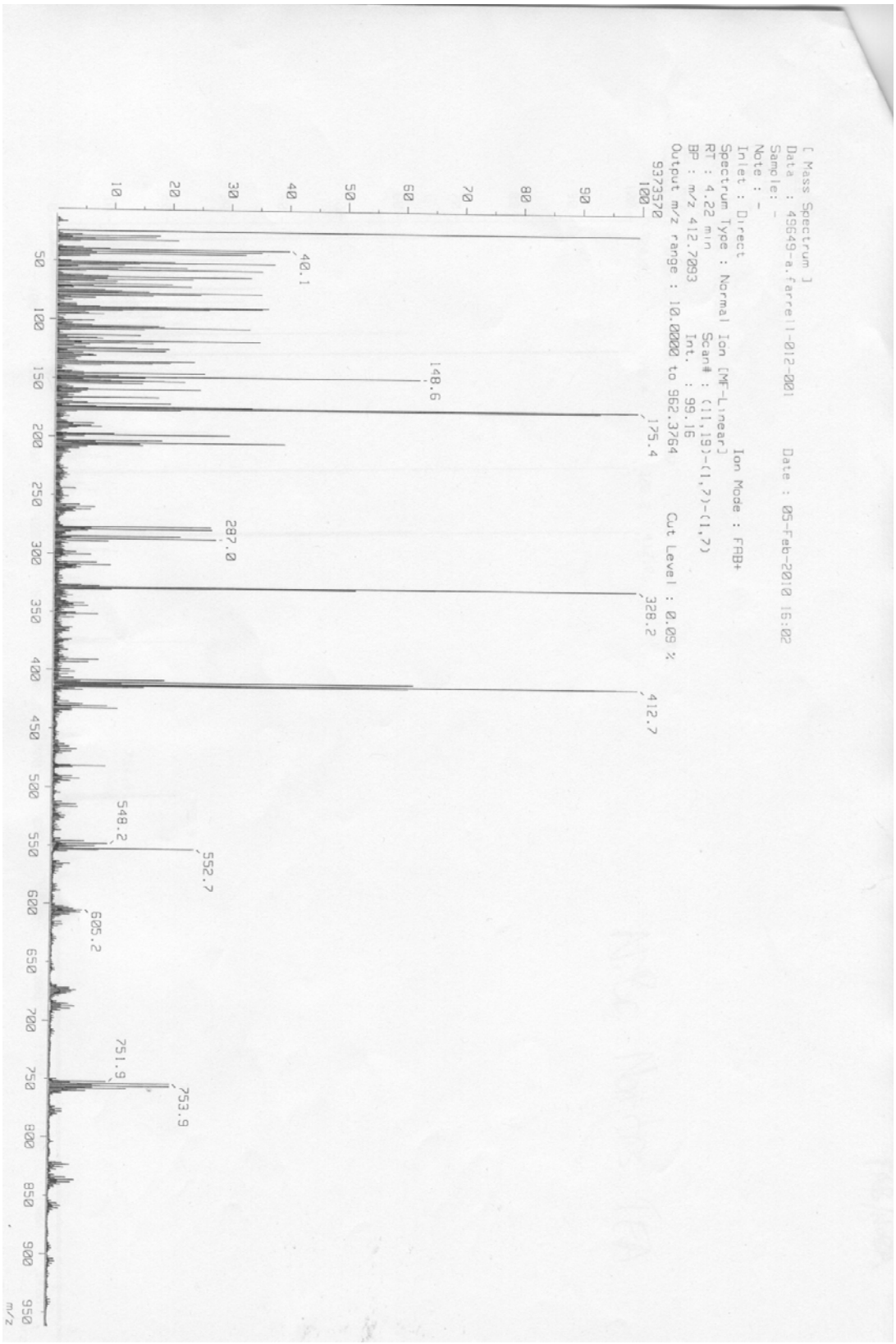

Figure E-4: The mass spectrum for the filtrate obtained from the reaction of $NiBr_2 \cdot 2H_2O$, triethanolamine and NaOMe in MeOH.